Numerical Simulation of the Structural Response of a Composite Rocket Nozzle during the Ignition Transient

Jean- François Philippe Pitot de la Beaujardiere

Submitted in fulfillment of the academic requirements for the degree of Master of Science in Mechanical Engineering

December, 2009

Supervisor: Professor Glen Bright

Co-Supervisor: Professor Evgeny Morozov

ACKNOWLEDGEMENTS

I would like to express my sincere gratitude to my supervisor, Professor Glen Bright of the University of KwaZulu-Natal and my co-supervisor, Professor Evgeny Morozov of the University of New South Wales for their much-valued guidance, encouragement and patience during the course of this degree.

In addition, I wish to give special thanks to the National Research Foundation for their generous funding of this work.

ABSTRACT

The following dissertation describes an investigation of the structural response behaviour of a composite solid rocket motor nozzle subjected to thermal and pressure loading during the motor ignition period, derived on the basis of a multidisciplinary numerical simulation approach. To provide quantitative and qualitative context to the results obtained, comparisons were made to the predicted aerothermostructural response of the nozzle over the entire motor burn period.

The study considered two nozzle designs – an exploratory nozzle design used to establish the basic simulation methodology, and a prototype nozzle design that was employed as the primary subject for numerical experimentation work. Both designs were developed according to fundamental solid rocket motor nozzle design principles as non-vectoring nozzles for deployment in medium sized solid rocket booster motors. The designs feature extensive use of spatially reinforced carbon-carbon composites for thermostructural components, complemented by carbon-phenolic composites for thermal insulation and steel for the motor attachment substructures.

All numerical simulations were conducted using the ADINA multiphysics finite element analysis code with respect to axisymmetric computational domains. Thermal and structural models were developed to simulate the structural response of the exploratory nozzle design in reference to the instantaneous application of pressure and thermal loading conditions derived from literature. Ignition and burn period response results were obtained for both quasi-static and dynamic analysis regimes.

For the case of the prototype nozzle design, a flow model was specifically developed to simulate the flow of the exhaust gas stream within the nozzle, for the provision of transient and steady loading data to the associated thermal and structural models. This arrangement allowed for a more realistic representation of the interaction between the fluid, thermal and structural fields concerned. Results were once again obtained for short and long term scenarios with respect to quasi-static and dynamic interpretations. In addition, the aeroelastic interaction occurring between the nozzle and flow field during motor ignition was examined in detail.

The results obtained in the present study provided significant indications with respect to a variety of response characteristics associated with the motor ignition period, including the magnitude and distribution of the displacement and stress responses, the importance of inertial effects in response computations, the stress response contributions made by thermal and pressure loading, the effect of loading condition quality, and the bearing of the rate of ignition on the calculated stress response.

Through comparisons between the response behaviour predicted during the motor ignition and burn periods, the significance of considering the ignition period as a qualification and optimisation criterion in the design of characteristically similar solid rocket motor nozzles was established.

DECLARATION

I hereby declare that this dissertation presents my own unaided work except where due acknowledgement has been given to others. This dissertation is being submitted to the University of KwaZulu-Natal for the Degree of Master of Science in Mechanical Engineering, and has not been submitted previously for any other degree or examination.

_____ Date _____

Jean-François Pitot de la Beaujardiere

_____ Date _____

Professor Glen Bright

To my parents, Marian and Gerard, whose boundless love, support and selflessness have cast the rock upon which I am now privileged to stand.

TABLE OF CONTENTS

NOMENCLATURE

Symbols

x, y, z	Cartesian coordinates
r, θ, z	Cylindrical coordinates
ρ	Mass density
t	Time
$\vec{v}$	Velocity vector
$\vec{\tau}_a$	Stress tensor
$\vec{f}^{\,B}$	Body force vector
E	Specific total energy
$\vec{q}$	Heat flux vector
q^B	Rate of heat generation
e	Specific internal energy
p	Static pressure
λ	Kinematic viscosity
μ	Dynamic viscosity
$\vec{I}$	Identity vector
k	Coefficient of thermal conduction
θ	Fluid temperature
$\vec{e}_a$	Velocity strain tensor
C_p	Specific heat at constant pressure
C_v	Specific heat at constant volume
$\vec{F}_n$	Inviscid flux term
$\vec{G}_n$	Viscous flux term
r, s	Two-dimensional isoparametric coordinate system
C	Specific heat capacity for solid

T	Solid temperature
k	Isotropic coefficient of thermal conduction
k_r, k_θ, k_z	Coefficients of thermal conduction in the radial, circumferential and axial directions
Q	Heat source or sink term
$\boldsymbol{C}$	Heat capacity matrix
$\boldsymbol{K}^{\boldsymbol{k}}$	Conductivity matrix
$\boldsymbol{K}^{\boldsymbol{c}}$	Convection matrix
q^s	Surface convective load
h	Convective heat transfer coefficient
θ_e	Environmental temperature
θ^s	Surface temperature
$\sigma_{rr}, \sigma_{\theta\theta}, \sigma_{zz}$	Radial, circumferential and axial stresses
$\sigma_{\theta r}, \sigma_{r\theta}, \sigma_{zr}, \sigma_{rz}, \sigma_{z\theta}, \sigma_{\theta z}$	Shear Stresses
u_r, u_θ, u_z	Radial, circumferential and axial displacements
c_{ij}	Compliance coefficients
$\varepsilon_{rr}, \varepsilon_{\theta\theta}, \varepsilon_{zz}$	Radial, circumferential and axial strains
$\varepsilon_{\theta z}, \varepsilon_{rz}, \varepsilon_{r\theta}$	Shear strains
$\alpha_r, \alpha_\theta, \alpha_z$	Radial, circumferential and axial coefficients of thermal expansion
ΔT	Instantaneous and initial temperature difference
E_r, E_θ, E_z	Elastic moduli with relative to the r, θ, z directions
$\nu_{\theta r}, \nu_{zr}, \nu_{\theta z}$	Poisson's ratios
$G_{r\theta}, G_{rz}, G_{\theta z}$	Shear moduli
$\boldsymbol{M}$	Element assemblage mass matrix
$\ddot{\boldsymbol{U}}$	Nodal acceleration vector
$\boldsymbol{U}$	Nodal displacement vector
$\boldsymbol{K}$	Element assemblage stiffness matrix

$\boldsymbol{R}$	Element assemblage load vector
$\rho^{(m)}$	Elemental mass density
$\boldsymbol{H}^{(m)}$	Displacement interpolation matrix
$\boldsymbol{B}^{(m)}$	Strain-displacement matrix
$\boldsymbol{C}^{(m)}$	Elasticity matrix
$\boldsymbol{R_B}$	Body force vector
$\boldsymbol{R_S}$	Surface force vector
$\boldsymbol{R_I}$	Initial stress load vector
$\boldsymbol{R_c}$	Concentrated load vector
d_f	Fluid displacement at interface
d_s	Solid displacement at interface
τ_f	Fluid stresses at interface
τ_s	Solid stresses at interface
v	Fluid velocity at interface
$\dot{d}_s$	Solid velocity at interface
$F(t)$	Force exerted on solid nodes at interface
h^d	Virtual quantity of solid displacement
t*	Normalised time
r*	Normalised radius
α	Thermal diffusivity
γ	Thermal penetration depth
$\Delta r_{\max}$	Maximum element dimension in the radial direction
Δr	Particular element dimension in the radial direction
N	Resolution factor

Abbreviations

SRM	Solid Rocket Motor
C-C	Carbon-Carbon
FEM	Finite Element Method

CFD	Computational Fluid Dynamics
SRN1	Solid Rocket Nozzle 1
SRN2	Solid Rocket Nozzle 2
TVC	Thrust Vector Control
C-P	Carbon-Phenolic
ITE	Integral Throat and Entrance
2D	Two-dimensional
3D	Three-dimensional
4D	Four-dimensional
ATS	Automatic Time Stepping
CFL	Courant-Friedrichs-Lewy
FSI	Fluid-Structure Interaction
BC	Boundary Condition
SP	Sample Point
TPZ	Thermal Penetration Zone

LIST OF FIGURES

CHAPTER 1

CHAPTER 2

CHAPTER 3

CHAPTER 4

CHAPTER 5

CHAPTER 6

APPENDIX A

LIST OF TABLES

APPENDIX A

CHAPTER 1

Introduction

The current state of solid rocket motor (SRM) propulsion technology serves testament to the enormous advancements that have been made in the fields of thermodynamics, fluid mechanics, materials science, design and manufacturing, since the first rudimentary solid rocket motors were developed in the ancient world. Today, technological advancements continue to be made at an impressive rate, as lower cost propulsion units of lower mass and increased reliability that can generate even higher levels of thrust are sought. This is particularly true for the case of SRMs employed to provide propulsion for space launch vehicles, as improvements in the technology's operational qualities ultimately lead to a decrease in the cost of space access – whether it be for commercial, scientific or military purposes.

The most significant deployment of SRM technology in the space launch vehicle industry is in a first stage 'booster' role, where SRMs are used to generate or contribute towards generating the immense levels of thrust that are required during the initial period of vehicle ascent. A prominent example of this type of application is the United States' Space Transportation System launch vehicle (Day (1970)), colloquially referred to as the space shuttle. This vehicle employs two first stage solid rocket boosters positioned either side of the craft's external liquid propellant tank, as illustrated in Figure 1.1. Other contemporary examples of similar booster SRM arrangements include the European Space Agency's Ariane V (Jorant (1993)), the Japanese Aerospace Exploration Agency's H-IIA (Shibato and Kuroda (2005)) and the Boeing Company's Delta II (Sirko (2003)) launch vehicles.

In addition to this primary booster role, SRMs are also used to a limited extent in high performance / high-altitude operations, where more refined thrust profiles of lower magnitudes are tailored to meet exacting orbital trajectory requirements. This class of application is demonstrated by the Inertial Upper Stage SRM-1 motor (Chase (1978)), and the STAR™ 27 high-altitude motor (Sutton and Biblarz (2001)), amongst others.

Figure 1.1 NASA's Space Transportation System launch vehicle (NASA Image Exchange Website)

As is the case with all chemical rocket motors, an SRM produces thrust by harnessing the energy liberated from a controlled chemical reaction between fuel and oxidiser propellants within a combustion chamber. As the propellants react in a confined volume, the heat of this reaction pressurises the products of combustion, which are subsequently expanded and accelerated through an exhaust nozzle to exceptionally high velocities. It is this conversion of chemical energy into kinetic energy that is responsible for the generation of thrust. SRMs are distinguished from other types of chemical rocket motors in that they generally combust a pre-mixed, heterogeneous mass of solid fuel and oxidiser propellant components that is encased within the combustion chamber.

Exposure to the extreme temperatures and pressures of the exhaust stream makes the environment within which a rocket motor nozzle operates particularly severe. These primary load sources combine to generate significant stresses, and as it is a characteristic of most materials to experience a degradation of mechanical properties with an increase in operating

temperature, it is of primary importance that nozzles are designed with sufficient capacity to dissipate thermal loading, to ensure that structural integrity is not compromised. This detail makes the design of solid rocket motor nozzles particularly challenging, as the action of heat dissipation can generally only be effected by the materials from which SRM nozzles are constructed.

As such, highly specialised, thermally resistant materials have had to be developed to fulfil this requirement. The advent of advanced reinforcements such as glass and carbon fibres has been particularly instrumental in the refinement of these materials, and has allowed for considerable progress to be made in the design optimisation of SRM nozzles (Sutton and Biblarz (2001)). By embedding reinforcing fibres within a refractory or ablative material, a composite material can be created with greatly improved mechanical and thermal properties. Such improvements include an increased specific strength and stiffness, greater thermal shock resilience and an increased resistance to ablation and/or erosion. In addition, the employment of fibre reinforcements enables the response behaviour of thermally resistant composites to be tailored according to particular design requirements, by modifying the type, volume fraction and spatial orientation of the fibres used.

The configurative architecture of medium to large scale SRM nozzles is typically comprised of an assembly of three important elements (Ellis (1975)). The first of these elements is the thermal liner, usually made from a combination of refractory and ablative materials, which serves as the nozzle's interface with the high temperature exhaust stream. The next element, the insulator, is usually manufactured from elastomeric or ablative materials and is employed to thermally isolate the hot thermal liner from the third element, the attach structure. The attach structure, commonly manufactured from aluminium, steel or titanium, provides the structural interface between the nozzle assembly and the SRM casing through which the exhaust gas expansion component of thrust is transferred. Often, the thermal liner components of a nozzle are limited to function solely in their thermal management capacity, without being able to provide overall structural integrity to the nozzle assembly. In such cases, the attach structure must be extended to fulfil this role.

To some extent, this limitation has been overcome by the development of advanced thermostructural composite materials, which are able to retain their strength and stiffness during

extensive periods of exposure to high temperatures without experiencing any significant property deterioration. A prominent thermostructural composite material currently used in SRM nozzle construction is Carbon-Carbon (C-C) (Berdoyes (1993)), which is comprised of carbon fibre reinforcements embedded within a carbon matrix. By employing thermostructural composites to serve as thermal liners, two important functions can be satisfied simultaneously, and the overall structural efficiency of the nozzle can be improved (Ellis (1975)).

In the design of SRM nozzles, as with generally all space launch vehicle components, achieving such gains in structural efficiency through the optimised use of enhanced design features and the most effective deployment of materials is a critical concern. By optimising the individual structures of a launch vehicle, the overall ratio of propellant mass to vehicle mass is increased, which in turn allows for the lifting of heavier payloads and thus an overall reduction in the cost per unit mass of payload launched. Thus, in the highly competitive environment of the global space launch vehicle industry, the exercise of structural optimisation has become a guiding force in the development of vehicle airframes and propulsion systems.

The SRM nozzle design process is a complex one, generally comprised of three individual phases in which the aerodynamic, thermal and structural design requirements of the nozzle are established and satisfied, based upon the anticipated SRM operational parameters. The inevitably high level of interrelatedness between each of these design disciplines mandates that an iterative approach is used to arrive at a nozzle design that most optimally satisfies the criteria of all three disciplines. Additional complications in the way of diverse and highly transient nozzle loading conditions that are difficult to accurately quantify, as well as the nonlinear, anisotropic thermal and mechanical behaviour exhibited by thermal composites, make the process of structural optimisation inherently complex.

The development of numerical simulation techniques has greatly enhanced the rapidity and reliability with which SRM nozzles can be designed and optimised. The finite element method (FEM) has been especially useful in the prediction of the combined thermal and structural response of SRM nozzles under operating loads – to such an extent that the technique has become the standard means of assessing the thermostructural performance of these structures. The discipline of computational fluid dynamics (CFD), whose development has paralleled that of structural numerical simulation, has advanced dramatically in its ability to analyse complex

flow phenomena such as turbulence and reacting and two phase flows. Consequently, CFD has found significant application in the simulation of SRM nozzle flow, allowing for the generation of high fidelity temperature and pressure loading data.

In spite of these considerable advances, the application of numerical simulation techniques in the context of SRM nozzle design continues to undergo significant development, and several elements of nozzle behaviour characterisation, material modelling and hence structural optimisation remain open to further exploration. Although the long-term structural behaviour of SRM nozzles is today well understood, their behaviour during periods of highly transient loading has not been considered as thoroughly. The most significant instance of transient loading is the particularly violent period of motor ignition. During this period, exhaust gas velocities, pressures and temperatures rise to operational values in remarkably short periods of time – having the potential to instigate appreciable stresses in these structures. In spite of the inherent severity of the SRM ignition process, the nature of SRM nozzle response during this event remains distinctly under-investigated, with little literature offering any treatment of the subject. In specific terms, a variety of determinations relating to SRM nozzle behaviour during ignition have yet to be made, including:

1. Whether a quasi-static or dynamic analysis approach is required to accurately capture the physical nature of the response.
2. The degree of aeroelastic coupling that occurs between an SRM nozzle and its associated exhaust stream.
3. The manner and magnitude in which thermal and mechanical load sources contribute to an SRM nozzle's structural response.
4. The sensitivity of the response to adjustments in the rate at which the ignition process is specified to occur.
5. The significance of the overall structural response of an SRM nozzle during the ignition process in comparison to that of the nozzle during the remaining period of the SRM's operation.

In essence therefore, the objective of the current work is to develop and employ numerical structural and fluid models to simulate and subsequently investigate the structural response of composite SRM nozzles during the rapid transient motor ignition period, and further, to compare

this simulated response to that of the nozzle during the considerably longer and steadier motor burn period.

The two nozzle designs considered, Solid Rocket Nozzle 1 (SRN1) and Solid Rocket Nozzle 2 (SRN2) were developed according to fundamental SRM nozzle design principles (Ellis (1975)) as non-vectoring nozzles for deployment in medium sized solid rocket booster motors. As far as materials are concerned, the designs made use of spatially reinforced carbon-carbon and two-dimensional carbon-phenolic composites, in addition to steel as their constituent materials. Modelling and simulation capacity was provided by the ADINA multiphysics finite element code (ADINA v8.5 (2008)), which was used to develop and analyse the axisymmetric thermal, structural and flow models considered.

The analysis of SRN1 was based on a thermal and structural model representation of the nozzle, and employed pressure and temperature loading conditions obtained from literature. The temperature loading condition was applied to the thermal model to derive transient ignition and burn period temperatures distributions. The structural model was subjected to the pressure loading condition in addition to mapped thermal data provided by the thermal model. In this manner, the combined response of the nozzle to thermal and pressure loading could be predicted.

For the analysis of SRN2 however, thermal and pressure loading conditions were derived through the implementation of a flow model specifically developed to simulate the unsteady and steady flow of combustion gases through the nozzle during the ignition and burn periods. Through the solution of the conjugate heat transfer problem, this flow model was used to establish a transient temperature distribution in the nozzle structure from which the induced thermoelastic response in the structure could be computed. On the other hand, wall pressure data were mapped directly onto the structural model to generate the associated structural response by coupling the flow and structural models.

By means of superposition, both response components were combined to determine the effective structural response of the nozzle during simulated motor ignition through the quantification of the resulting displacement and stress histories and distributions. Comparisons between structural responses derived through the implementation of quasi-static and dynamic solution regimes allowed the inertial nature of the response to ignition period loading to be established. In

addition, the nature of the aeroelastic interaction between the nozzle structure and the exhaust flow field during the ignition period was investigated by means of comparing the uncoupled fluid-structure response to the coupled response.

The burn period response of the SRN2 structure was resolved using a thermal and structural model of the nozzle, with loading being applied through the use of unvarying temperature and pressure distributions, derived from an associated flow model. By comparing the structural response derived for this period to that predicted for the ignition period, the significance of the stresses encountered in the nozzle during motor ignition with respect to the generally analysed burn period thermostructural response was established.

CHAPTER 2

Composite Rocket Nozzle Design and Analysis

2.1 Principles of Solid Rocket Motor Operation

Common to the operation of all solid rocket motors is the manner in which propulsive thrust is generated; by the combustion of a premixed solid propellant charge in a confined volume, and the subsequent acceleration of the products of this combustion through an exhaust nozzle. Whilst the process itself is constituted by a collection of complex chemical, fluid dynamic and heat transfer phenomena, in an overall sense, the underlying operating principle of SRMs is comparatively simple. As such, solid rocket motors are in general, significantly less complicated in configuration and construction than their liquid propellant counterparts, which is a considerable advantage of this technology. Based on the works of Sutton (1963) and Sutton and Biblarz (2001), a brief overview of the fundamental principles of solid rocket motor operation will now be provided, in particular reference to booster solid rocket motors used for space launch vehicle applications.

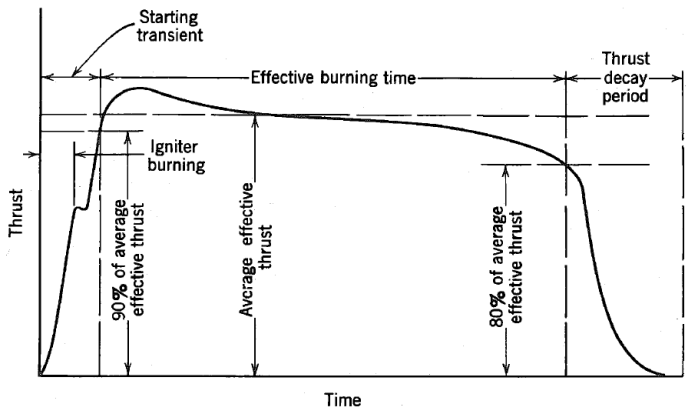

Figure 2.1 Operational phases of an SRM (Sutton (1963)).

The operation of an SRM can effectively be divided into three phases of activity: the starting transient, the effective burning time and the thrust decay period. Figure 2.1 shows a generic

SRM thrust vs. time curve, and indicates the thrust characteristics associated with each of these phases. The starting transient describes the start-up of an SRM; the brief, highly transient period between the initiation of motor ignition and the point at which the motor has begun to generate a functional level of thrust. The effective burning time is the most significant activity phase, defining the relatively long period of stable and sustained thrust generation. That is, the phase in which the motor provides useful propulsion to the launch vehicle. The final phase or thrust decay period describes the rapid fall in the motor's thrust output at the end of its burn, once all of the solid propellant has been consumed. The total duration for which medium to large booster SRMs typically operate ranges between 60 and 120 seconds.

In general terms, an SRM is essentially comprised of four primary components; a propellant grain, an igniter, a motor case, and an exhaust nozzle – each of which fulfils a unique and fundamental function. The arrangement of these principal components is illustrated in Figure 2.2, which depicts a partial cross-sectional view of the Pegasus launch vehicle booster SRM.

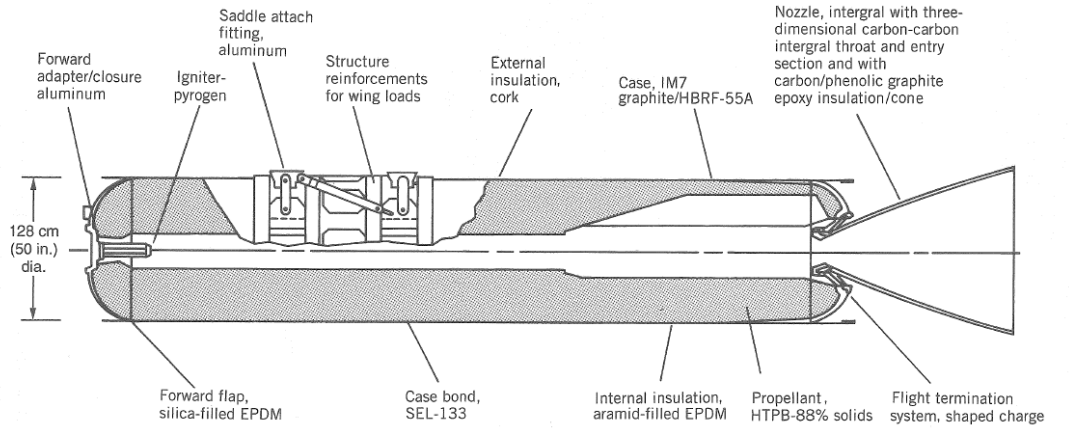

Figure 2.2 Typical design configuration of a booster SRM (Sutton and Biblarz (2001)).

The propellant grain is, in essence, the heterogeneous mass of solid propellant that is combusted within the confines of the motor and is the source of the motor's propulsive energy. In SRMs, combustion occurs at temperatures typically exceeding 3000K, promoting the conversion of

chemical energy to thermal energy at efficiencies that range between 95 and 99.5%. Three main classes of propellant are employed in propulsive applications; composite, double-base and composite-modified double-base. The composite class is however the type used exclusively in contemporary launch vehicle booster SRMs.

Composite propellants liberate thermal energy through the reaction that takes place between the oxidiser and fuel, which is initiated at a particular activation energy level. In their most conventional form, they are manufactured by mixing together a powdered crystalline oxidiser (most commonly ammonium perchlorate) at a mass fraction of between 60 and 72%, a powdered metal (usually aluminium) at a mass fraction of up to 22%, and an elastomeric binder (typically hydroxyl terminated polybutadiene rubber or similar compounds) at a mass fraction of between 8 and 16%. The inclusion of powdered aluminium increases the energy density and hence performance of a motor, but introduces solid particles of aluminium oxide into the exhaust stream, which has certain drawbacks. In non-aluminised propellants, the powdered aluminium component is excluded altogether, resulting in an exclusively gaseous, single phase exhaust stream. The chemical cross-linking of the binder and resulting solidification of the cast propellant grain is generally instigated by the addition of a curing agent and subsequent heat treatment.

For launch vehicle booster SRM applications, propellant grains are typically manufactured in separate segments that are transported to the launch site individually, owing to their considerable size. In terms of their physical arrangement, assembled booster grains are most frequently cylindrical in configuration, featuring a central internal cavity or port running along the motor's longitudinal axis, as illustrated in Figure 2.2. In certain instances however, a set of multiple internal ports may be used.

Various port cross-sectional profiles can be employed, including tube, star, slots and tube, and wagon wheel profiles. It is common place to utilise more than one cross-sectional profile over the length of the grain, as is demonstrated by Figure 2.3, which shows the grain cross-sections for each segment of the Space Shuttle SRM. The initial geometry of the port profile determines the manner in which the motor's thrust will vary over the duration of its operation, that is, whether the level of thrust will remain neutral, progress or regress as the propellant is consumed.

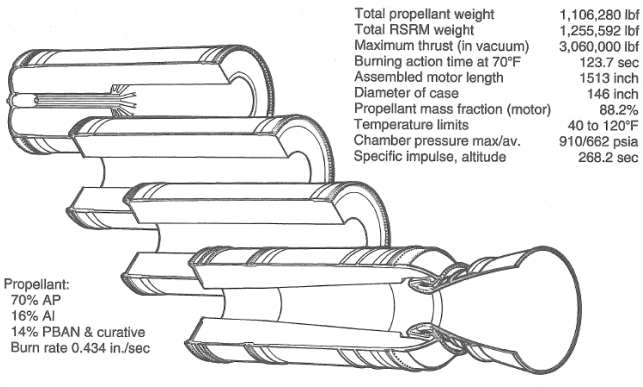

Figure 2.3 Variation of the Space Shuttle SRM's propellant grain port profile (Sutton and Biblarz (2001)).

The SRM ignition process is comprised of a series of complex and highly transient events, generally taking place over a few tenths of a second in the case of large booster SRMs. In general terms, the process can be divided into three specific phases. The first phase, known as the ignition time lag interval, defines ignition activity between the initial activation of the igniter and the point in time at which the first regions of the propellant grain catch alight. The second phase, known as the flame-spreading interval, represents the period after the grain surface first catches alight until all of the remaining exposed surfaces of the grain are ignited. The final phase, known as the chamber-filling interval, covers the last portion of the ignition process during which the combustion chamber is completely filled with combustion gases, and equilibrium chamber pressure and flow are reached. Figure 2.4 shows a typical ignition transient trace for an SRM in terms of both motor chamber pressure and igniter pressure, with the three phases of the ignition process clearly indicated.

Igniters used in large booster SRMs are typically of the pyrogen type and are often mounted at the fore end of a motor, supported by its forward closure in some manner, as depicted in Figure 2.2. A pyrogen igniter is in essence a small SRM, which starts the booster grain combustion process primarily through convective heat transfer between its hot, high velocity exhaust gases and the grain's surface. Such igniters are generally activated by the flow of an electrical current through a heating element that is surrounded by a small quantity of primer material, which in turn energetically decomposes and sets the igniter's propellant grain alight. As the igniter propellant burns, it ejects hot combustion gases and in some cases hot solid

particles or liquid droplets that are aimed down the length of the internal port towards the rear of the motor. These constituents subsequently come into contact with and ignite the exposed surfaces of the grain. Once ignited, combustion occurs on these exposed surfaces and regresses into the virgin propellant grain in a direction normal to the burning front, and at a burning rate that is dependent on a variety of parameters, including the composition of the propellant, the combustion chamber pressure and the combustion gas temperature, amongst others.

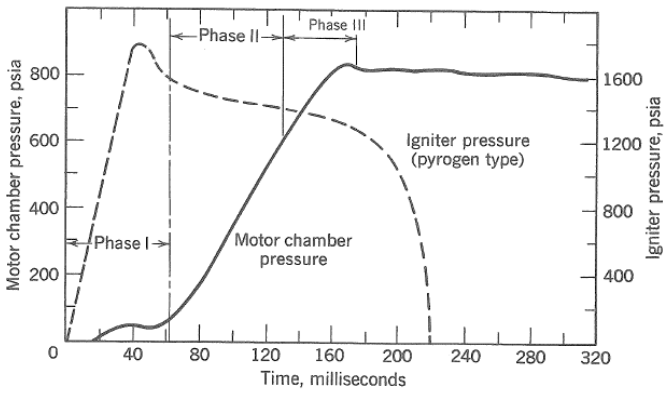

Figure 2.4 The three phases of SRM ignition
(Sutton and Biblarz (2001)).

The tremendous pressures that are developed in an SRM during the process of propellant combustion are contained by the motor's case. Large booster SRM cases generally have lengths of between 2 and 7 times their diameters, and are most frequently constructed in individual sections from high strength steel alloys into which the segmented propellant grains can be cast, although in certain instances, cases may be manufactured as monolithic filament wound composite structures. The assembled case is sealed at its fore end with a forward structural closure of some description, and terminates at its aft end with an adapting boss to accommodate the mounting of the exhaust nozzle. Irrespective of the type of material used to construct it, an SRM case requires some form of thermal protection to prevent it from being heated to failure temperatures during operation, especially in regions of the motor where the case is not initially protected by the grain. Such protection is provided for by an intermediate layer of insulator

material, most commonly an elastomer containing an additional filler substance, which is applied to the internal surfaces of the motor case.

The combustion products generated within the combustion chamber are comprised of highly pressurised, but low density gases, and to generate significant levels of thrust these gases need to be accelerated to considerable velocities by the motor. To achieve this, combustion gases are expelled from the motor through a converging-diverging de Laval nozzle, in which the gases are expanded from chamber pressure to the external pressure at the nozzle's outlet, and accelerated to supersonic velocities. The convergent and divergent portions of the nozzle are known as the entrance and exit cone respectively, whilst the region where the nozzle is narrowest is called the throat. Figure 2.5 shows a simplified cross-sectional schematic of the converging-diverging profile of a rocket nozzle and illustrates its fundamental elements.

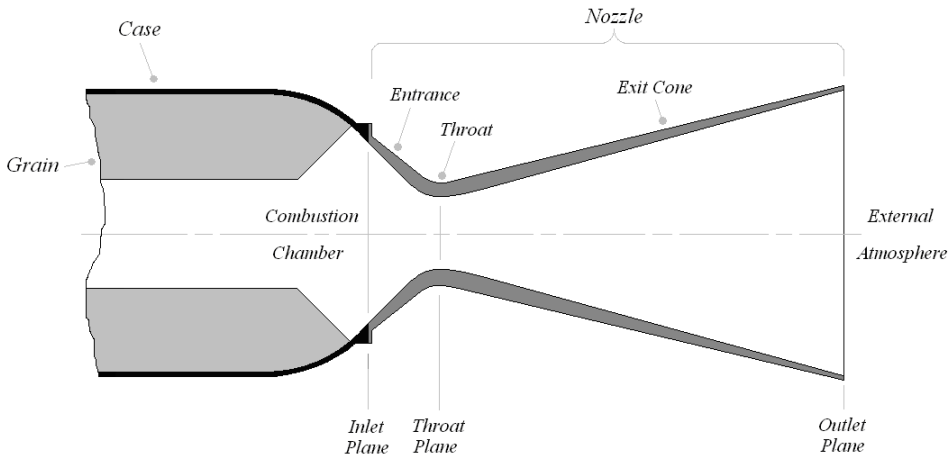

Figure 2.5 The fundamental elements of a rocket nozzle.

As predicted by gas dynamic theory for flow through a converging-diverging duct, there exists a critical ratio between the static pressure at its inlet plane and the static pressure imposed at its outlet plane, which once reached, results in the acceleration of the flow from subsonic velocity at the inlet to sonic velocity at the duct's throat. At this pressure ratio, flow in the divergent part of the duct essentially remains wholly subsonic, decelerating as the duct aperture increases. As the inlet pressure is increased from this level, flow just beyond the throat becomes supersonic, expanding as the nozzle diverges, but then suddenly decelerates to subsonic velocity over a

normal shock that develops as the flow is forced to return back to the ambient pressure at the outlet. With the inlet pressure continuing to rise, the location of the normal shock moves rearward and the portion of supersonic flow in the nozzle increases until the shock arrives the duct outlet. When this condition is reached, the flow undergoes acceleration in both the convergent and divergent sections of the duct, and if the flow's pressure at the outlet plane equals the ambient pressure infinitesimally beyond this plane, the flow is known to have been perfectly expanded.

Below this perfect expansion pressure ratio, when the normal shock exists within the divergent portion of the nozzle, the flow is classified as being over-expanded, whilst above it, when the flow pressure at the outlet plane exceeds the neighbouring ambient pressure, the flow is classified as being under-expanded and undergoes final expansion to ambient pressure over an expansion shock. The nature of this important effect for one-dimensional, steady, inviscid flow is displayed in Figure 2.6, which shows the axial distribution of pressures in a de Laval nozzle as a function of varying outlet pressures.

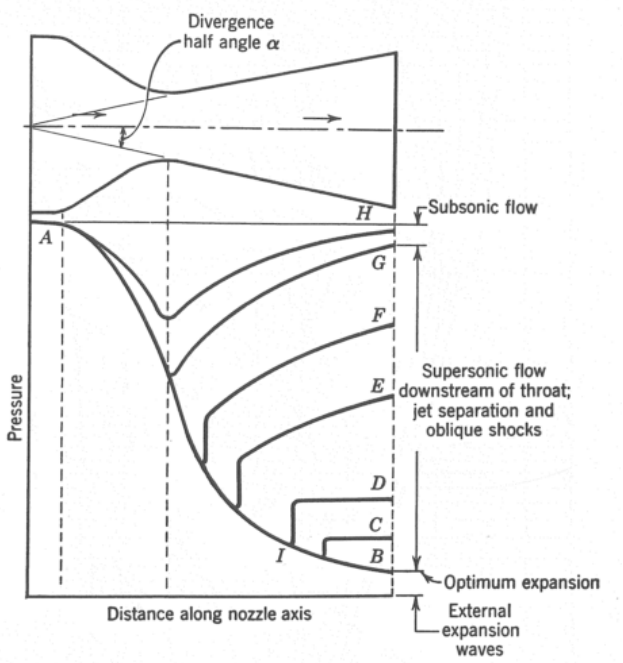

Figure 2.6 Axial distribution of pressure in a de Laval nozzle
for a variety of pressure ratios (Sutton (1963)).

In the instance of flow within an SRM nozzle, the compressible fluid is comprised of the products of combustion, the duct inlet pressure is effectively the combustion chamber's static pressure measured just before the nozzle inlet, and the ambient pressure maintained at the duct outlet is, by default, the atmospheric pressure to which the nozzle is exhausting. During the SRM ignition process the combustion chamber pressure rises from an ambient value to a nominal operational value as the proportion of the grain that becomes ignited increases, whilst the nozzle outlet pressure remains steady. As a result, once the ratio between the instantaneous nozzle inlet pressure and atmospheric pressure reaches the critical value, flow at the nozzle's throat becomes sonic. As ignition progresses, the pressure ratio increases and the shock that is generated as a result is forced to travel towards the nozzle outlet at a speed proportional to the rate at which the inlet pressure is increasing.

Once the combustion chamber has reached its nominal operating pressure and the launch vehicle has begun its ascent, a variation in the nozzle's expansion ratio will still occur. This is because as the launch vehicle climbs through the Earth's atmosphere, the local atmospheric pressure falls, thus effectively increasing the pressure ratio between the nozzle's inlet and outlet. As a rocket motor generates thrust most efficiently when its exhaust stream undergoes perfect expansion, an important element of SRM nozzle design is selecting the optimal ratio of outlet area to throat area, and hence the expansion ratio, for a designated combustion chamber pressure and launch vehicle flight profile. In general, SRM booster motor nozzles are designed such that perfect expansion occurs at some altitude in the lower atmosphere, be it at sea level or moderately higher, whilst SRM nozzles used in high-altitude operations are designed to exhaust to ambient pressures closer to vacuum.

As described in the work of Courant and Friedrichs (1977), in reality, two-dimensional, viscous and turbulence effects result in the formation of an axisymmetric oblique shock between the nozzle surface and a smaller, centralised normal shock. The consequential influence of the oblique shock is to detach the flow from the nozzle surface at a position slightly downstream of its origin on the nozzle wall. In the region between the nozzle wall and the separated jet stream, a zone of fluid recirculation can occur in the presence of an external atmosphere, where air is drawn in from the outlet plane and entrained by the jet. The complex effects of such phenomena in the context of rocket nozzle flow are given particular attention in the works of Moríñigo and Salvá (2007), Verma et al (2006), and Östlund (2002), and are illustrated in Figure 2.7.

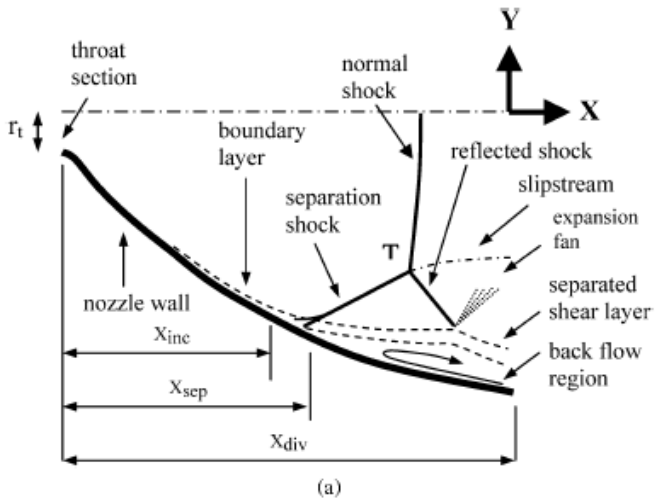

Figure 2.7 Shock phenomena and flow separation in an over-expanded rocket nozzle (Verma et al (2006)).

2.2 Solid Rocket Motor Nozzle Design and Construction

The work of Ellis (1975) provides a comprehensive guide to the discipline of solid rocket motor nozzle design, and despite enormous advances that have taken place in respect of material technology and numerical analysis techniques since its publication, a significant portion of its material remains entirely applicable. Beforehand, the subject was broached in minor detail in the text of Sutton (1963), and subsequently, additional works including those of Hildreth (1988), Truchot (1988), Prescott and Macocha (1996) and Sutton and Biblarz (2001) amongst others have provided relevant updates to the state of the art, which extend the fundamental design principles compiled in Ellis (1975). As such, the following discussion is predominantly based on the work of Ellis (1975), with references being made to additional sources where applicable.

2.2.1 Nozzle Design Configurations

With respect to the physical architecture of SRM nozzles, two basic configurations are employed, as demonstrated by the axisymmetric schematics shown in Figure 2.8. The classical form is known as the external configuration, where the entire nozzle structure is positioned outside of the combustion chamber. The alternative approach is the submerged configuration,

where a significant portion of, or in the extreme case, the entire nozzle is inserted into the combustion chamber.

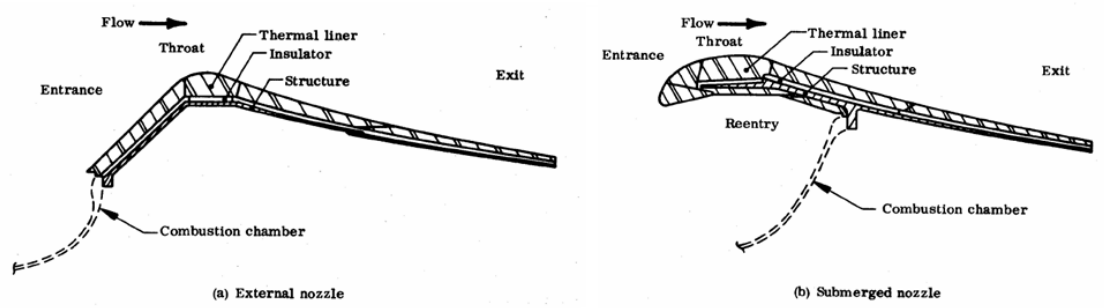

Figure 2.8 Basic SRM nozzle configurations (adapted from Ellis (1975)).

The primary advantage of the external configuration is that the nozzle is inherently simpler in terms of both design and fabrication, and can thus be manufactured at a lower cost. A distinct advantage of the submerged configuration however, is that this layout makes more efficient use of space and contributes to reducing the SRM's overall inert mass (Sutton and Biblarz (2001)). Submerged nozzles are significantly more complex to design, as their submerged portions are exposed to thermal and aerodynamic loading on their external surfaces in addition to their internal surfaces. Consequently, this configuration is also more costly.

With regards to the geometry of the nozzle exit cone, two configurations are generally used, as shown in Figure 2.9. The conical exit cone is the simpler of the two configurations, where the angle of nozzle divergence is kept constant, whilst the contoured exit cone diverges nonlinearly, with a higher divergence angle at the start of the profile, decreasing as it reaches the exit. Divergence of the nozzle profile beyond the throat plane is required to allow the expansion that occurs in the entry region to continue at supersonic velocities. The jet diverges in response, and a portion of the flow's axial momentum is lost as a result. To limit this divergence loss effect, a conical nozzle with a lower divergence angle could be used, but would have to be considerably longer and thus heavier for the same expansion ratio to be obtained. By employing a contoured profile however, divergence loss is reduced by some extent, as in comparison to a conical exit cone of the equivalent expansion ratio, the profile angle at the exit of the contoured exit cone is lower.

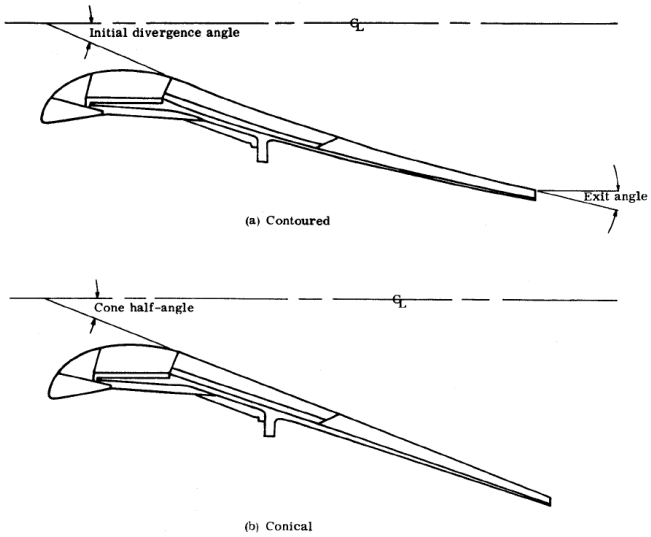

Figure 2.9 Conical and contoured exit cone configurations (Ellis (1975)).

In addition, the same level of expansion can be reached with an exit cone that is shorter and lighter, and thus of higher structural efficiency. Although relatively more complicated to design and fabricate than conical exit cones, for large, high performance SRM nozzles, the increased production cost incurred is outweighed by the associated increase in the propulsion system's performance. Consequently, the majority of SRM nozzles employed in launch vehicle applications feature contoured exit cones, although instances still exist where conical profiles are used (Yoo et al (2003)).

Extendable exit cone configurations are often employed to limit the length of inter-stage structures required between consecutive launch vehicle stages, by allowing high expansion exit cones to be 'collapsed' while not in use during the first period of the flight, as discussed in Lacoste et al (2002). Once the stage below separates from the upper portion of the launch vehicle, the exit cone extensions are extended into place by actuators before motor ignition takes place, significantly increasing the nozzle's effective expansion ratio. Although extended exit cones find frequent deployment in high altitude upper stage SRMs, they are generally not used in a booster SRM role.

It is often necessary for SRMs used in launch vehicle applications to possess some form of thrust vector control (TVC) for vehicle guidance and stability purposes. TVC systems generally fall within two distinct categories relating to how the physical vectoring of the exhaust stream is achieved. In the first category, the nozzle remains fixed, whilst the exhaust stream is manipulated by the TVC system, whereas in the second category, part of or the entire nozzle is made to pivot by the actuating action of the TVC system to achieve vectoring. Various schemes have been developed in either category, but in terms of launch vehicle applications and particularly in the case of large SRM boosters, the contemporary integral moveable nozzle technique, shown in Figure 2.10, has evolved to become the industry standard (Sutton and Biblarz (2001)).

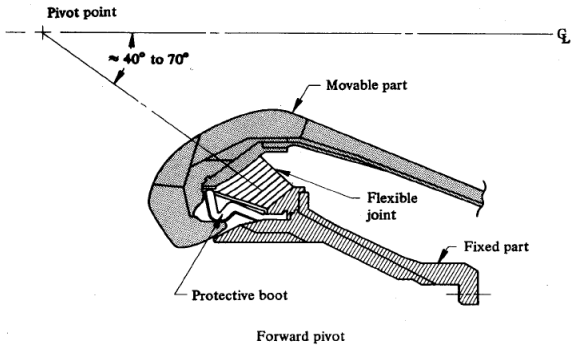

Figure 2.10 Basic details of an integral moveable SRM nozzle (adapted from Ellis (1975)).

In this method, the entire nozzle is mounted on a sealed flexible joint comprised of alternate spherical sections of flexible and rigid layers, often made from elastomeric materials and steel. Nozzles of this nature are typically submerged, with the pitch and yaw motions of the nozzle being instigated by two actuators 90 degrees apart from each other, and accommodated for by the cumulative shear deformation experienced in the flexible layers of the joint.

2.2.2 Materials of Construction

As referred to in the previous chapter, the architecture of a conventional SRM nozzle generally consists of an arrangement of three important elements; the thermal liner, insulation and the attach structure, each with its own particular set of material characteristics requirements. The

typical arrangement of these three elements is shown for both an external and submerged nozzle configuration in the axisymmetric cross-sectional illustrated in Figure 2.11.

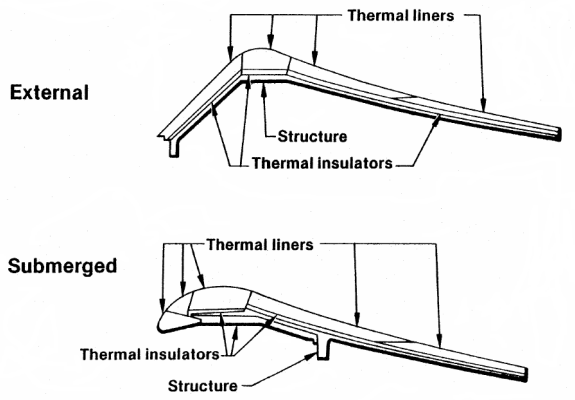

Figure 2.11 Typical thermal liner, insulator and attach structure configurations (Ellis (2006)).

The function of the thermal liner is to provide an aerodynamic contour to the exhaust stream that experiences minimal profile variation during operation, and to protect the remaining portion of the nozzle from the severe environment imposed by the flow. In general, thermal lining must be applied to regions of the nozzle that experience high levels of heat flux, such as the throat, in addition to areas that are exposed to high levels of erosion.

As described in Sutton and Biblarz (2001), erosion is a complex phenomenon in which material is stripped away from the nozzle through the action of high temperature and high velocity gas flow, attack from chemically aggressive species in the gas flow and physical material abrasion attributable to solid particles that may be entrained by the gas flow. Erosion effects are particularly severe in areas where the nozzle's surface is perpendicular to the local flow direction, such as the leading edge of a submerged nozzle's entrance, where the abrasive effect of particles is at its highest. Significant erosion also occurs in the throat region of the nozzle, where the removal of nozzle material leads to an enlargement of the throat diameter and thus an undesirable decrease in combustion chamber pressure and SRM thrust. In this instance, the primary erosive mechanism involved is chemical attack aided by high levels of heat flux and not abrasion, as particulates travel parallel to the nozzle surface in this region.

Materials used in the construction of thermal liners can be grouped into two general groups: thermally stable materials, which are materials that do not chemically decompose at elevated working temperatures, and thermally unstable materials, which undergo a chemical decomposition of some nature at such temperatures. Thermally stable materials used in SRM nozzle construction include polycrystalline and pyrolytic graphite, refractory metals such as tungsten and molybdenum, carbon-carbon, ceramics and ceramic matrix composites. Although materials of this classification generally experience a change in mechanical properties when appreciably heated by the exhaust stream within a nozzle, they are able to retain a reasonable degree of structural integrity at typical nozzle operating temperatures for effectively an indefinite period of time. If heated significantly further, thermally stable materials will eventually melt or vaporise. Thermally stable materials are not, however, completely immune to chemical attack from the exhaust stream, and as such will generally experience a limited degree of erosion.

Thermally unstable materials used in thermal liners are generally composite materials incorporating a plastic matrix material – predominantly phenolic resin – which is commonly reinforced by carbon fibres, although a variety of other reinforcing fibres are used, including glass, silica and graphite fibres. In certain cases however, elastomers can be used in nozzle regions where flow velocities are very low (Mach < 0.2). Although materials of this category undergo a significant amount of degradation upon exposure to high temperatures, this degradation process is endothermic and limits the rate at which further degradation takes place.

In the context of nozzle operation, this process forms the basis of a complex aerothermochemical process known as ablation, and as such, thermally unstable materials are most commonly referred to as ablative materials. As explained in Sutton and Biblarz (2001), the ablation process starts with an initial degradation of the surface of the composite, in which the matrix material undergoes endothermic chemical decomposition to yield a layer of carbonaceous char in addition to pyrolysis gases, which are entrained by the exhaust stream. With time, the char layer deepens and continued thermal protection is provided to the virgin ablative material below by the conductive resistivity of the char and further endothermic decomposition of the matrix below this layer. An additional cooling effect is provided by the pyrolysis gas boundary layer that forms between the exhaust stream and the degraded material's surface. Although the char layer remains relatively stable, its poor mechanical properties result in surface erosion, exacerbated in certain regions of the nozzle by the impingement of solid particles upon its surface.

The addition of fibre reinforcements to ablative materials is made to improve the thermostructural properties and ablation resilience of such materials. Ablative composites are manufactured in a variety of ways, depending on the designated function of the component being fabricated and the type of reinforcement being used. Reinforcement can be continuous, where fibres are deposited in filament form for unidirectional reinforcement, tape or woven cloth form for bidirectional reinforcement, or they can be discontinuous, where short strand fibres provide randomly oriented reinforcement.

The most economical method of manufacturing large, axisymmetric ablative composite thermal liners is the tape winding technique, where resin impregnated reinforcing tape is applied to a rotating mandrel to form the thickness of the part. The fibre orientations achievable using this method are shown in Figure 2.12.

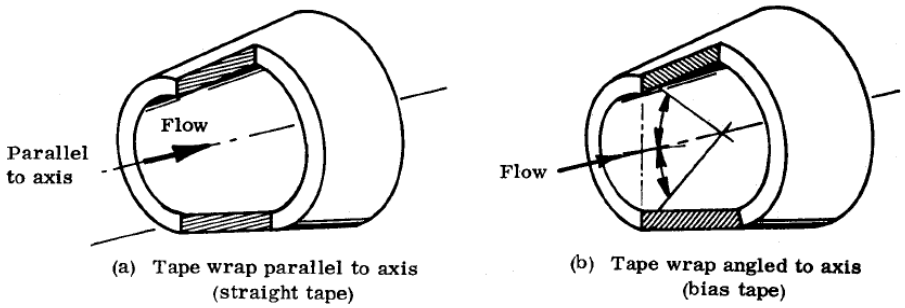

Figure 2.12 Possible tape winding fibre orientations (adapted from Ellis (1975)).

For optimum ablation resistance to the exhaust stream, fibres are laid up at an orientation perpendicular to the direction of flow. However, as the reinforcing fibres generally possess higher thermal conductivity than associated plastic matrix materials, such an orientation increases the depth of thermal penetration. In addition, the production of parts with a perpendicular fibre orientation using tape winding is not feasible and is more difficult and expensive to carry out using other techniques. Consequently, the tape reinforcement is normally wound at an angular bias with respect to the direction of flow within the nozzle. As far as material behaviour is concerned, rotationally symmetric ablative composite structures manufactured using the tape winding technique can generally be characterised as cylindrically orthotropic about the axis of rotation, with respect to both mechanical and thermal properties.

The selection of an appropriate material for a designated thermal liner component is based on the consideration of a variety of factors including the overall nozzle performance requirements, the position of the part and the associated local operating conditions, and material and fabrication costs. Thermal lining of the throat region is usually undertaken using thermally stable materials that offer good resistance to erosion to preserve the throat's dimensional qualities, such as polycrystalline graphite (small nozzles), pyrolitic graphite (small to medium nozzles), and carbon-carbon (small to large nozzles). Notable advances in the processes involved in the synthesis of carbon-carbon components has allowed this material to be deployed in a throat thermal lining capacity in some of the largest SRM nozzles developed, such as the nozzle of the Ariane V space launch vehicle booster SRM (Bussiere and Mora (1994)). A partial cross-sectional view of the Ariane V SRM nozzle and the nozzle's carbon-carbon throat thermal liner components are shown in Figure 2.13.

Figure 2.13 Ariane V SRM nozzle and carbon-carbon throat thermal liner components (Aubard (2001)).

For medium to large nozzles, where a greater rate of erosion can be tolerated or counteracted through adjustments to the propellant grain burn characteristics, thermally unstable ablative composites are used to line the throat region. A prominent example of this approach is the Space Shuttle reusable solid rocket motor nozzle which is lined almost exclusively with a carbon-phenolic (C-P) ablative composite (Sutton and Biblarz (2001)).

Conditions encountered at the nozzle entrance upstream from the throat region are particularly severe as a consequence of appreciable heating rates and surface impingement of solid particles entrained in the flow. As a result, thermal liner components in this area are normally constructed from carbon-phenolic or carbon-carbon composites. As a consequence of the lower temperatures encountered in exit region of a nozzle, in addition to its divergent nature, the thermal loading and erosion of thermal liners operating in this position is less extensive. The materials of construction most commonly used here include carbon-phenolic, glass-phenolic and silica-phenolic ablative composites, whilst carbon-carbon composites are also used, particularly in upper stage SRM applications, as described by Truchot (1988) and Ellis and Berdoyes (2002).

During motor firing thermal liners become extremely hot, and to protect the integrity of the structural elements of the nozzle, appropriate insulation needs to be provided. This is essentially the primary purpose of insulators in SRM nozzles. Most commonly, a separate set of dedicated insulators is used, although it is possible to avoid the use of insulators altogether by increasing the thickness of the thermal liner material. Two types of materials are used in the construction of insulators; fibre reinforced plastics and filled elastomers. The predominant reinforcements used for the fibre reinforced plastics category are glass and silica fibres as a consequence of their superior thermal resistance, although carbon fibres have been used in some cases (Yoo et al (2003)). The predominant matrix materials are phenolic and epoxy resins.

In terms of insulator fabrication, the tape wrapping technique for continuous reinforcement and the die moulding technique for discontinuous reinforcement are the methods most commonly used. An advantage of using continuous reinforcement in the manufacture of insulator components is the construction of a part of superior strength. In some cases, this added strength can provide sufficient support to the associated thermal liner that the need for an additional layer of structural support is eliminated altogether. With regards to the filled elastomer material category, commonly used filler materials include carbon and silica in the form of either powder

or chopped strands, whilst butadiene-acrylonitrile is a typical elastomer. Contrary to the case of thermal liner components, where environmental conditions demand the use of multiple materials for an optimal design, often one type of insulator material will suffice.

The essential function of the support or attach structure of an SRM nozzle is firstly, to act as the structural backbone of the nozzle, supporting the thermal liner and insulator components, and secondly, to provide for the attachment of the nozzle assembly to the SRM case. Two types of materials are most commonly used in the construction of attach structures; metals, including steel, aluminium and titanium, and composite materials, including glass-epoxy and carbon/graphite-epoxy composites. Metals are most frequently employed for the construction of structural members supporting the entry and throat region, whilst composites are the materials of choice for exit cone structures. In regards to nozzle-to-case attachment, a variety of techniques exist, although the bolted joint is the technique of choice as it allows for accurate nozzle alignment and is not size limited. This technique involves the fastening of the nozzle to the case at a mating flange interface that is clamped by a number of bolts around its circumference.

2.2.3 Carbon-Carbon Composites

The development of the carbon-carbon (C-C) composites has had a profound effect on SRM nozzle technology. This is as a result of their superior thermo-stability and impressive structural performance at very high working temperatures; often in excess of 2500˚C. In addition, carbon-carbon composites are lower in density in comparison to other high temperature materials such as ceramics and refractory metals and are generally less prone to erosion and or ablation than ablative composites. Furthermore, they exhibit excellent thermal shock resistance as a consequence of low coefficients of thermal expansion and high thermal conductivities. Each of these qualities is of great importance in the context of SRM nozzle design.

Another particularly advantageous and curious thermostructural property of C-C composites is the increase in strength that they exhibit above temperatures of approximately 1200˚C (Windhorst and Blount (1997)). A significant weakness of C-C composites however, is their susceptibility to oxidation at temperatures above 500˚C (Windhorst and Blount (1997)). Importantly, this phenomenon is the primary contributor to the erosion of C-C SRM nozzle structures, as discussed in Thakre and Yang (2008), Bianchi et al (2008) and Shimada et al (2007). The significant improvements in structural and operating efficiencies that C-C

composites can enable through their application in SRM nozzles are outlined in Ellis (1973), Ellis (1974) and Ellis and Berdoyes (2002).

In carbon-carbon composites, carbon fibres are used to reinforce a carbon or graphite matrix. A wide variety of reinforcement architectures are used, including unidirectional, two dimensional and multi dimensional or spatially reinforced schemes. The manufacture of C-C composites is a complex and lengthy process that can be approached in a variety of ways, depending on the starting raw materials used. Whichever technique is used, the fundamental elements of the process are the same, as outlined in Figure 2.14.

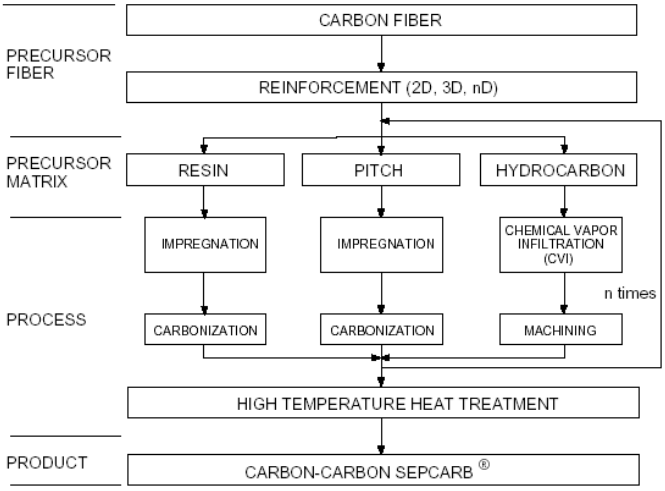

Figure 2.14 The carbon-carbon production process
(Lacoste et al (2002)).

Fabrication starts with the arrangement of the carbon fibre reinforcement preform according to the dimensional requirements. Two-dimensional configurations can be made by weaving and filament winding dry fibre yarns, whilst spatially reinforced schemes can be produced by braiding, knitting and needle weaving dry fibre yarns, or assembling pultruded composite rods. The next step in the process is infiltration of the matrix precursor material into the reinforcement preform. Three precursor materials are most commonly used; polymeric resins, pitch and hydrocarbon gases. Following infiltration, the next stage is the carbonization of the matrix precursor material. When a resin or pitch is used, carbonization is conducted after infiltration in

a separate exercise via pyrolysis of the matrix precursor to yield a porous carbonaceous char in its place. When hydrocarbon gases are used in a chemical vapour infiltration process, carbonization takes place in parallel with infiltration, as the gas is passed through a fibre preform heated to high temperatures to instigate carbon deposition. In either instance, the resulting carbonized matrix preform exhibits a high level of porosity and must undergo a series of further infiltration and carbonization cycles to raise its density to the required level. Once a satisfactory density has been obtained, the part undergoes a heat treatment to partially graphitize the carbon matrix material. As discussed in detail in Tarnopol'skii et al (1992) the nature of the heat treatment regime employed has a significant effect on the resultant reinforcement and matrix properties, as a consequence of microstructural changes.

According to Tarnopol'skii et al (1992), first generation C-C composites employed two dimensional reinforcement schemes. Whilst possessing significantly better in-plane strength than homogeneous graphite, these composites had inferior strength properties in the transverse direction and were prone to delamination failure – especially for thick laminates (Berdoyes and Thebault (2005)). The introduction of spatially reinforced C-C composites eliminated this weakness with the addition of reinforcing fibres normal to the original two-dimensional reinforcement plane, yielding a notable increase in thermostructural resilience and ablation resistance. As such, spatially reinforced C-C composites have enjoyed much success in their application in the construction of SRM nozzles (Delneste and Perez (1983)).

Two popular spatial reinforcement architectures used in the construction of thick C-C SRM nozzle components, particularly throat liners, are three dimensional and four dimensional schemes, whose unit cells are shown in Figure 2.15. The three dimensional configuration is created by the arrangement of reinforcement in the three principal orthogonal directions, whereas the four dimensional architecture features additional reinforcement at angles of $\pm 45^{\circ}$ in one plane.

Thinner SRM nozzle components fabricated from C-C composites, such as carbon-carbon exit cones, were initially manufactured using woven fabric lamina or tape wound carbon fibre preforms. As only two-dimensional reinforcement was imparted using this technique, such components were often prone to delamination failures during thermal loading. A solution to the challenging problem of providing transverse reinforcement to the thin carbon-carbon structures

was developed in the way of preforms generated by fabric needling. In this process, stacked layers of carbon fibre fabric are interlinked in the transverse direction by a multitude of fibres inserted into position by the repetitive action of an array of needles, as described by Lacoste et al (2002) and Berdoyes and Thebault (2005). The C-C material produced from such a preform has significantly improved transverse and inter-lamina shear strength, and therefore much greater resistance to delamination.

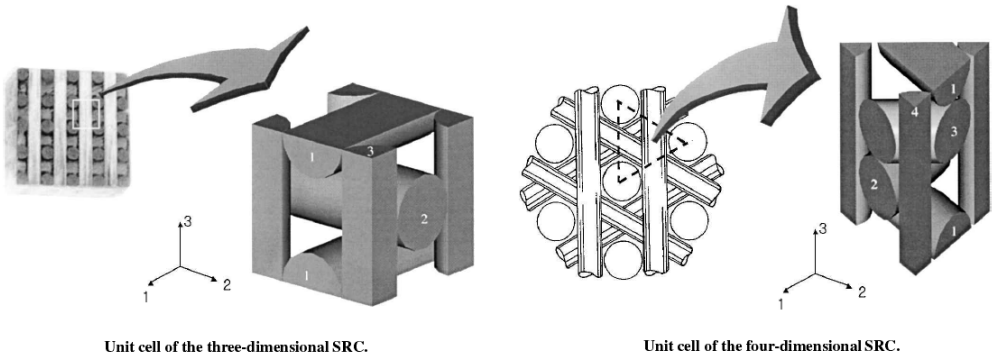

Figure 2.15 Three and four dimensional reinforcement architectures (adapted from Yoo et al (2003))

The material behaviour of carbon-carbon composites is complex, and is a matter still receiving much research attention. C-C composites generally display pseudo-elastoplastic characteristics as a consequence of fibre delamination and microcracking of the matrix (Tarnopol'skii et al (1992)) and possess mechanical properties that are strongly dependent on the configuration of the reinforcement used (Delneste and Perez (1983), Neumeister et al (1996)). In addition, mechanical properties of C-C composites show a strong dependence on temperature (Aubard (2001)) and on physical scale (Ladevèze et al (2000)), particularly in the case of spatial reinforcement architectures.

Material models have evolved over time in regards to their ability to approximate the behaviour of a variety of C-C materials. Delneste and Perez (1983) developed and implemented an elastoplastic finite element material model for four dimensional C-C composites, whilst Stanton and Kipp (1984) developed and validated a non-linear model for two dimensional C-C composites on the basis of experimental data. A more comprehensive elastoplastic material model for four dimensional C-C composites was provided by Aubard et al (1998), which

reasonably described internal damage mechanisms and attempted to model the effects of fibre-matrix debonding at the free edges of the composite. As an extension of this work, Ladevèze et al (2000) developed a finite element meso-model of a composite specimen to study the nature of free edge debonding and investigate the relationship between macroscopic strain and the debonding phenomenon.

2.2.4 General Design and Analysis Process

As described in Ellis (1975), the optimised design of SRM nozzles is a complex iterative process that involves the simultaneous consideration of aerodynamic, thermodynamic and structural design elements, in order to engineer a structure that satisfies numerous product requirements whilst remaining within the limits of imposed constraints. As such, the design process is initiated with an assessment of the expected propulsion system characteristics, from which key parameters including motor burn duration, nominal chamber pressure, nozzle expansion ratio, thrust vectoring factors and case attachment specifications are established. Equally important is the establishment of design constraints such as allowable nozzle weight and size, allowable throat size enlargement, required levels of operational reliability, fabrication capacity, manufacturing costs and developmental deadlines etc. The design process is essentially divided into three sequential phases: aerodynamic design, thermal design and structural design.

The primary objective of the aerodynamic design phase is to develop the wetted surface geometry of the nozzle such that the conversion of the combustion energy to the kinetic energy of the flow is maximised. Based on the expected combustion chamber pressure characteristics, the operational altitude envelop and various other parameters of the SRM being considered, the appropriate entrance contraction and exit expansion ratios of the nozzle can be determined using one dimensional gas dynamic theory. Once these values have been set, the interior geometric characteristics of the nozzle entrance, throat and exit regions (and exterior contour of the entrance, if the nozzle is submerged) are then selected in accordance with any specific design requirements or constraints, such as thrust vector control or production costs. Aerodynamic analysis is preceded by a preliminary thermochemical analysis to determine the thermodynamic properties and the composition of the flow, and a transport-property analysis to determine effective flow properties such as viscosity and thermal conductivity, amongst others. Once these properties have been obtained, an aerodynamic analysis can proceed in which the nozzle's thrust

coefficient is evaluated and the magnitude of nozzle thermal and aerodynamic loading is determined.

The purpose of the thermal design phase is to develop a nozzle wall structure that is able to preserve the aerodynamic contour of the nozzle to the design standard, and that retains temperatures at all points in the nozzle to within associated material limits. This is achieved through the appropriate designation and correct sizing of materials at each region of the nozzle, based on the anticipated degree of thermal loading. Thermal loading emanates from three modes of heat transfer; convection, radiation and the impingement of hot solid particles. Convective effects dominate in the supersonic flow domain, whilst in regions of the flow where velocities are less than Mach 0.8, radiation effects should be considered for the accurate evaluation of thermal loading. Particle impingement heating effects are generally confined to areas of subsonic flow and direct particle impact on the nozzle.

Once the degree of heat transfer has been determined, the thermal response of the nozzle is evaluated. For components constructed from thermally stable materials, a thermal conduction analysis in conjunction with a chemical and mechanical erosion analysis is usually carried out for this purpose. For parts made from thermally unstable materials however, a more comprehensive ablation analysis is required, that considers chemical decomposition and energy absorption, mass transfer and pyrolysis gas boundary layer development. Once such analyses have been carried out, the degree of nozzle regression and the temperature distribution in the structure at various times during operation can be established.

The structural design phase entails the development of a physical nozzle architecture that is able to safely retain its structural integrity when subjected to loading encountered during operation, as well as to loading attributable to handling, transport, testing, etc. A breakdown of load sources present during SRM operation is shown in Table 2.1. The most significant internal loading of the nozzle is imposed by the exhaust stream, in the complementary form of internal pressure or aerodynamic loading and thermal loading. The internal pressure generates stress as it acts to force the nozzle away from the combustion chamber whilst simultaneously expanding it, whereas thermal stress results in the structure as a consequence of differential thermal expansion. Thermal stresses are frequently of primary concern in the structural design of SRM nozzles.

Load Source	Associated Load Types
Exhaust Stream	Thermal Loading
	Internal Pressure (Aerodynamic) Loading
Thrust Vector Control System	Asymmetrical Internal Pressure Loading
	Mechanical Actuation Loading
Flight Trajectory Environment	Dynamic Pressure Loading
	Wind Loading
	External Thermal Loading
	Gravitational Loading
	Acceleration Loading
	Vibration Loading

Table 2.1 Sources of SRM nozzle loading during operation (Ellis (1975)).

If thrust vector control is employed, the asymmetrical internal pressure loading imposed on the nozzle during vectoring manoeuvres results in the generation of asymmetrical stresses in the nozzle. In addition, the loading applied at the location where the TVC system attaches to the nozzle can result in significant localised stress generation. As indicated in Table 2.1, various other loading sources associated with the flight trajectory environment contribute to nozzle stress, and for comprehensive design, should be considered.

Once all relevant sources of structural loading have been identified and evaluated, the proposed nozzle's operational structural integrity can be analysed. Considering the almost universal application of orthotropic materials in medium to large SRM nozzle construction, an analytical facility with the capacity to accommodate such behaviour is normally used. In addition, analysis may require the consideration of unsymmetrical loading, nonlinear material properties and dynamic response behaviour.

In the past, due to severely limited analysis capability, design parameters would be derived on the basis of simplified closed form analytical solutions, empirical relationships, experimental data and past experience. Once the primary design cycle had been completed, the preliminary design would then be assessed using crude analytical techniques to establish its viability. If indicated to be deficient in any way, the next design cycle iteration would take place where required changes would be made, until a satisfactory nozzle design was obtained. At this point, a

prototype nozzle would be manufactured and undergo an extensive testing regime to confirm the aerodynamic, thermal and structural validity of the design. Only once this extended design and testing procedure had been carried out could production of the flight nozzle begin.

The development of numerical simulation techniques, computer aided design methodology and powerful computational hardware, in addition to significantly more accurate material characterisation, has greatly streamlined the process of SRM nozzle design, allowing for designs to be generated with much greater confidence than before. Now, comprehensive analysis can take place after each design phase, producing accurate boundary conditions for the phase that follows, and allowing for the final design to be reached with greater rapidity.

2.3 Numerical Simulation of Solid Rocket Motor Nozzles

2.3.1 Numerical Simulation of SRM Nozzle Flows

The flow of combustion products in SRM exhaust nozzles has been analysed using numerical techniques by a variety of researchers since as early as the 1960s, as evidenced, for example, by the work of Kliegel and Nickerson (1967). Owing to the complex physical nature of SRM nozzle flow however, the simulative power of such techniques has been restricted by the pace of developments in computational hardware, software and numerical formulations. With respect to the indices of capacity, accuracy and efficiency, early efforts in this field today appear primitive in comparison to contemporary work – indicative of the phenomenal advances that have occurred in the discipline.

Numerical simulation of SRM nozzle flows – and the numerical simulation of any chemical rocket motor nozzle flow for that matter – can be categorised in broad characteristic terms as pertaining to the modelling of either steady or unsteady flow states. As steady flow is time-invariant, its simulation is significantly less computationally challenging than that of unsteady flow – with regards to a variety of important considerations. Consequently, early simulation endeavours focused primarily on the consideration of steady nozzle flow.

Regan et al (1971) presented a technique for the simulation of the two dimensional flow of a two phase fluid through an axisymmetric nozzle using a finite difference discretization of the flow's governing equations, and determined flow fields and particle trajectories for various nozzle

contours and particle sizes. Serra (1972) introduced a numerical method based on the Lax-Wendroff procedure to solve the time dependent equations of inviscid subsonic-supersonic flows in nozzles, using special numerical treatments to attain greater solution stability and improved accuracy in flow shock capture. A significant advantage of the time dependent nature of the solution was that it allowed for the homogeneous treatment of the subsonic and supersonic flow regimes, whose governing equations exhibit elliptic and hyperbolic characteristics respectively. Analysis of steady, inviscid, two dimensional, two-phase nozzle flows in the transonic region was undertaken by Jacques and Seguin (1974) using an iterative numerical technique, to provide initial conditions for the segregated solution of the downstream supersonic flow field. Chang (1976) examined three dimensional, inviscid, supersonic flow of a homogeneous, thermally non-conductive fluid through nozzles of different cross-sectional configurations, using a shock capturing finite difference scheme. In a separate work, Chang (1980) applied a MacCormack finite difference scheme in conjunction with a boundary fitted coordinate system to solve the time-dependent, two-dimensional, inviscid flow of both one- and two-phase fluids within nozzles of arbitrary profiles. The characteristic differences associated with each flow type were evaluated by varying solid particle size and mass fraction parameters.

Chang (1983) extended the method used in his earlier work, Chang (1976), to account for two-phase flow by including models for momentum and energy transfer between gas and particle phases in viscous three-dimensional supersonic nozzle flows. Once again, effects associated with the variation of particle parameters for flows in various nozzles were investigated. The techniques used in this work were then used to simulate three-dimensional one- and two-phase flows in the transonic region of the Titan III SRM canted nozzles in Chang (1990), with computed results showing good agreement with associated test data.

Variations in two-phase nozzle flow characteristics attributable to different particle sizes and mass fractions were also investigated by Hwang and Chang (1988), using a time-dependent MacCormack finite difference discretization of the governing equations for a two-dimensional flow regime, that were derived in conjunction with a particle trajectory model to account for the solid phase. The study, which included viscous effects and a flow turbulence model, also provided preliminary insight into the degree of coupling existing between the gas and solid phases. Flow turbulence in SRM nozzle flows was also considered by Jones and Shukla (1998),

who simulated the steady, viscous, compressible flow in an axisymmetric nozzle using the Baldwin-Lomax turbulence model and the MacCormack finite difference scheme.

The establishment of the numerical techniques used in the simulation of steady nozzle flow paved the way for the development of the more sophisticated approaches required to solve transient nozzle flow, where provision needs to be made for the conservation of flow variables in both the spatial and time domains, for accurate physical representation. Transient rocket nozzle flow field simulation during motor ignition has been undertaken by various researchers, predominantly in regards to liquid rocket motors. Considering, however, that the principles governing solid and liquid rocket motor flows are essentially the same, it is felt that a review of works in reference to both forms of propulsion should be made.

Chen and Chakravarthy (1994) investigated the features associated with unsteady separated nozzle flows during motor start-up and throttle-down events within a 1/16 scale J-S2 liquid rocket engine nozzle, by numerically solving the axisymmetric form of the time-dependent, viscous, compressible Reynolds-averaged Navier-Stokes equations, with mathematical closure being provided by a separate turbulence model. The temporal and spatial development of flow features such as the Mach disk, separation shock as well as shock induced vortices during the ignition transient were observed.

Nasuti and Onofri (1998) used a shock fitting and tracking technique to simulate axisymmetric, viscous nozzle flow during motor start-up by numerically solving the non-conservative form of the Navier-Stokes equations. The shock fitting and tracking method allowed for the economic and explicit capture of the non-stationary shock features. Results indicated the presence of two separate vortex regions being generated by both viscous and inviscid flow structures. In addition, the effect of these vortex phenomena on contributing to nozzle flow instability was evaluated.

Mouronval et al (2002) employed a finite difference-based numerical scheme to solve the time-dependent, two-dimensional and axisymmetric Euler equations describing the transient, inviscid flow within a constant-area tube terminated by a diverging conical nozzle, where the flow was initiated by an incident shock wave. Various typical flow characteristics were captured by the solution, and the effects of changing the conical divergence angle and incident shock wave velocity were investigated. As a continuation of this work, a study by Mouronval and Hadjadj

(2005) employed the equivalent solution scheme to simulate the unsteady flow initiated by an incident shock wave within a nozzle of a more complex geometry.

Chang et al (2005) applied the space-time conservation element / solution element method to numerically simulate axisymmetric, unsteady rocket nozzle flows. A distinguishing characteristic of this method is its treatment of the space and time domains of the solution as a single entity, providing inherent variable conservation in both domains. In particular, the work considered the transient flow through the JPL benchmark nozzle, simulating the evolution of both viscous and inviscid flow fields. The typical flow structures associated with either regime were captured without the deployment of turbulence or flow separation models, with the distinct differences between the two treatments being clearly indicated. In general, excellent agreement between the computational results and equivalent experimental data was obtained. As an extension of this work, Chang et al (2006) went on to apply the space-time conservation element/solution element technique in three-dimensional form to simulate the unsteady flow within a canted rocket nozzle.

2.3.2 Numerical Simulation of SRM Nozzle Structural Response Behaviour

The simulation of the operational structural response behaviour of SRM rocket nozzles using numerical means has been undertaken by a number of researchers, considering either the response to pressure loading, thermal loading, or a combination of the two. As discussed previously, thermal loading generally generates the highest levels of stress in an SRM nozzle, and as such, it is the numerical simulation of the thermostructural behaviour of such nozzles during operation that has been given the most research attention. In terms of operational regimes, it would appear that efforts have only been made to simulate nozzle response during periods of steady SRM operation. Indeed, despite an exhaustive survey of available literature, no publications could be found offering treatment to the response modelling of composite SRM nozzles during the motor ignition period. This deficiency clearly highlights the novelty of the current study.

One of the first references made to the use of computational tools to numerically simulate the quasi-static thermostructural behaviour of SRM nozzles was in the work of Lemoine (1975), which essentially described the state of the art in SRM nozzle design and analysis at that time.

Owing to the then inadequacies in composite material modelling, numerical techniques such as the finite element method were restricted to the role of providing guidance to the design process. Lapp and Quesada (1992) described the significant advances that had taken place in the application of numerical simulation tools for SRM nozzle analysis since the 1970s. Key elements of the nozzle design and analysis process were discussed, in addition to the use of the finite element method for resolving thermal and structural responses, and adaptive mesh techniques to model nozzle erosion. The application of such techniques was described in the context of the design of two SRM nozzles, including that of the Ariane V booster SRM.

Mukherjee and Sinha (1997) carried out an investigation into the thermostructural behaviour of rotationally symmetric spatially reinforced composite structures using the finite element method. As an example, the thermostructural response of an uncooled composite nozzle in steady-state thermal operation was simulated, and a comparison of the predicted thermal and stress behaviour of this nozzle for different constituent materials, including C-C and metal matrix composites was made, clearly illustrating the superior thermostructural properties of C-C composites in this class of application.

Vandenboom and Heister (1998) conducted a transient, two-dimensional thermostructural analysis of a C-C composite rocket nozzle internally coated with a thin layer of silicon carbide for oxidation protection. Numerical simulation of both the thermal and subsequent structural response was achieved using a finite element code, and the analysis period was limited to the first 3 seconds of nozzle operation. Results indicated that stress levels induced by thermal loads typically exceeded those generated by aerodynamic loads by one to two orders of magnitude, and that such stresses were direct functions of the elastic moduli and coefficients of thermal expansion of the materials of construction. Another interesting observation made was that for this particular nozzle configuration, maximum stress levels were encountered approximately 1 second into the simulation, tapering off as the depth of thermal penetration increased.

The finite element method was again used by Cozart and Shivakumar (1999) to numerically predict the transient stress response of a three-dimensional braided composite ablative rocket nozzle, with the effects of material ablation being accounted for in the constituent thermal and structural models. The simulation considered a 20 second motor burn period, with combustion chamber parameters being varied to determine the sensitivity of the structural response of the

nozzle to such parameters. For the nozzle configuration considered, results showed a predominantly compressive radial stress response, increasing significantly towards the thermally affected zone. In terms of stress in the hoop direction, the response was primarily tensile in nature, whilst axial strain was shown to be negligible throughout the nozzle.

Yoo et al (2003) numerically simulated the response of a spatially reinforced C-C integral throat and entrance structure to burn period pressure and thermal loading, using a finite element approach. The structure's unsteady temperature distribution was generated by a transient heat transfer model and mapped to the structural model, whilst pressure loading was applied directly to the structural model. The thermostructural performance of three-dimensional and four dimensional C-C reinforcement architectures was assessed in an elastic sense and results exhibited the expected asymmetrical and symmetrical deformation responses, respectively. The maximum deformation computed under thermal and pressure loading was approximately 25 times greater than that encountered when just pressure loading was considered, whilst the most severe stresses predicted were found to be in the nozzle's hoop direction.

Ramesh Kumar et al (2005) undertook an extensive thermostructural analysis of composite structures, incorporating temperature dependent properties, and subjected to thermal, thermo-chemical and mechanical loading, using the finite element method. In particular, a coupled thermostructural stress analysis of an SRM nozzle comprised of various orthotropic and isotropic materials was carried out. The solution was attained using an iteratively coupled thermal-structural model scheme, and employed temperature-dependent death elements to account for the effects of ablation. Once again, results indicated the strong presence of hoop stress, and predominant thermal stress effects.

2.3.3 Numerical Simulation of SRM Nozzle Fluid-Structure Interaction

The problem of aeroelasticity in rocket nozzles has been considered by Lefrançois et al (1999) and Lefrançois (2005), who conducted work on developing a finite element model based on an arbitrary Lagrangian-Eulerian formulation for studying fluid-structure interaction, with particular application to rocket engine nozzles. It was also considered in the work of Schwane and Xia (2005), who undertook numerical investigations into rocket nozzle fluid-structure interaction associated with side load generation during over-expanded flow operation. However,

as extensive as the above works may be, all of these studies pertain to applications involving nozzle geometries and wall materials characteristic of liquid rocket motors, and do not consider the loading imposed on the nozzle wall by the time-dependent movement of flow shocks during the ignition transient. In addition, none of these studies accounted for the structural response of the nozzle beyond the stipulation of mean nozzle wall displacements.

In terms of the investigation of FSI phenomena in solid propellant rocket motors, a collection of studies have been conducted. Johnston and Murdock (1994) investigated the fluid-structural interaction within an SRM by examining the developing propellant core flow field and the associated propellant grain deformation within a motor following ignition. Johnston (1996) then conducted an FSI analysis of the Ariane V booster SRM during the motor's ignition transient, examining the coupled response of the propellant grain and core flow at sequentially lower levels of elastic modulus. Parsons et al (2000) undertook numerical simulations of rocket motors involving the three-way coupling of the propellant core flow, the propellant and motor case, and the combustion of the propellant. Montesano et al (2005, 2008) considered a similar case as they developed a numerical model to consider the effects of coupled structural and acoustic oscillations on propellant combustion. Again, although these studies provide extensive insight into FSI phenomena pertaining to solid rocket motor operation, they do not include any consideration of such phenomena in relation to the structural response of SRM nozzles.

CHAPTER 3

Multidisciplinary Numerical Simulation Methodology

3.1 Introduction

The numerical simulation work undertaken in this study comprised three fundamental simulation activities; modelling of the exhaust gas flow through the nozzle to establish wall pressure and temperature boundary conditions, modelling of heat transfer within the nozzle to establish an associated temperature distribution, and modelling of the nozzle's resultant structural response to the imposed loading conditions. All three of these simulation activities were carried out using the ADINA system, which is a multidisciplinary finite element code capable of modelling problems related to solid mechanics, heat transfer and fluid mechanics, in addition to coupled field interactions.

Considering the exploratory nature of this research, and in addition to factors such as software, computational and data resource limitations, a variety of assumptions relating to the fluid, thermal and solid models developed in this study were necessary, in order for its scope to remain manageable. The overarching assumption made with respect to all three models was the reduction of the physical dimension of each problem to two-dimensional axisymmetric domains. This assumption was primarily required in order to keep the computational size of the respective simulations to within practicable limits.

With regards to rocket nozzle flow field modelling however, certain effects can contribute to the generation of a circumferential flow component, resulting in a truly three-dimensional flow field. In addition, real nozzle flow during motor ignition is typically characterised by asymmetric three-dimensional flow behaviour as a consequence of complex flow separation phenomena (Nasuti and Onofri (1998), Östlund (2002)). Without significant computational processing power, full three-dimensional modelling of asymmetric unsteady nozzle flows is generally prohibitive, and without the advanced treatment of flow turbulence, ineffective. Having said this, the use of an axisymmetric assumption can still yield important insight into flow characteristics,

with a useful level of accuracy – as evidenced by the work of Chang et al (2005). As such, it is believed that this assumption in relation to the current work can be considered acceptable.
An additional assumption made in reference to the physical flow domain was the simulation of the exhaust stream only up to the nozzle exit plane. That is, the exhaust plume external to the nozzle was not considered, owing to the significant computational expense of accommodating this large additional flow domain. Although doing so provides a more realistic set of flow conditions at the outlet in comparison to a strictly imposed boundary condition, a consideration of the available computational resources suggested that modelling this region would be impractical.

Additional assumptions made relate particularly to the characteristics of the simulated flows. Although real nozzle flows are characteristically turbulent in nature, a lack of information relating to the designation of turbulence parameters specific to SRM nozzle flows prompted the specification of a laminar flow approximation instead. In addition, owing to limitations in the capabilities of the ADINA system, the flow was specified as single phase, i.e. purely gaseous, having reached chemical equilibrium before entering the nozzle inlet, and remaining chemically frozen during expansion through the nozzle. The single phase approximation is reasonable when non-aluminised SRM propellants are being considered, and as such, only flow properties relating to non-aluminised combustion products are used. With regards to this assumption, in reality, a state of chemical equilibrium is generally not achieved before combustion products are entrained by the nozzle – although the affect of continued reaction on macro flow characteristics is typically minor. As such, the flow medium was treated as an ideal gas.

In so far as thermal modelling of nozzle structures was concerned, the most significant assumption employed was the omission of the effects of radiative thermal loading. More specifically, convection was the only mode of heat transfer considered in this work. This assumption was required primarily because of the considerable difficulty that was encountered in obtaining suitable emissivity parameters for the combustion gases and nozzle materials considered. As described by Sutton (1963), although the contribution to nozzle wall heat transfer made by combustion gas radiation is significantly less than that associated with convection, it becomes appreciable at very high combustion temperatures and when solid particles are

entrained in the exhaust flow. Having said this, only a non-aluminised propellant having a relatively low flame temperature was considered in this work when thermal loading conditions were simulated. As such, it was felt that for the purposes of an exploratory study, the exclusion of the radiation heat transfer mode would be acceptable.

For all burn period thermal simulations and for the first ignition period structural response simulation, orthotropic thermal conduction was modelled. For the third ignition period simulation incorporating conjugate heat transfer however, an isotropic conduction approximation had to be made as a result of software limitations. The error incurred by this approximation was assessed and observed to be minor as a direct consequence of the shallow thermal penetration encountered during the ignition period. An additional assumption made in both cases was the specification of perfect thermal conduction across the various substructure interfaces of the nozzle designs considered.

With regards to solid mechanics modelling, the most significant assumption employed was the treatment of both isotropic and orthotropic materials of construction as elastic solids. Whilst, in the context of the structural problem being examined, such a specification is perfectly applicable for the case of isotropic materials, it does not realistically represent the complex pseudo-plastic stress-strain behaviour of C-C composites in particular. However, owing to the distinct lack of readily available material data related to this behaviour, an elastic approximation was unavoidable.

An additional assumption relating to the orthotropic materials modelled in this study was the homogenisation of their constituent components, without which, simulations would have become prohibitively expensive in a computational sense. In addition, the effects of material loss associated with erosion and ablation were not modelled owing to the complex nature of such effects. Such phenomena show negligible manifestation during the ignition transient period, but have a significant material removal effect over the entire burn duration. This being said, the nozzle designs considered in this work were specifically designed to minimise the error associated with such an approximation. Finally, in terms of the dynamic solid modelling undertaken, no material or structural damping was considered as a consequence of the difficulties encountered in obtaining parameters associated with realistic damping mechanisms. The effect of making this assumption was ultimately found to be inconsequential.

3.2 Flow Modelling

In the current work, all nozzle flows were simulated using the 'ADINA-F' program of the ADINA system, which is capable of simulating the steady or unsteady, viscous or inviscid, compressible or incompressible, and laminar or turbulent flow of fluids, with or without mass and/or heat transfer. In particular, ADINA-F's high-speed compressible flow model was employed for nozzle flow simulations. As described in ADINA R&D, Inc (2008), the conservative form of the Navier-Stokes equations that describe the time-dependent flow of viscous and compressible fluids is used to form the basis of this flow model. The computational domain for an axisymmetric flow simplification is shown in Figure 3.1.

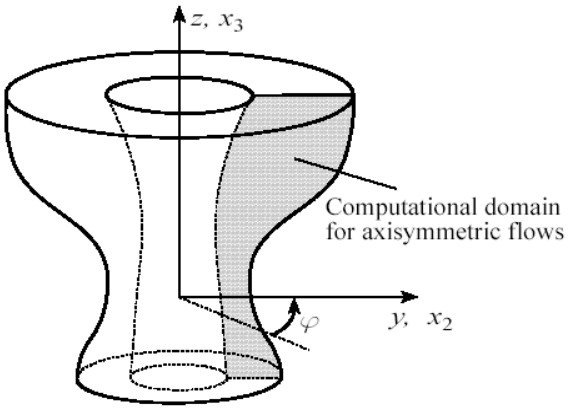

Figure 3.1 Computational domain for axisymmetric flows (ADINA R&D, Inc. (2008)).

Relative to the cylindrical coordinate system (y, φ, z) indicated in Figure 3.1, solutions are defined in the global y-z plane, where the y coordinate is representative of the *r* cylindrical coordinate. With the gradient operator designated as

$$\nabla \equiv E_2 \frac{\partial}{\partial x_2} + E_3 \frac{\partial}{\partial x_3} \tag{3.1}$$

the constituent Navier-Stokes equations for mass, momentum and energy conservation can be written for a cylindrical coordinate system in vector form as

$$\frac{\partial(y\rho)}{\partial t} + \nabla \cdot (y\rho\vec{v}) = 0 \tag{3.2}$$

$$\frac{\partial}{\partial t}(y\rho\vec{v}) + \nabla \cdot [y(\rho\vec{v}\vec{v} - \vec{\tau}_a)] = y\vec{f}^{\,B} + \vec{f}_a \tag{3.3}$$

$$\frac{\partial}{\partial t}(y\rho E) + \nabla \cdot [y(\rho\vec{v}E - \vec{\tau}_a \cdot \vec{v} + \vec{q})] = y(\vec{f}^{\,B} \cdot \vec{v} + q^B) \tag{3.4}$$

where ρ is the density, t is the time, $\vec{v}$ is the velocity vector, $\vec{\tau}_a$ is the stress tensor, $\vec{f}^{\,B}$ is the body force vector, E is the specific total energy, $\vec{q}$ is the heat flux vector, and q^B is the specific rate of heat generation associated with the flow. The independent variables specified for the solution of the above equations are the conservative variables $\rho, \rho\vec{v}$ and ρE.

The specific total energy, the fluid stress tensor and the heat flux vector, which is assumed to obey Fourier's law of heat conduction, are respectively defined as

$$E = \frac{1}{2}\vec{v} \cdot \vec{v} + e \tag{3.5}$$

$$\vec{\tau} = [(-p + \mu y^{-1}\nabla \cdot (y\vec{v})]\vec{I} + 2\lambda\vec{e}_a + 2\lambda\Delta\vec{e}_a \tag{3.6}$$

$$\vec{q} = -k\nabla\theta \tag{3.7}$$

where e is the specific internal energy, p is the pressure and μ and λ are the dynamic and kinematic viscosities of the fluid. $\vec{I}$ is the identity vector. Variables k and θ are the heat conductivity coefficient and temperature of the fluid, respectively. The vector $\vec{e}_a$ is the velocity strain tensor, written as

$$\vec{e}_a = \frac{1}{2}(\nabla\vec{v} + \nabla\vec{v}^{\,T}) \tag{3.8}$$

For mathematical closure of this system of governing equations, state equations which establish the relationship between the flow variables p, ρ, θ and e must be introduced. For ideal gas flow, as is the case in this work, the state equations can be derived from the ideal gas law as

$$p = (C_p - C_v)\rho\theta \tag{3.9}$$

$$e = C_v\theta \tag{3.10}$$

where C_p and C_v are the constant pressure and constant volume specific heats of the fluid, respectively.

The Navier-Stokes equations are discretized by ADINA-F using a combined finite volume / finite element approach. As discussed in ADINA R&D, Inc. (2008), the flow through a given control volume can be described by two distinctive normal flux terms – the dominant inviscid flux term, denoted as $\vec{F}_n$, and the viscous flux term, denoted as $\vec{G}_n$. ADINA-F uses a finite volume discretization to compute the flux $\vec{F}_n$, whilst using a finite element discretization to solve the flux $\vec{G}_n$. In a physical sense, the control volumes required by this flux splitting approach are generated on a framework of the elements prescribed by the finite element discretization. This arrangement for the case of a planar or axisymmetric two-dimensional flow domain is illustrated in Figure 3.2.

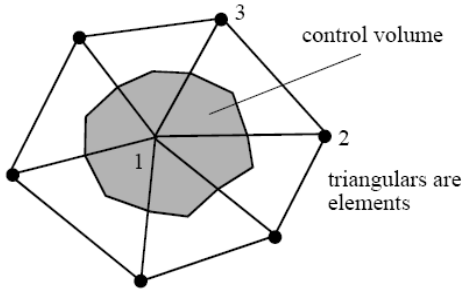

Figure 3.2 The arrangement of a control volume amongst triangular finite elements (ADINA R&D, Inc. (2008)).

When used to discretize high-speed compressible flows, standard low-order finite element approaches are generally not able to capture the discontinuities associated with shocks and other characteristic phenomena efficiently (Hendriana and Bathe (2000)). However, by combining the strengths of the finite element and volume methods in the form of the flux-splitting technique described above, ADINA-F is able to provide for shock capture using coarser and hence less computationally expensive mesh schemes.

Owing to its suitability for use in discretizing both low and high Reynold's Number flow regimes, ADINA-F's two-dimensional, axisymmetric, three-noded triangular fluid element was employed exclusively for all flow simulations undertaken in this study. The element is displayed in Figure 3.3, where the denotations '1', '2' and '3' represent the nodes at which all variables are defined, whilst '0' represents an auxiliary node not used explicitly for the final element solution. The parameters 'r' and 's' represent the element's isoparametric coordinate system.

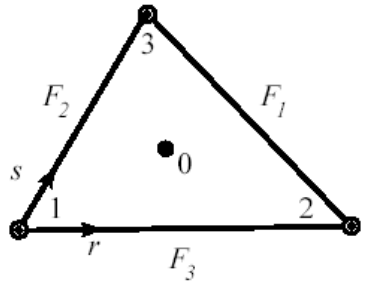

Figure 3.3 The two-dimensional, three-node triangular fluid element (ADINA R&D, Inc. (2008)).

As is the case with all axisymmetric elements used in the ADINA code, the element described above is defined in the positive global YZ plane over a rotational span of one radian, with the Z axis designated as the axis of symmetry.

The discretized equations particular to the high-speed compressible flow model of ADINA-F are solved using linearization and iterative techniques, due to their nonlinear characteristics. Specifically, such equations are iteratively resolved on the basis of solutions obtained for the associated set of linearized algebraic equations, in a process known as outer iteration. For the solution of the algebraic equations themselves, ADINA-F provides for either a direct or iterative

approach. When the iterative method is employed, solutions are obtained through a procedure termed inner iteration.

For this work, outer iterations were carried out using the Newton-Raphson technique as this is the method prescribed by ADINA-F for problems discretized with the two-dimensional, three-noded finite element. The resolution of the algebraic equation systems generally imposes the most significant demand on computational resources. As such, a number of direct and iterative solution techniques are available in ADINA-F, each with particular strengths and weaknesses. The most effective direct technique, ADINA-F's sparse solver, is particularly well suited for resolving very large systems of equations but at the price of significant memory requirements. For small to moderate problems that are well conditioned, ADINA-F's iterative methods provide efficient solutions with significantly less memory demands – in certain cases arriving at the solution more rapidly than the sparse solver. Selection of the most appropriate approach was made on the basis of numerical experimentation, and ultimately, the code's Right Preconditioned Generalized Minimal Residual iterative solver was found to be the most effective.

Implicit time integration was employed for all transient problems, using the Euler backward integration method. ADINA-F's automatic time-stepping CFL facility was incorporated into the solution process to aid solution convergence, with a user defined Courant-Friedrichs-Lewy number of 3 being used in a time relaxation role. Owing to the considerable temporal gradients of certain boundary conditions applied in the unsteady simulations of this study, the code's automatic time-stepping (ATS) option was also utilised in all transient fluids models to allow for convergence to be obtained at a reasonably sized time step. If convergence is not achieved for a particular user specified time step, ADINA-F automatically subdivides the time step into smaller sub time steps and attempts the computation again, until a solution is obtained or the specified maximum number of time steps is reached. In this way, flow solutions are only saved at the user specified time steps, making the size of the solution more manageable. The maximum number of subdivisions allowed for all fluid flow computations was set at 10.

For all transient flow problems considered, in-wall nozzle temperature distributions defined at the element nodes were resolved in the fluid model for each time step using ADINA-F's conjugate heat transfer function, and mapped onto the associated solid model nodes using a mapping file. To achieve this, 'solid' elements were defined in the fluid model to represent the

physical regions of the solid model. This approach is depicted in Figure 3.4. In the event of inconsistent nodal coordinates between the coincidental solid domains, mapping is accomplished via linear interpolation.

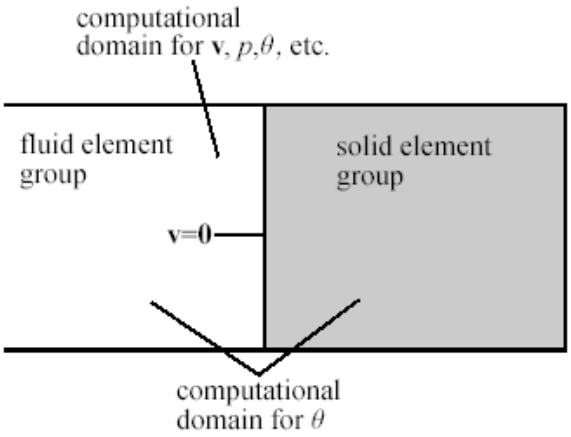

Figure 3.4 Conjugate heat transfer domains
(ADINA R&D, Inc. (2008)).

In developing the solution to a conjugate heat transfer problem, the computational domain of the continuity and momentum equations comprises the fluid elements, whilst the associated domain of the energy equation consists of the fluid and solid elements.

With regards to the initial and boundary conditions prescribed for the flow problems considered in this study, the application of such conditions will be explained in the specific context of the model development process.

3.3 Thermal Modelling

The modelling of long term heat transfer within the nozzle structure was accomplished using the 'ADINA-T' program of the ADINA system. The program has the capacity to simulate the steady or transient transfer of heat via conduction, convection and radiation modes, through media exhibiting constant, temperature dependent or time dependent isotropic and orthotropic properties.

Determinations of transient nozzle temperature distributions over durations longer than the ignition periods considered were made using dedicated thermal models constructed and analysed in the ADINA-T program, instead of employing the conjugate heat transfer facility of ADINA-F. This approach was adopted because of the significant temperature field error that would have been incurred with an isotropic conduction approximation for long periods of thermal loading. By employing ADINA-T to derive the solutions, its orthotropic conduction capability could be exploited.

In the cylindrical coordinate system, (r, θ, z), the problem of unsteady, axisymmetric thermal conduction in a homogeneous, rotationally symmetric orthotropic medium is described by the following governing equation, derived on the basis of Fourier's law:

$$\rho \cdot C \frac{\partial T}{\partial t} = \frac{1}{r} \frac{\partial}{\partial r}\left(k_r r \frac{\partial T}{\partial r} \right) + \frac{\partial}{\partial z}\left(k_z \frac{\partial T}{\partial z} \right) + Q \tag{3.11}$$

where r and z represent the radial and axial directions, respectively, ρ and C are the medium's density and specific heat capacity, respectively, T is the temperature in the medium, k_r and k_z are the thermal conductivities in the r and z directions, respectively, and Q represents either the heat source or sink terms.

ADINA-T uses a finite element scheme to discretize the governing equation of heat conduction, based on the principle of virtual temperatures that is described in the work of Bathe (2006), to give the following equilibrium equation for a transient, linear analysis employing Euler backward integration:

$$\boldsymbol{C} \cdot {}^{t+\Delta t}\dot{\boldsymbol{\theta}} + (\boldsymbol{K}^k + \boldsymbol{K}^c) \cdot {}^{t+\Delta t}\boldsymbol{\theta} = {}^{t+\Delta t}\boldsymbol{Q} + {}^{t+\Delta t}\boldsymbol{Q}^e \tag{3.12}$$

where $\boldsymbol{C}$ is the heat capacity matrix, ${}^{t+\Delta t}\dot{\boldsymbol{\theta}}$ is the vector of the time rate of temperature change at all nodal points at a time of $t + \Delta t$, $\boldsymbol{K}^k$ and $\boldsymbol{K}^c$ are the conductivity and convection matrices, respectively, ${}^{t+\Delta t}\boldsymbol{\theta}$ is the vector of temperatures at all nodal points at a time of $t + \Delta t$, ${}^{t+\Delta t}\boldsymbol{Q}$ is the nodal point heat flow input vector evaluated at a time of $t + \Delta t$, and ${}^{t+\Delta t}\boldsymbol{Q}^e$ is the

vector of nodal point heat flux attributable to convection boundary conditions, once again, for a solution time of $t + \Delta t$.

For the first ignition period thermal response simulation, ADINA-T's two-dimensional, axisymmetric, nine-noded, quadrilateral conduction element was employed. For subsequent thermal simulations however, the four-noded version of this element featuring linear interpolation was specified, at is generated a more accurate response to severe and rapid thermal loading regimes. A schematic of the nodal layout and coordinate system of the four-noded element is shown in Figure 3.5.

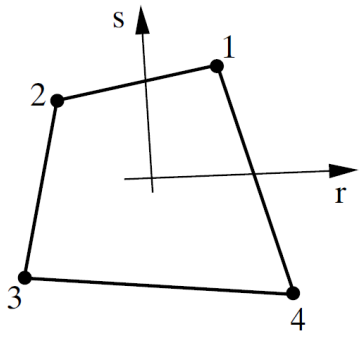

Figure 3.5 The axisymmetric, four-noded, quadrilateral thermal element (adapted from ADINA R&D, Inc. (2008)).

To prescribe the convective cooling effect occurring at the interface of the nozzle surface and the external atmosphere, ADINA-T's axisymmetric line convection element was used in conjunction with the associated axisymmetric conduction element at the atmospheric boundary. The surface convective load, q^s, is given as

$$q^s = h\left(\theta_e - \theta^s\right) \tag{3.13}$$

where h is the local heat transfer coefficient, θ_e is the environmental temperature and θ^s is the temperature of the surface. For all cases in the present study, the local heat transfer coefficient was treated as constant.

Insofar as material modelling is concerned, an isotropic conduction model with an isotropic specific heat capacity was used to represent the isotropic materials of construction, whilst the orthotropic constituents were modelled using an orthotropic conduction model featuring an isotropic specific heat capacity. Although in reality, the conductivity and specific heat capacity properties of thermal composites exhibit an appreciable dependence on temperature, the significant difficulties encountered in attempting to obtain comprehensive temperature-dependent data for the materials employed, made the approximation of temperature-independent thermal properties a necessary one.

In terms of the solution of the discretized governing equation of heat transfer, three solvers are offered by ADINA-T; a direct skyline solution method, an iterative solver and a sparse solver. In light of the reasonably small computational size of the thermal models considered, the solver time savings provided by an iterative solution procedure were not significant, whilst the memory cost of using a purely direct approach was not justifiable. As such, the sparse solver was employed to generate solutions to all thermal models. For time integration in transient problems, the Euler backward integration scheme was used.

For the transport of the resolved temperature field from the thermal model to the solid model, two approaches are available in the ADINA-T program. If an identical mesh is used to discretize the thermal and solid models, the temperature output file written by ADINA-T is used to assign the nodal temperatures of the solid mesh on a node-for-node basis. If the non-coincidental meshes are used, nodal mapping is achieved via spatial interpolation. Similar procedures are carried out with regards to the temporal component of the problem, if either model is characterised by different time increments.

3.4 Structural Modelling

Structural modelling was carried out using the ‘ADINA’ program of the ADINA system, which can accommodate the linear and nonlinear analysis of static and dynamic problems characterised by isotropic elasticity or plasticity, orthotropic elasticity, in addition to isotropic or orthotropic thermoelasticity. With respect to the work described here, structural problems were simulated both in a quasi-static sense, where the time-dependent displacement variations occurred only as a result of a transient thermal strain influence, and in a dynamic sense, where the time-varying

contribution of inertial effects was explicitly modelled through specific time domain discretization.

The general equations governing the solid mechanics of a given medium consist of the equations of motion, the constitutive equations and the strain-displacement relations. In light of the fact that both isotropic and cylindrically orthotropic materials are being simulated under static and dynamic regimes in this study, the above equations will be discussed henceforth in the most general spatial and temporal terms applicable.

For the cylindrical coordinate system, (r, θ, z), the elastodynamic equations of motion in the absence of material damping can be written as

$$\frac{\partial \sigma_{rr}}{\partial r} + \frac{1}{r}\frac{\partial \sigma_{\theta r}}{\partial \theta} + \frac{\partial \sigma_{zr}}{\partial z} + \frac{1}{r}\left(\sigma_{rr} - \sigma_{\theta\theta}\right) = \rho \frac{\partial^2 u_r}{\partial t^2} \tag{3.13}$$

$$\frac{\partial \sigma_{r\theta}}{\partial r} + \frac{1}{r}\frac{\partial \sigma_{\theta\theta}}{\partial \theta} + \frac{\partial \sigma_{z\theta}}{\partial z} + \frac{2}{r}\sigma_{r\theta} = \rho \frac{\partial^2 u_\theta}{\partial t^2} \tag{3.14}$$

$$\frac{\partial \sigma_{rz}}{\partial r} + \frac{1}{r}\frac{\partial \sigma_{\theta z}}{\partial \theta} + \frac{\partial \sigma_{zz}}{\partial z} + \frac{1}{r}\sigma_{rz} = \rho \frac{\partial^2 u_z}{\partial t^2} \tag{3.15}$$

where σ_{rr}, $\sigma_{\theta\theta}$ and σ_{zz} are the radial, circumferential and axial stresses, respectively, $\sigma_{\theta r}$, $\sigma_{r\theta}$, σ_{zr}, σ_{rz}, $\sigma_{z\theta}$ and $\sigma_{\theta z}$ are the associated shear stresses, ρ is the mass density of the medium, u_r, u_θ and u_z are the displacements in the radial, circumferential and axial directions, respectively, and t denotes the variable of time. The omission of the velocity-dependent damping terms is appropriate since the effects of material damping on the dynamic nozzle response were not considered. For the static consideration, the right hand side time derivatives vanish to yield the elastostatic equations of equilibrium.

For cylindrically orthotropic media, the constitutive equations relating the elastic and thermoelastic strains to the directional stress states can be expressed in matrix form as

$$\begin{bmatrix} \varepsilon_{rr} - \alpha_r \Delta T \\ \varepsilon_{\theta\theta} - \alpha_\theta \Delta T \\ \varepsilon_{zz} - \alpha_z \Delta T \\ \varepsilon_{\theta z} \\ \varepsilon_{rz} \\ \varepsilon_{r\theta} \end{bmatrix} = \begin{bmatrix} c_{11} & c_{12} & c_{13} & 0 & 0 & 0 \\ c_{12} & c_{22} & c_{23} & 0 & 0 & 0 \\ c_{13} & c_{23} & c_{33} & 0 & 0 & 0 \\ 0 & 0 & 0 & c_{44} & 0 & 0 \\ 0 & 0 & 0 & 0 & c_{55} & 0 \\ 0 & 0 & 0 & 0 & 0 & c_{66} \end{bmatrix} \cdot \begin{bmatrix} \sigma_{rr} \\ \sigma_{\theta\theta} \\ \sigma_{zz} \\ \sigma_{\theta z} \\ \sigma_{rz} \\ \sigma_{r\theta} \end{bmatrix} \tag{3.16}$$

where c_{ij} are the compliance coefficients, ε_{rr}, $\varepsilon_{\theta\theta}$ and ε_{zz} are the radial, circumferential and axial elastic strains, respectively, and $\varepsilon_{\theta z}$, ε_{rz} and $\varepsilon_{r\theta}$ are the associated elastic shear strains. The thermoelastic strain contribution is represented by the product, $\alpha_i \Delta T$, where α_r, α_θ and α_z are the coefficients of thermal expansion in the radial, circumferential and axial directions, respectively, and ΔT is the difference between the localised instantaneous and initial temperatures in the medium.

To compute ΔT, the instantaneous temperature distribution is prescribed by the thermal output file originating from the associated thermal model in the case of a thermostructural simulation with explicit thermal modelling, or flow model in the case of a conjugate heat transfer resolution. It should be noted that in either scenario, the structural and thermal solutions were not coupled. That is, although the temperature field solution affected the structural response, the converse effect was omitted from the thermoelastic solution.

The compliance coefficients can be further expanded in terms of the principle elastic moduli and Poisson's ratios as follows:

$$\begin{aligned} c_{11} &= \frac{1}{E_r},\ c_{12} = \frac{-\nu_{\theta r}}{E_\theta},\ c_{13} = \frac{-\nu_{zr}}{E_z} \\ c_{22} &= \frac{1}{E_\theta},\ c_{23} = \frac{-\nu_{\theta z}}{E_z},\ c_{33} = \frac{1}{E_z} \\ c_{44} &= \frac{1}{G_{r\theta}},\ c_{55} = \frac{1}{G_{rz}},\ c_{66} = \frac{1}{G_{\theta z}} \end{aligned} \tag{3.17}$$

where E_r, E_θ, E_z, are the elastic moduli with relative to the r, θ, z directions, respectively, $\nu_{\theta r}$, ν_{zr}, $\nu_{\theta z}$ are the associated Poisson's ratios, and $G_{r\theta}$, G_{rz} and $G_{\theta z}$ are the associated shear moduli of the medium.

To provide closure to the governing equations, the equations relating elastic strains to displacements can be written as

$$\varepsilon_{rr} = \frac{\partial u_r}{\partial r} \tag{3.18}$$

$$\varepsilon_{\theta\theta} = \frac{u_r}{r} + \frac{1}{r}\frac{\partial u_\theta}{\partial \theta} \tag{3.19}$$

$$\varepsilon_{zz} = \frac{\partial u_z}{\partial z} \tag{3.20}$$

and for elastic shear strains to displacements, as

$$\varepsilon_{r\theta} = \varepsilon_{\theta r} = \frac{1}{2}\left[\frac{\partial u_\theta}{\partial r} + \frac{1}{r}\frac{\partial u_r}{\partial \theta} - \frac{u_\theta}{r}\right] \tag{3.21}$$

$$\varepsilon_{\theta z} = \varepsilon_{z\theta} = \frac{1}{2}\left[\frac{1}{r}\frac{\partial u_z}{\partial \theta} + \frac{\partial u_\theta}{\partial z}\right] \tag{3.22}$$

$$\varepsilon_{zr} = \varepsilon_{rz} = \frac{1}{2}\left[\frac{\partial u_r}{\partial z} + \frac{\partial u_z}{\partial r}\right] \tag{3.23}$$

In regards to the above, the specification of an axisymmetric analysis domain introduces the following conditions relating to the elastic strain and shear strain expressions:

$$\varepsilon_{\theta\theta} = \frac{u_\theta}{r},\ \varepsilon_{\theta r} = \varepsilon_{r\theta} = 0,\ \varepsilon_{\theta z} = \varepsilon_{z\theta} = 0 \tag{3.24}$$

The discretization of the equation of motions, Equations 3.13-3.15, is carried out by ADINA using a finite element scheme, to yield the following classical representation:

$$\boldsymbol{M}\ddot{\boldsymbol{U}} + \boldsymbol{K}\boldsymbol{U} = \boldsymbol{R} \tag{3.25}$$

where $\boldsymbol{M}$ is the element assemblage mass matrix, $\ddot{\boldsymbol{U}}$ and $\boldsymbol{U}$ are the nodal acceleration and displacement vectors, respectively, $\boldsymbol{K}$ is the element assemblage stiffness matrix and $\boldsymbol{R}$ is the load vector associated with the element assemblage. Of course, for the elastostatic condition, the equilibrium equation reduces to

$$\boldsymbol{K}\boldsymbol{U} = \boldsymbol{R} \tag{3.26}$$

For a given element, m, the mass matrix, stiffness matrix and load vector can be expressed respectively as:

$$\boldsymbol{M} = \sum_{m} \int_{V^{(m)}} \rho^{(m)} \boldsymbol{H}^{(m)T} \boldsymbol{H}^{(m)} dV^{(m)} \tag{3.27}$$

$$\boldsymbol{K} = \sum_{m} \int_{V^{(m)}} \boldsymbol{B}^{(m)T} \boldsymbol{C}^{(m)} \boldsymbol{B}^{(m)} dV^{(m)} \tag{3.28}$$

$$\boldsymbol{R} = \boldsymbol{R}_{\boldsymbol{B}} + \boldsymbol{R}_{\boldsymbol{S}} - \boldsymbol{R}_{\boldsymbol{I}} + \boldsymbol{R}_{\boldsymbol{C}} \tag{3.29}$$

where $\rho^{(m)}$ is the elemental mass density, $\boldsymbol{H}^{(m)}$ is the displacement interpolation matrix, $\boldsymbol{B}^{(m)}$ is the strain-displacement matrix, $\boldsymbol{C}^{(m)}$ is the elasticity matrix, and $\boldsymbol{R}_{\boldsymbol{B}}$, $\boldsymbol{R}_{\boldsymbol{S}}$, $\boldsymbol{R}_{\boldsymbol{I}}$ and $\boldsymbol{R}_{c}$ are the vectors of body forces, surface forces, initial stress loads and concentrated loads, respectively.

Spatial discretization of the solid domains considered in this study was achieved using ADINA's isoparametric displacement-based finite elements; more specifically, the two-dimensional, axisymmetric, nine-node, quadrilateral solid element. With respect to the global coordinate

system, the nodal layout and isoparametric coordinate system of this element is illustrated in Figure 3.6.

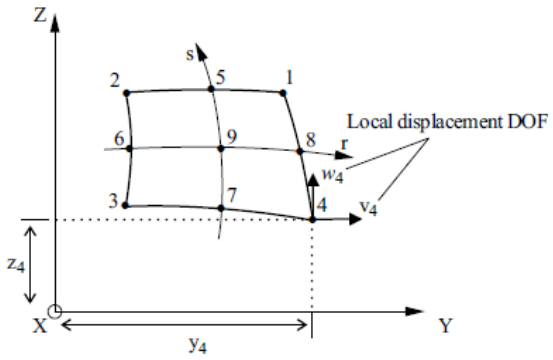

Figure 3.6 The axisymmetric, nine-noded, quadrilateral, solid element (adapted from ADINA R&D, Inc. (2008)).

In respect of Figure 3.6, it is important to take note of the global cylindrical coordinate system used by ADINA. When such a coordinate system is invoked implicitly through the specification of axisymmetric modelling, for example, the Cartesian coordinate annotation X, Y and Z is retained. However, instead of representing a Cartesian axis system, X, Y and Z are used to respectively represent the r, θ and z elements of the cylindrical coordinate system. As such, the axisymmetric plane rz is denoted in ADINA as the plane YZ.

Under the loading conditions being considered, the materials employed in all solid models were assumed to exhibit an elastic response behaviour characterised by small displacements and small strains. As such, the stress and strain outputs generated by ADINA are given in terms of the Cauchy stress and engineering strain, respectively. In cases where either a combination of thermal and mechanical loading or thermal loading alone was applied, ADINA's thermo-orthotropic material model was used to describe all orthotropic regions, whilst the thermo-isotropic model represented all isotropic regions. In instances where just mechanical loading was being considered, the elastic-orthotropic and elastic-isotropic models were selected for these purposes, respectively. Once again, as a consequence of severely limited material data resources, the elastic moduli, shear moduli, Poisson's ratios and coefficients of thermal expansion were

assumed to be temperature-independent, although in reality, such properties generally exhibit temperature dependence for the range of temperatures being considered in this work.

Owing to the material and geometric linearity of the solid mechanics problems at hand, the static and dynamic finite element equilibrium Equations 3.26 and 3.25 are subsequently characterised as linear themselves. The resolution of the static equilibrium equation can be carried out in ADINA using either a direct sparse solver or an iterative solution algorithm. As was the case for thermal modelling, the sparse solver approach was adopted, for similar reasons.

In terms of dynamic modelling, the primary consideration in terms of the solution approach to select relates to whether an explicit or implicit time integration technique needs to be employed. This selection should ideally be made based on a number of factors, including the time scale of the solution, the degree of model nonlinearity, the available computational resources and the degree to which susceptibility to numerical instability can be tolerated. It is well known that explicit time integration schemes are only conditionally stable; that is, the numerical stability of the solution can only be assured if the time step size is below a critical value determined on the basis of wave speed and minimum finite element size. Implicit schemes on the other hand, are unconditionally stable – at the cost of increased computational effort, however.

Although explicit methods exhibit greater computational efficiency in solving problems characterised by rapid loading transients, as the finer details of the analysis parameters associated with this study were initially unknown, a decision was made at the outset to approach the solution of all dynamic problems using implicit time integration. In this way, the generation of stable dynamic solutions was guaranteed, even if it was at the cost of extra computational effort.

In addition, as explicit time integration cannot be used to solve dynamic problems involving fluid-structure interaction in the ADINA system, the use of an implicit approach for all disciplines resulted in greater computational uniformity. Implicit time integration was implemented with a step-by-step direct integration approach using the Newmark method. As per the recommendations of ADINA R&D, Inc. (2008), the trapezoidal rule was observed, where the α and δ Newmark time integration parameters were set at 0.25 and 0.5, respectively.

Finally, with regards to the nature of the applied loading conditions and constraints associated with the two nozzle design structural models, further details will accompany the description of the construction of these models in the coming chapters.

3.5 Fluid-Structure Interaction Modelling

Two forms of interaction between a flow and the structure within or around which the flow occurs, can be modelled using the ADINA system's ADINA-FSI program – the implementation of which is described in detail in ADINA R&D, Inc. (2008). The first technique, referred to as two way coupling, allows for the flow to influence the structure, and then for the structure to influence the flow field in return, and is coupling in its truest sense. The second type is known as one way coupling and only accommodates the influence of the fluid on the structure. To avoid confusion, the solution derived using the former technique will henceforth be referred to as the coupled solution, whilst that obtained using the latter method will be referred to as the uncoupled solution.

In the current study, both classifications of field coupling were considered. In the case of either approach, the interaction simulated only exists with respect to the transfer of stress between the fluid and solid domains. To accommodate the additional effects relating to the transfer of heat between the two fields, an extension of the ADINA-FSI program known as ADINA-TFSI can be used. H owever, this application is not compatible with the incorporation of the high-speed compressible flow model to describe the flow component of the fluid-structure interaction. As such, the fluid-structure interaction (FSI) modeling carried out in this work was limited to the consideration of mechanical (pressure) loading alone.

Ordinarily, solid models are solved by the ADINA system in reference to a Lagrangian coordinate system, with the primary unknown in the solution being the nodal displacements of the solid. Fluid models, on the other hand, incorporate a Eularian coordinate system, and do not account for any distortion of the fluid domain. The objective in simulating fluid-structure interaction however, is to account for such a distortion and to examine the subsequent effects on the fluid flow. To overcome this problem, fluid models that form part of FSI analyses in ADINA-FSI are formulated using an Arbitrary-Langrangian-Eularian (ALE) coordinate system, and include displacement as a solution output. The physical coupling of the fluid and solid

models is achieved through the definition of the following kinematic and dynamic conditions at the FSI boundary – which is geometrically coincidental in the fluid and solid models (ADINA R&D, Inc. (2008)):

$$d_f = d_s \tag{3.30}$$

$$n \cdot \tau_f = n \cdot \tau_s \tag{3.31}$$

In Equations 3.30 and 3.31, d_f and d_s are the displacements of the fluid and solid at the interface, respectively, n is the normal direction of the fluid-structure interface, and τ_f and τ_s are the fluid and solid stresses at the interface, respectively. By differentiating Equation 3.30, the kinematic condition, with respect to time, one arrives at the fluid velocity condition for the case of zero velocity slip at the FSI boundary, where v and $\dot{d}_s$ are the fluid and solid velocities at the fluid-structure interface, respectively:

$$n \cdot v = n \cdot \dot{d}_s \tag{3.32}$$

The coupling solution begins with the calculation of fluid nodal positions on the fluid-structure interface, following which the displacements of the nodes in the rest of the fluid domain are computed. Subsequently, the governing equations are solved with respect to the ALE coordinate system to compute solutions of the fluid variables. The fluid traction is then integrated along the interface to calculate the force, *F(t)*, exerted on the solid nodes at the interface, shown by

$$F(t) = \int h^d \tau_f \cdot dS \tag{3.33}$$

where h^d is the virtual quantity of solid displacement. The resolution of nodal forces allows the displacement of the solid and hence the fluid domain to be reevaluated, and thus, following an iteration procedure to bring the displacement of fluid boundary to within a tolerance distance of the solid boundary, the coupled solution cycle repeats itself.

In this study, the “two way coupling” solution technique was used to compute the coupled response of the nozzle structure, whilst the “one way coupling” solution technique was used to compute the uncoupled structural response. Furthermore, the latter technique was used to obtain the separate mechanical loading solution for the ignition transient period.

In transient FSI modelling, the fluid model’s solution time specifications prescribe the overall solution time specification of the FSI analysis; that is, the number of time steps and the time step size of the FSI analysis are set in the fluid model and are automatically applied to the associated solid model. In addition, the time integration of the coupled set of fluid and solid equations in transient FSI analyses must naturally be consistent. A choice between the implicit Euler backward difference integration scheme and a composite integration approach are available for use. Considering that the Euler method was specified in the fluid model, this technique was also selected for all FSI analysis work conducted in this study on the grounds of uniformity. In terms of the solution approach used to couple the fluid and solid models for this study, an iterative technique was used in cases involving two-way coupling, whilst one-way coupling was resolved using a direct approach.

3.6 Validation of Numerical Simulation Methodologies

Naturally, to have confidence in the fidelity of the results generated by a given numerical simulation technique, the applicability of such a technique for a given set of problem conditions should be verified by some form of validation – either by comparing the results of the numerical solution to those of an associated analytical or experimental solution, or to the solution of an already validated numerical approach for similar problem conditions.

In this regard, efforts were made to demonstrate, as reasonably as was possible, the suitability of the fluid, thermal, solid and fluid-structure interaction numerical simulation methodologies used in this study. The validation of the thermal and thermoelastic methodologies was achieved through the undertaking of a dedicated validation study, whereas the fluid and fluid-structure interaction simulation methodologies employed were justified as far as possible by a survey of relevant literature.

As far as the solutions generated by ADINA-F are concerned, the fidelity of two key elements of these solutions required scrutiny: firstly, the accuracy of the high-speed compressible flow formulation, and secondly, the accuracy of the conjugate heat transfer facility. The solution performance of the ADINA-F code for the case of steady, two-dimensional compressible flow over a semi-infinite flat plate was validated in ADINA R&D, Inc. (2008) by comparing the numerical solution to the analytical one presented by Schlichting (1979); with good results agreement being observed. As far as high-speed compressible flow modelling is concerned, Bathe et al (1995) employed the ADINA-F code to solve the problem of steady, two-dimensional, high Reynold's number / high Mach number flow over a flat plate featuring a compression corner. In comparison to the experimental measurements presented by Holden (1978) for identical conditions, satisfactory agreement in flow parameter solutions was obtained. As a demonstration of the shock-capturing capabilities of ADINA-F, the solution generated by this code for the problem of steady supersonic flow over a bump disturbance in a channel was compared to the solutions obtained via higher order finite element schemes specifically developed for compressible flows in the work of Hendriana and Bathe (2000). In comparison to the higher order codes, results pertaining to the distribution of density in the fluid domain obtained by ADINA-F showed very good agreement, with a well-defined density discontinuity at the location of the standing compression shock.

The fidelity of the ADINA-F high-speed compressible flow model for the case of unsteady flow conditions was, in effect, unable to be established – primarily because of the modelling complexities at hand, and the lack of readily available analytical or experimental data relating to such problems. Having said this, a few sets of useful numerical results have been published; including the work of Chang et al (2005), to which comparisons of associated numerical results obtained using ADINA-F could be made. As the task of generating such results was itself comparable to the magnitude of the overall study, the performance of such an exercise was felt to be unrealistic in the context of the overall study time frame. Although this decision ruled out the possibility of a quantitative verification of the code, it would still remain possible to make assessments on the grounds of the qualitative behaviours associated with the ADINA-F solutions. Fortunately, the transient start-up flow of combustion products through a rocket motor nozzle exhibits a number of distinctive features, such as flow separation points, flow separation and Mach disk shocks, etc. that display strong time-dependence. This consideration made for a relatively straightforward qualitative validation assessment of the results generated in this study.

Such a measure of assessing the numerical validity of the solutions derived was considered adequate considering the nature of this work.

In terms of the validation of results obtained through the implementation of the ADINA and ADINA-T solid and thermal modelling programs, a number of cases were examined. The fundamental assumption made here was that if validity was demonstrated for the case of mechanical and thermal loading of orthotropic materials, this would automatically infer the validity of the methodologies used for the case of the mechanical and thermal loading of isotropic materials, considering the greater behavioural complexity associated with orthotropic media.

With regards to the accuracy of the ADINA code in modelling the response of orthotropic materials to mechanical loading, numerical validity was demonstrated by an assessment made in the work of ADINA, R&D, Inc. (2008). The assessment considered the problem of a simply supported square orthotropic plate subjected to uniform pressure loading. The results obtained using ADINA were compared to the analytical results provided by Timoshenko and Woinowsky-Krieger (1959), and showed excellent agreement with respect to displacement and stress predictions.

In the case of the thermal and thermoelastic response modelling of an orthotropic material, no reference validations are presented in ADINA, R&D, Inc. (2008). As such, a validation study was undertaken to assess the capabilities of the ADINA-T and ADINA codes in this regard. For this to be achieved, it was clear that the procedure should involve the comparison of numerically derived results, to those for a problem as reflective as possible of the geometry and material architecture featured by composite SRM nozzles in general.

Following a review of literature presenting solutions of this type, it was found that the most suitable solution was featured in the work of Kardomateas (1990). This study involved the transient quasi-static analysis of thermal stresses in an infinite thick hollow orthotropic cylinder, subjected to the application of a temperature loading condition at the inner surface of the tube. The analytical solution presented for this problem was derived through the use of Hankel asymptotic expansions for Bessel functions of the first and second kind.

The glass/epoxy tube, having an inner and outer radius of 20mm and 36mm respectively, featured a circumferential primary fibre orientation and is subjected to a thermal load of 100˚C applied at its inner surface. Upon closer examination of the data presented in the above work, certain anomalies were discovered and as a result, the work of Dao-Sheng (2003) featuring the identical example investigated by Kardomateas was used to provide improved results for the purposes of data comparison.

In the ADINA system, the problem was replicated by a pair of thermal and structural models, each comprised of 200 two-dimensional axisymmetric elements, with 20 elements in the thickness direction. The solid model was fully constrained along its lower edge, and employed the temperature data file generated by the thermal model to provide the required thermal inputs. In order to simulate the stiffness of the infinite tube examined by Dao-Sheng, it was established that a length of 0.5m, with results sampling through the wall thickness midway along the length of the tube, sufficiently eliminated the rigidity errors created by the constrained and free ends.

Kardeomateas' solution for the temperature field was demonstrated to be correct, and as such, his results for the wall temperature distribution at two normalised times, t*, were employed for validation purposes. The temperature distributions predicted by ADINA and Kardomateas are depicted in Figure 3.7, as a function of normalised radial distance from the inner wall, r*. Comparisons of radial stress, radial displacement, hoop stress and axial stress profiles were made with Dao-sheng's results at the equivalent normalised times and are presented in Figures 3.8-3.11.

From these figures, it can clearly be seen that there is very good overall agreement between the results produced by ADINA, and those predicted by Dao-Sheng, with no large variances in response trends. Although there is an underestimation in the magnitudes of both radial stress distributions, the correlation is particularly impressive with respect to all other comparisons. Figure 3.12 demonstrates the convergence of the finite element solution towards the analytical one for the case of radial stress, as a function of the thickness direction element density. Gross errors are present for an element density of 5, although these are effectively rectified for an element density of 10, providing reasonable agreement with the analytical prediction. It is interesting to note that increasing this density by a factor of 2 results in little change in the stress profile, suggesting that solution mesh independence may be present at such a mesh density.

Irrespective of this observation, the overall response agreement infers the suitability of both the ADINA-T and ADINA codes for this class of problem.

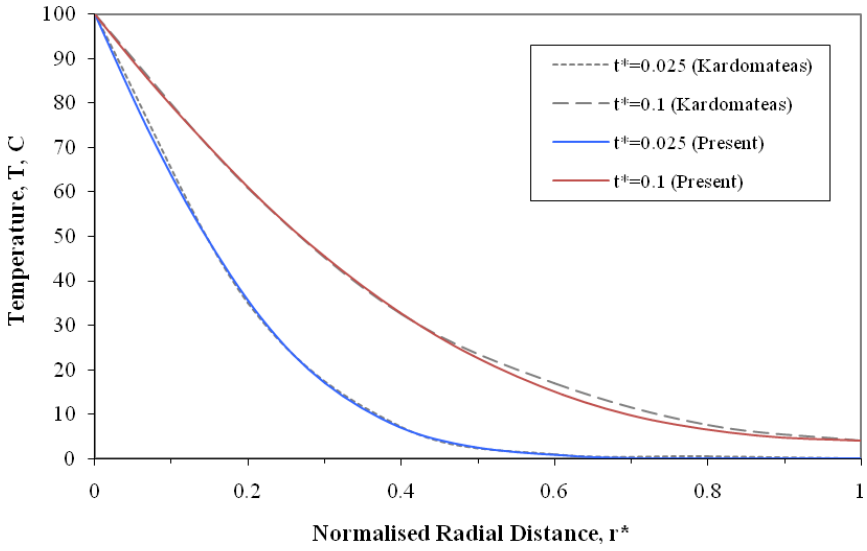

Figure 3.7 Temperature versus normalised radial distance.

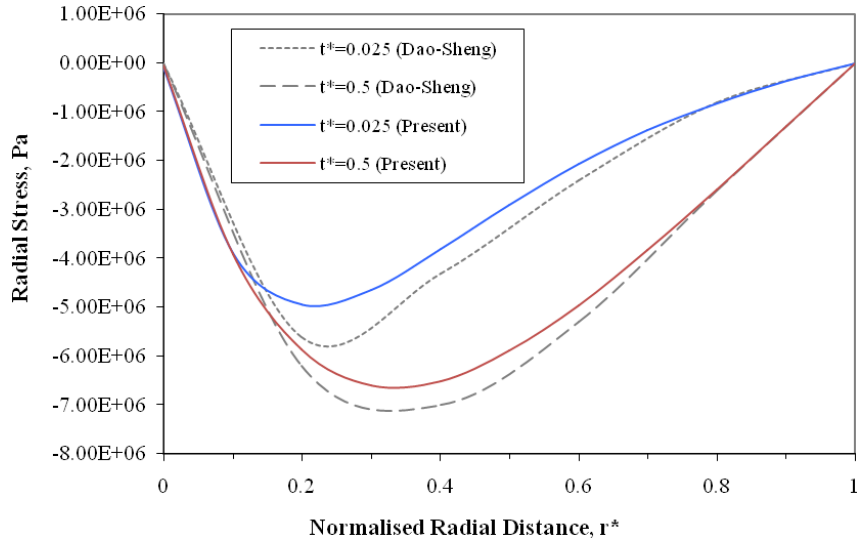

Figure 3.8 Radial Stress versus normalised radial distance.

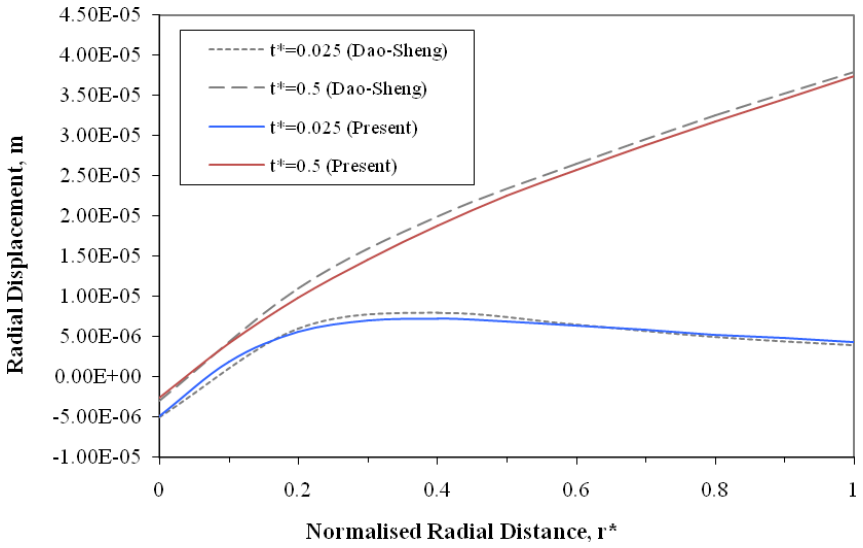

Figure 3.9 Radial Displacement versus normalised radial distance.

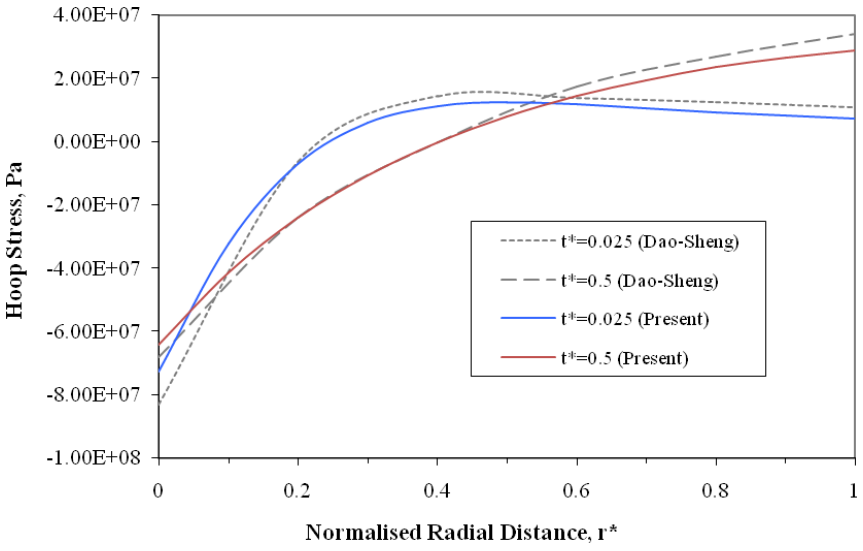

Figure 3.10 Hoop stress versus normalised radial distance.

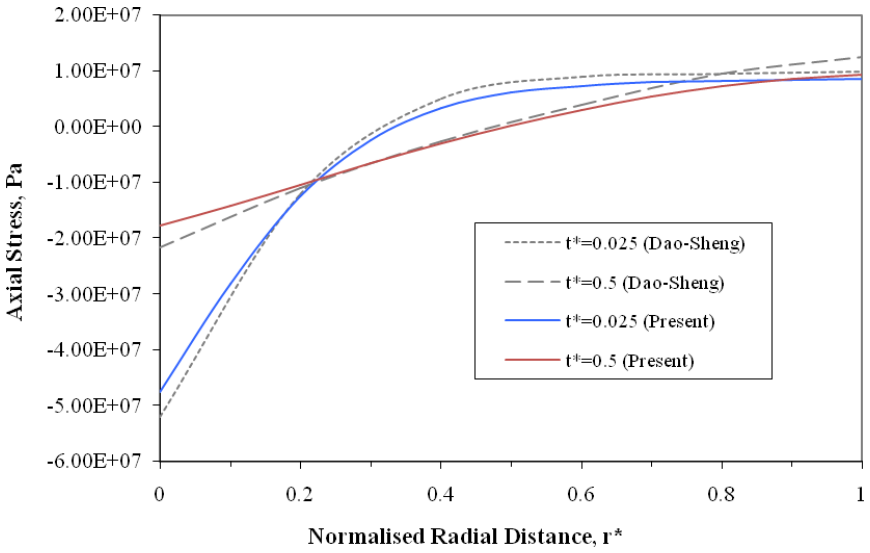

Figure 3.11 Axial stress versus normalised radial distance.

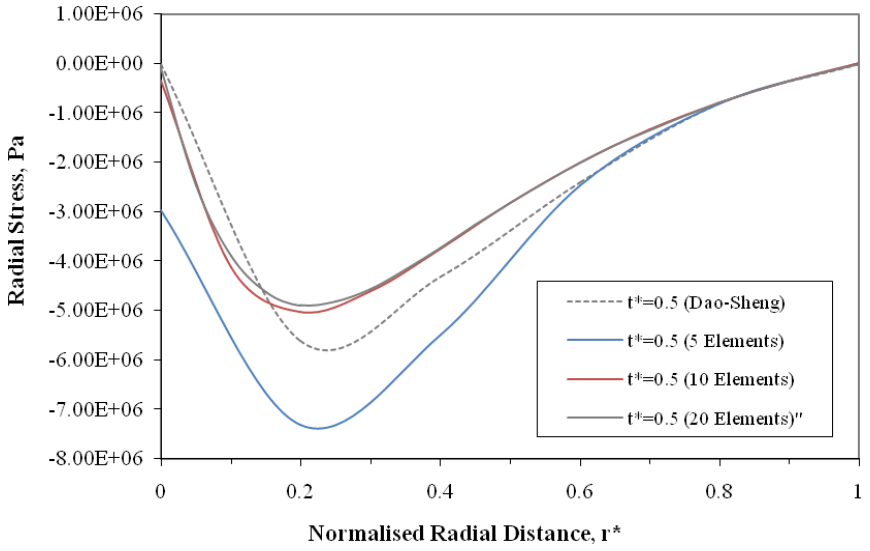

Figure 3.12 Convergence of the finite element solution for radial stress profile.

Insofar as the validation of the elastodynamic modelling of orthotropic media subjected to thermal and mechanical loading is concerned, the fidelity of the ADINA system could not be explicitly established. Despite attempts to numerically simulate the elastodynamic and

thermoelastodynamic behaviour predicted for the cylindrically orthotropic thick shells considered in the works of Xi et al (2000) and Cho et al (1998), agreement was generally poor. Two significant factors may have strongly influenced this result: the difficulty in accurately simulating infinite shell length using standard kinematic constraints and the effect of the spatial finiteness of the numerical models on elastic wave propagation and interaction. Having said this however, validation of the dynamic behaviour of an isotropic cylinder simulated by a model employing two-dimensional, axisymmetric elements and implicit Newmark time integration is demonstrated in ADINA R&D, Inc. (2008). The numerical solution obtained using the ADINA program is shown to be in good agreement with the theoretical solution presented by Reismann and Padlog (1967). Once again, in consideration of the exploratory nature of this work, such validation was deemed acceptable.

With respect to the modelling of fluid-structure interactions involving high-speed compressible flow is concerned, the validity of ADINA's FSI approach could not entirely established for the problem being considered in this study. Although the validity of the technique has been demonstrated for a variety of general problem classes in the works of Bathe et al (1995), Bathe et al (1999) and Zhang et al (2003), none of these works established the validity of the code for high-speed compressible flow problems.

Once again, the separate exercise of conducting a validation study in reference to an analytical solution of a simple problem involving aeroelastic coupling, such as the one derived by Evseev and Morozov (2001), which considers the aeroelastic interaction of shock waves with composite shells , was felt to be beyond the scope of this study. Irrespective of whether the validity of the technique when used to solve problems incorporating high-speed compressible flows has been established, the ADINA-FSI code has been used to simulate fluid-structure interaction for supersonic flow conditions. Kroyer (2003) employed the code to investigate aeroelastic instability effects associated with the actuation of aircraft control surfaces in supersonic flows, and demonstrated its capability in simulating complicated interaction phenomena.

It is ultimately the complexity associated with fluid-structure interaction phenomena, particularly those of a transient nature, which makes the validation of associated numerical solutions difficult if not impossible. Considering this inherent condition, it was felt that in light of the fact that the fidelity associated with ADINA's fundamental fluid, thermal and solid

analysis capabilities had in most respects been demonstrated, absolute confidence in the code's FSI simulation capacity was not required for useful exploratory observations to be made.

3.7 Conclusion

The multidisciplinary numerical simulation activities of this study have been outlined, and the methodologies employed in their implementation have been described. Furthermore, the various assumptions that have had to be made in respect of nozzle flow, thermal and structural modelling have been discussed in detail. As far as the ADINA finite element code is concerned, the suitability of its application in the simulation activities has, for the most part, been established. The coming chapters will now focus on detailing the application of these simulation methodologies in deriving the structural response of two solid rocket nozzle designs to loading encountered during the ignition and burn periods.

CHAPTER 4

Simulation of the Structural Response of a Composite SRM Nozzle to Instantaneous Thermal and Pressure Loading

4.1 Introduction

The first ignition period structural response simulation of a composite SRM nozzle considered in this study was devised to serve as an introduction to the implementation of the numerical simulation methodologies discussed in the previous chapter. The simulation employed the Solid Rocket Nozzle 1 (SRN1) design as the subject of analysis and considered the response of this structure to the instantaneous application of steady-state thermal and pressure loading conditions. In particular, the simulation utilised a set of thermal and structural models, without any incorporation of exhaust flow modelling. To provide context to the results obtained, the burn period structural response of SRN1 was simulated for the same loading conditions and finite element models.

Over and above its introductory nature, the primary objective of the simulation was to investigate and characterise the nature of the response of SRN1 to instantaneous thermal and pressure loading during the simulated ignition event. Furthermore, a key outcome of the simulation was to determine whether quasi-static modelling of the structure predicted its response sufficiently or if a dynamic analysis regime was required fully capture response phenomena.

The temperature and pressure loading conditions were derived on the basis of results presented in literature and were applied directly to the wetted surfaces of the thermal and structural models. To establish the suitability of SRN1's design, the burn period thermal and structural responses were simulated and demonstrated that the design provided reasonable performance with respect to the purposes of the current investigation. The structure's ignition response was then simulated using quasi-static and dynamic solution regimes, and results were evaluated at a number of locations within the axisymmetric plane of SRN1's entrance and throat region.

The development of the constituent models, the application of the simulation methodologies and the interpretation of the subsequent numerical results will now be discussed in greater detail.

4.2 Analysis Parameters

4.2.1 Solid Rocket Nozzle 1

In light of the difficulty encountered in obtaining the design details of any existing SRM nozzles, the designs examined in this work had to be developed by the author on the basis of the general SRM nozzle design principles discussed extensively in Ellis (1975). Solid Rocket Nozzle 1 was the first of these designs to be developed, fulfilling an exploratory function.

The primary design criterion was to create a nozzle that was as simply configured as possible, whilst exhibiting the fundamental features common to established medium scale booster SRM nozzles. A review of various nozzle profiles was conducted to determine key design characteristics that could guide the development of the SRN1 architecture. Specifically, the geometries and materials of construction employed for the thermal liners, insulators and attach structures of the nozzles were examined closely. One particular nozzle design featured in Ellis (1975), the BE-3A4, exhibited an attractive configuration, possessing a minimal number of subcomponents and a simple geometry. The BE-3A4 design is shown in Figure 4.1.

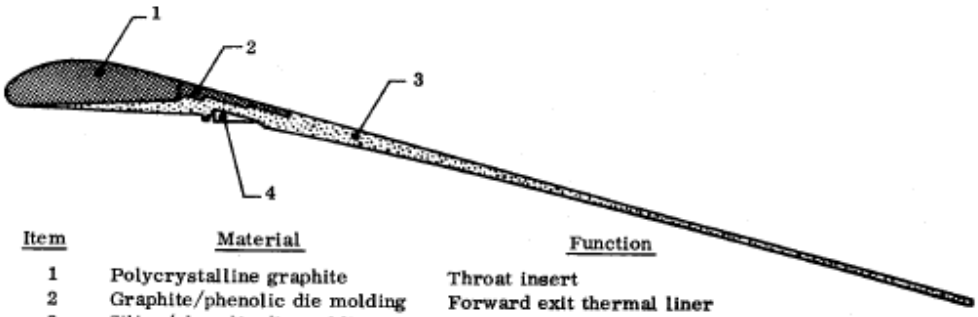

Item	Material	Function
1	Polycrystalline graphite	Throat insert
2	Graphite/phenolic die molding	Forward exit thermal liner
3	Silica/phenolic die molding	Throat insulation, aft exit liner, insulation, and structure
4	Aluminum	Attach structure

Figure 4.1 The BE-3A4 nozzle (Ellis (1975)).

As can be seen in Figure 4.1, the BE-3A4 design employs a polycrystalline graphite throat insert, which also provides the nozzle's inner entrance contour, and die molded graphite- and

silica-phenolic composites for the fore and aft exit cone sections, respectively. The aft exit cone section extends forward, providing insulation to the small aluminium attach structure and support to the throat insert. This detail illustrates the efficient use of thermal composites in the design, as aft exit cone section is able to act as both a thermal liner and a structural element, in addition to providing insulation to the thermally vulnerable attach structure.

The geometry of the subcomponents and wetted surface is relatively straight forward. The entrance region profile is uncomplicated and the exit cone features a conical exit contour with a moderate half angle and expansion ratio. As far as motor integration is concerned, the location of the attach structure indicates that the nozzle is partially submerged within the motor's combustion chamber. In addition, the design of the attach structure indicates that the nozzle is rigidly attached to the combustion chamber and does not accommodate gimballing for thrust vector control. It is as a consequence of this overall design simplicity, that the BE-3A4 nozzle provided a useful model upon which SRN1 configuration could roughly be based.

The design of Solid Rocket Nozzle 1 is shown in Figure 4.2, and is given dimensional detail in Appendix A. SRN1 was designed as a submerged nozzle featuring a 16% level of submergence, which is proportionally similar to that of the BE-3A4 design. SRN1 also features a fairly similar architecture, comprising four main substructures: an integral throat and entrance (ITE), a conical exit cone, an insulator and an attach structure.

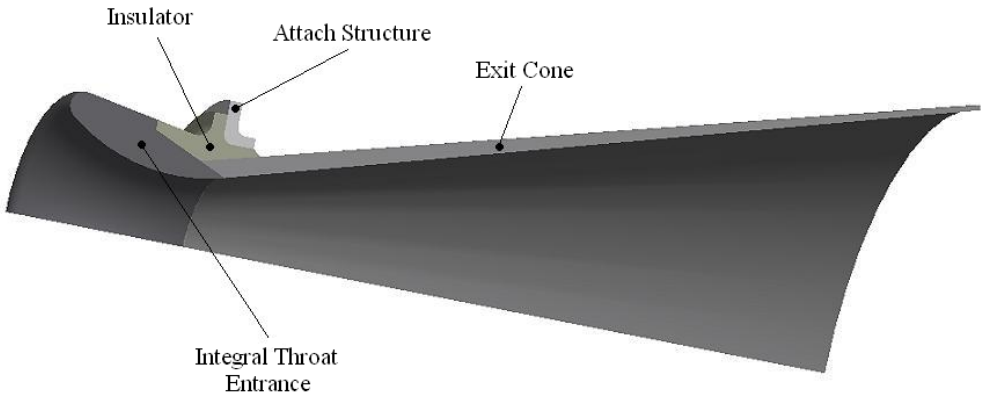

Figure 4.2 Structural configuration of SRN1.

The design differs in terms of the materials of construction however; mainly to ensure that it is as representative of the state-of-the-art as possible. Furthermore, in consideration of the axisymmetric nature of the analysis, only rotationally symmetric materials could be assigned in the design. Instead of employing polycrystalline graphite for the ITE, a 4D spatially reinforced carbon-carbon composite was designated, which exhibits far superior thermostructural and erosion resistant qualities. In place of die molded silica-phenolic insulation, a 2D tape wound carbon-phenolic composite was specified for the insulator, as thermal and mechanical properties were obtainable for this material. Since this study did not consider the effects of ablation, it was important that a thermally stable material was selected for the exit cone to ensure realistic simulation of the structure's response during the relatively long motor burn period. Consequently, a 3D spatially reinforced carbon-carbon material was chosen for this case, instead of a reinforced phenolic material. In terms of general dimensions, SRN1 has a nominal length of 1 m and a throat diameter of 0.144 m. The exit cone half angle is 15˚, the entrance-to-throat area ratio is 3 and the exit-to-throat area ratio is 10 – each of which is in line with design practice.

4.2.2 Nozzle Material Properties

Acquiring suitable mechanical and thermal properties for the composite materials prescribed in the SRN1 design also proved to be a significant challenge, particularly because such data is commonly proprietary in nature. After an extensive review of related literature, a collection of applicable properties was found in the work of Yoo et al (2003), which describes the thermoelastic analysis of an SRM nozzle comprising spatially reinforced carbon-carbon as well as tape-wound carbon phenolic composites. The data obtained from this source and employed in the finite element thermal and structural models of SRN1 are reflected in Table 4.1. The data is presented in reference to a cylindrical coordinate system, where *r*, θ and *z* denote the radial, circumferential and axial directions, respectively. $E_{\theta\theta}$, E_{zz}, E_{rr}, $G_{\theta z}$, $G_{\theta r}$, G_{zr}, $\upsilon_{\theta z}$, υ_{zr}, $\upsilon_{\theta r}$, k_{θ}, k_z, k_r, α_{θ}, α_z and α_r, are the moduli of elasticity, shear moduli, Poison's ratios, thermal conductivities and coefficients of thermal expansion in their associated directions, respectively, whilst C_p and ρ are the materials' specific heat capacity and density, respectively.

The effect of temperature on material properties was not considered in the analysis undertaken by Yoo et al (2003) and no details regarding the thermal dependence were presented in their work. Despite numerous efforts, the author was unable to obtain any further data associated with

these materials, and consequently, an assumption of temperature independence had to be made in the SRN1 simulations.

Property	4D C-C	3D C-C	2D C-P	Steel
$E_{\theta\theta} = E_{zz}$, GPa	24.6	34.42	74.5	205
E_{rr}, GPa	30.65	34.42	15.71	205
$G_{\theta z}$, GPa	9.17	2.552	5.017	78.13
$G_{\theta r} = G_{zr}$, GPa	2.48	2.552	4.65	78.13
$\nu_{\theta z}$	0.341	0.083	0.1	0.28
$\nu_{zr} = \nu_{\theta r}$	0.0664	0.083	0.54	0.28
$k_\theta = k_z$, W/mK	14.45	13.96	2.38	40.6
k_r, W/mK	14.14	13.96	0.38	40.6
$\alpha_\theta = \alpha_z$, x10^{-6} /°C	4.58	4.76	-1.5	14.6
α_r, x10^{-6} /°C	4.97	4.76	27	14.6
C_p, J/kgK	1159	1153	1206	595
ρ, kg/m^3	1507	1514	1329	7800

Table 4.1 Mechanical and thermal properties of the constituent materials.

4.2.3 Loading Conditions

The two predominant sources of nozzle loading simulated in this study were combustion gas pressure and thermal loading. Quite clearly though, in order to accurately represent the manner in which pressure and heat are applied to an SRM during ignition, loading conditions must be given resolution in both a spatial and temporal sense. That is, one expects a magnitude variation according to position along the nozzle wall and according to time, as an SRM ignition event is inherently unsteady.

This presented a difficulty however, as the techniques required to reproduce such loading conditions were beyond the scope of the current simulation. It therefore became clear that the loading conditions applied in the simulation could only be coarsely approximated. The approach that was finally adopted to achieve this was to define the spatial component of the loading conditions with wall pressure and temperature distributions obtained for steady flow conditions, and to describe the temporal component of the conditions with a simple time function – assuming that the pressure and thermal loading rates were identical.

As far as the spatial component is concerned, three techniques for defining the distribution of nozzle wall pressures and temperatures were considered. Analytically, these parameters could

have been approximated using one-dimensional gas dynamic theory, assuming steady and inviscid compressible flow. The application of this technique is able to yield reasonable results for the core region of nozzle flows, providing fairly accurate temperature and pressure distributions. Although static pressure at the nozzle wall can also be predicted to an acceptable accuracy, wall-side temperatures are significantly overestimated as the viscous boundary layer that forms in real nozzle flow is obviously not captured by such a model. Since the significance of thermoelastic stresses in SRM nozzles has been widely published, it was clear that the thermal loading condition needed to be as realistic as possible and a decision was therefore made not to employ this approach.

The two remaining approaches entailed using either computationally or experimentally derived data. Since the focus of the current exercise was to provide an introduction to the task of ignition period structural response modelling, an extension of that task to include flow modelling was deemed too complex at this early stage of the study. It was therefore concluded that the use of experimental data presented in literature should rather be explored.

Conveniently, the loading conditions employed by Yoo et al (2003) for their analysis were presented in their work. In the absence of similar data from any other sources of literature reviewed, this information was used to develop the loading conditions employed for the current simulation. These conditions are presented in Figures 4.3 and 4.4, where pressure and temperature distributions prescribed along SRN1's wetted surface are shown as functions of axial distance from the nozzle's entrance plane, respectively.

As far as the specification of the temporal component of these loading conditions is concerned, both ramp and Heaviside type functions were considered. Although it was recognised that the specified loading rate would likely influence the nature of SRN1's structural response significantly, as a first approach, a step function was chosen to model both pressure and temperature loading conditions. In theory, the application of the Heaviside function in the ignition period simulation scenario suggests obvious characteristics: at simulation time $t = 0^-$, the loading magnitudes are zero, and at $t = 0^+$, the loading magnitudes take on nominal values. But when implemented practically in a temporally discontinuous context, such as in a transient finite element solution, the instantaneous rise in values can only be approximated as a very steep ramp function; the length of which spans the very first time step in the solution. When the word

‘instantaneous’ is used in reference to the current simulation therefore, it is being used to describe this approximation.

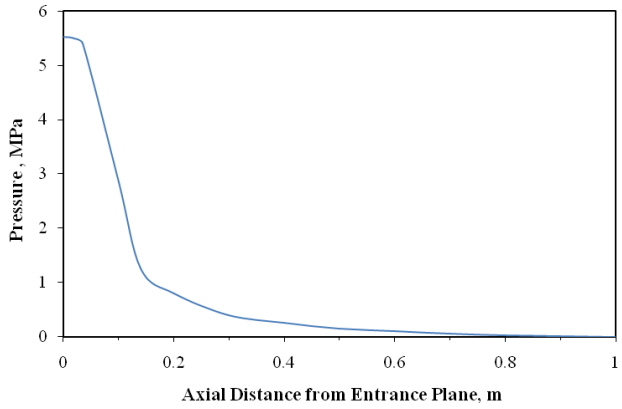

Figure 4.3 SRN1 wall pressure distribution.

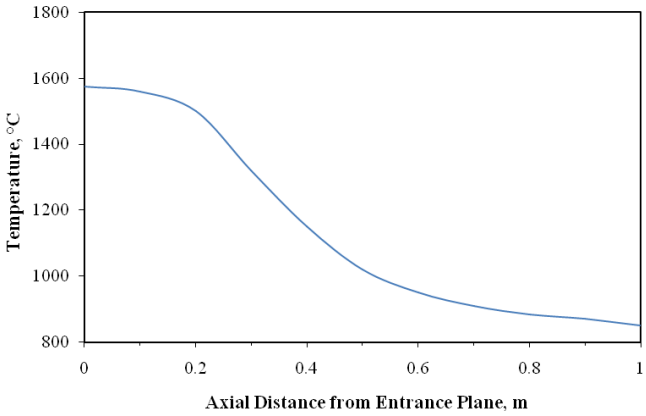

Figure 4.4 SRN1 wall temperature distribution.

4.2.4 Modelling Approach

The modelling approach adopted for the current simulation is effectively the most fundamental method that can be used for simulating the structural response of a nozzle subjected to pressure and thermal loading. As implied already, the approach employed two finite element models to which predefined boundary conditions were applied. The first model was developed in the ADINA system’s thermal simulation module, ADINA-T, and served as a thermal representation

of SRN1, whilst the second model provided a structural representation of the nozzle and was developed in the ADINA module.

For both the ignition period and burn period scenarios, the structural response simulation was carried out using a two stage solution scheme. The process would begin with the transient thermal simulation, where the axisymmetric temperature distribution in SRN1 was resolved for the stipulated time period and loading condition. Temperature data at each node of the thermal model was then saved in the form of a temperature mapping file written to memory by ADINA-T. The structural simulation would then be run, with the axisymmetric structural model being subjected to both the pressure loading condition and the nodal temperature input from the mapping file. In this manner, the thermostructural displacements and thus stresses attributable to the thermal expansion and or contraction of the nozzle could be computed and accounted for as part of the structural simulation. For ignition period modelling, the process followed was identical, whether a quasi-static or dynamic structural solution regime was being implemented. Either solution regime could be invoked in ADINA through a simple specification of the solution type required. A flow chart depicting the modelling approach employed for the current study is presented in Figure 4.5.

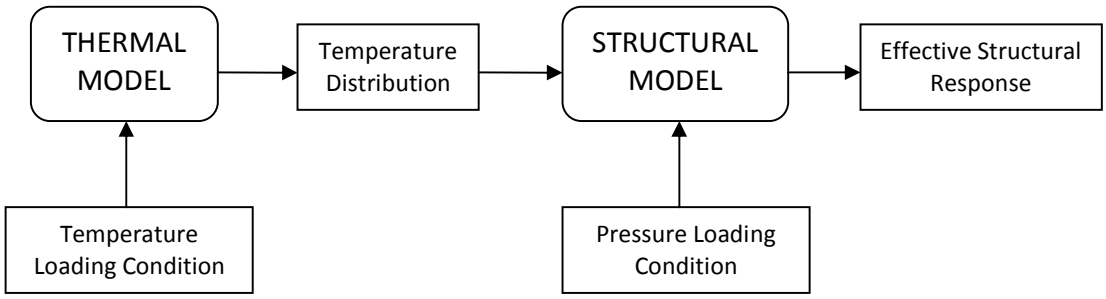

Figure 4.5 General SRN1 modelling approach.

4.3 Structural and Thermal Modelling

4.3.1 Geometry Definition

The first specific modelling task undertaken was the creation of the two dimensional geometry in ADINA-T representing an axisymmetric section of SRN1. This was achieved by specifying line element start and end points within the YZ plane of the global coordinate system, from which

straight lines, arcs and subsequently surfaces could be developed. This approach was selected in preference to importing the geometry from a dedicated solid modelling program as it allowed for greater control of the finite element mesh density distribution. A drawback to this method however, was that it resulted in the generation of a fairly unstructured mesh. This is as a consequence of the fact that the ADINA system limits the definition of surfaces to either 3 or 4 points or 3 or 4 enclosing lines. Considering the number of points required to define the model, certain additional lines at irregular orientations were required to divide loops consisting of 5 or more lines, to allow for the definition of surfaces. This 'quilting' technique resulted in the overall geometry comprising a multitude of smaller surfaces. The final SRN1 axisymmetric geometry is shown in Figure 4.6.

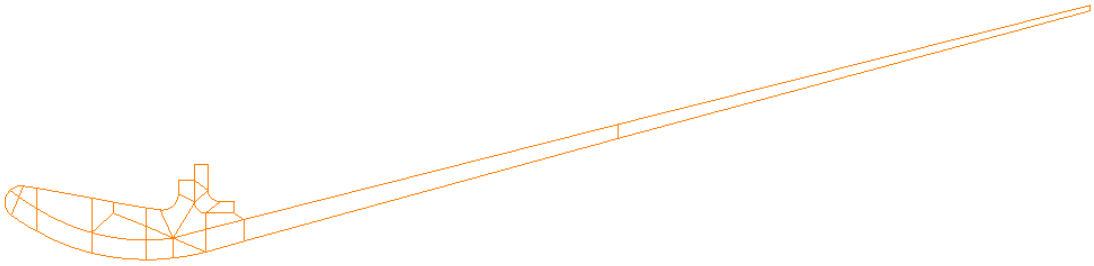

Figure 4.6 Axisymmetric finite element model geometry.

Once the geometry had been created, the number of subdivisions along each of its line elements was set. By setting these subdivisions, the mesh seed points were established and hence the local mesh density could be specified according to anticipated requirements. In this regard, the strategy employed was relatively straightforward. It was decided that as a first iteration, the mesh density be kept as uniform as possible and that the subdivisions be arranged to generate a mesh of as high a quality as was possible. Finally, this subdivided thermal model geometry was copied into the ADINA module to provide identical geometric parameters for the structural model.

4.3.2 Boundary Conditions

With respect to the thermal problem, two boundary conditions were assigned; the first, to represent the imposed temperature loading condition, and the second, to represent convection of heat from the nozzle's outer wall to the surrounding atmosphere. Although not critical for the short ignition period simulation, the latter boundary condition would be needed for the burn

period simulation to avoid the specification of an unrealistic adiabatic boundary by default. A heat transfer coefficient of 0.15 m^{-1} was specified at the convection boundary, as employed by Kardomateas (1990). Thermal loading was applied to the lines representing SRN1's wetted surface according to the distribution shown in Figure 4.4, using ADINA-T's spatial function facility. It should be noted that for the outer surface of SRN1's entrance region, a uniform thermal loading of the maximum magnitude was applied to simulate heating of this area.

Two boundary conditions were also required for the structural model. To constrain the model, a condition of full fixity in translation and rotation was imposed upon the three lines associated with the outer edges of the attach structure. The degree and location of this constraint was felt to be most representative of the circumferential joint that would hypothetically exist between the nozzle and motor casing. The pressure loading condition was applied to the relevant lines of the model by the use of spatial line functions, according to the stipulated distribution depicted in Figure 4.3. Once again, to define the pressure loading on the outer surface of the entrance region, the maximum magnitude of pressure loading was applied to this area.

4.3.3 Finite Element Meshing

The accurate capture of elastodynamic wave propagation using the finite element method requires the prescription of particularly high mesh densities. Unavoidably however, this comes at significant computational expense. The approach adopted in this exercise therefore, was to initially employ a relatively coarse and computationally economical mesh. If propagation effects appeared to manifest in the solution generated with this coarse density, the mesh could be refined to increase the accuracy of the response. A similar argument applied to the mesh density employed in the thermal model, as the instantaneous temperature loading condition and short analysis duration suggested the specification of a fine mesh density, particularly in the vicinity of the heated boundaries. Considering the preliminary nature of the exercise however, it was felt that the generation of an approximate transient temperature solution would provide a useful foundation for further refinement.

Two physical phenomena had to be represented by the finite element mesh used for SRN1's thermal model; the two-dimensional conduction of heat through the nozzle from its heated boundary, and the one-dimensional convection of heat from the nozzle's outer wall to the external atmosphere. The first task in developing the conduction element mesh was the

specification of three thermally orthotropic material models to represent the 4D C-C, 3D C-C and 2D C-P composites, and one thermally isotropic material model to represent the steel. These material models were defined according to their associated properties of thermal conductivity and specific heat reflected in Table 4.1. Axisymmetric element groups were subsequently created for each of these materials on the basis of the element characteristics elaborated upon in Chapter 3. Thereafter, the 26 surfaces of the geometry were meshed using ADINA-T's 9-noded axisymmetric conduction elements, with each element group corresponding to a set of surfaces representing a given substructure.

To describe convection, a constant convection 'material' was defined to specify the heat transfer coefficient and a convection 'load' was defined to specify the external environmental temperature. A line convection element group was then created to enable the one-dimensional convection elements to be meshed along the designated convection boundary. The overall thermal mesh was comprised of 978 elements and is shown in Figure 4.7. The location of the convection boundary condition and convection elements is indicated by the orange line and the element groups representing SRN1's four substructures can be distinguished by the different colours prescribed to each region.

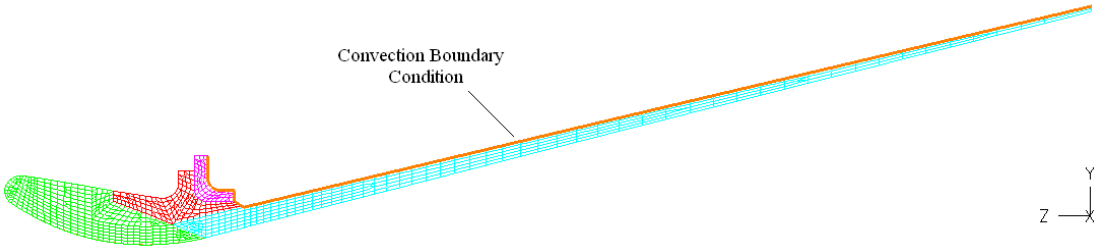

Figure 4.7 The meshed SRN1 thermal model.

The process of developing the structural mesh effectively paralleled that followed for creating the thermal mesh, however only one general element type was used. Firstly, three thermo-orthotropic material models and one thermo-isotropic material model were specified, representing the elastic properties of the constituent materials reflected in Table 4.1. Axisymmetric element groups corresponding to each material were then created to give definition to the elements to be used to represent the four substructures, and the structural mesh

was subsequently generated using ADINA's 9-noded axisymmetric solid elements. As the line subdivisions in the structural model were the same as those applied in the thermal model, and as both models employed quadrilateral elements, the distribution of elements in each model was identical.

As far as specifications relating to structural damping are concerned, it was decided that in the absence of appropriate damping parameters for SRN1's materials of construction, damping of the nozzle would not be considered. The resulting structural mesh of 909 elements is shown in Figure 4.8, and for illustration purposes, the distribution of the applied pressure loading condition is also graphically depicted in this figure. An enlarged view of SRN1's entrance and throat region is shown in Fig. 4.9, detailing the mesh applied in this area and the location of the structural model's full fixity constraint.

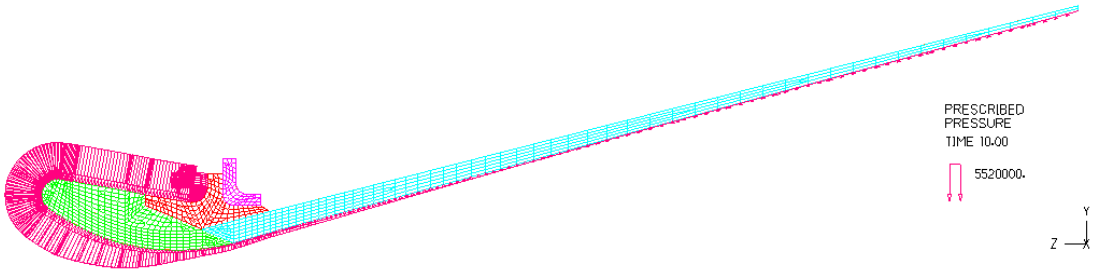

Figure 4.8 The meshed SRN1 structural model.

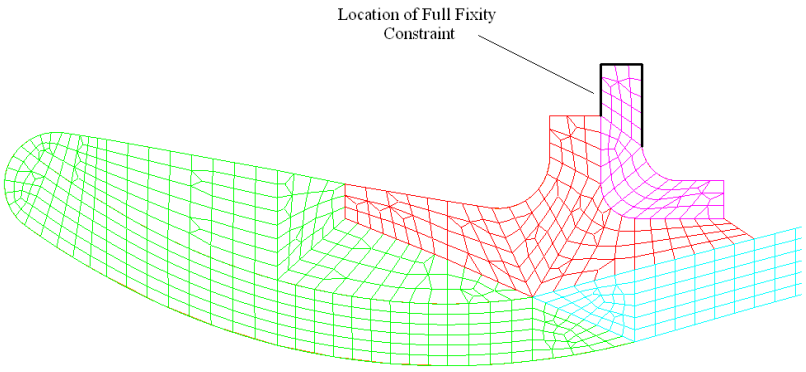

Figure 4.9 Throat and entrance mesh detail and full fixity constraint location.

4.3.4 Simulation Time Parameters

The quasi-static assessment of SRN1's structural response during the motor burn period was the first simulation performed in this exercise. To simulate this phase of operation, the pressure and temperature loading conditions were applied to the nozzle at nominal magnitude for a period of sixty seconds. As far as time discretization is concerned, an analysis time step size of 0.1 s was selected, resulting in a solution comprising 600 time steps. Since a quasi-static solution was being considered, it was felt that these specifications would comfortably provide sufficient temporal resolution to the problem.

The second simulation was concerned with the structure's response during the motor ignition phase, immediately after the instantaneous application of the loading conditions. Owing to the potential manifestation of vibratory effects in this response, discretization in the temporal sense needed to be of much higher resolution than in the case of the burn period simulation. In this regard, a time step size of $2x10^{-4}$ s was selected for this purpose and applied for 250 steps, resulting in a total analysis period of 0.05 s. All other modelling parameters remained unchanged, however.

To determine the inertial nature of SRN1's response, the ignition period simulation comprised two separate analyses, the first evaluating the structural response in a dynamic sense, while the second generating a quasi-static solution for comparative purposes.

4.3.5 Results Sampling

The substructure that received particular attention in the current study was SRN1's integral throat and entrance (ITE). As a consequence of its submergence and other factors, the ITE would be subjected to the most severe thermal and pressure loading of the four substructures, and it thus provided an appropriate case for examination. In order for the thermal and structural models to realistically simulate the response behaviour of the ITE during operation, SRN1 was analysed in its entirety to allow for any physical interactions between the ITE and the surrounding substructures to take place.

Sampling of thermal and structural response data from the constituent models was achieved through the use of a series of sample contours and points, which are shown in the axisymmetric

projection of the ITE in Figure 4.10. In this manner, a wide range of substructure responses could be obtained as functions of both position and time.

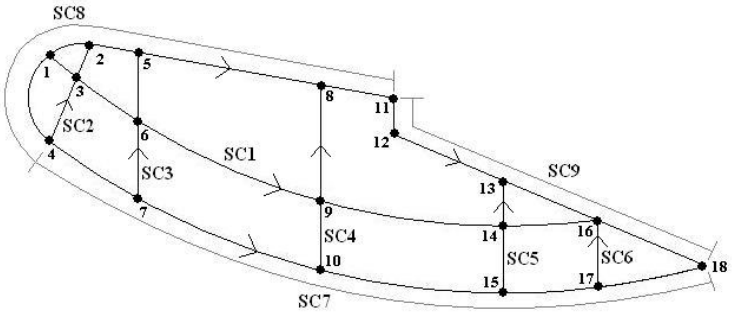

Figure 4.10 Integral throat and entrance sample contours and points.

4.4 Results and Discussion

4.4.1 Motor Burn Period Assessment

The primary objective of carrying out the motor burn period assessment was to determine whether the SRN1 design would perform within a reasonable thermal and structural envelope and thus constitute an acceptable exploratory design. Following the solution run, the output files of the two constituent models were opened in ADINA's post-processing module and the resultant thermal and structural responses of the nozzle were evaluated. The temperature histories at sample points 8, 9 and 10 over the one minute simulation period are shown in Figure 4.11, whilst band plots of the temperature distribution in the nozzle at solution times of 10 s, 30 s and 60 s are shown in Figure 4.12.

In reference to Figure 4.11, the early thermal response at sample points SP8 and SP10, which are located on the outer and inner surfaces of the integral throat and entrance, clearly illustrate the manner in which the temperature loading condition rises to its nominal value between t = 0 and t = 0 + Δt. Furthermore, the nature of the temperature history at SP9 is reasonable in consideration of the fact that SP9 is positioned approximately halfway between SP8 and SP10. Importantly, the response also suggests that thermal equilibrium has not been established in the ITE at the conclusion of the 60 s burn.

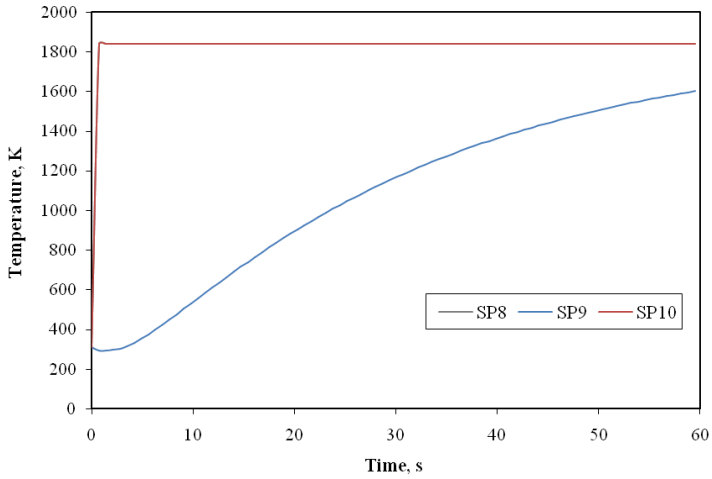

Figure 4.11 Temperature histories at sample points 8, 9 & 10.

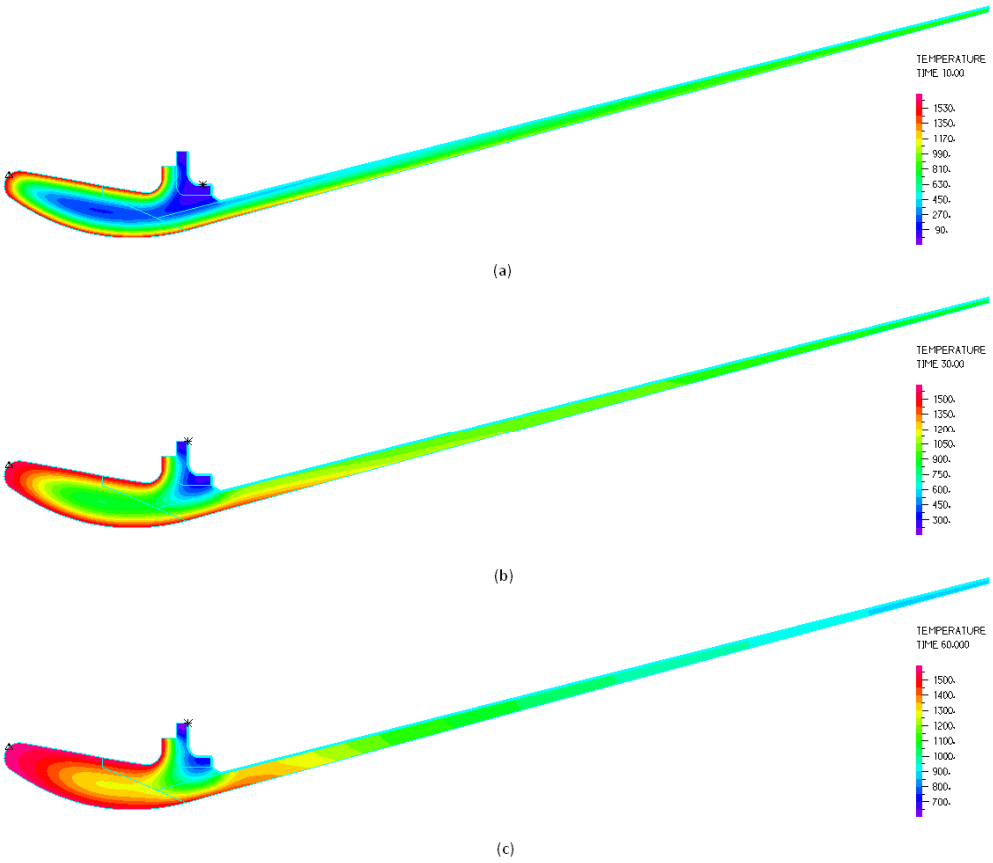

Figure 4.12 Temperature distributions in SRN1 at (a) t = 10 s, (b) t = 30 s and (c) t = 60 s.

The temperature distributions shown in Figure 4.12 clearly illustrate the evolution of the temperature field within SRN1 during the simulation period. As expected, the severe thermal loading at the entrance and throat region results in significant heating of the ITE and insulator, whereas temperatures encountered in the exit cone are lower, particularly over the last two-thirds of this substructure. The low thermal gradients that are shown to exist in the radial direction across the ITE and exit cone in the final plot provide a graphical demonstration of the relatively high thermal conductivities of the 4D and 3D carbon-carbon materials. As far as the performance of the insulator is concerned, it appears that a fair degree of thermal protection is offered to the attach structure, although its thickness in the axial direction would ideally have to be increased to limit temperatures in the adjacent region of the attach structure to acceptable levels. For the purposes of an exploratory exercise however, the overall design appeared to be reasonable as far as thermal characteristics are concerned.

In terms of the structural response of the nozzle, the variation in stress with time at SP8, SP9 & SP10 were investigated to provide a basic indication regarding the structural validity of the SRN1 design. The hoop, radial and axial stress profiles at these sample points are shown as functions of time in Figures 4.13-4.15, whilst the corresponding maximum/minimum stress magnitudes at the three locations are displayed in Table 4.2.

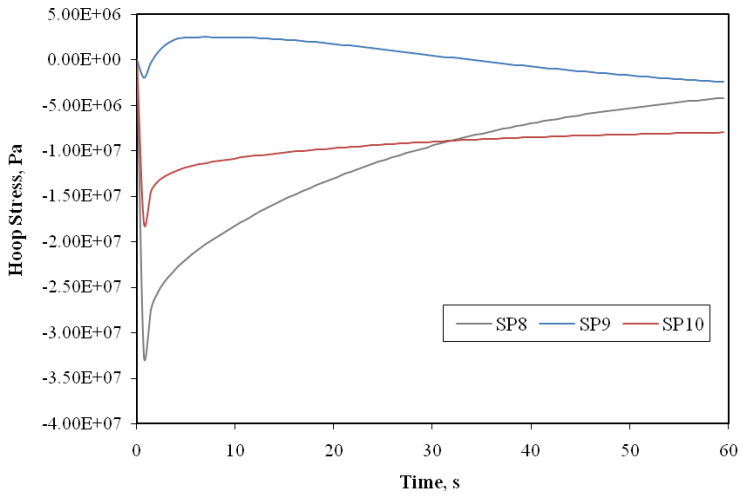

Figure 4.13 Quasi-static hoop stress histories at sample points 8, 9 & 10.

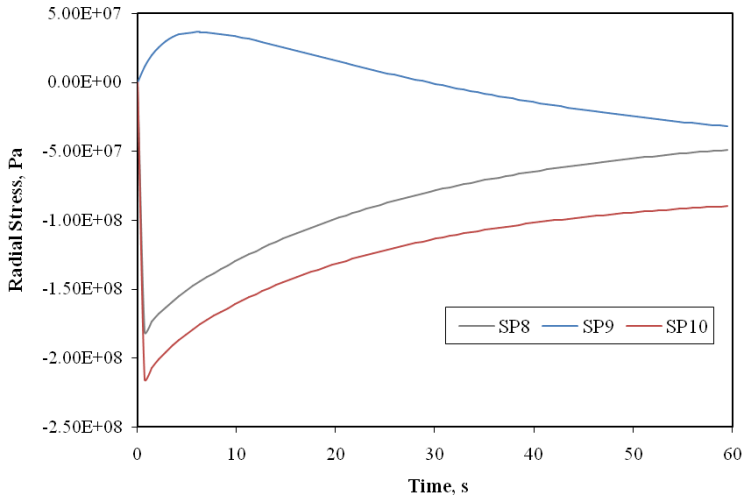

Figure 4.14 Quasi-static radial stress histories at sample points 8, 9 & 10.

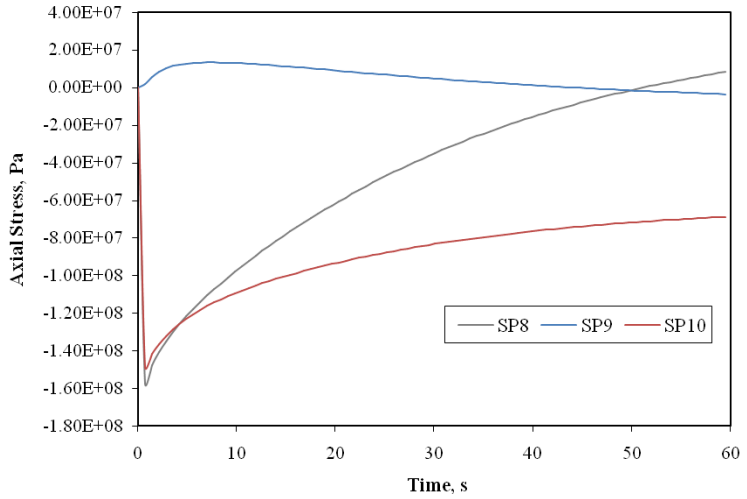

Figure 4.15 Quasi-static axial stress histories at sample points 8, 9 & 10.

Stress (MPa)	**Hoop**			**Radial**			**Axial**		
	SP10	SP9	SP8	SP10	SP9	SP8	SP10	SP9	SP8
Maximum	0.00	36.38	0.00	0.00	2.48	0.00	0.00	13.29	8.30
Minimum	-215.40	-32.02	-181.13	-17.95	-2.47	-32.49	-148.58	-3.52	-157.33

Table 4.2 Maximum and minimum stresses at sample points 8, 9 & 10.

As reflected in Figures 4.13 – 4.15, the instances of maximum/minimum stresses highlighted in Table 4.2 all occur within 5 seconds of motor ignition. As time progresses and the depth of thermal penetration increases, differences in thermal expansion within the ITE relax, and stresses subsequently decrease and level off as their steady-state values are approached. It is clear that during the burn period, compressive stresses at the specified sample points in the ITE are predicted to be significantly greater in magnitude than tensile stresses. The highest tensile stress is shown to occur at SP9 in the hoop direction and is well within the general tensile strength capacity of spatially reinforced Carbon-Carbon materials. However, the magnitude of the highest compressive stress, encountered at SP10, is appreciable and modifications to the design would be required to reduce the compressive stresses in this region, and the compressive hoop and axial stresses present at SP8 and SP8 to acceptable levels. For the purposes of this work however, and in view of the reasonable thermal performance of the nozzle, it is reasonable to conclude that the SRN1 design provides a satisfactory representation insofar as thermal and structural considerations are concerned.

4.4.2 Ignition Period Dynamic Structural Response

As far as the ignition period results are concerned, it was felt that it would ultimately be more useful to record the structural responses at sample points as a function of time, as opposed to recording such responses along sample contours at a particular time. In light of this, data for dynamic and quasi-static hoop, radial and axial stresses were captured at sample points 2, 3, 4, 8, 9, 10, 13, 14 and 15 to provide through-the-thickness response histories along sample contours 2, 4 and 5. These three sample point groups were chosen as they allowed for assessments to be made at the surface, within the surface, and in the case of SP13, at the interface with another substructure. The resulting stress response histories are presented in Figures 4.16 – 4.25.

In general consideration of these results, a variety of definite trends were observed. The most notable of these is that the response predicted by the dynamic solution regime was characterised as oscillatory in all cases. The frequency at which this vibration occurs suggests that the instigation and subsequent propagation of elastodynamic waves has taken place. Another significant trend was the manner in which this dynamic solution, without exception, oscillated about the associated quasi-static solution. That is, the mean of the dynamic oscillations coincided with the quasi-static solution at identical points in time, with no divergence between

the two responses during the period of analysis. This result is consistent with the nature of the problem however, considering its prescribed geometric and physical linearity.

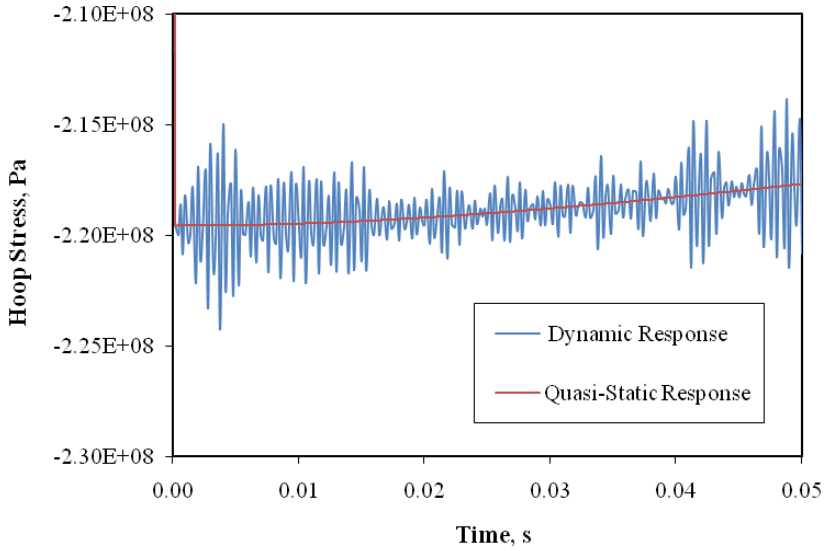

Figure 4.16 Dynamic and quasi-static hoop stress response at sample point 2.

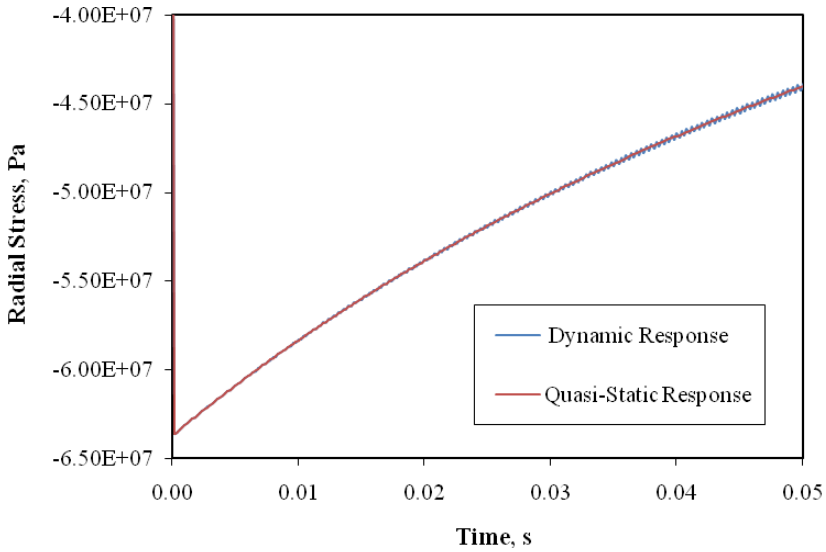

Figure 4.17 Dynamic and quasi-static radial stress response at sample point 2.

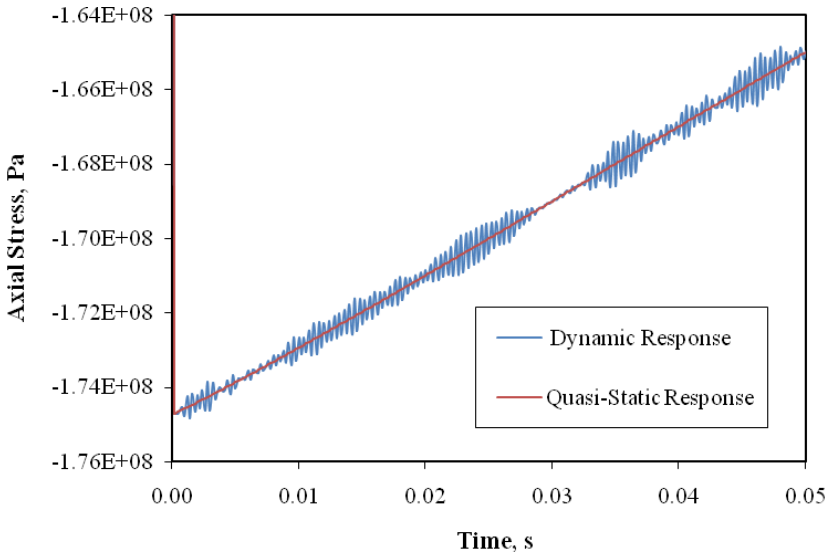

Figure 4.18 Dynamic and quasi-static axial stress response at sample point 2.

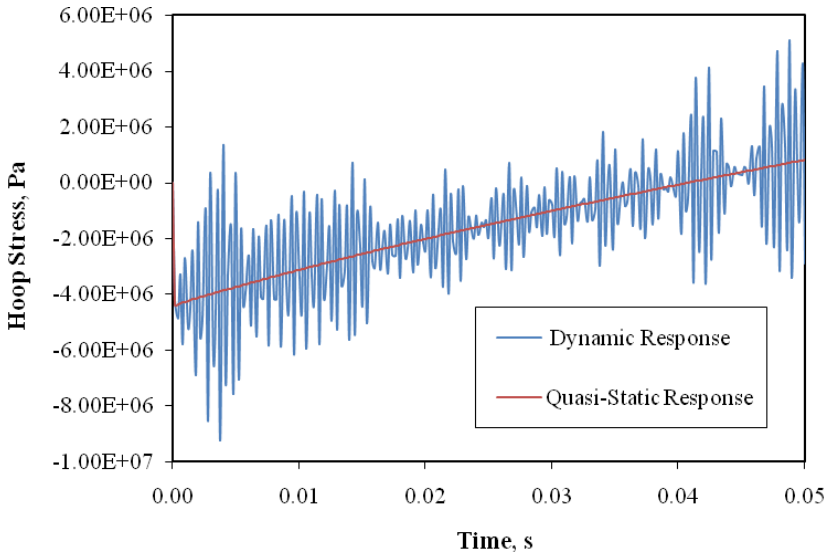

Figure 4.19 Dynamic and quasi-static hoop stress response at sample point 3.

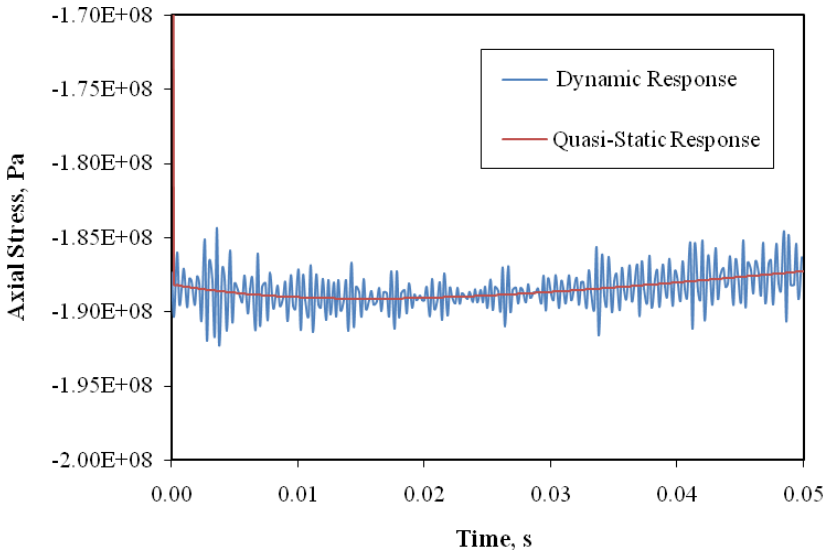

Figure 4.20 Dynamic and quasi-static axial stress response at sample point 8.

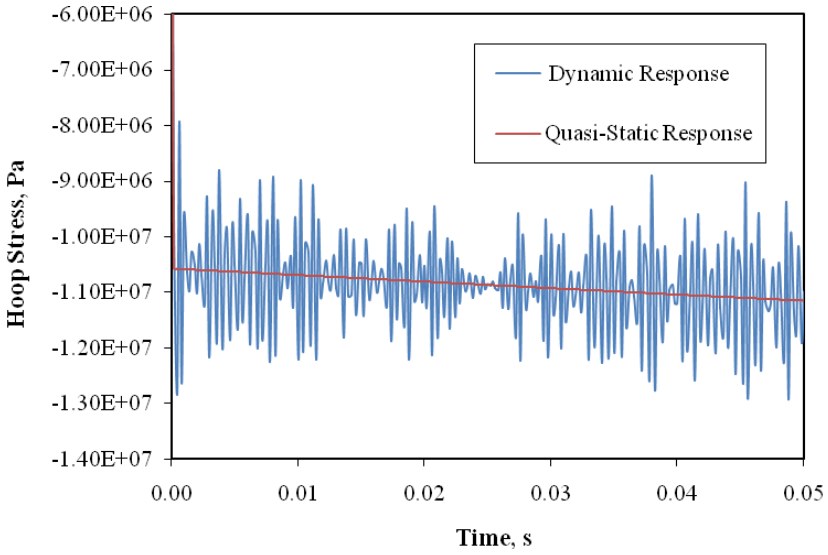

Figure 4.21 Dynamic and quasi-static hoop stress response at sample point 13.

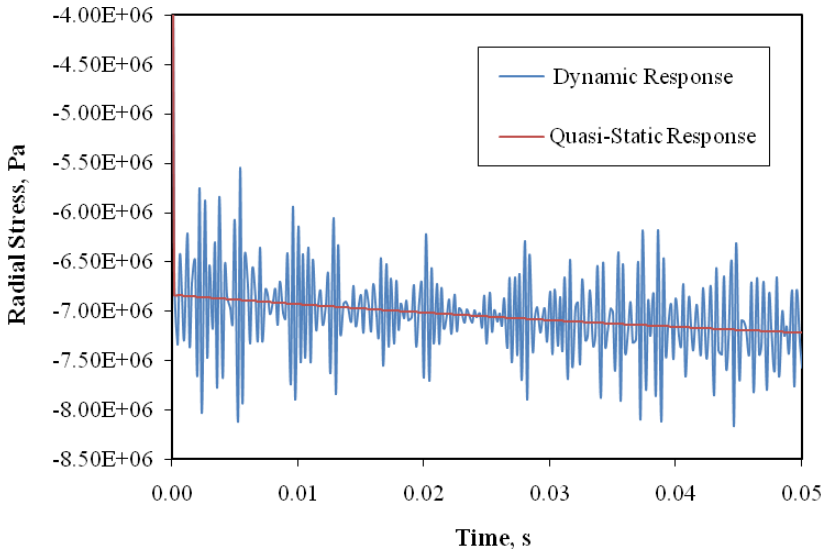

Figure 4.22 Dynamic and quasi-static radial stress response at sample point 13.

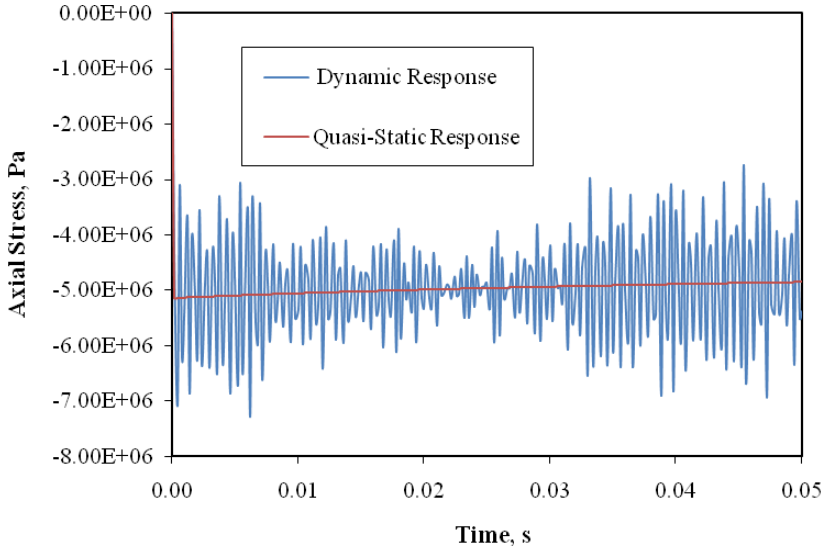

Figure 4.23 Dynamic and quasi-static axial stress response at sample point 13.

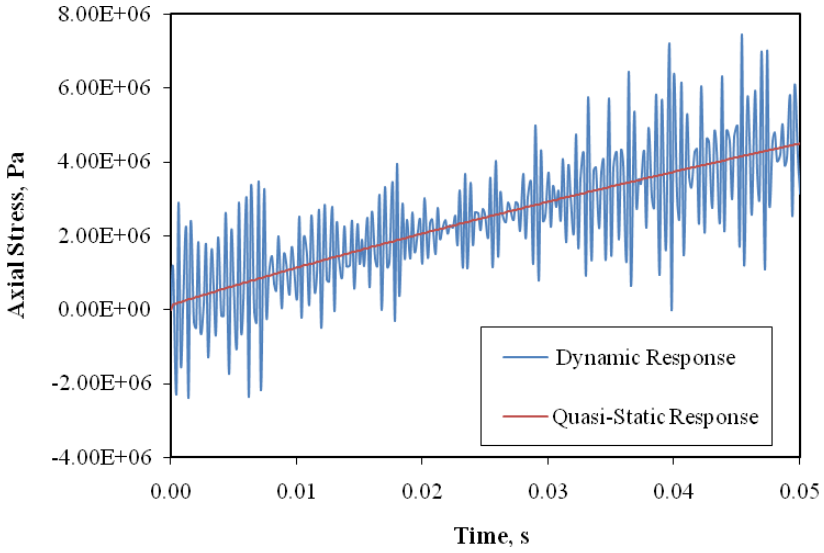

Figure 4.24 Dynamic and quasi-static axial stress response at sample point 14.

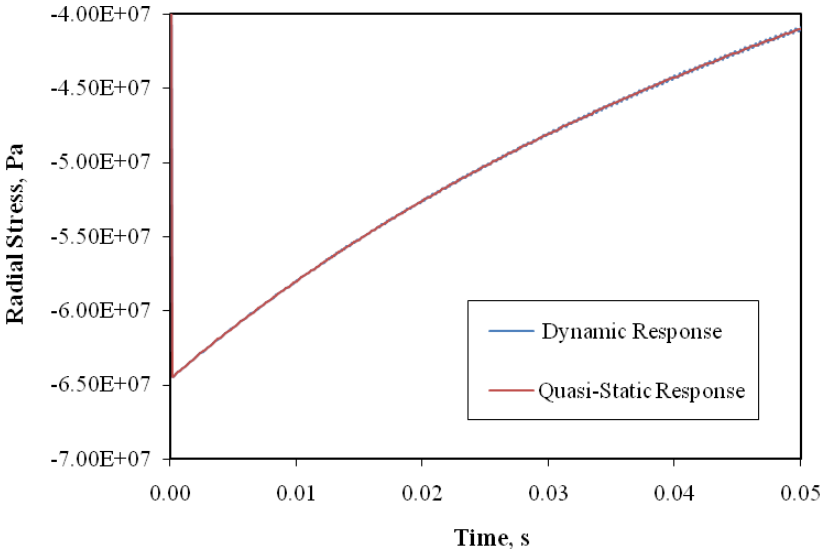

Figure 4.25 Dynamic and quasi-static radial stress response at sample point 15.

Another interesting pattern that emerged was that at all sample points assessed, apart from SP14, the hoop, radial and axial stress responses were predicted to be compressive immediately after the application of loading at t = 0 s. Only the axial stress response at SP14, shown in Figure 4.24 differs in this regard, remaining tensile for the duration of the analysis. In general however, both the dynamic and quasi-static responses remained compressive for this period, apart from the hoop stress response at SP3, which undergoes a transition from compressive to tensile stress at approximately t = 0.04 s, as illustrated in Figure 4.19.

In terms of the variance of the through-the-thickness dynamic hoop, radial and axial stress responses at sample points along sample contours 2, 4 and 5, several interesting behaviours were observed. Chief among these was the degree of oscillation predicted to occur in the dynamic radial sress responses at sample points situated on the free surfaces of the ITE, as depicted in Figures 4.17 and 4.25. At these locations, it is clear that the amplitude of oscillation is considerably lower than in the case of radial stress profiles at points submerged within the ITE, such as SP13 shown in Figure 4.22, where the highest amplitude is in the order of 1.25MPa. Similar behaviour was observed in the axial stress profile for SP2, where oscillation is significantly lower than in the case of axial stress responses evaluated at other positions. This difference in behaviour is most likely attributable to SP2's proximity to the leading edge of the ITE, where inertially induced stresses would be less prevalent. Oscillatory magnitudes naturally increase towards the centre of the substructure however, as indicated by the axial stress response of SP8 shown in Figure 4.20.

Insofar as response behaviour at the interface between the C-C ITE and the C-P insulator substructures is concerned, stress historiess shown in Figures 4.21-4.23 are similar to the responses predicted at other submerged sample points, with comparable dynamic amplitudes and quasi-static trends.

As discussed previously, all dynamic stress responses derived from the current ignition period simulation oscillate about the quasi-static solution, irrespective of the sampling position or class of stress. The degree by which the magnitude of the dynamic response exceeds that of the quasi-static response is therefore the most critical consideration in determining the significance of accounting for inertial effects in analyses of this nature. From observations of the response of the ITE to instantaneous loading, it appears that this discrepancy varies quite substantially.

For instance, in the hoop stress response at SP3 (Figure 4.19), the most severe stress predicted by the dynamic analysis exceeds that of the quasi-static analysis by 137%, with a compressive stress of 9.24MPa – which is however a relatively low stress level. By contrast, in the radial stress response at SP15 (Figure 4.25), the most severe stress predicted by the dynamic analysis only exceeds that of the quasi-static analysis by 0.28%. Interestingly, in the most extreme stress response, the hoop stress response at SP15, the largest variance in compressive stresses estimated by either analysis regime is only fractionally greater than 1%.

In general however, the majority of the responses observed showed a significant variance between the dynamic and quasi-static solutions, with 10 out of the 27 responses sampled featuring a maximum stress magnitude variance of over 15%. This result clearly illustrates that although the dynamic thermostructural response follows the trend predicted by the quasi-static solution, considerable discrepancies exist between the maximum and minimum stress magnitudes in either case. Furthermore, in view of the complex stress-interaction nature of contemporary failure criteria formulations for composite materials, the results obtained in this exercise suggest that inertial effects may need to be considered in the assessment of the ignition period structural response of structures of this nature, subjected to similar loading conditions.

With regards to the result discussed above, it is quite apparent that in order to ascertain a more accurate representation of the ignition response of the ITE and indeed the SRN1 nozzle as a whole, significant revisions to the simulation models would be required. The most significant changes would perhaps relate to the characteristics of the meshes employed by the thermal and structural models. In particular, the mesh density and distribution associated with both models would have to be refined to enable the effects of extremely rapid loading rates to be captured with improved accuracy. Furthermore, the temporal discretization of the structural problem would require further refinement in order to ensure that the waveform of the apparent elastodynamic perturbations is given sufficient definition.

In a general sense, carrying out such refinement activities would have constituted a significant undertaking. Considering the approximate nature of the available pressure and temperature loading conditions, it was felt that instead of pursuing model refinement activities, it would be more beneficial to focus on establishing an exhaust flow modelling capacity from which more representative loading conditions could be derived. In this manner, the refinement of subsequent

models could be made on a more realistic basis. It was therefore decided that the current simulation efforts be concluded to allow the development of a more advanced modelling approach to be pursued.

4.5 Conclusion

The current numerical simulation efforts served as an introduction to the methodologies involved in simulating the structural response of a composite SRM nozzle to instantaneously applied pressure and thermal loading. In particular, efforts were concerned with the response modelling of Solid Rocket Nozzle 1 during both motor burn and ignition scenarios, using predefined loading conditions and a fairly rudimentary modelling approach.

An axisymmetric thermal model was developed to predict the burn and ignition period transient temperature distributions within the nozzle, which were subsequently employed by an associated axisymmetric structural model to allow the subsequent dynamic and/or quasi-static response of the nozzle to be modelled. The motor burn period analysis results demonstrated the suitability of the SRN1 design, whilst the ignition period analysis results illustrated significant discrepancies between the responses within the integral throat and entrance that were predicted by the dynamic and quasi-static solution regimes. Furthermore, for the instantaneous loading conditions considered, the presence of elastodynamic wave propagation within the ITE was clearly indicated in the dynamic solution, having the general effect of increasing maximum compressive and tensile stresses by an appreciable margin.

In spite of these notable observations, it was ultimately decided that instead of pursuing further model refinement efforts, the capacity to model transient nozzle flows be developed to enable the provision of higher fidelity loading conditions. The development of this capacity and the characteristic ignition period structural response subsequently derived in the resulting simulation will be discussed in the following chapter.

CHAPTER 5

Simulation of the Structural Response of a Composite SRM Nozzle to Transient Pressure Loading

5.1 Introduction

In light of the restricted representation provided by the ignition period loading conditions employed in the previous simulation, work on exhaust flow model development was initiated with the intention of generating more realistic loading conditions, at least in a qualitative sense. In addition, a new nozzle design, Solid Rocket Nozzle 2 (SRN2), was created to provide an analysis subject fifty percent larger in size and with a design layout more characteristic of modern booster SRM nozzles. These efforts proved constructive, and following a process of model refinement, the first ignition period structural response simulation incorporating flow modelling was undertaken. This simulation serves as the subject of the following chapter.

The primary objective of the simulation was to evaluate the nature of the response of the SRN2 structure to pressure loading derived from an unsteady ignition period flow simulation. Furthermore, the degree of aeroelastic coupling between the nozzle and the flow field during the ignition transient was to be assessed using the fluid-structure interaction capacity of the ADINA system. Consideration was not given to thermal nozzle loading in this initial multidisciplinary simulation to limit the complexity of the problem to an intermediate level.

Inlet conditions for the flow model were derived on the basis of an SRM combustion chamber ignition pressure history obtained from literature and an assumed temperature transient. Steady and unsteady flow simulations were carried out, and the resultant flow fields were qualitatively evaluated to determine the validity of the solutions generated. The transient wall-side pressure distribution resolved by the unsteady flow model was applied to a structural model of SRN2 via a fluid-structure boundary condition, to generate the ignition period structural response. By specifying the fluid-structure interaction iteration conditions, both the coupled and uncoupled responses could be developed. The modes of fluid-structure interaction during the ignition period for the current conditions were characterised and overall structural deformations of the

nozzle were observed. In addition, stress responses from four locations within the nozzle predicted by coupled and uncoupled solution regimes were investigated. Finally, comparisons between these data were made to shed light on the extent of the interaction between SRN2 and its associated exhaust gas flow field, during a typical ignition transient.

5.2 Analysis Parameters

5.2.1 Solid Rocket Nozzle 2

A new nozzle design, Solid Rocket Nozzle 2 (SRN2), was developed to serve as the analysis subject for the current simulation. In general terms, the SRN2 design features an architecture which is more consistent with that of modern booster SRM nozzle designs. The design does however still employ the four basic substructures: an integral throat entrance (ITE), an exit cone, an insulator and an attach structure. A cross-sectional view of the SRN2 design is shown in Figure 5.1.

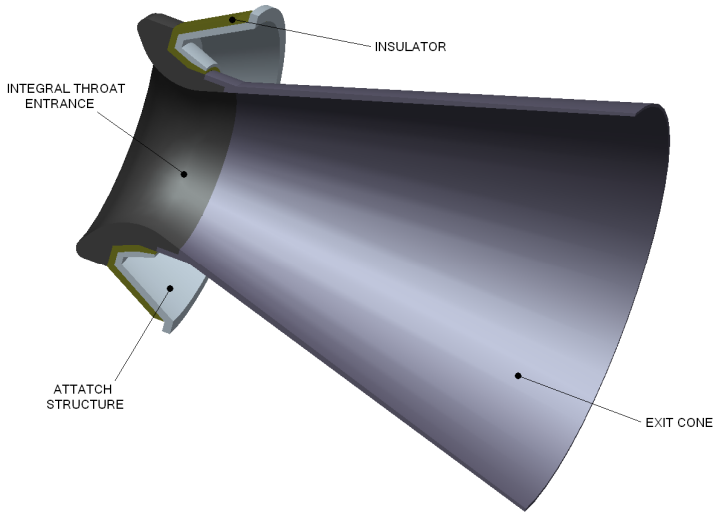

Figure 5.1 Solid Rocket Nozzle Design 2.

As can be seen in Figure 5.1, when compared to that of SRN1, the SRN2 ITE is more complex in design, extends further downstream of the throat and features a sharper, shorter convergence with a contraction ratio of 2.5. The exit cone is joined to the ITE via a more elaborate interface that allows acute corners to be avoided and is comparatively thinner over its length than the

SRN1 exit cone. The exit cone divergence half angle has been increased to 17.5º and the expansion ratio has been reduced slightly to a value of 8, but the exit cone contour remains conical. The SRN2 attach structure is also comparatively larger and more sophisticated, providing for a high aperture attachment to the SRM combustion chamber and more comprehensive support of the composite substructures. The insulator has consequently been extended to provide the necessary protection to the highly submerged attach structure. Once again, the nozzle was assumed to be rigidly attached to the combustion chamber via a circumferential bolted joint.

In physical terms, SRN2 is significantly larger than SRN1. With the distance from leading edge to exit plane measuring 1.5 m, SRN2 is 50% longer than SRN1, although the level of submergence has been reduced from 16% to 12%. In addition, the throat diameter has been increased significantly from 0.144 m on SRN1 to 0.45 m on SRN2. The major dimensions of SRN2 are displayed in Figure 5.2. Greater dimensional detail is provided in Appendix A.

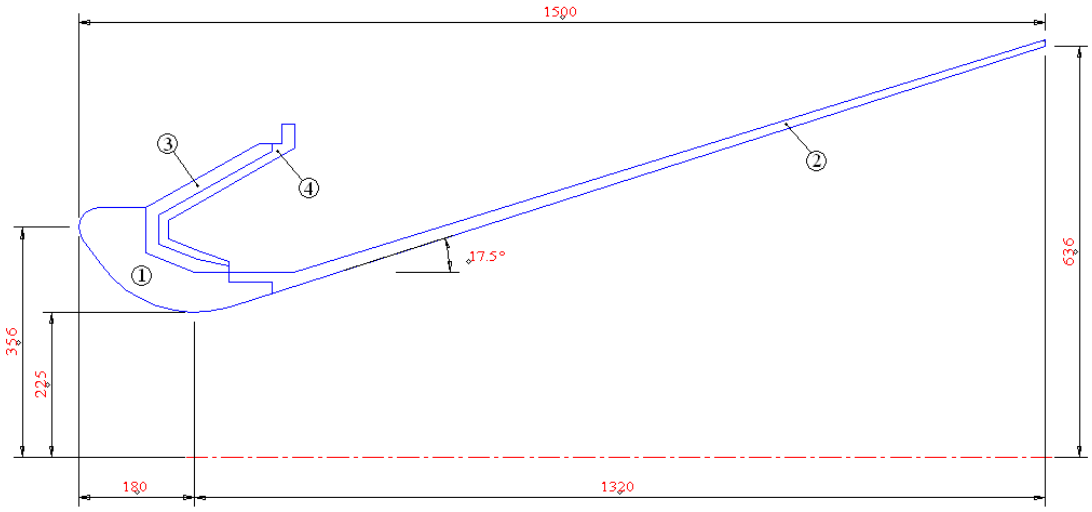

Figure 5.2 Major dimensions of Solid Rocket Nozzle 2.

5.2.2 Nozzle and Flow Material Properties

The material properties of Yoo et al (2003) incorporated in the previous study were used once again to define SRN2's materials of construction. The only difference in the current application of this data was the specification of the 3D carbon-carbon material for both the ITE and the exit

cone substructures, to simplify the problem slightly. The mechanical properties of SRN2's materials of construction are shown in Table 5.1 again, for the sake of convenience. Once more, *r*, θ and *z* denote the radial, circumferential and axial directions, respectively, whilst $E_{\theta\theta}$, E_{zz}, E_{rr}, $G_{\theta z}$, $G_{\theta r}$, G_{zr}, $\upsilon_{\theta z}$, υ_{zr}, $\upsilon_{\theta r}$ and ρ stipulate the moduli of elasticity, shear moduli, Poison's ratios and density of the materials, respectively. As the response of the nozzle to pressure loading alone was of interest in the current simulation, thermal material properties were not considered.

Property	**3D C-C**	**2D C-P**	**Steel**
$E_{\theta\theta} = E_{zz}$, GPa	34.42	74.5	205
E_{rr}, GPa	34.42	15.71	205
$G_{\theta z}$, GPa	2.552	5.017	78.13
$G_{\theta r} = G_{zr}$, GPa	2.552	4.65	78.13
$\nu_{\theta z}$	0.083	0.1	0.28
$\nu_{zr} = \nu_{\theta r}$	0.083	0.54	0.28
ρ, kg/m^3	1514	1329	7800

Table 5.1 Mechanical properties of the SRN2's constituent materials.

As far as properties defining combustion gases flowing through the nozzle are concerned, data were required that were consistent with flow modelling simplifications stipulated in Chapter 3; namely that only a single phase, non-reacting and temperature independent flow could be considered. After a review of related literature, an appropriate set of properties were obtained in the work of Montesano et al (2008), where the data were employed in an investigation into the effects of structural and acoustic coupling on propellant combustion in a solid rocket motor. The properties specific to the current simulation are quantified in Table 5.2.

Property	**Value**
Ratio of Specific Heats, γ	1.2
Specific Heat at Constant Pressure, C_p, J/kgK	2000
Dynamic Viscosity, μ, kg/ms	8.07e-5
Thermal Conductivity, k, W/mK	0.195
Particle Mass Fraction, %	0

Table 5.2 Properties of simulated exhaust gas.

5.2.3 Flow Domain Definition

Once the design of SRN2 had been established, the axisymmetric domain within which the flow of combustion products would be modelled needed to be defined. Definition of this domain was based upon the geometric configuration of the aft flow passage of the hypothetical SRM associated with the SRN2 design. As such, the flow domain, illustrated axisymmetrically in Figure 5.3, incorporates two physical boundaries – representing the internal contours of the SRN2 and the hypothetical propellant grain, and three virtual boundaries – representing the domain inlet, outlet and axis of symmetry.

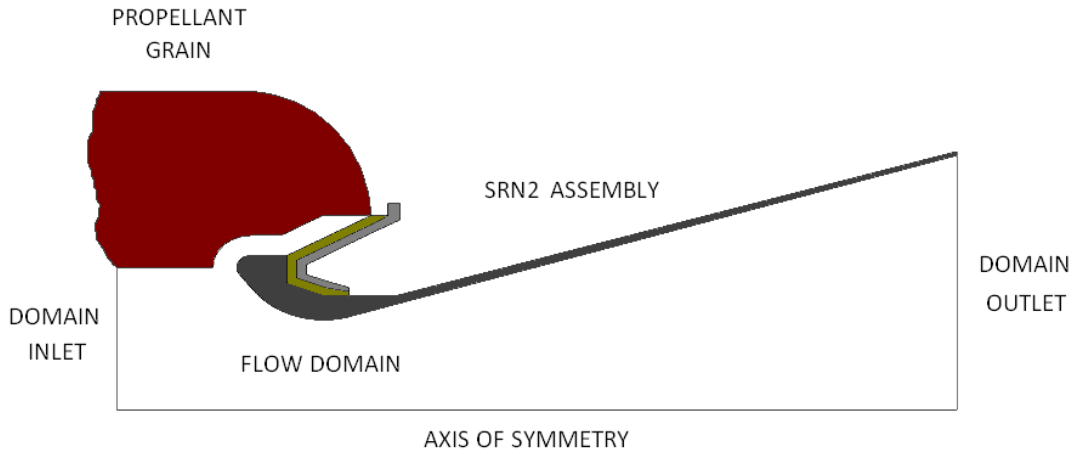

Figure 5.3 Analysis flow domain and associated boundaries.

As far as the propellant grain profile shown in Figure 5.3 is concerned, the recession of the propellant grain surface to accommodate the SRN2 is necessary to maximise combustion surface area and is a common design approach. Owing to the appreciable complexity of modelling the combustion and mass flow occurring at the propellant grain surface, this surface has had to be treated as an inert wall, and adiabatic in the case of the current simulation. Furthermore, in consideration of the mathematical impositions associated with the flow model's inlet boundary condition, it was necessary to position the domain inlet upstream of SRN2's leading edge.

5.2.4 Ignition Transient

As discussed in Chapter 2, the SRM ignition process is a complex event composed of a series of highly transient phenomena that are governed by various physical and chemical properties. Therefore, to accurately describe the evolution of the flow ahead of the SRM nozzle during the

ignition process requires either comprehensive experimental measurements of actual test firing parameters or the use of complex numerical ignition simulation codes – exercises beyond the scope of this work. Consequently, a simplified approach had to be adopted for the current simulation, which involved the use of ignition data published in literature to define the development of the flow through the nozzle.

Naturally, this approach needed to be consistent with the inlet boundary conditions appropriate to this class of problem in the ADINA-F program. As the problem is effectively a de Laval duct scenario, ADINA-F's 'subsonic inlet' boundary condition was the most accurate condition available. This condition requires that a pair of flow variables be defined on the inlet boundary in certain combinations of static pressure, enthalpy, static temperature, density and velocity magnitude. By defining the time-varying evolution of such a pair of variables at the inlet of the flow domain, the flow within the nozzle can be 'driven' in a simulated ignition event. Whilst employing basic step and ramp functions to describe the evolution of the selected set of variables can be employed as an approximation, such functions are only able to provide a highly simplified temporal representation of this transient period. As such, it was decided that more comprehensive data, measured or predicted at the aft of a combustion chamber for an actual SRM ignition process should be sought instead.

After an extensive review of related literature, it was determined that the most applicable variables to use at the domain inlet were static pressure and static temperature. As the variation in pressure at the aft end of the propellant port during SRM ignition is a commonly assessed parameter, data of this nature was available for a variety of motors. Ultimately, the selection of which pressure history to use was based on motor scale, as the duration of an ignition event is generally proportional to the size of the SRM concerned. Thus, to provide pressure definition to the inlet condition, a pressure history was obtained from the work of Johnston (1996), representing the simulated aft chamber pressure of the Ariane 5 SRM booster as a function of time during motor ignition. For application in the current study, all critical discontinuities in the curve from Johnston (1996) were reproduced as piecewise time function to represent the increase in static pressure at the SRN2 inlet during ignition, and an identical maximum pressure of 5.86MPa was used. The normalised representation of this curve is shown in Figure 5.4.

An associated temperature history was not presented by Johnston (1996), however. The temperature characteristic for the inlet boundary condition therefore had to be approximated as a ramp function, based on the assumption that the time at which the maximum temperature at the nozzle inlet is reached, is equivalent to the time at which the igniter pressure spikes - at approximately 0.025s. At this time, the mass flow through the nozzle is primarily attributable to the combustion of the igniter charge and it is assumed that the exhaust gas has reached its maximum temperature of 3000K at this peak pressure. This temperature magnitude was determined on the basis of the flame temperature of the propellant considered by Montesano et al (2008). The normalised temperature history is also reflected in Figure 5.4.

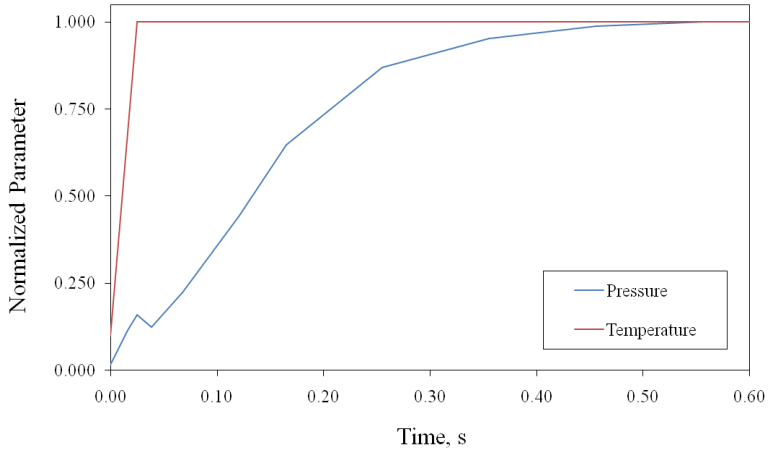

Figure 5.4 Simulated ignition pressure and temperature transients.

5.2.5 Modelling Approach

The incorporation of flow modelling in the current simulation increased the complexity of the task at hand considerably. However, as the simulation was concerned with determining the response of SRN2 to pressure loading alone, the modelling approach employed remained fairly straightforward, as only two independent models were required. The first model, a flow model representing the exhaust stream within SRN2, was developed in the ADINA System's computational fluid dynamics module, ADINA-F, whilst the second model, representing the nozzle structure, was once again developed in the structural module, ADINA.

For both the coupled and uncoupled ignition period simulations, initial conditions specifying the flow variables in the domain before the ignition process started, and boundary conditions

qualifying flow variables along the periphery of the domain were prescribed in the flow model. In addition, the governing parameters of time step size and total solution time were also specified in this model.

The first step in the overall solution process is the resolution of the flow variables after the time period, Δt, has elapsed. Included in this solution is a determination of the fluid forces at the nodes representing the interface between the flow and the nozzle structure, which are identified by the definition of a fluid-structure interface. The fluid force distribution at this interface and time in the flow solution are then relayed to the structural model, following which the structural response over the time period, Δt, is resolved. If the flow and structural models are uncoupled, then the flow model is automatically solved for the next time step and the process continues. If however, the models are coupled, the displacement of the nozzle and hence the fluid-structure interface at $t = 0+ \Delta t$ is relayed back to the flow model, where the flow field is resolved once more. In doing so, the response of the structure is allowed to influence the flow within it. This iterative process will continue until a converged solution is reached, following which the overall solution can progress to the next time step. The general modelling approach described here is graphically depicted in Figure 5.5 for the coupled solution case.

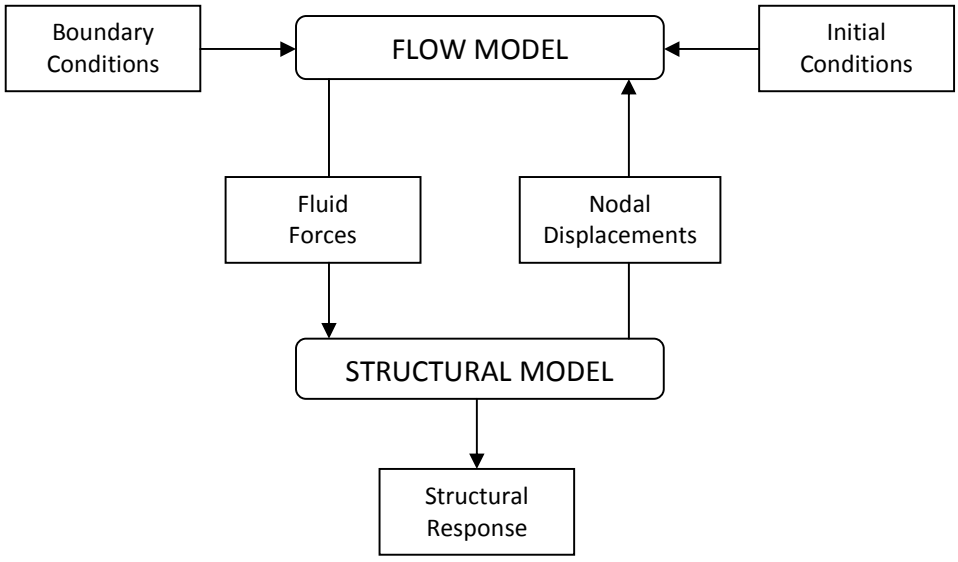

Figure 5.5 SRN2 pressure response modelling approach.

5.3 Flow Modelling

5.3.1 Geometry Definition

In an identical manner to the SRN1 simulation, the axisymmetric flow domain geometry was created using a combination of points, lines and surfaces lying in the global YZ plane. Once again, the overall geometry was developed from a series of 15 four-sided surfaces. The complete flow model geometry is shown in Figure 5.6.

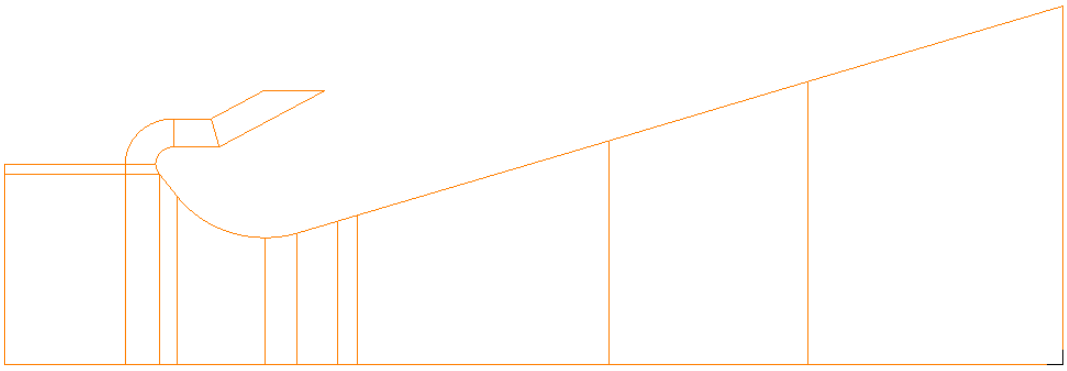

Figure 5.6 Axisymmetric flow model geometry.

Mesh seed points were prescribed by the specification of line subdivisions according to the anticipated local mesh density requirements. In this regard, two important considerations needed to be made. Firstly, as a normal shock was expected to progress down the length of the exit cone during the simulation period in response to an unsteady domain inlet pressure, the mesh density over this entire region needed to be sufficient – particularly in the axial direction – to provide for reasonably accurate shock capture at each instant in time. In addition, as viscous flow was being modelled, a suitably fine mesh density adjacent to all wall surfaces in the direction of the surface normal was needed to provide acceptable resolution of the associated boundary layer.

5.3.2 Initial Conditions

For transient flow simulations, the specification of initial conditions is necessary to describe the state of the flow field being analysed at the start of the simulation. Such conditions must usually be physically representative of the event being modelled in order for realistic results to be obtained. Another consideration that needs to be made regarding the use of representative initial

conditions is their impact on the numerical convergence of the flow solution. Indeed, in certain cases it may be necessary to employ fictitious initial conditions to assure convergence at the beginning of a solution.

For the current case, it is assumed that in reality, the gas within the nozzle is at rest, at atmospheric pressure and at room temperature immediately before the ignition transient is initiated. Following a period of numerical experimentation, it was found that for the specified pressure and temperature inlet conditions and by employing a sufficiently small time step size, these parameters could be applied as initial conditions without any convergence issues. The initial conditions employed for the transient flow simulations of this study are summarised in Table 5.3.

Flow Variable	**Prescribed Value**
Y-Velocity	0 m/s
Z-Velocity	0 m/s
Pressure	100 kPa
Temperature	298 K

Table 5.3 Flow domain initial conditions.

5.3.3 Boundary Conditions

Boundary conditions were assigned to the perimeter of the flow domain to replicate the physical qualities of the two physical and three virtual boundaries that were used to define it. The location of these boundary conditions, denoted as BC1, BC2, BC3, BC4 and BC5, respectively, is shown in Figure 5.7, with the corresponding parameters being detailed in Table 5.4.

The interface between the exhaust flow and the SRN2 structure, shown as BC1, was defined using ADINA-F's fluid-structure interaction boundary condition to allow for the transfer of force and displacement data between the flow and structural models. BC2, which was defined using the wall boundary condition, represents the propellant grain boundary. This inactive boundary condition was employed as propellant combustion was not accounted for in this study. In consideration of the very short time scale of the simulation, such a simplification was felt to be reasonable as any mass flow from the surface in question would be minor so soon after the initiation of the ignition event.

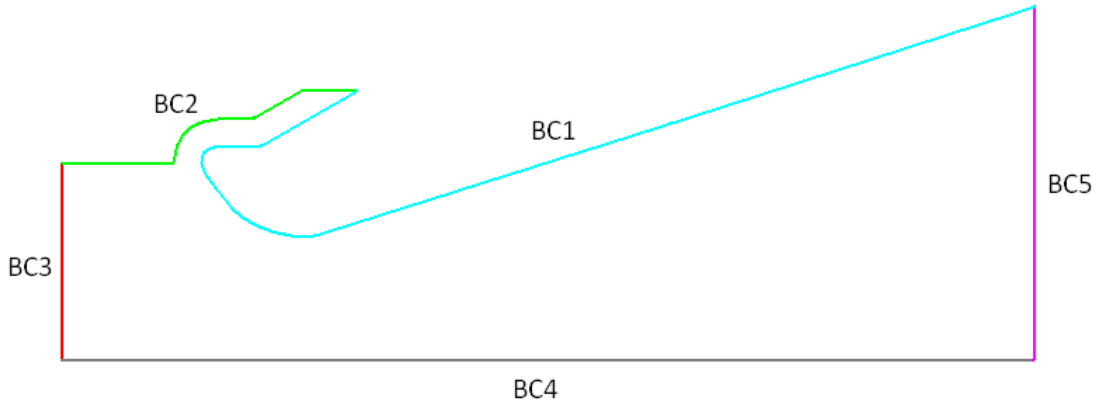

Figure 5.7 Flow model boundary conditions.

Boundary Condition	Type	Value
BC1	Fluid-Structure Interaction	No Slip, Adiabatic
BC2	Wall	No Slip, Adiabatic
BC3	Subsonic Inlet	P(t), T(t)
BC4	Symmetry	-
BC5	Outlet Control	P = 100 kPa

Table 5.4 Flow domain boundary conditions.

The flow domain inlet, indicated as BC3, was defined using ADINA-F's subsonic inlet boundary condition, at which the ignition transient pressure and temperature functions discussed above were prescribed. Temporal variation of these two parameters was achieved using time functions which scaled their magnitudes as a function of time. The domain's axis of symmetry was defined using the symmetry boundary condition (BC4), whilst the domain outlet was defined using ADINA-F's outlet control boundary condition (BC5) at which the flow's pressure was set to atmospheric pressure to simulate the nozzle's interface with the external environment.

5.3.4 Finite Element Meshing

Owing to the material uniformity of the flow domain, the generation of its finite element mesh was relatively straightforward procedure. Following the creation of the flow domain's geometry and the prescription of the line subdivisions, a flow material model was defined in the ADINA-F module according to the properties reflected in Table 5.2. An axisymmetric element group was

then generated for this material based on the general fluid element characteristics discussed in Chapter 3. The 15 surfaces representing the domain were then meshed using 5192 of ADINA-F's 3-noded triangular axisymmetric fluid elements. The overall flow domain mesh is depicted in Figure 5.8, which demonstrates the application of a relatively fine mesh density in the axial direction of the nozzle and adjacent to the nozzle surface, for shock and boundary layer capture, respectively. Figure 5.9 shows the mesh structure at the nozzle's entrance and throat region in greater detail.

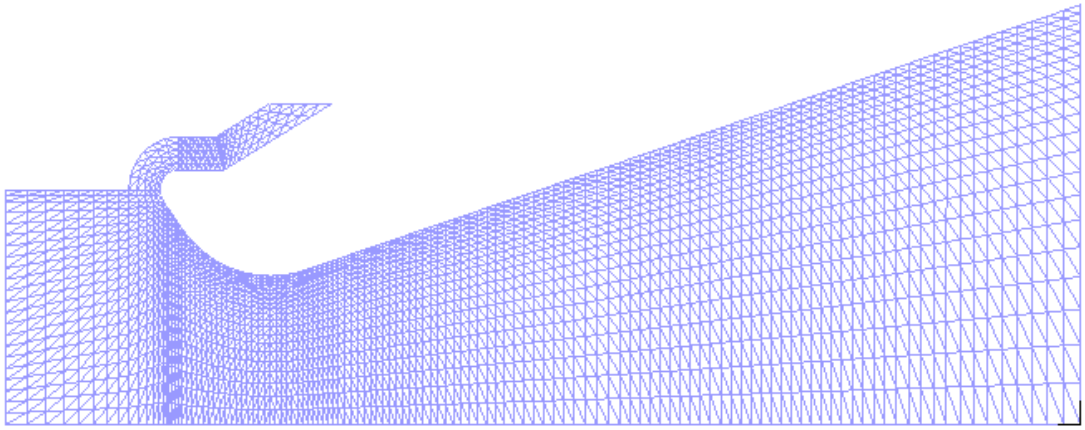

Figure 5.8 Flow model finite element mesh.

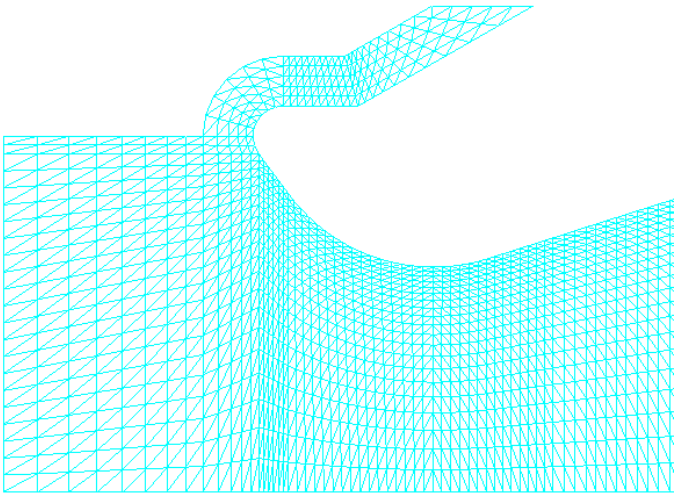

Figure 5.9 Mesh detail at the entrance and throat region.

5.3.5 Simulation Time Parameters

A series of investigative flow simulations were conducted to establish the optimal time parameters required for the solution of the flow problem. With respect to the overall simulation time span, it was observed that an analysis period of 0.3 s provided sufficient time for the most significant transient flow effects within the nozzle to take place. In consideration of the limited computational resources available, it was apparent that a full duration simulation of 0.6 s would provide little additional information, whilst being twice as computationally expensive. A total simulation time of 0.3 s was therefore employed.

In terms of temporal discretization, it was desired that as large a time step as possible be used to limit the solution size. The primary constraint in this respect however, is that the numerical stability of an unsteady flow problem is generally dependent on the time step size selected. That is, for the current simulation a critical time step size existed beyond which the solution would fail to converge. Following experimentation, it was established that with the aid of ADINA-F's automatic time stepping facility and using a Courant-Friedrichs-Lewy number of 3 to relax this sensitivity, the solution time step size could be raised as high as $1x10^{-4}$ s and still run stably.

Consequently, a scheme employing three thousand 1e-4 s time steps to generate a solution 0.3 s in length was used for the current flow simulation. Furthermore, as the overall simulation time parameters are controlled in the fluid model for fluid-structure interaction (FSI) simulations in the ADINA System, the time parameters for both the flow and structural solution components were specified in the flow model. The differentiation between a coupled and uncoupled FSI solution is made according to the maximum number of FSI iterations specified by the user. For an uncoupled solution, the maximum number of iterations is set to one, whilst if a coupled solution is desired, the number is set to an integer greater than one.

5.4 Structural Modelling

5.4.1 Geometry Definition

The axisymmetric structural model geometry was created as a collection of the four substructure geometries by respectively defining points, lines and surfaces in the global YZ plane, in the method discussed previously. To provide for sample point locations and to accommodate geometric complexities, the final geometry comprised 30 individual surfaces, as depicted in Figure 5.10.

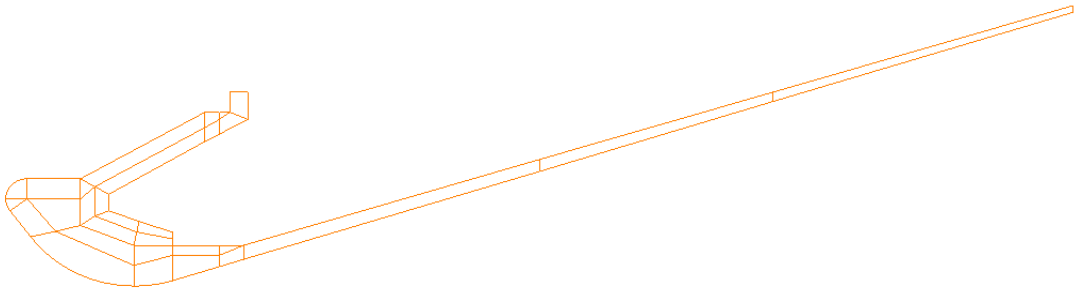

Figure 5.10 Axisymmetric structural model geometry.

Once the geometry had been established, line subdivisions were specified for each line element in preparation for the surface meshing operation to follow. In this regard, consideration was given to the distribution of subdivisions applied along the fluid-structure interface in the flow model. Although a nodal mismatch between interface nodes of the flow and structural models can be accommodated by the ADINA System using an interpolation function, for the sake of error minimisation, an identical distribution of subdivisions was applied to the interface of the structural model. Subdivisions along the remaining line elements were effectively based on the scale of the interface subdivisions, with the minimisation of element distortion being of primary concern.

Once again, it was felt that if it was warranted by the presence of an elastodynamic response signature, the coarseness of the resulting mesh could be refined improve the accuracy of the response. In terms of a quasi-static response regime however, it was believed that the specified subdivisions provided sufficient mesh density to achieve reasonable response accuracy.

5.4.2 Boundary Conditions

The structural model was subjected to three boundary conditions, BC1, BC2 and BC3, as depicted in Figure 5.11. A fluid-structure interaction boundary condition (BC1) was applied to the wetted surface of the model to define the numerical interface with the flow model. To represent the circumferential joint between SRN2 and the hypothetical motor casing, the structural model was constrained with full fixity (BC2) on the three lines associated with the outer edges of the attach structure. Finally, a pressure load of 100 kPa was applied to the external surfaces of the nozzle to represent the presence of atmospheric pressure.

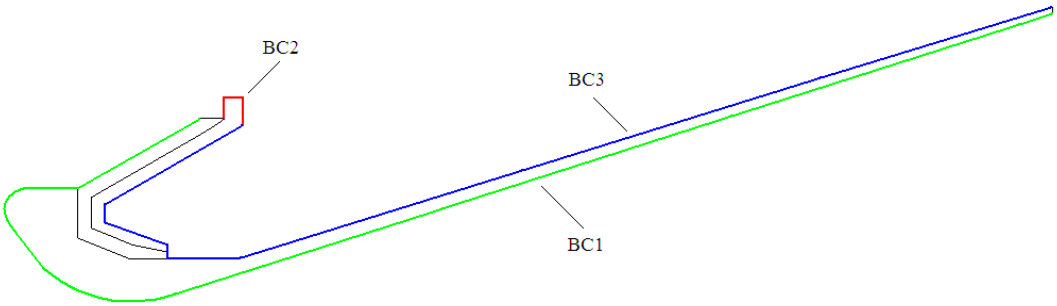

Figure 5.11 Structural model boundary conditions.

5.4.3 Finite Element Meshing

On completion of the geometric and boundary condition specifications, one isotropic and two orthotropic material models were defined to represent SRN2's constituent materials according to the properties listed in Table 5.1. Three element groups were subsequently classified on the basis of each of these material models.

The surfaces representing the four substructures were then meshed using ADINA's 9-noded axisymmetric solid elements, resulting in the creation of a finite element model comprising 842 elements. The completed finite element mesh is displayed in Figure 5.12, with SRN2's entrance and throat region shown in greater detail in Figure 5.13. The subtle variation in mesh density prescribed by biasing the line subdivisions can be seen from these figures.

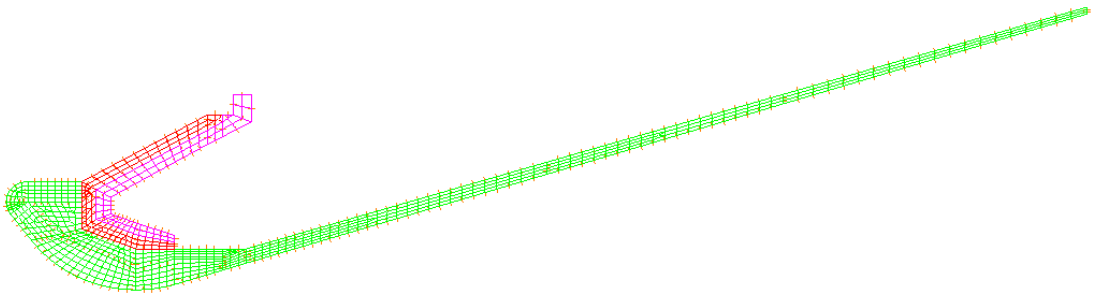

Figure 5.12 Structural model finite element mesh.

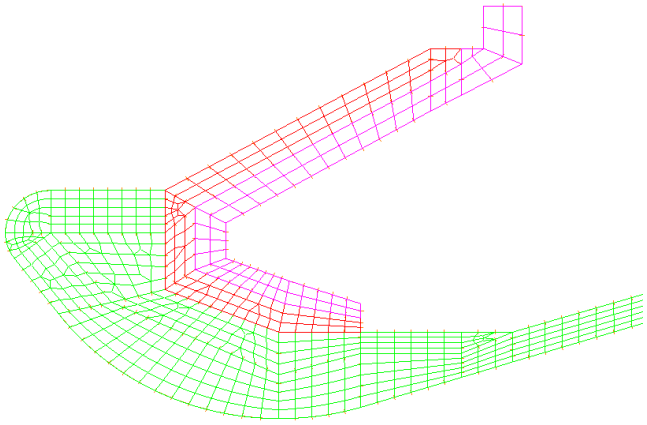

Figure 5.13 Mesh detail at the entrance and throat region.

5.4.4 Results Sampling

From experience gained in the SRN1 simulation, results sampled at points rather than along contours proved to be more informative, especially in the case of a vibratory response. Furthermore, oscillations were typically more severe at subsurface points as opposed to points on the wetted surface. Consequently, response histories derived from the current simulation were sampled at submerged points, denoted alphabetically in Figure 5.14. Positions A to E represent mid-surface points at the tip of the exit cone, halfway along the length of the exit cone, at the root of the exit cone, at the throat of the nozzle and at the leading edge of the ITE, respectively. The spread of these positions across the SRN2 geometry allowed for responses in relatively stiff and flexible regions of the nozzle to be observed.

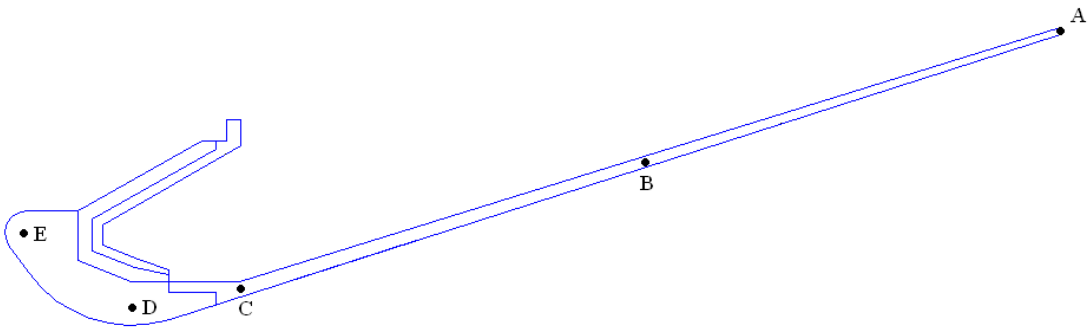

Figure 5.14 The position of sampling points A, B, C, D and E on SRN2.

5.5 Results and Discussion

5.5.1 Assessment of Simulated Steady Flow Field

Before confidence could be placed in results generated by the transient flow simulation representing the ignition event, the performance of the flow model was assessed for the significantly simpler scenario of steady state operation at nominal inlet conditions. In this manner, qualitative irregularities detected for this simpler flow case would provide an early indication of an erroneous model and/or solution scheme.

Band plots depicting Mach number, pressure and density distributions throughout the flow domain under steady flow conditions are shown collectively in Figure 5.15. Inspection of the Mach number distribution in relation to the associated contour scale provides immediate indication of the subsonic to supersonic transition of the flow's velocity in the vicinity of SRN2's throat. Downstream of the throat, the flow undergoes supersonic expansion until the exit plane, with contours in the core flow region demonstrating the two-dimensional nature of the expansion. Development of the surface boundary layer is also clearly shown in Figure 5.15 (a), and a slight disturbance of the boundary layer in the vicinity of the exit plane is indicated – potentially as a result of interaction with an external shock.

The predicted static pressure distribution is also typical of choked convergent-divergent nozzle flow and exhibits the significant expansion of the combustion gases that occurs over the length of SRN2. The associated contour gradient indicates that the greatest degree of expansion occurs in the transonic region of the flow, with the two-dimensional effects of nozzle's curvature on the flow's expansion clearly visible. The variation of density in the nozzle, shown in Figure 5.15 (c) follows a similar trend, decreasing rapidly as flow expansion occurs, as is expected. This plot also predicts the flow stagnation that would occur in reality at the bottom of the annular pocket created between the nozzle and propellant grain, as indicated by the small zone of particularly high density.

As a further steady flow assessment, the variation of Mach number, static pressure and density along SRN2's axis of symmetry and wall was plotted as a function of distance from the leading edge position. The Mach number variation is shown in Figure 5.16. In accordance with the specification of a zero slip surface, the velocity at the wall is shown to be zero along the length of the nozzle. Along the axis of symmetry, the classical convergent-divergent nozzle Mach

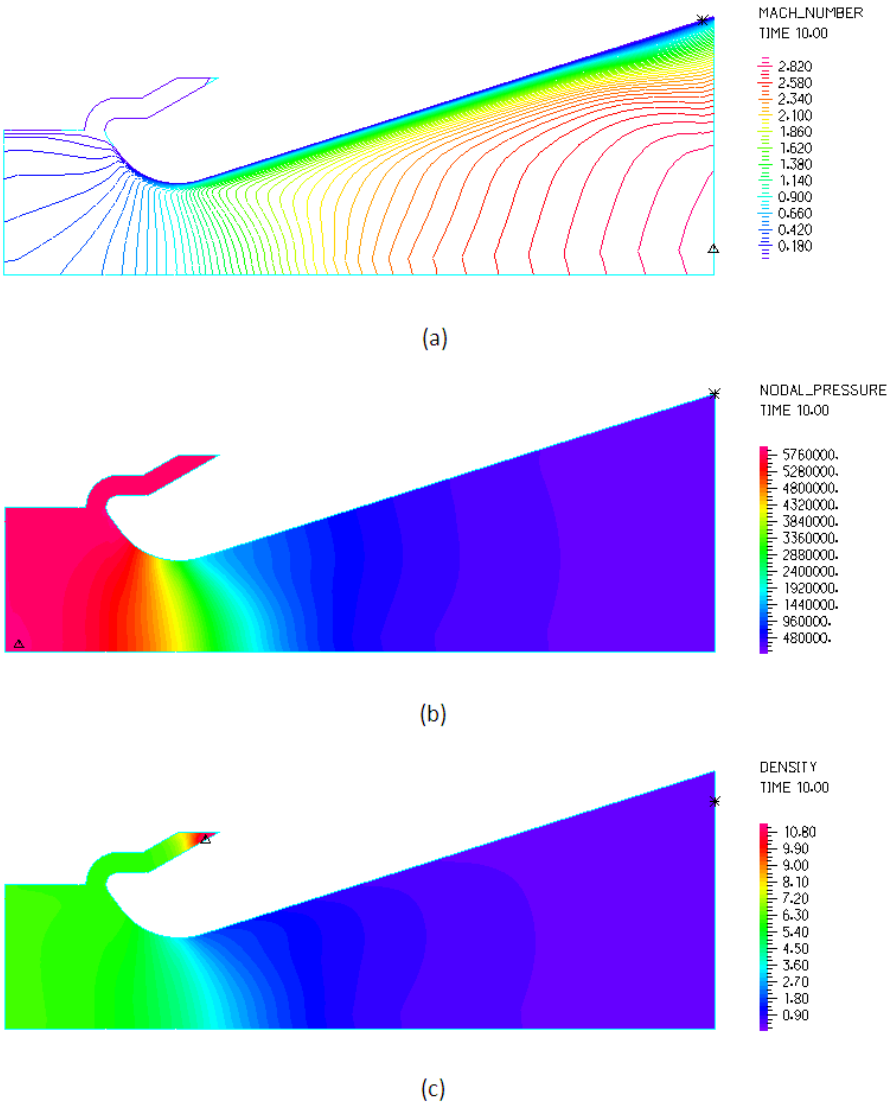

Figure 5.15 Band plots of (a) Mach number, (b) pressure and (c) density distributions under steady flow conditions.

number curve is observed, with the flow reaching sonic velocity just beyond SRN2's throat and accelerating to a speed a fraction under Mach 3 at the exit plane.

As far as the variation of pressure is concerned, which is plotted in Figure 5.17, the expected trends are once again observed. Significant discrepancies are noted to exist between variations along the axis of symmetry and the nozzle wall, however. The higher wall pressure at the leading

edge of SRN2 in comparison to that predicted on the axis of symmetry can be attributed to pressure recovery, as the flow in the region adjacent to the leading edge remains fairly stagnant. Further along the nozzle, the pressure at the wall falls significantly below that predicted on the axis of symmetry for the equivalent axial displacement. In reference to Figure 5.15 (b), it would appear that this difference can be attributed to the two-dimensional nature of the flow expansion.

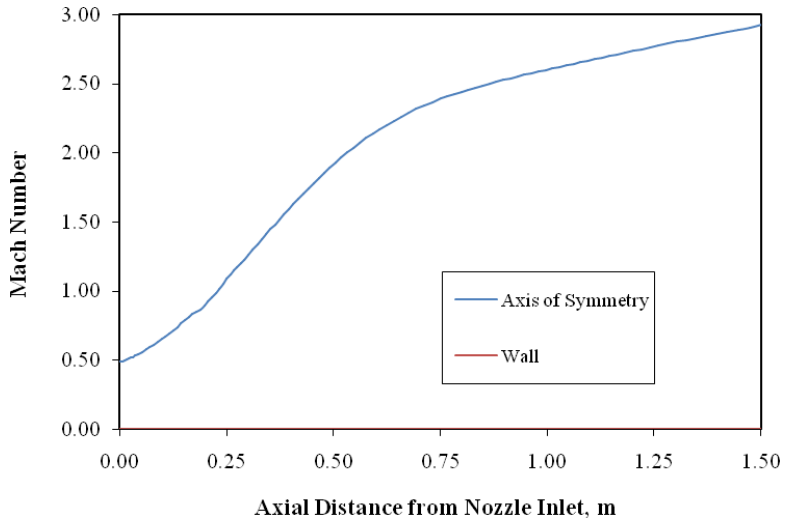

Figure 5.16 Axial Mach number distributions for steady flow conditions.

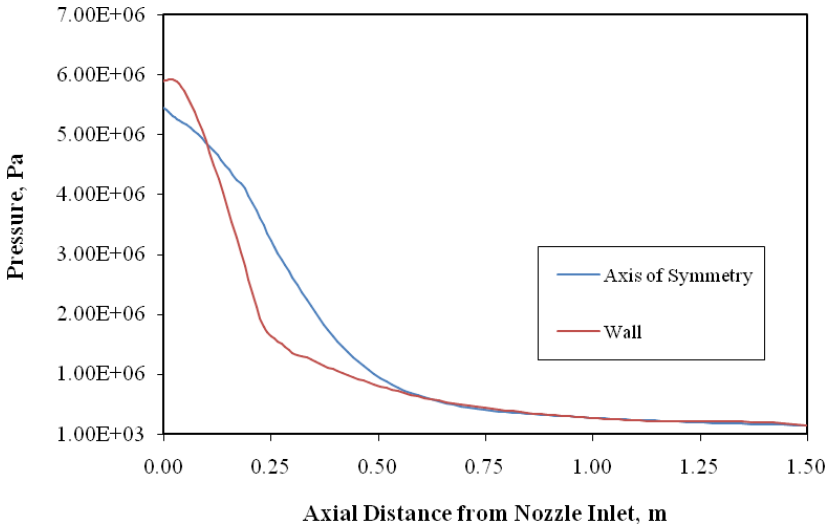

Figure 5.17 Axial pressure distributions for steady flow conditions.

In terms of the variation of density with axial displacement, Figure 5.18 displays virtually identical characteristics. The discrepancy occurring between the wall and axis of symmetry data towards the end of SRN2 can be attributed to boundary layer effects. Interestingly, the boundary layer disturbance at the end of the nozzle indicated in Figure 5.15 (a) registers as a slight density rise in Figure 5.18.

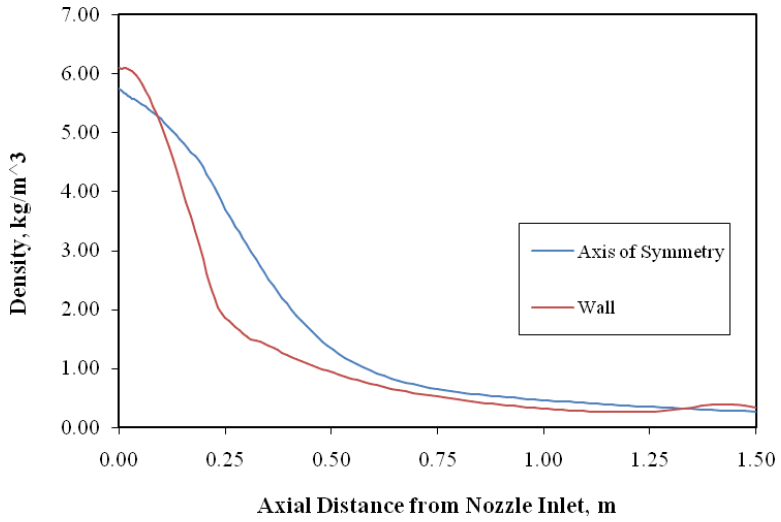

Figure 5.18 Axial density distributions for steady flow conditions.

In a qualitative sense, the data reflected above indicates that the flow model was able to correctly predict the variations of Mach number, static pressure and density characteristic of steady flow through convergent-divergent nozzles, with no obvious errors being observed. In response to this finding, an assessment of the simulated transient flow field was subsequently conducted.

5.5.2 Assessment of Simulated Transient Flow Field

For this assessment, the full 0.3 s period of transient flow was simulated and plots of Mach number, static pressure and density distributions were once again investigated, at solution times of 0.005 s, 0.02 s and 0.3 s. These times were selected as they each represent characteristic instances during the evolution of the flow. Results are presented for each flow variable in Figures 5.19, 5.20 and 5.21, respectively.

Figure 5.19 shows Mach number distributions in the flow domain at each of these three time points. At t = 0.005 s, the scaled contours indicate that flow immediately downstream of the throat has just surpassed sonic speed, as the domain inlet pressure has risen past the critical pressure. At this pressure however, the flow is still severely over-expanded by the nozzle and recompresses over a normal shock approximately one third of the way along the exit cone; although this shock is more clearly shown in the density distribution depicted by Figure 5.21 (a). The contours at this time also indicate the ingress of combustion gases into the annular propellant grain pocket. Densification in this region is also demonstrated by the density distribution, along with apparent flow stagnation occurring on the converging contour of the nozzle entrance. Interestingly, the pressure distribution shown in Figure 5.20 (a) depicts a compaction of gases ahead of the shock to pressures significantly above the latent atmospheric pressure, in a plunger type action.

As demonstrated by Figure 5.19 (b), a complex set of flow phenomena are shown to have manifested in the aft region of the exit cone by a time of 0.02 s. The normal shock observed at t = 0.005 s has travelled towards the exit plane as the inlet pressure is raised further, and the flow is still notably over-expanded as evidenced by its separation from the exit cone, roughly halfway along the exit cone's length. The pressure distribution shown in Figure 5.20 (b) also indicates the presence of the normal shock, and an observation of the density plot depicted in Figure 5.21 (b) (with a truncated scale range to improve resolution) reveals the presence of an oblique separation shock emanating from the flow separation point and intersecting the normal shock. The velocity vector plot displayed in Figure 5.22 shows the direction of the velocity vectors at an equivalent time of 0.02 s, and significantly indicates the presence of flow recirculation in the flow region adjacent to the separated jet. In a qualitative sense, these observations agree very well with those articulated in literature regarding the flow characteristic associated with over-expanded flows, such as the diagram of Verma et al (2006) shown in Figure 2.7 of Chapter 2.

Figures 5.19 (c), 5.20 (c) and 5.21 (c) depict the flow at the end of the simulation, 0.3 s into the ignition event. As can be seen, The Mach number, pressure and density distributions indicate relatively complete expansion of the combustion gases, with no flow separation or shocks being visible in the flow domain, although a degree of evolution to the flow occurs from 0.3 s to steady conditions, as indicated by Figure 5.15.

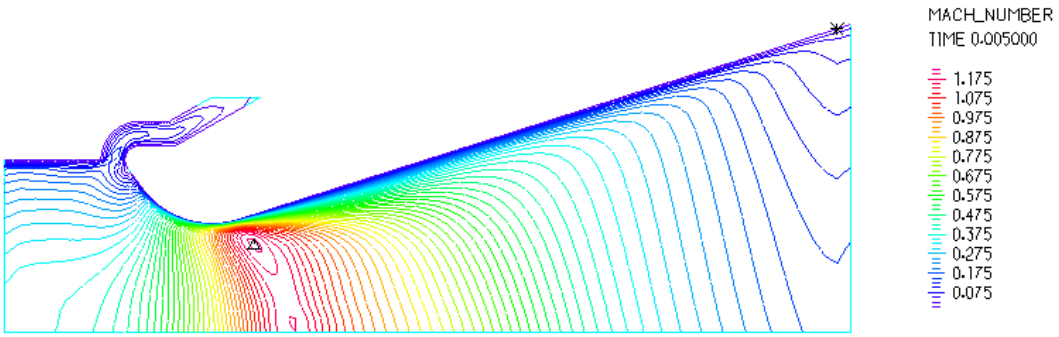

(a)

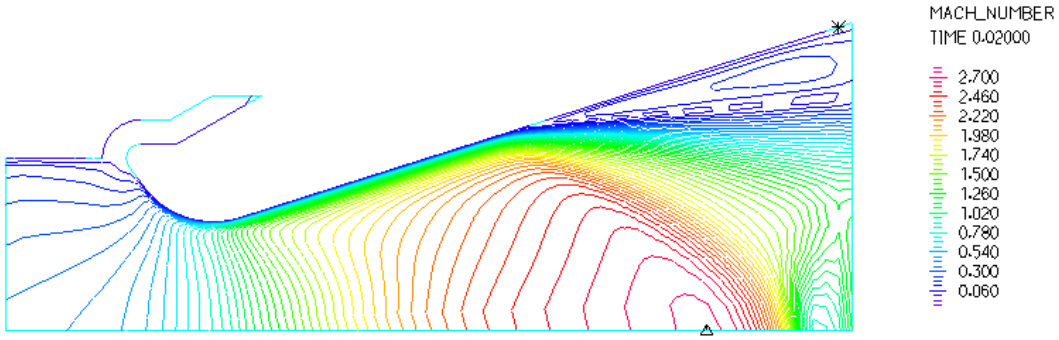

(b)

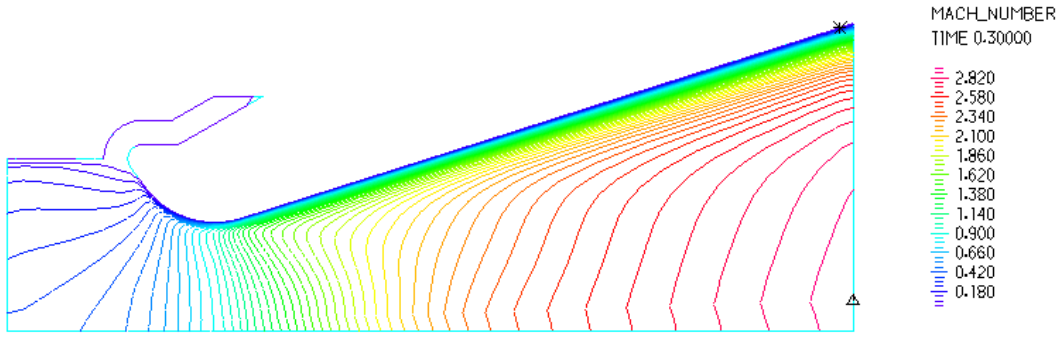

(c)

Figure 5.19 Mach number distributions at (a) t = 0.005 s,
(b) t = 0.002 s and (c) t = 0.3 s.

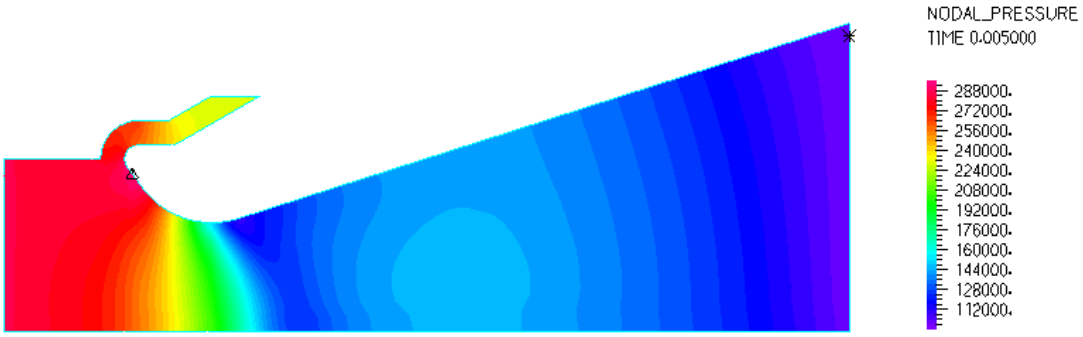

(a)

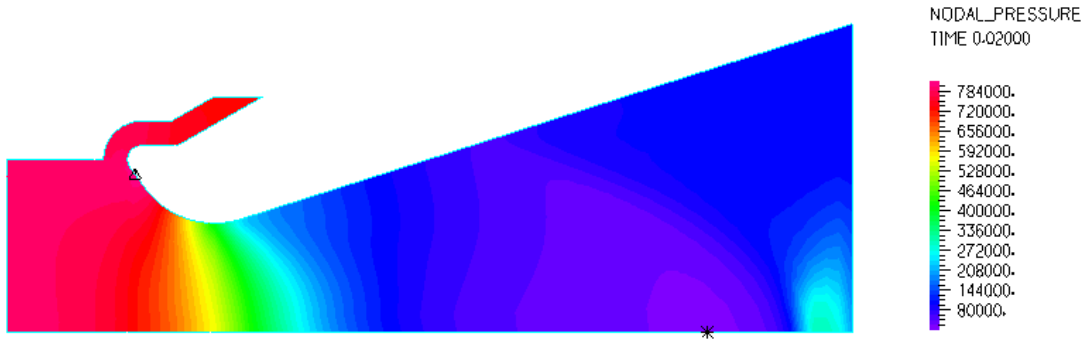

(b)

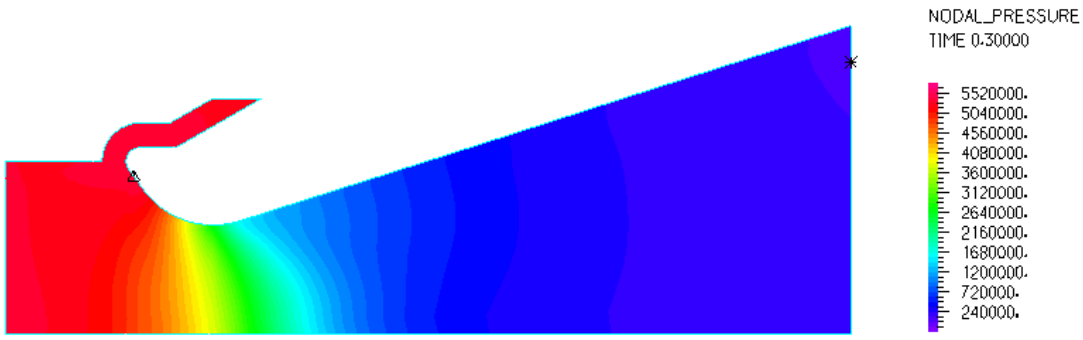

(c)

Figure 5.20 Pressure distributions at (a) t = 0.005 s,
(b) t = 0.002 s and (c) t = 0.3 s.

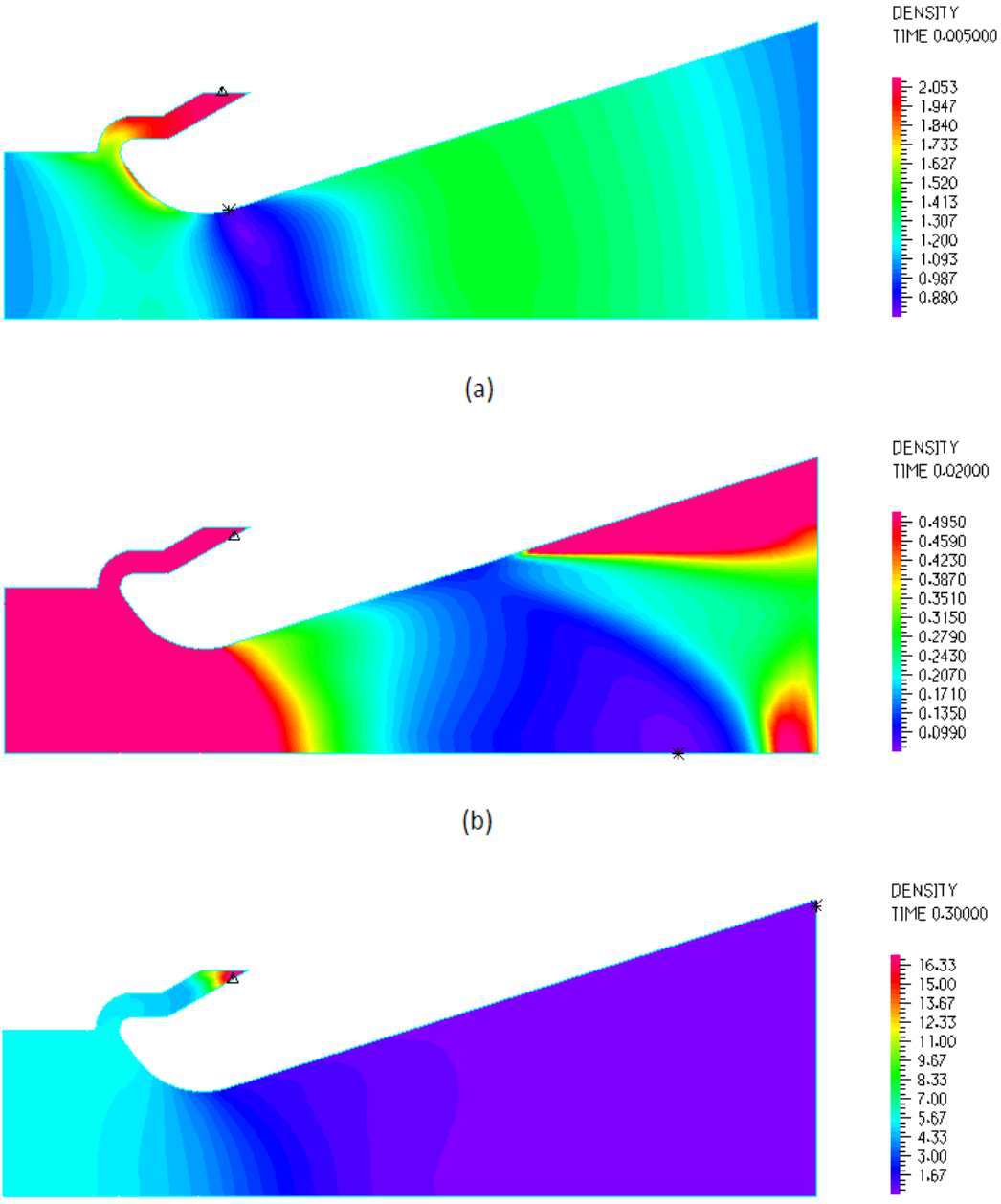

Figure 5.21 Density distributions at (a) t = 0.005 s, (b) t = 0.002 s (truncated scale range) and (c) t = 0.3 s.

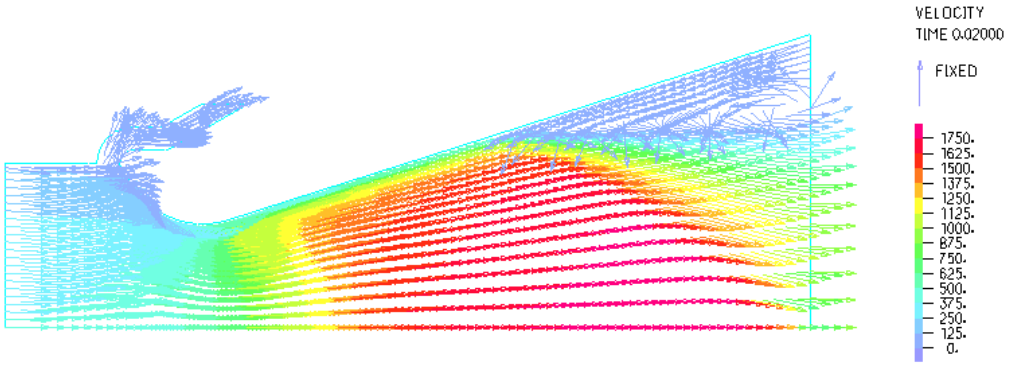

Figure 5.22 Distribution of simulated velocity vectors at t = 0.02 s.

Finally, to demonstrate the difference between the flow fields predicted by inviscid and viscous flow models, results are now presented for inviscid Mach number distributions at 0.005s, 0.01 s and 0.3 s adjacent to the associated viscous results, in Figures 5.23, 5.24 and 5.25, respectively.

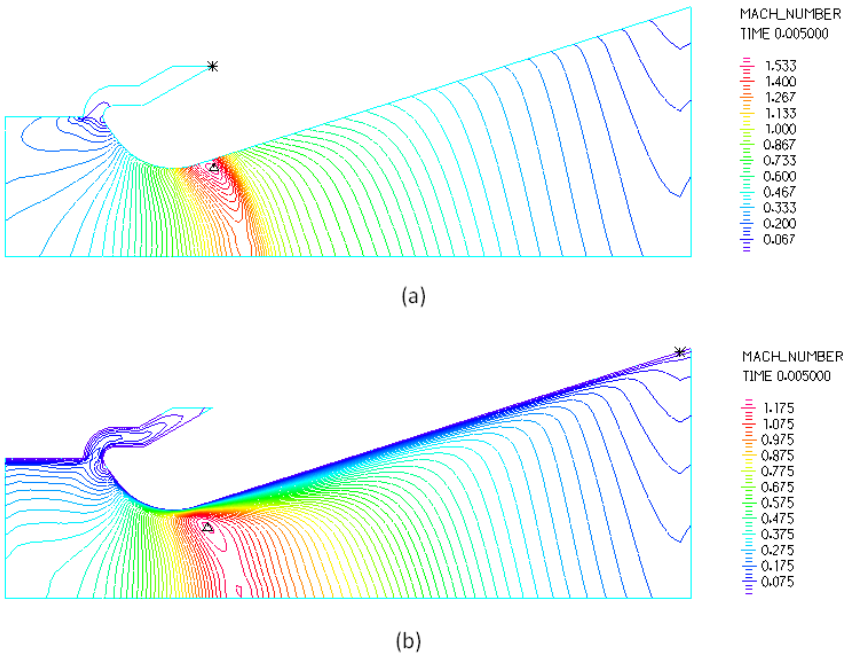

Figure 5.23 Mach number distributions at t = 0.005 s for (a) inviscid solution and (b) viscous solution.

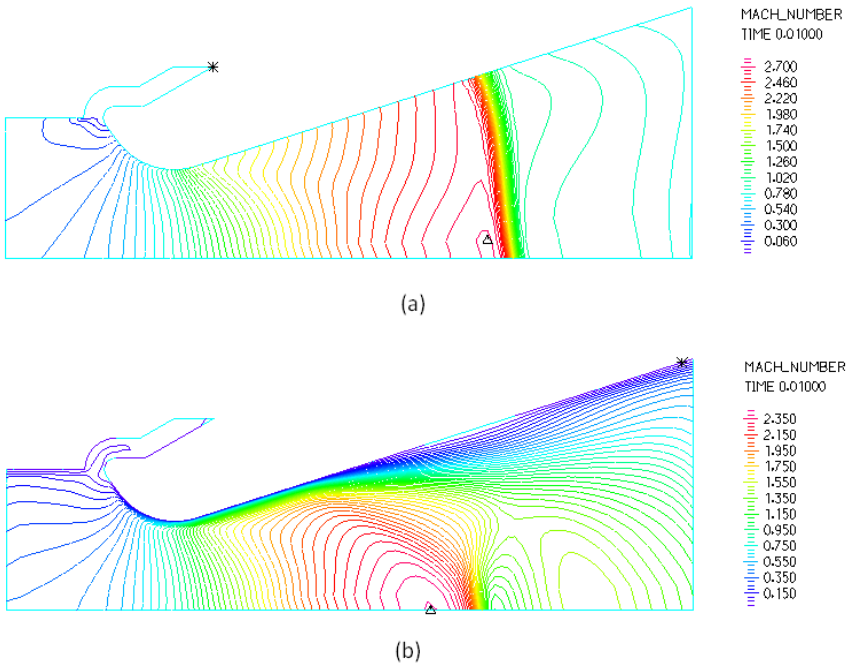

Figure 5.24 Mach number distributions at t = 0.02 s for (a) inviscid solution and (b) viscous solution.

Significant differences in the results predicted by either model are observed. The most notable deficiency in the inviscid results is the obvious absence of any boundary layer structures. In addition, the progression of the normal shock with increasing inlet pressure appears to occur more rapidly in the inviscid flow model, as viscous resistance does not have to be overcome and the sub and supersonic flow regions are more clearly defined. Also, the normal shock is more acute and considerably less deformed than in the case of the viscous model. For the solution at t = 0.3 s, the viscous model indicates a well-developed boundary layer, whilst in the inviscid model, higher flow velocities at SRN2's exit plane are predicted. These observations clearly point to the importance of including viscous effects in the simulation of transient nozzle flow, if the loading of the nozzle structure is to be realistically represented.

From this assessment of the simulated transient flow field, it can be concluded that the SRN2 flow model provides a reasonable qualitative approximation, at least, of the development of the flow structures known to take place in rocket nozzles during motor start-up.

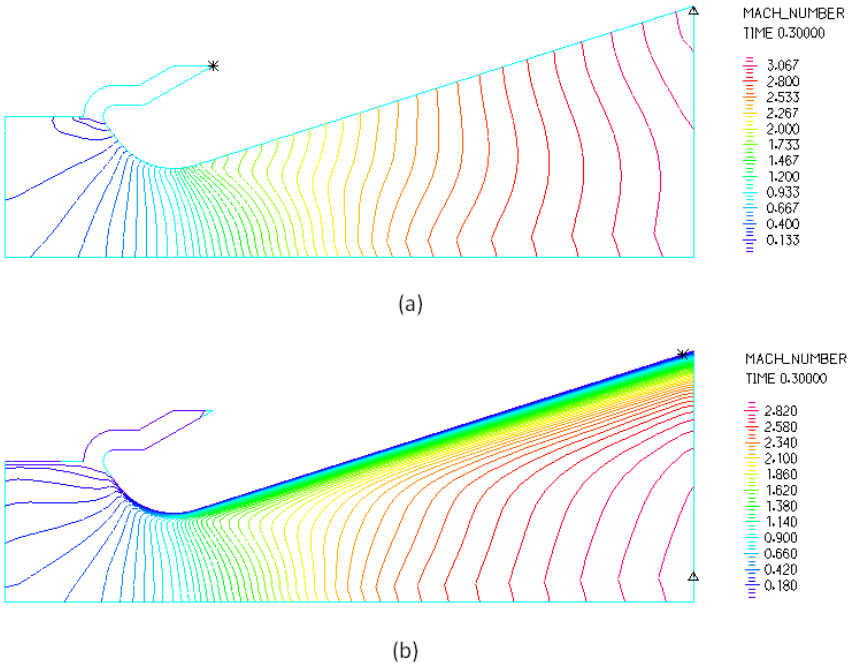

Figure 5.25 Mach number distributions at t = 0.3 s for (a) inviscid solution and (b) viscous solution.

5.5.3 Characteristic Fluid-Structure Interaction Modes

The transient displacement response of the nozzle was compared to the development of the flow field to gain an understanding of the characteristic modes of interaction occurring during the ignition event. In addition, the stress response of composite components of SRN2 in the hoop, radial and axial directions was examined to establish the manner in which these indices vary with time. Deformed band plots showing hoop, radial and axial stress distributions at times of 0.005 s, 0.02 s and 0.3 s are shown in Figsures 5.26, 5.27 and 5.28, beneath plots of flow domain pressure distributions at equivalent times. For the sake of clarity, the deformation of the nozzle has been magnified 500 times.

At solution time of 0.005 s, the gases compressed ahead of the advancing normal shock are shown to have a clear effect on the structure, as the increased pressure in this region forces a slight expansion of the exit cone, as indicated by a zone of tensile hoop stress in the adjacent region. Hoop stresses are shown to be mild and predominantly compressive in nature in the

carbon-phenolic insulator and negligible in the integral throat and entrance. Radial stresses in the nozzle are for the most part mild and compressive in nature, apart from a region of tensile stress at the tip of the insulator. Although there appears to be a greater variance in the axial stress distribution, magnitudes are generally negligible in the insulator and ITE. The increased compressive axial stress in the exit cone upstream of the normal shock can be attributed to the axial thrust generated by the zone of compaction.

By 0.02 s, the normal shock has advanced further still, leaving a zone of partial vacuum in its wake. Where this zone makes contact with nozzle surface, the external atmosphere is shown to compresses the exit cone generating compressive hoop stresses in this region. This phenomenon is indicated once again at a later stage of the ignition transient at a time of t = 0.045 s. The advancement of the flow shocks had however been retarded at this stage by the periodic decline in chamber pressure following the igniter charge pressure spike at t = 0.025 s. Further upstream in the throat region at 0.02 s, the super-atmospheric pressure adjacent to this area imparts mild tensile hoop stresses in the ITE and at the head of the exit cone. Radial stresses in the structure are shown to be predominantly compressive and mild in nature, apart from small zones of tensile stress encountered around stress concentrators along the periphery of the insulator. The axial stress distribution is dominated almost entirely by negligible compressive stress, although isolated areas of mild compressive stress are indicated in the insulator.

By the final solution time of 0.3 s, all major disturbances in the flow field are shown to have left the domain. The displacement response is characterised in particular by the significant distortion of the forward section of the nozzle in reaction to the now considerable combustion chamber pressure. Similarly, significant distortion in the radial direction is observed at the start of the exit cone as a result of the high internal to external pressure differential in this region. The predicted hoop stress distribution shows a wide variation from moderate compressive stress levels to moderate tensile stress levels. Tensile stresses dominate in the exit cone, whilst compressive stresses are predominant in the insulator and ITE, which is consistent with nature of the pressure loading present. Radial stresses appear to remain mild throughout the nozzle, apart from at the geometric stress concentrators. Axial stresses are for the most part moderately compressive in nature, although two bands of moderate tensile stress are shown to exist in the insulator. Areas of moderate compressive axial stress are predicted in the region of the normal interface between the insulator and the ITE, as would be expected.

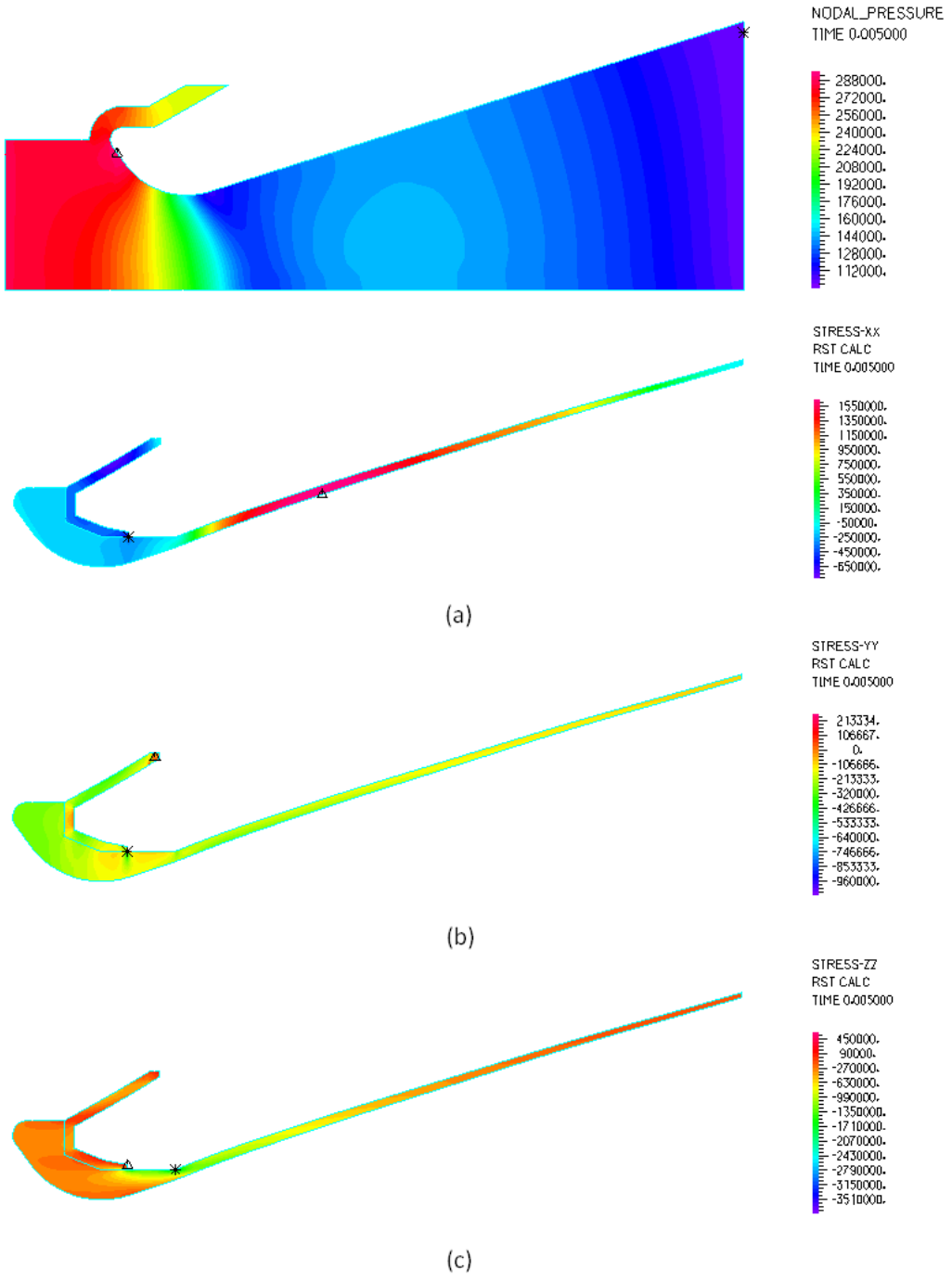

Figure 5.26 Deformed band plots of (a) hoop stress, (b) radial stress and (c) axial stress at t = 0.005 s.

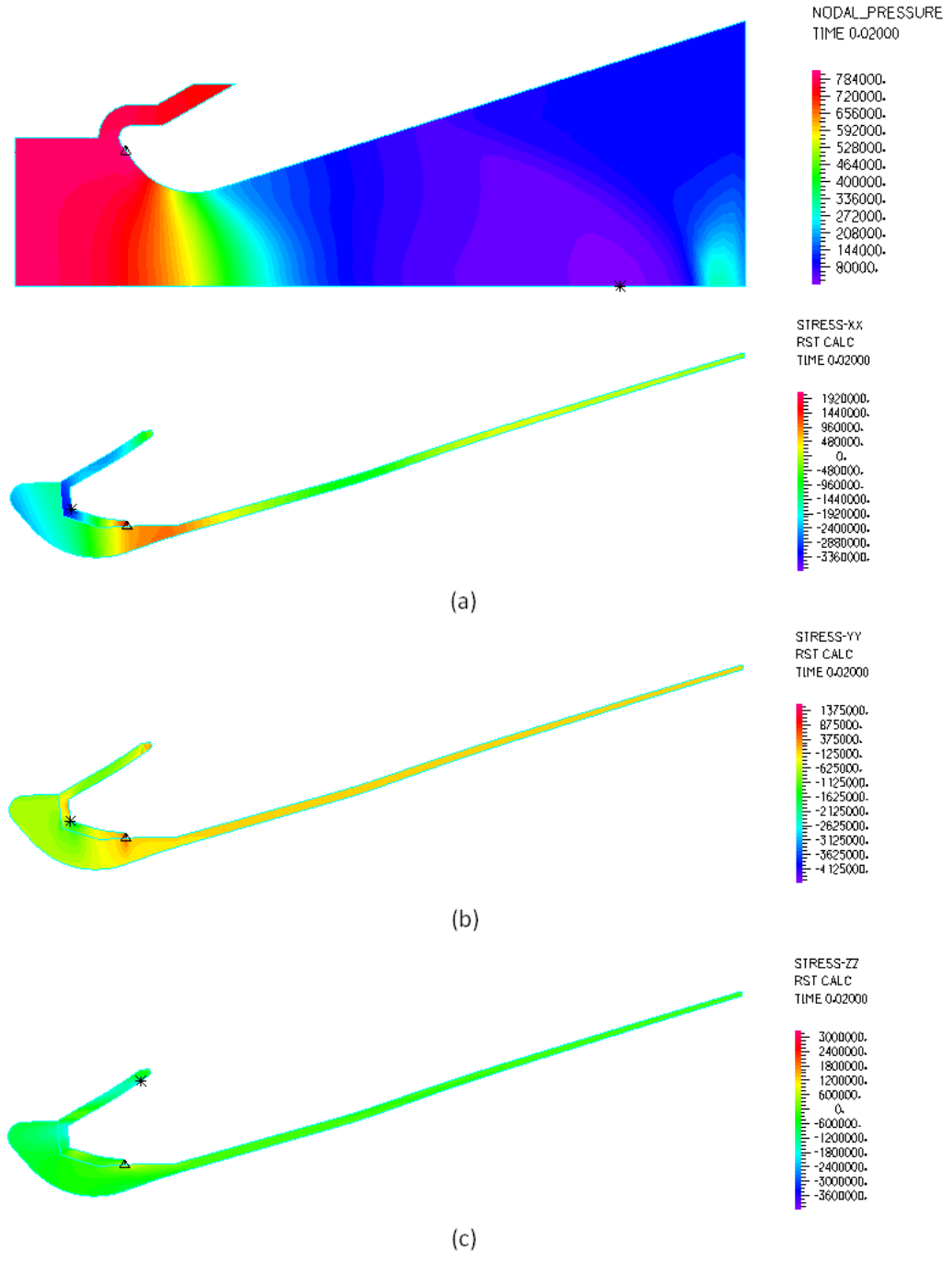

Figure 5.27 Deformed band plots of (a) hoop stress, (b) radial stress and (c) axial stress at t = 0.02 s.

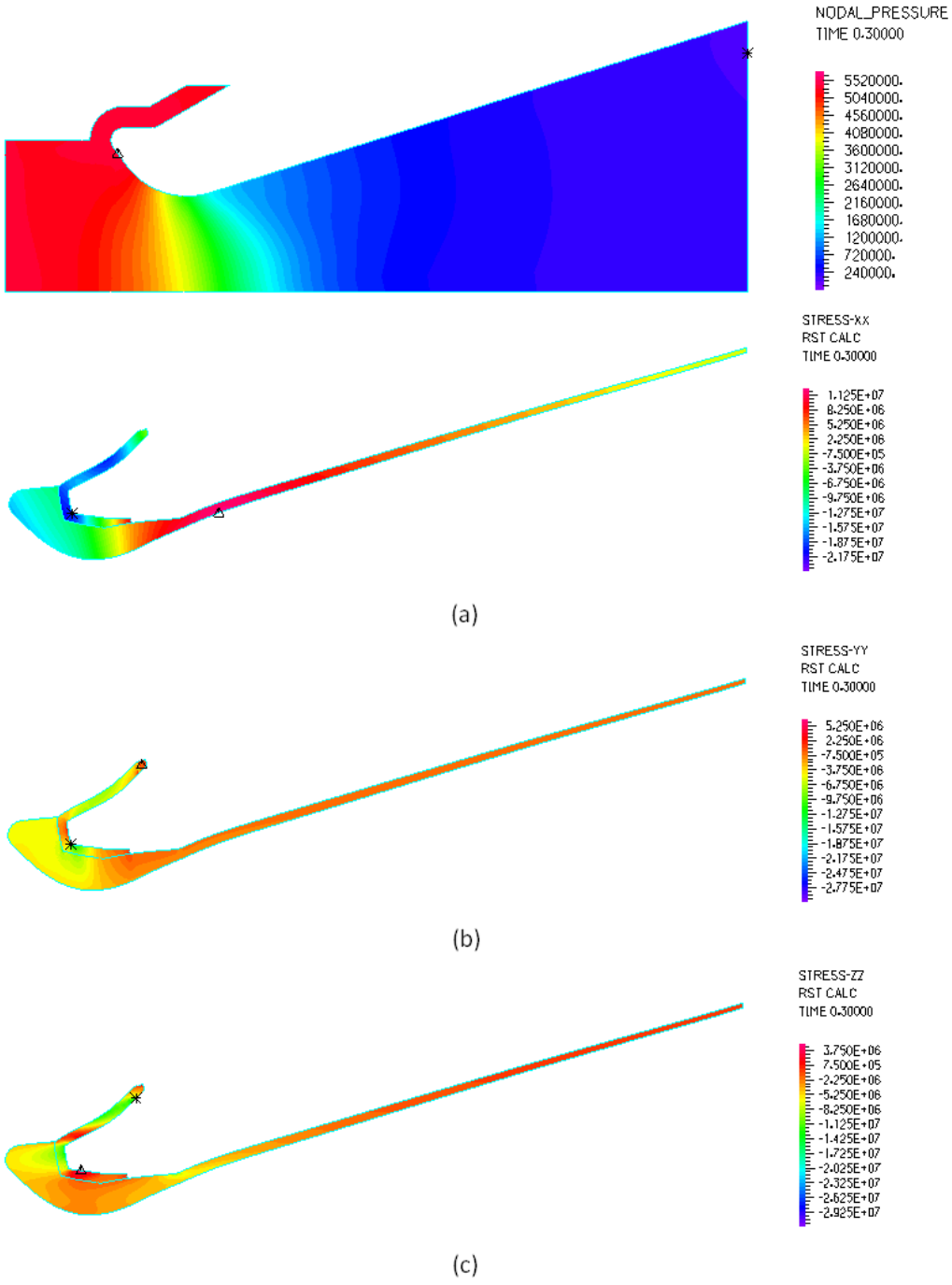

Figure 5.28 Deformed band plots of (a) hoop stress, (b) radial stress and (c) axial stress at t = 0.3 s.

From these results, it is clearly apparent that a measurable interaction takes place between the exhaust flow field and the nozzle structure during the early stages of the ignition transient. Predicted hoop, radial and axial stress levels during this period appear to be at most moderate in magnitude. The question that remains to be answered however is whether the interaction occurring between the SRN2 structure and its flow field is characterised by aeroelastic coupling, or whether this interaction is uncoupled, simply comprising the response of the nozzle to the largely unaffected development of the flow field.

5.5.4 Coupled and Uncoupled Structural Responses at Sample Points

In reference to the equations governing fluid-structure interaction in the ADINA code discussed in Chapter 3, conjugate fluid-structural influence is communicated between the fluid and solid domains through the kinematic condition at the interface boundary. Thus, the best assessment of whether strong coupling effects exist is achieved by considering the displacement behaviour of the nozzle predicted by the coupled and uncoupled solutions at specific sample locations. Such behaviour is shown for sample points A, B, C, D and E as functions of time, in Figures 5.29-5.33.

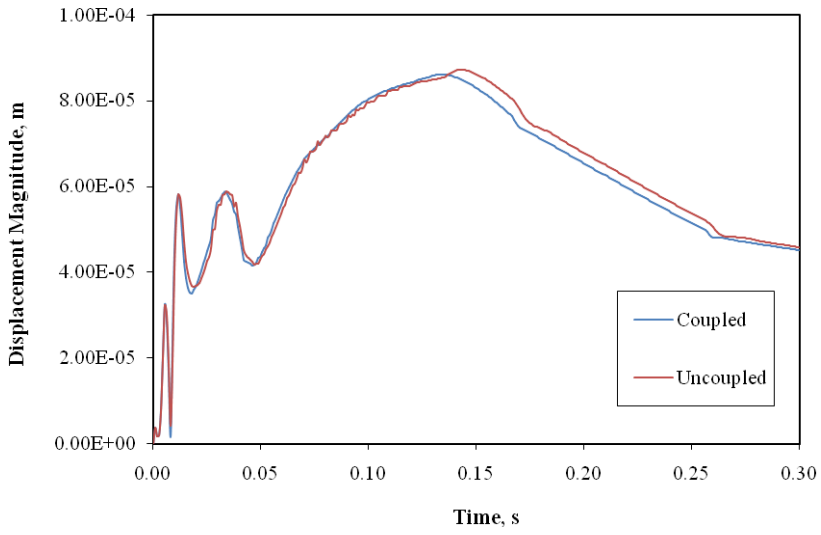

Figure 5.29 Coupled and uncoupled displacement magnitude histories at point A.

Interestingly, by observing the displacement response histories extracted for points A-E, it is clear that the discrepancy between results predicted by the coupled solution in comparison with

the uncoupled solution is minor. The only discernable variations between the two solutions are found at sample points A and B, both located at thin wall sections on the exit cone, which represent the most flexible areas on the nozzle. This observation immediately indicates that coupled interaction between the fluid and the structure does not take place at interfaces where the structural stiffness at the boundary is high, exactly as predicted by theory.

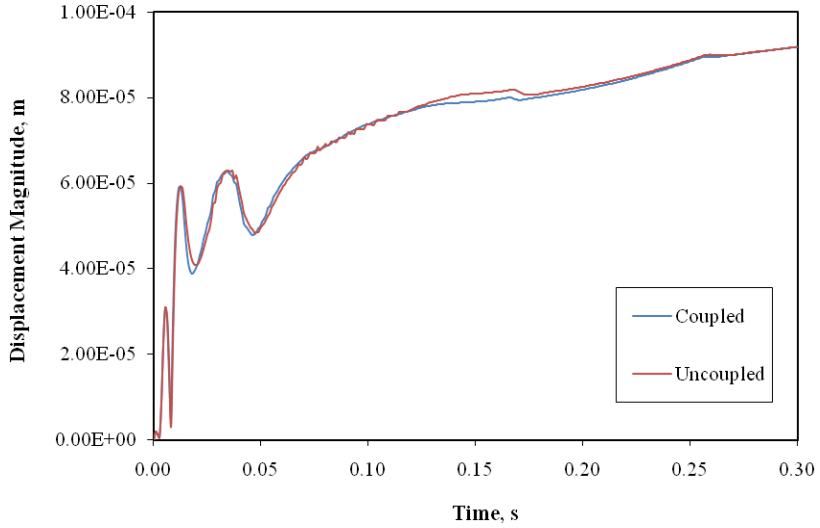

Figure 5.30 Coupled and uncoupled displacement magnitude histories at point B.

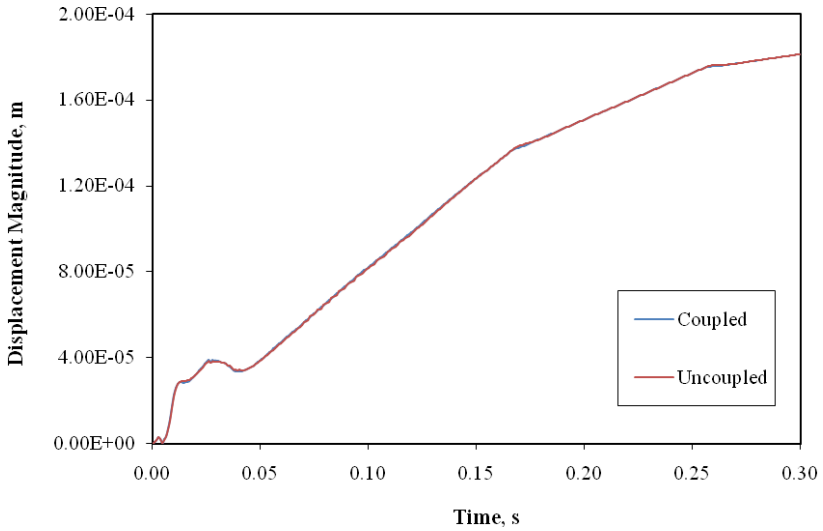

Figure 5.31 Coupled and uncoupled displacement magnitude histories at point C.

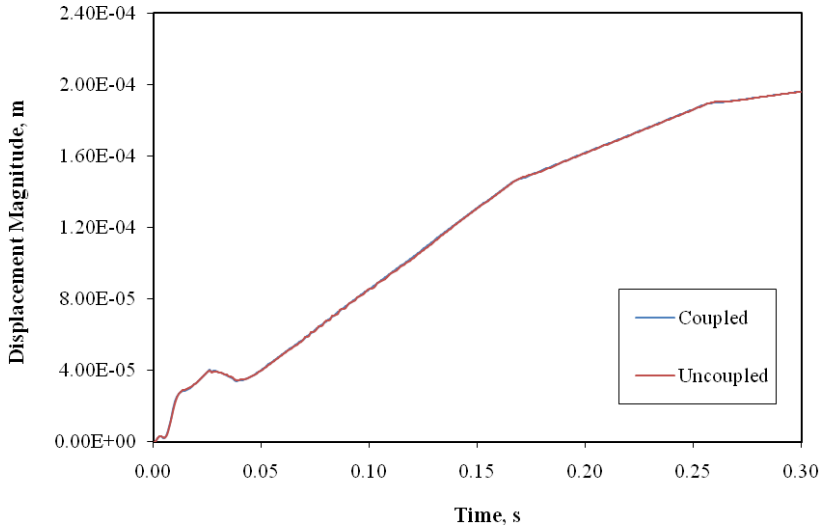

Figure 5.32 Coupled and uncoupled displacement magnitude histories at point D.

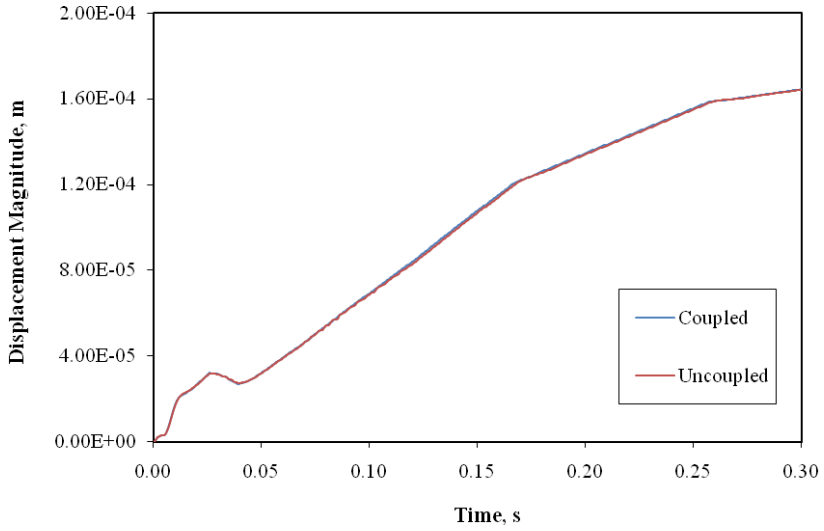

Figure 5.33 Coupled and uncoupled displacement magnitude histories at point E.

Also indicated by the displacement magnitude traces is that for all sample points, the highest structural displacement rates occur within the first 0.05 s of the ignition transient. The interaction modes referred to in Figures 5.26, 5.27 and 5.28 are also clearly represented, especially at sample points A and B. The trace discontinuities occurring at roughly 0.17 s and 0.27 s can be

attributed to the associated discontinuities in the time function defining the temporal growth of pressure at the nozzle inlet.

In terms of the stress response alternately predicted by the coupled and uncoupled solutions, results depicted in Figures 5.29-5.33 imply that measurable discrepancies between the two solution schemes are only likely to occur at points A and B, where the structure's stiffness is at its lowest. Figures 5.34-5.37 show the most significant time variation of circumferential, radial or axial stresses observed at these two points.

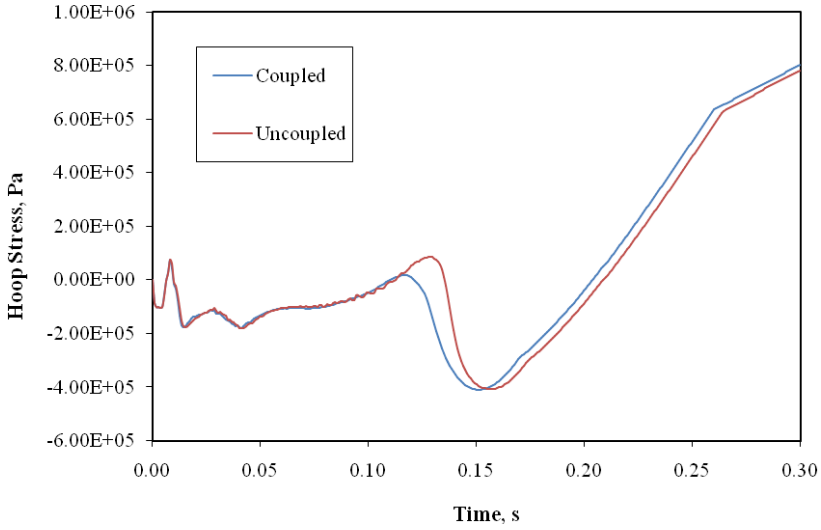

Figure 5.34 Coupled and uncoupled hoop stress histories at point A.

What is immediately obvious is the relatively low magnitude of the predicted stresses generated by the application of pressure loading alone – at no time do the respective stress levels exceed 2MPa at either point A or B, a value far below the failure stresses of the specified C-C material. It is evident therefore that the contribution made by dynamic pressure loading during the ignition transient to the development of stresses in the exit cone is essentially negligible – a noteworthy result. If one considers the transient pressure distribution predicted during the ignition transient, this observation is completely justifiable, as the pressure differential across the outer and inner surfaces of the exit cone and over the passage of the flow separation is comparatively low.

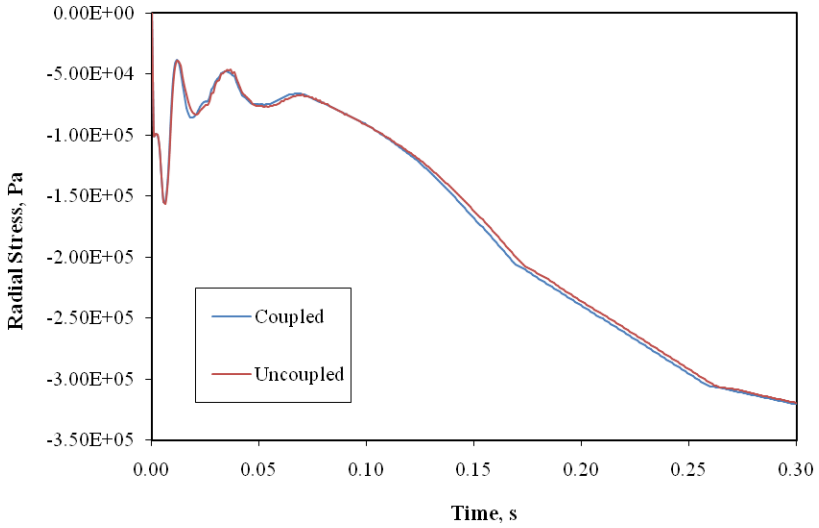

Figure 5.35 Coupled and uncoupled radial stress histories at point B.

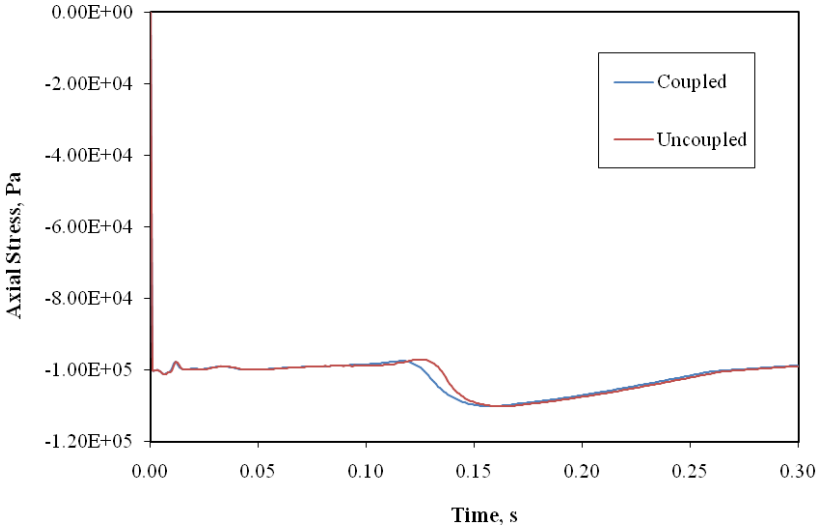

Figure 5.36 Coupled and uncoupled axial stress histories at point A.

Perhaps a more significant observation is the absence of the high frequency oscillatory stress signature which would be expected if any elastodynamic vibration was present. This suggests at least from the perspective of pressure loading, that the loading rates considered for the current case are not rapid enough to instigate stress waves at any point in the structure. The manner in which the perturbations in the initial period of the displacement magnitude and stress response

histories shown for points A and B dissipate rapidly during the course of the ignition event, suggests that these oscillations are not representative of general structural vibration either. This conclusion is based on the fact as that damping was not prescribed in the structural model, any inertial vibrations would be free to continue unless of course, a damping effect was generated by the flow. This possibility can be ruled out in the face of the minor discrepancy between the coupled and uncoupled solutions, however.

As far as the discrepancy between the coupled and uncoupled stress solutions at points A and B is concerned, the predicted differences are generally small. The most considerable discrepancy occurs for the circumferential stress response at point A, where the effect of coupling the solution domains has 'accelerated' the stress response. Similar effects were observed for the radial and axial stress traces at both points, although less distinct. In general, the discrepancy in the magnitude of the stresses predicted at the sample points by either solution is slight, although circumferential and axial stress responses at point A are an exception to this characteristic.

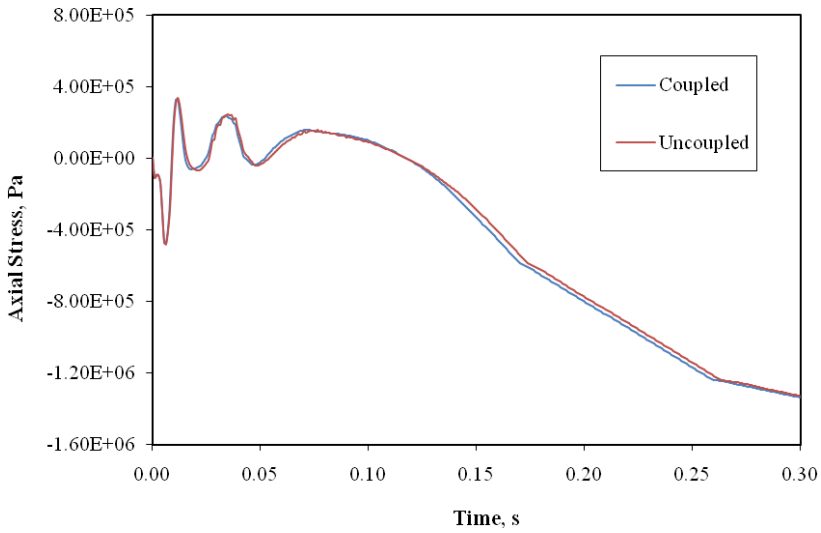

Figure 5.37 Coupled and uncoupled axial stress histories at point B.

To elaborate on the matter of the low levels of circumferential, radial and axial stress experienced by the exit cone, it should be borne in mind that during solid rocket motor operation, thermal loading generally contributes significantly more to the generation of stresses in SRM nozzles than pressure loading alone (Ellis (1975), Yoo et al (2003)). Had thermal

loading been considered in this work, it is anticipated that the levels stress in the heated substructures would have risen substantially, at least on a localised basis. The exact effect that thermal loading would have on the degree of coupling between the solution domains, if such loading had been accounted for, is however much more difficult to predict.

It is clear though, that coupling effects are most pronounced when structural deformations are considerable, and when such deformations occur at relatively high rates. Structural deformations attributable to thermal loading occur as a consequence of differential material expansion, but require the degree of heat penetration to be pronounced for any significant distortions to be induced. If one considers the brief thermal loading period that an SRM ignition transient represents, such a limited time period may not be sufficient to allow for significant thermal diffusion, and hence structural deformation, to take place.

In view of the severity of thermal loading in comparison to pressure loading however, the potential for thermally generated nozzle distortions during an SRM ignition process, particularly in the exit cone, cannot be overlooked and therefore requires further investigation.

5.6 Conclusion

The current chapter has described the numerical simulation of the structural response of the SRN2 nozzle to ignition period pressure loading derived from a transient combustion gas flow model. In addition, it has outlined an investigation into the degree of aeroelastic coupling occurring between the SRN2 nozzle and its associated exhaust gas flow field during the ignition event. The latter assessment was made on the basis of simulations involving the coupled and uncoupled fluid-structure interaction of the structural and flow models. Furthermore, the design of the SRN2 structure and the development of the constituent numerical models are detailed.

An overview of the modes of fluid-structure interaction that occur during the ignition period was provided, and displacement and stress response histories were presented for specified sample points within the nozzle. Observations indicate that for the particular conditions considered, the effects of aeroelastic coupling on the response of the nozzle were generally minor, and that for the current case, the uncoupled solution regime yielded a sufficient representation of the response. The results have demonstrated that pressure loading in isolation generates only

moderate stresses throughout the nozzle's four substructures. Significantly no evidence of stress wave instigation or general structural vibration was found, indicating the insignificance of the inertial terms in resolving the equations of motion in response to pressure loading alone.

Although the current simulation represented a significant technical advancement from that discussed in the previous chapter, limitations in the capacity of the ADINA System prevented the fluid-structure interaction facility from being used to transfer thermal loading data from the flow model to the structural model. As such, a technique had to be developed that would enable such data to be extracted and applied to the structural model, in order for associated thermoelastic effects to be accounted for in the structural response. The implementation of this technique, in addition to the results obtained for the full structural response will be discussed in the following chapter.

CHAPTER 6

Simulation of the Structural Response of a Composite SRM Nozzle to Transient Thermal and Pressure Loading

6.1 Introduction

As an advancement of the work described in Chapter 5, the current chapter outlines the modelling methodology developed to additionally incorporate the effects of thermoelasticity in the simulated ignition period response of Solid Rocket Nozzle 2. Details of the flow, thermal and structural models employed in the simulation are provided and a wide range of results relating to the ignition and burn period response of the structure are presented and discussed.

To overcome the inability of the ADINA-FSI program to thermally couple the flow and structural models, an additional solution path was developed which employed ADINA's conjugate heat transfer capability to relay transient temperature data from a dedicated flow model to an associated thermostructural model. As in the simulation described in Chapter 5, a set of flow and structural models was solved simultaneously to derive the response of the structure to pressure loading. The effective ignition period structural response of the nozzle was obtained by the superposition of the responses derived by each of these solution paths.

A comprehensive sensitivity study was conducted to determine the maximum allowable finite element size that could be used to discretize the highly localised zone of thermal penetration. The thermal solution flow and structural models were then constructed according to these discretization requirements, on the basis of the flow and structural models described in the previous chapter. An additional set of thermal and structural models was developed for the purposes of deriving the structural response of SRN2 during the motor burn period. The wall temperature and pressure loading conditions required for this simulation were obtained from a quasi-steady flow simulation.

The ignition period simulation results highlighted several important characteristics associated with the response of the SRN2 structure. These included determinations regarding the potential

for aeroelastic coupling, the evolution of stress distributions, the extremities of the stress response envelope and the inertial characteristics of the response. Comparisons were also made between the ignition and burn period structural simulation results to determine the significance of stresses induced during ignition in the context of stresses generated during the operation of the motor. Two additional ignition period structural simulations carried out in reference to temporally-scaled versions of the benchmark ignition transient, allowed the sensitivity of the nozzle's structural response to the motor ignition rate to be determined.

6.2 Analysis Parameters

6.2.1 Nozzle and Propellant Material Thermal Properties

To accommodate the thermoelasticity associated with the current problem, the collection of material properties employed in the previous simulation was extended to include the thermal properties reported in Yoo et al (2003) and used in the SRN1 simulation. For the sake of convenience, the relevant properties are shown again in Table 6.1 with respect to a cylindrical coordinate system, where k_θ, k_z, k_r, α_θ, α_z and α_r are the thermal conductivities and coefficients of thermal expansion in their associated directions, respectively, whilst C_p and ρ are the materials' specific heat capacity and density, respectively.

Property	**3D C-C**	**2D C-P**	**Steel**
$k_\theta = k_z$, W/mK	13.96	2.38	40.6
k_r, W/mK	13.96	0.38	40.6
$\alpha_\theta = \alpha_z$, x10^{-6} /˚C	4.76	-1.5	14.6
α_r, x10^{-6} /˚C	4.76	27	14.6
C_p, J/kgK	1153	1206	595
ρ, kg/m^3	1514	1329	7800

Table 6.1 Thermal properties of SRN2's constituent materials.

Owing to solution difficulties encountered when using the adiabatic wall condition to describe the propellant grain boundary in certain flow simulations, thermal properties were also assigned to represent the propellant. This designation was made on the approximate assumption that for the period of interest, the propellant grain would absorb heat from the exhaust gases and not actively combust. As heat transfer to such an inert propellant grain would be comparatively low during this phase, the thermal properties of the propellant would have a negligible effect on the adjacent flow stream and accurate definition of such properties is therefore not crucial.

Nonetheless, approximate thermal properties were derived for a hypothetical ammonium perchlorate (AP) / hydroxyl-terminated polybutadiene (HTPB) propellant for the purposes of the simulation. This oxidiser/fuel combination is commonly employed as a non-aluminised propellant. The effective thermal properties of the propellant (assumed to be homogeneous) were calculated on the basis of 75% AP to 25% HTPB mass ratio using general constituent thermal properties and the rule of mixtures. The resulting values for thermal conductivity, specific heat capacity and density are displayed in Table 6.2.

Property	**AP/HTPB Propellant**
k, W/mK	0.16
C_p, J/kgK	1500
ρ, kg/m^3	1730

Table 6.2 Thermal properties of the AP/HTPB propellant.

6.2.3 Scaled Ignition Transients

To assess the sensitivity of SRN2's structural response to the rate of SRM ignition, two additional ignition transients defining the the variation of pressure at the flow domain inlet, were considered. The additional transients are shown in relation to the original 0.6 s transient from which they were derived by temporal scaling in Figure 6.1.

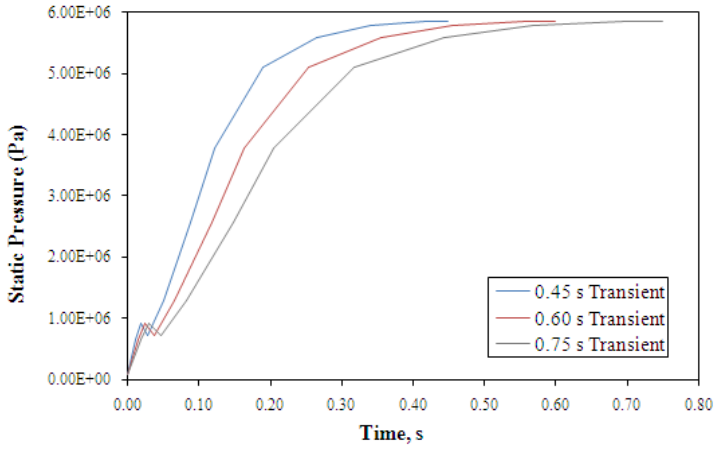

Figure 6.1 Scaled pressure transients.

The duration of the first scaled transient was reduced by 25%, whilst the duration of the second was increased by 25%, yielding transients 0.45 s and 0.75 s in length, respectively. Correspondingly, additional transients defining the variation of temperature at the flow domain inlet were generated in an identical manner. Figure 6.2 shows the additional temperature transients in relation to the temperature transient considered previously.

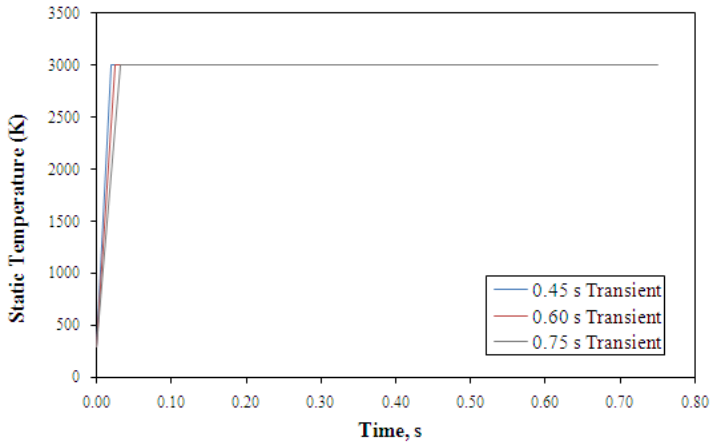

Figure 6.2 Scaled temperature transients.

6.2.4 Ignition Period Modelling Approach

The ADINA fluid-structure interaction facility could not be employed to relay a transient temperature boundary condition primarily as a result of the fact that when compressible flow is being considered, interaction can only be simulated with respect to force and not heat flux. To counter this significant limitation, an indirect ignition period modeling approach was developed to allow the combined effects of thermal and pressure loading to be accounted for. As illustrated in Figure 6.3, this indirect approach utilised two simulation paths, designated T (thermal) and P (pressure), to compute the response of SRN2 to thermal and pressure loading in isolation. Each path comprised a flow model, to generate the associated loading condition, and a structural model, to which the loading condition was then applied to derive the required response.

To generate the thermal stress response, Flow Model T was solved as a conjugate heat transfer (CHT) problem to establish the transient temperature distribution in the nozzle, which was in turn mapped to Structural Model T where the thermostructural problem could be solved.

Structural Model T was solved in respect of both the static and dynamic equations of motion, in order for the inertial nature of the thermal loading problem to be assessed.

To generate the pressure stress response, Flow Model P was solved to determine the pressure distribution along the nozzle's wetted surface, which was subsequently mapped to Structural Model P at each solution time step using the FSI facility in uncoupled mode to allow the structural response to be established. As it had already been established that the pressure stress response associated with this problem displayed negligible vibratory characteristics, the solution of Structural Model P was derived using a quasi-static simplification.

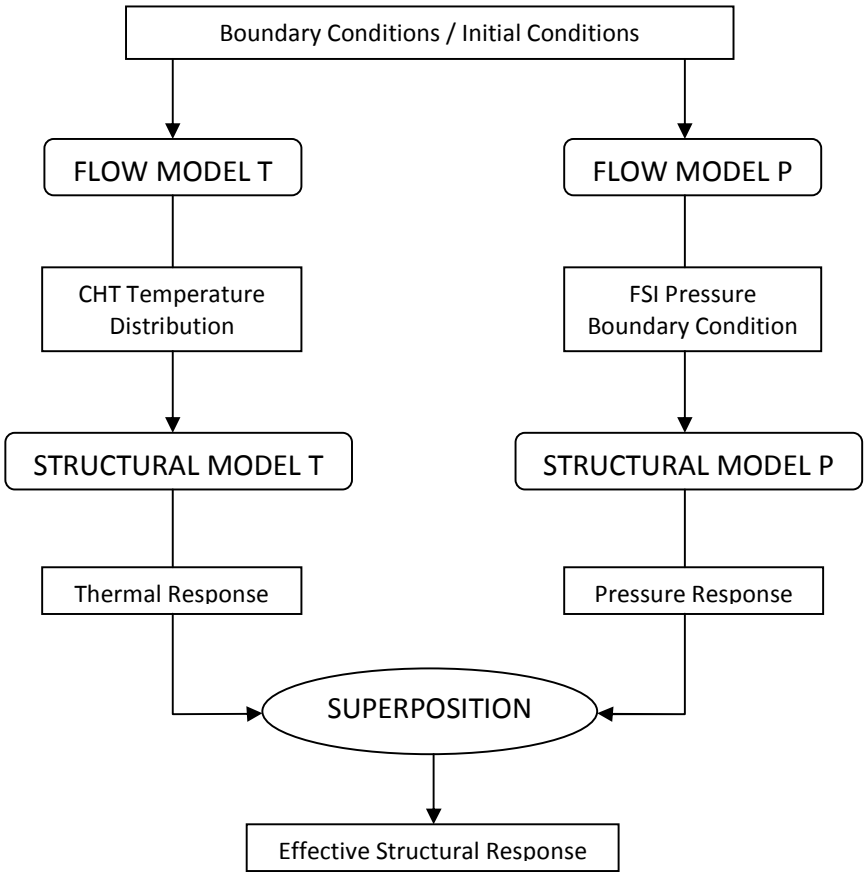

Figure 6.3 Ignition period modelling approach.

Finally, to calculate the combined effective response, results generated by either structural model were superimposed at each increment in time. It should be noted, of course, that the application of such a straightforward augmentation approach prevents the SRN2 structure from influencing the overall flow through the nozzle in response to thermal loading. That is, Flow Model T and Structural Model T are uncoupled.

6.2.5 Burn Period Modelling Approach

To simulate the response of SRN2 to pressure and thermal loading during the burn period, the modelling approach employed was similar to that used in the simulation described in Chapter 4. To derive the transient temperature distribution in SRN2 during a 60 s burn period, a thermal model was constructed and subjected to a steady temperature boundary condition along the nozzle's wetted surface. This temperature distribution was then mapped to an associated structural model, which in turn was subjected to steady pressure loading. By simultaneously accounting for thermal and pressure loading in this manner, the structural model was able to calculate the effective burn period structural response of the nozzle.

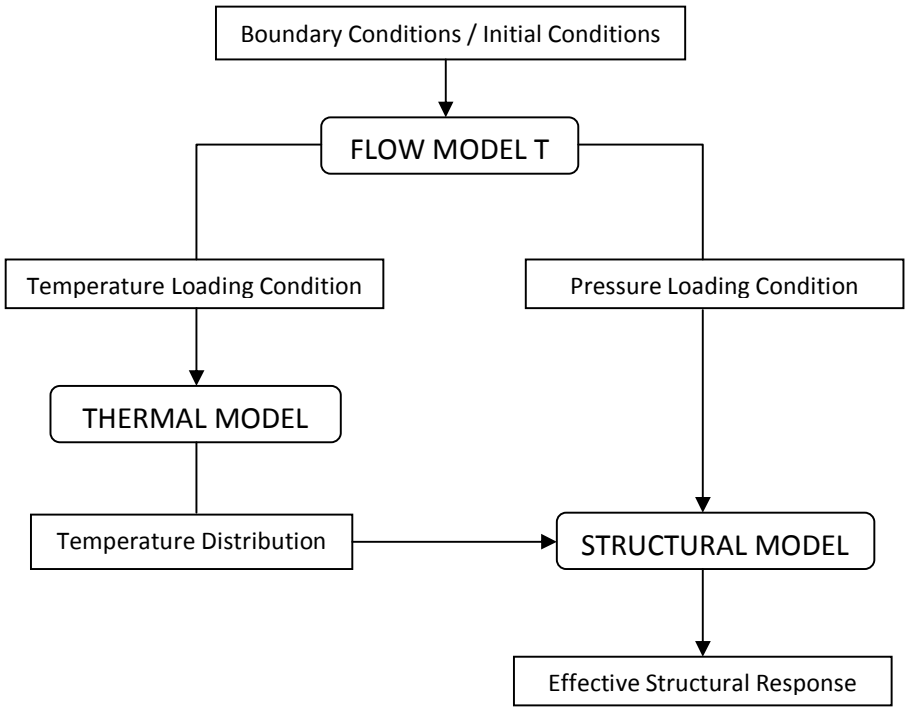

Figure 6.4 Burn period modelling approach.

In the current case however, the required nozzle wall temperature and pressure distributions were calculated using Flow Model T. Temperatures and pressures were recorded at specific points in the Flow Model T results file, and spatial functions were then used to prescribe the variation of the two parameters along the wetted surfaces of the thermal and structural models. The overall modelling approach is outlined in Figure 6.4.

6.3 Thermal Penetration Zone Element Sizing

The phenomenon that was of most particular interest in the current simulation was the effect that rapid heating of SRN2's wall would have on its structural response. Naturally, it was desired that this phenomenon be simulated with as much accuracy as the available computing capacity would allow. In view of the high thermal loading magnitudes and rates associated with the transient convective heating of the nozzle, it became clear that thermal and structural mesh densities much higher than had previously been used would have to be employed to describe the thermal penetration zone (TPZ). A critical exercise therefore, was to determine the maximum dimensions of the thermal and structural elements that could be applied in this zone to describe it with acceptable accuracy. By doing so, the computational size of the problem could be minimised.

The depth of heat penetration would vary considerably along the wetted surface of the SRN2 nozzle as a consequence of differential heating rates and magnitudes. In theory therefore, the optimum distribution of TPZ elements would have been based on an assessment of heat penetration at numerous locations along the nozzle wall. To avoid such an involved undertaking, it was decided to base element sizing calculations on the maximum depth of heat penetration likely to be encountered in the nozzle during a 0.3 s simulation interval. Even if this conservative approach reduced the solution efficiency, it ensured that the TPZ would be adequately discretized.

To estimate the maximum depth of heat penetration, the governing differential equation for unsteady one-dimensional heat conduction in a semi-infinite slab was considered:

$$\frac{\partial T}{\partial t} = \alpha \frac{\partial^2 T}{\partial x^2} \tag{6.1}$$

Here T is the temperature in the medium at a given position in the direction of the x dimension and at a time t, and α is the thermal diffusivity of the medium. Although strictly speaking, heat conduction within rotational structures occurs with respect to the cylindrical form of Equation 6.1, as the anticipated depth of thermal penetration was significantly smaller in dimension than the diameter at which it would occur, the application of Cartesian coordinates was deemed an acceptable approximation.

It can be shown analytically that the penetration depth, γ, which defines the distance at which the local temperature is just 0.1% above the slab's ambient temperature at a time t may be solved as

$$\gamma = 4\sqrt{\alpha t} \tag{6.2}$$

Despite being independent of the magnitude of the applied thermal loading, the solution provided by Equation 6.2 predicts the thermal penetration depth in response to the instantaneous application of such loading. In relation to this condition, Figure 6.5 shows temperature histories at various points along the SRN2 wall which were derived from the flow model considered in the previous chapter. As can be seen, although at some positions there is a rapid rise in temperature, the rate of this increase is clearly not instantaneous. The specification of the instantaneous loading condition would therefore predict a slightly greater depth of penetration than would be encountered in reality, leading to a more conservative estimation.

Using the diffusivity of the 3D C-C material in the radial direction, calculated as 8.00×10^{-6} m^2/s, and for a total simulation time period of 0.3 s, the penetration depth was calculated to be 6.2 mm from the heated surface. To account for any two-dimensional conduction occurring adjacent to contours with sharp radii or corners, the TPZ element band was specified in Flow Model T and Structural Model T to be 8 mm deep.

The next parameters that needed be resolved were the dimensions of the models' TPZ elements in the directions normal and parallel to the heated surface. As the highest thermal gradient would exist in the normal direction, element sizing in this direction was of particular importance. A sensitivity study was therefore undertaken to determine the effect of element size on the transient

thermoelastic response of an internally heated cylinder using the ADINA-T and ADINA modules. In doing so, the optimal dimensions for the TPZ elements in Flow Model T and Structural Model T could be estimated.

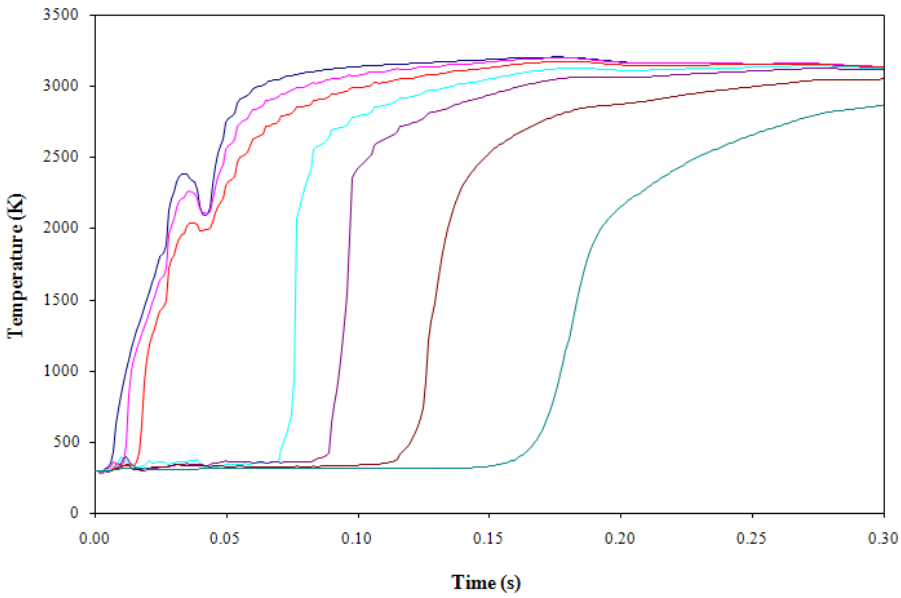

Figure 6.5 SRN2 wall temperature histories at points of interest.

As the transient thermal gradients to be encountered in the TPZ were directly proportional to the rate at which the temperature on the nozzle surface would rise, the loading condition applied in the sensitivity study was derived on the basis of the most severe temperature evolution encountered in the results shown in Figure 6.5. This was indicated to occur at a point on the exit cone positioned roughly one quarter down its length and the temperature history at this point is shown in Figure 6.6.

The transient loading condition for the sensitivity study was approximated as a ramp function based upon the parameters dT, representing the change in temperature, and dt, representing the time over which this change occurs, shown in Figure 6.6. These parameters were measured to be 2212 K and 0.014 s, respectively. It should be noted that the flow model from which this data was extracted treated the nozzle wall as an adiabatic boundary, which would inevitably lead

to an overestimation of temperature magnitudes at the wall, and in the case of this study, a conservative estimation of thermal penetration.

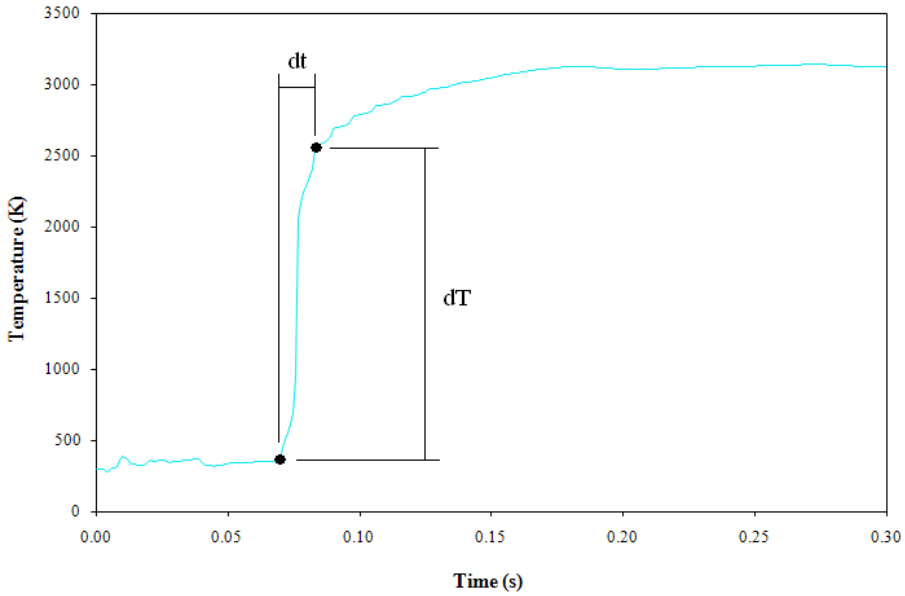

Figure 6.6 Temperature history at point of maximum thermal loading rate.

The base level element size in the radial direction was calculated as the 99.9% thermal penetration depth in the cylinder subjected to the instantaneous application of 2212 K to its inner surface after a period of 0.014 s. In this manner, the maximum element dimension in the radial direction, $\Delta r_{\max}$, was established to be 1.33 mm. For higher mesh densities, the particular radial dimension, Δr, was governed by a resolution factor, N, such that

$$\Delta r = \frac{\Delta r_{\max}}{N} \tag{6.3}$$

The particular axial dimension of the thermal element was governed by a specified aspect ratio of 5. The test cylinder was 100m in length, and had an internal diameter of 450 mm and a wall thickness of 12 mm – the latter two dimensions being equivalent to the dimensions at the point of interest on the exit cone. Linear interpolating 4-noded axisymmetric conduction elements were used to discretize the thermal model to avoid errors typically generated by the quadratic interpolation associated with the 9-noded conduction elements, when subjected to high thermal

gradients. To establish the sensitivity of the response of the test cylinder, thermal and structural simulations were carried out for resolution factors of 1, 2, 3 & 4. Results for the predicted temperature and hoop stress distributions within the first 8 mm of the heated boundary are shown at three instances in time in Figures 6.7-6.12.

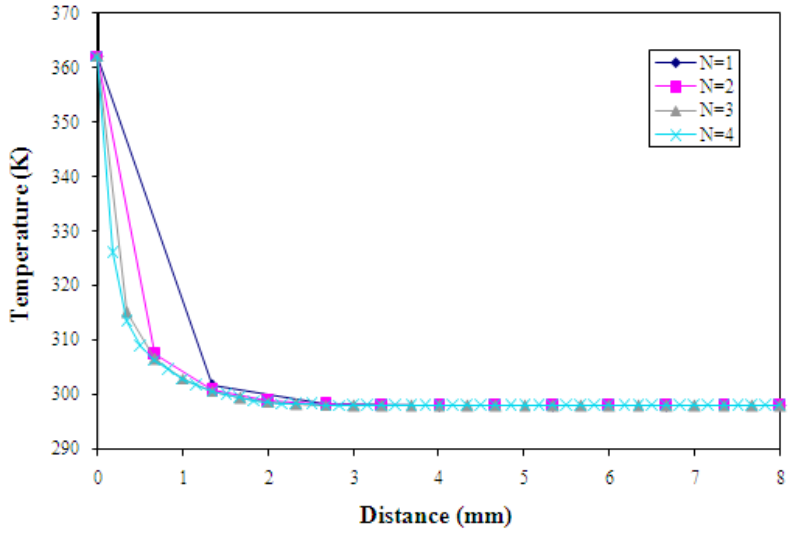

Figure 6.7 Test cylinder temperature profile at 0.07 s.

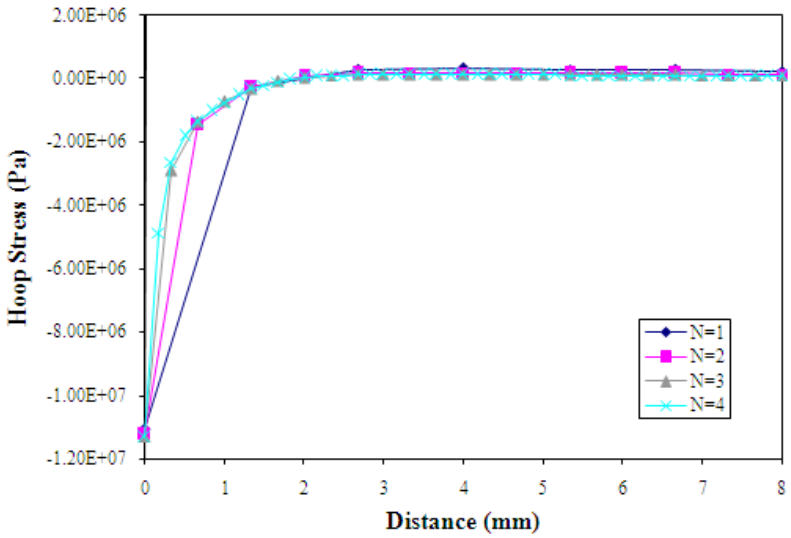

Figure 6.8 Test cylinder hoop stress profile at 0.07 s.

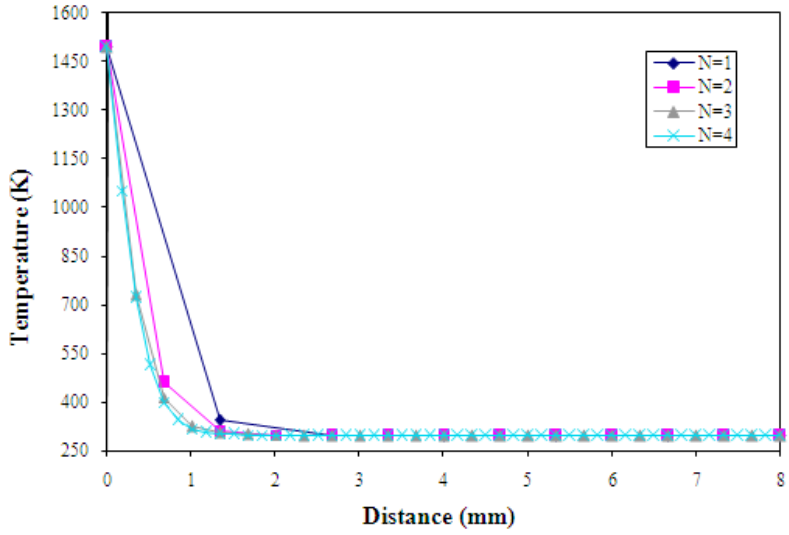

Figure 6.9 Test cylinder temperature profile at 0.083 s.

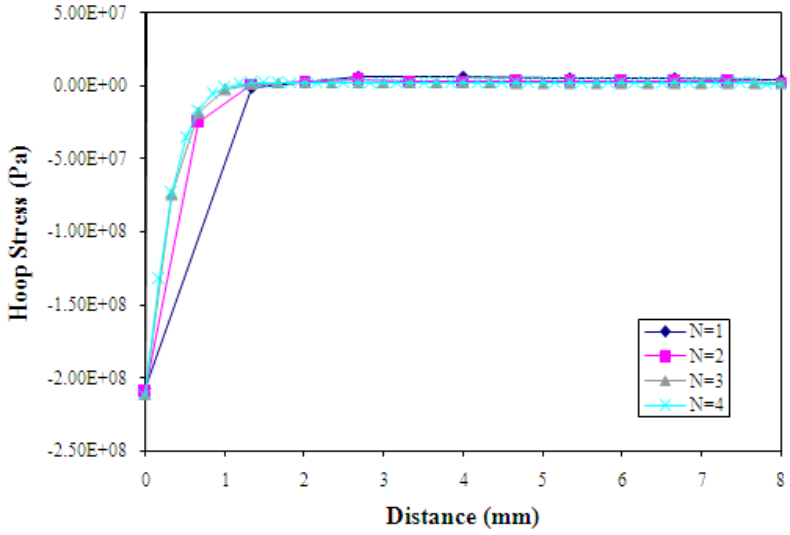

Figure 6.10 Test cylinder hoop stress profile at 0.083 s.

As expected, the mesh characterised by a resolution factor of 4 provides the smoothest and most representative thermal and hoop stress distributions at each time, especially whilst loading is still in progression at t = 0.07 s. The coarser discritizations stipulated by the lower resolution factors of 1 & 2 induce a slight overestimation of the penetration depth as demonstrated by Figure 6.9, resulting in the generation of slightly higher tensile hoop stresses in the cool region of the

cylinder. By a time of 0.3 s however, the temperature and hoop stress profiles predicted by all four mesh densities are shown to be in good agreement. It is also interesting to note the small variation in the maximum compressive hoop stress predicted to occur at the heated surface by each mesh. Clearly however, the most accurate representation of the transient thermal penetration and stress generation is provided by a mesh resolution factor of 4.

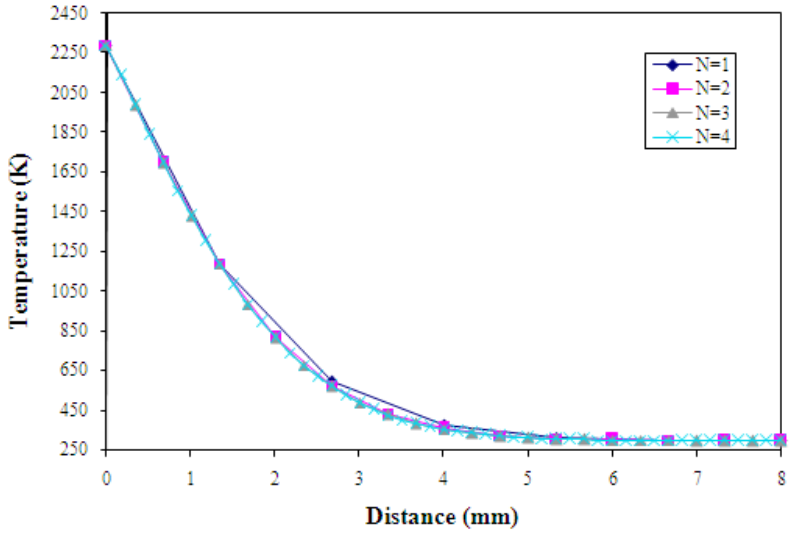

Figure 6.11 Test cylinder temperature profile at 0.3 s.

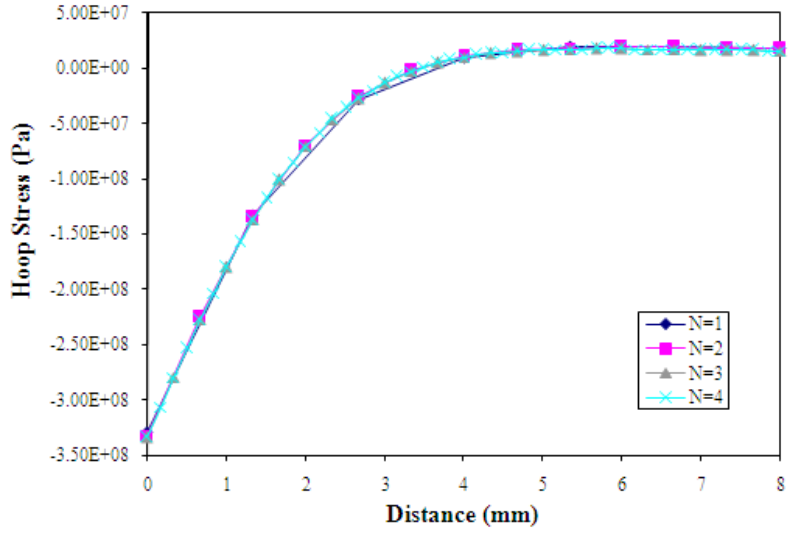

Figure 6.12 Test cylinder hoop stress profile at 0.3 s.

Of course, the accuracy of any numerical solution is generally related to its discretization resolution and hence computational size. In this respect, the time taken to compute solutions to the thermal and structural problems for the range of resolution factors were investigated to evaluate the cost of each solution in relation to its accuracy. The results of this assessment are displayed in Figure 6.13 and demonstrate the dramatic increase in the computational time required for an increase in resolution factor. A significant difference in the thermal and structural solution times that manifests with an increase in resolution factor can also be observed.

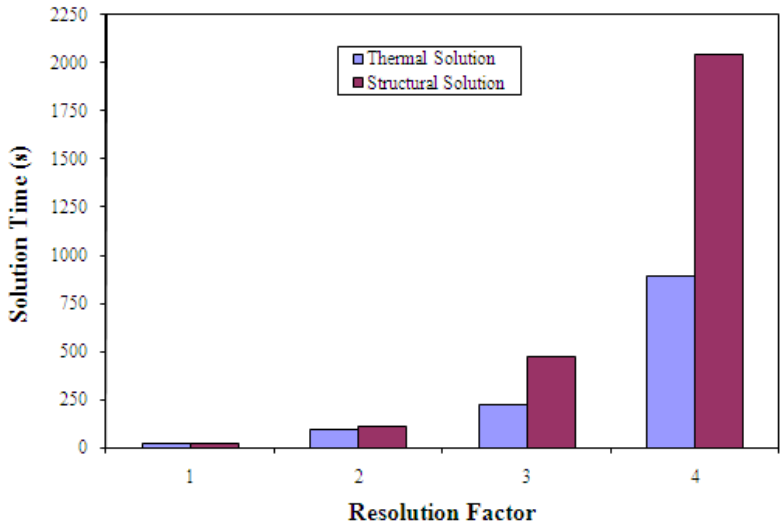

Figure 6.13 Variation of solution times with resolution factor.

It is useful to consider the results reflected in Figure 6.13 in the context of the relative solution error existing between hoop stress predictions using a resolution factor of 4, and those computed for factors of 1, 2 & 3. Figure 6.14 shows a comparison in hoop stresses predicted at the inner, heated surface of the cylinder, whilst Figure 6.15 makes this comparison at the outer, cool surface of the cylinder, for the three solution times.

These results demonstrate the decrease in relative error with respect to an increase in solution time and an increase in resolution factor. Interestingly, the decrease in the rate at which error decreases with resolution factor suggests that mesh independence in the solution is nearing. Figure 6.15 also illustrates the significant hoop stress error at the cold surface, generated by the artificially deep thermal penetration zone arising from coarse discretization, particularly for

earlier solution times. Although very large discrepancies are shown to exist for the resolution factor 4 solution, the low magnitude of the predicted stresses mitigated concern in this regard. More significantly however, the relative error in the maximum stresses predicted at the hot surface is shown to be small, even for a resolution factor of 1 and at the earliest solution time.

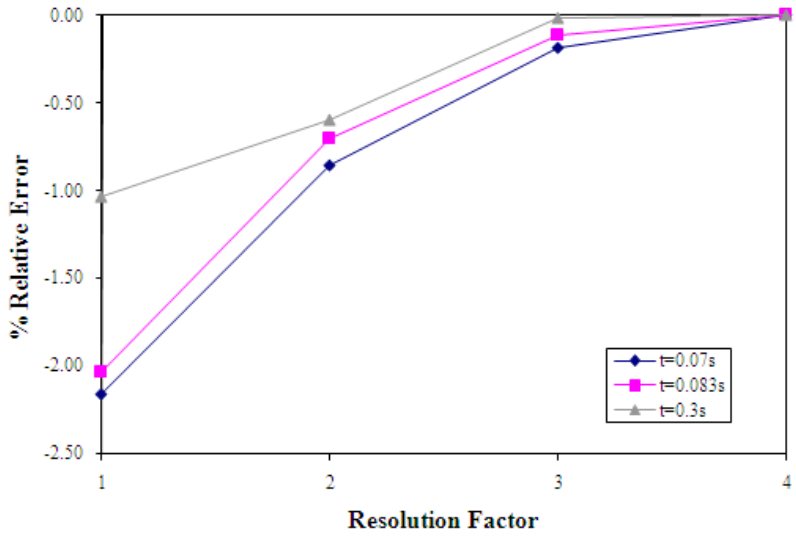

Figure 6.14 Relative hoop stress error at hot surface.

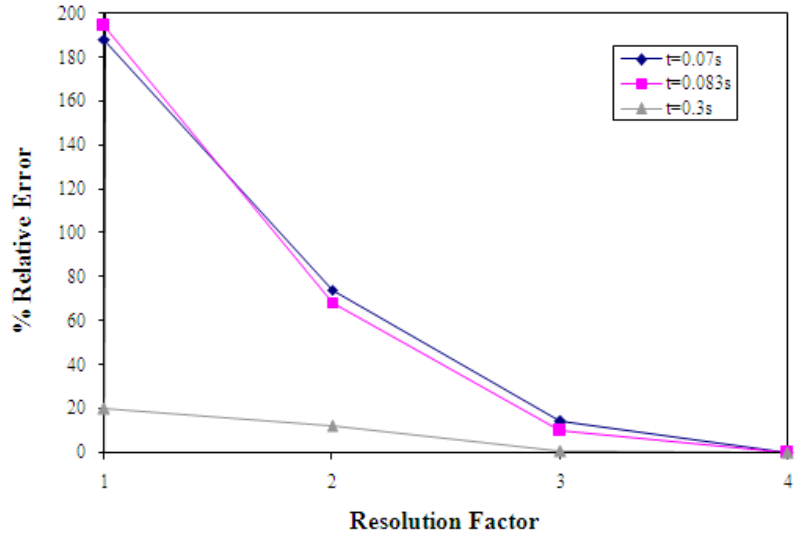

Figure 6.15 Relative hoop stress error at cold surface.

Three issues were considered in determining the most suitable TPZ element size. These comprised the cost of employing each mesh resolution factor in relation to the accuracy of the resulting solution, the restrictions that the TPZ element size placed on discretization in the flow models, and the capacity of the computational resources available for use. After careful consideration of these issues, a resolution factor of 3 was selected to scale the discretization of the TPZ bands in Flow Model T and Structural Model T.

6.4 Flow Modelling

6.4.1 Flow Model T

Flow Model T was effectively developed as an extension of the flow model considered in Chapter 5. It was constructed using the same approach and to identical flow domain dimensions as its predecessor, and employed the same combustion gas properties and initial conditions. It differed considerably however, in its inclusion of 'solid' elements to determine the unsteady temperature distribution in SRN2's thermal penetration zone and to represent the non-adiabatic propellant grain boundary.

As shown in Figure 6.16 and described by Table 6.3, six specific boundary conditions denoted as BC1, BC2, BC3, BC4, BC5 and BC6, were used to describe the periphery of the flow domain. The subsonic inlet, symmetry and outlet control boundaries indicated by BC4, BC5 and BC6 are identical to those used in the previous model, whist BC1, BC2 and BC3 denote the non-slip, non-adiabatic boundaries of the solid element groups representing the exit cone, ITE, insulator and propellant grain, respectively.

Insofar as the solid element groups are concerned, the conjugate heat transfer simulation facility of the ADINA-F program is unable to model the conduction of heat in a thermally orthotropic medium. As such, the 3D carbon-carbon and 2D carbon-phenolic composite materials constituting the exit cone, ITE and insulator had to be approximated as isotropic in their thermal conduction. Although clearly not ideal, it was felt that this simplification wouldn't induce excessive error as a consequence of the very shallow thermal penetration anticipated in the structure, particularly in the insulating 2D C-P material. Furthermore, the conductivities of the 3D C-C material are identical in the radial and axial directions, limiting error further. In light of this equivalence in directional thermal conductivities, the thermal conductivity of the material defining the 3D C-C solid element group was specified as 13.96 W/mK. For the 2D C-P solid

element group, the axial thermal conductivity of 2.38 W/mK was specified on the basis that it would allow for greater thermal penetration.

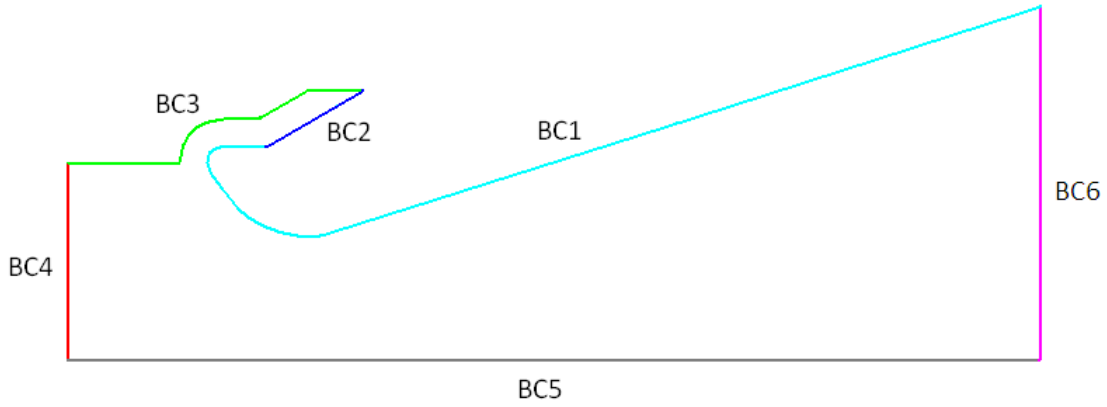

Figure 6.16 Location of Flow Model T boundary conditions.

Boundary Condition	Type	Associated Conditions/Values
BC1	Solid Element Group: C-C	No Slip, Non-Adiabatic
BC2	Solid Element Group: C-P	No Slip, Non-Adiabatic
BC3	Solid Element Group: Propellant	No Slip, Non-Adiabatic
BC4	Subsonic Inlet	P(t), T(t)
BC5	Symmetry	-
BC6	Outlet Control	$P=P_{atm}$

Table 6.3 Flow Model T boundary condition parameters.

With respect to Flow Model T's finite element mesh, the mesh density in the solid domain representing the thermal penetration zone was effectively governed by the results of the element size sensitivity study. As a conjugate heat transfer simulation in ADINA-F requires that the nodes of the solid and fluid domains are coincident, this discretization determined the subdivision sizing on the flow side of the interface as well. This condition inevitably contributed to a high mesh density in the general flow domain, significantly higher than that of the previous flow model.

Although considerably more expensive in a computational sense, this finer discretization also promoted improved shock definition and a better resolution of the boundary layer. In total, Flow

Model T employed a collection of 158 068 three-noded axisymmetric solid and fluid elements. The combined solid and flow domain finite element mesh is displayed in Figure 6.17, whilst a detailed view of the discretization applied at the entrance and throat region is provided by Figure 6.18. The latter figure clearly indicates the position of the TPZ element band in the ITE, insulator and propellant grain.

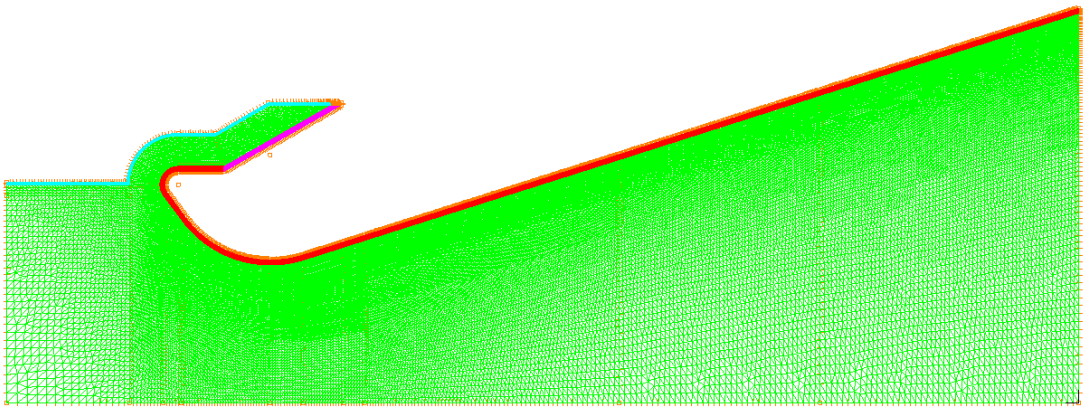

Figure 6.17 Flow Model T finite element mesh.

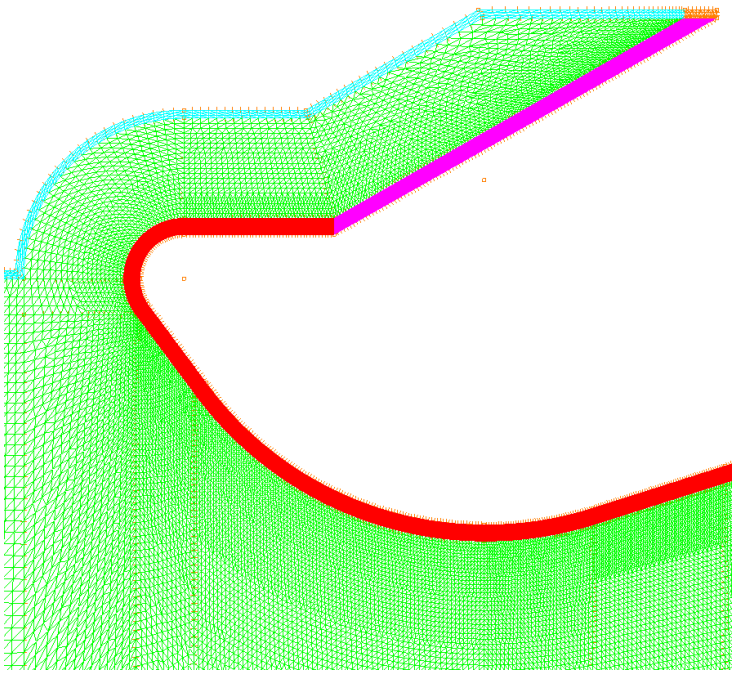

Figure 6.18 Mesh detail at the entrance and throat region.

Four separate simulations were undertaken using Flow Model T; a simulation for each of the three transients and a quasi-steady simulation to generate thermal and pressure loading data for the burn period thermal and structural models. This latter simulation was termed quasi-steady as it provided a representation of the steady flow field 1 s after ignition by means of a transient solution, as opposed to a time invariant solution. If a steady solution had been sought, the temperature loading condition obtained at the nozzle wall would have been unrealistically high, as the domain could not be bounded externally by a convection boundary and did not represent the entire nozzle structure. As such, it was desired to obtain wall temperature and pressure distributions a fair time after the flow domain inlet conditions had reached nominal values, but before the rate of heat transfer was slowed significantly by thermal saturation of the solid domain. Furthermore, owing to the extremely large memory requirements of the Flow Model T results file for the 0.3 s simulations, a solution of greater than a few seconds would have become unmanageable and was ruled out. In respect of these concerns, a simulation time of 1 s was selected as a reasonable compromise. The details of the time step configuration used for each simulation are shown in Table 6.4.

Model	**Solution Period**	**Transient**	**Time Step Configuration**
Flow Model T	0.3 s	0.6 s	3000 x 1e-4 s
		0.45 s	1500 x 1e-4 s
			+ 50 x 5e-5 s
			+ 125 x 1e-3 s
		0.75 s	1500 x 1e-4 s
			+ 50 x 5e-5 s
			+ 125 x 1e-3 s
Flow Model T (Quasi-steady)	1 s	0.6 s	1650 x 1e-4 s
			+ 30 x 5e-5 s
			+ 820 x 1e-3 s

Table 6.4 Flow model time step configurations.

6.4.2 Flow Model P

Flow Model P differed from the original flow model described in Chapter 5 only in respect of its finite element mesh, shown in Figure 6.19, which featured a finite element scheme identical to that Flow Model T for the sake of consistency. The same flow domain geometry, combustion gas properties and initial and boundary conditions were however employed. Along the SRN2

wall, a fluid-structure interaction boundary was once again specified to generate an interface with Structural Model P for an uncoupled FSI simulation between the two models.

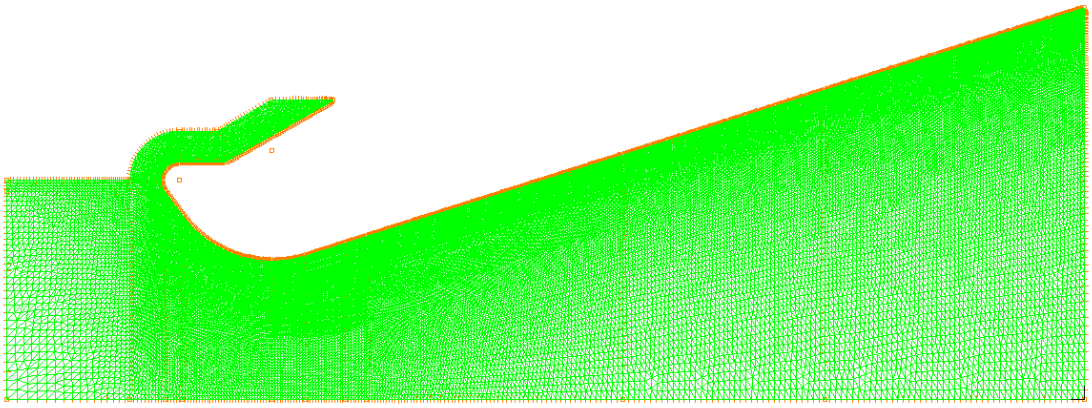

Figure 6.19 Flow Model P finite element mesh.

In light of the strong similarities between Flow Model T and Flow Model P, the same time step configurations applied in each of the three Flow Model T ignition period simulations were used for the associated Flow Model P simulations, as indicated in Table 6.5.

Model	Solution Period	Transient	Time Step Configuration
Flow Model P	0.3 s	0.6 s	3000 x 1e-4 s
		0.45 s	1500 x 1e-4 s
			+ 50 x 5e-5 s
			+ 125 x 1e-3 s
		0.75 s	1500 x 1e-4 s
			+ 50 x 5e-5 s
			+ 125 x 1e-3 s

Table 6.5 Flow Model P time step configurations.

6.5 Thermal Modelling

6.5.1 Burn Period Thermal Model

The Burn Period Thermal Model was developed to simulate the evolving thermal field in the SRN2 structure during a 60 s motor operation scenario. It was constructed in the ADINA-T

module using the same two-dimensional surface geometry employed for the structural model considered in the previous chapter.

The model's instantaneously applied temperature loading condition was obtained from the 1 s Flow Model T simulation. Temperatures were recorded at eleven points along the nozzle wall to generate a temperature distribution that was applied to the model using ten linear spatial functions. The position of each spatial function start and end points is indicated in Figure 6.20, with the temperatures specified at each point detailed in Table 6.6.

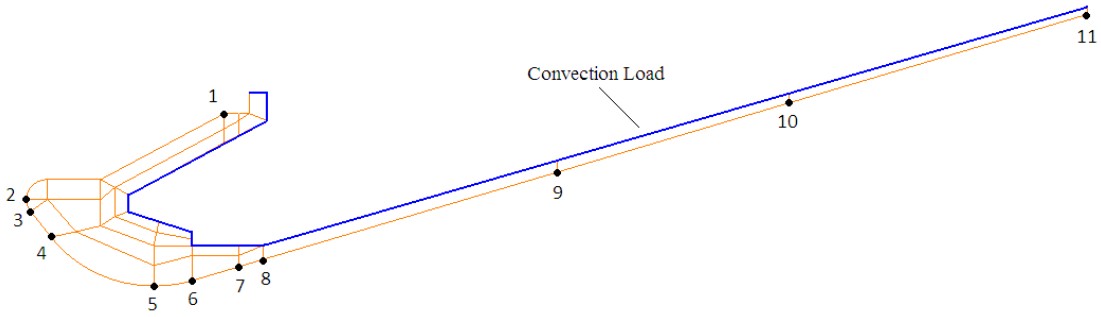

Figure 6.20 Burn period loading specification points.

Geometry Point	Prescribed Temperature (K)
1	1832
2	1832
3	2020
4	2113
5	2819
6	2674
7	2517
8	2434
9	1457
10	1017
11	655

Table 6.6 Prescribed temperatures at geometry points.

It should be noted that the temperature applied at point 1 was artificially prescribed to be the same temperature at the nozzle's leading edge point, point 2. The reason for this imposition is to cater for the local heating effect that would arise from combustion at the adjacent surfaces of the

propellant grain, which could not be accommodated for in the 1 s simulation. To account for convection heat transfer from the nozzle to the external atmosphere, a convection load was applied to the external surfaces of the model in reference to an ambient temperature of 298 K and a constant heat transfer coefficient of 0.15 m^{-1}. The location of this load is highlighted in Figure 6.20.

As far as material specification in the Burn Period Thermal Model is concerned, three material models were generated according to the data included in Table 6.1, to define the 3D C-C, 2D C-P and steel constituents. Following this, three conduction element groups and one convection element group were created in preparation for meshing of the geometry.

Discretization was governed by the same geometry subdivision scheme used in the structural model described in Chapter 5. In consideration of the long duration of the simulation, the moderate mesh density prescribed by this scheme was deemed to be acceptable. The mesh was generated using a combination of four-noded axisymmetric conduction elements and three-noded boundary convection elements. Four-noded elements were used to represent thermal conduction to avoid the mid-element temperature error induced during rapid thermal loading by quadratic temperature interpolation in more elaborate elements.

The architecture of the Burn Period Thermal Model finite element mesh is presented in Figure 6.21. Finally, as far as temporal discretization is concerned, the 60 s transient temperature solution comprised 600 time steps, each 0.1 s in length.

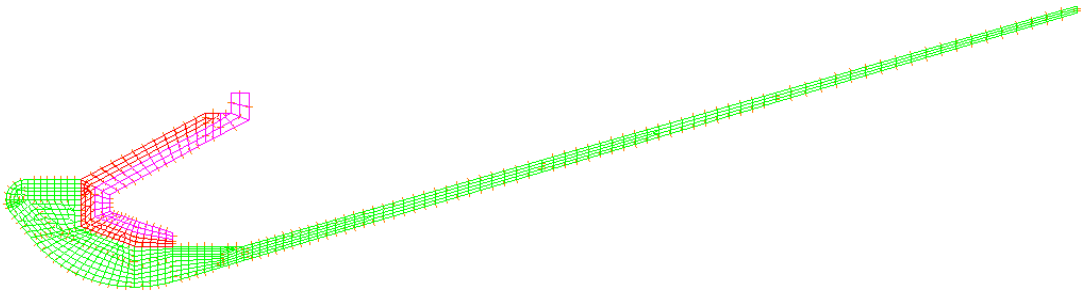

Figure 6.21 Finite element mesh of the Burn Period Thermal Model.

6.6 Structural Modelling

6.6.1 Structural Model T

Structural Model T employed the same thermo-orthotropic/isotropic materials, element groups and full fixity constraint as the previous SRN2 structural model, but did not possess an FSI boundary condition through which pressure loading could be applied. Furthermore, it utilised a significantly denser mesh scheme designed to accommodate the band of thermal penetration zone elements.

The mesh was composed of 37 996 four-noded axisymmetric solid elements, the predominant number of which were employed to discretize the TPZ band. Four-noded elements had to be employed instead of the more efficient nine-noded elements, to enable node-to-node reading of the thermal mapping file used to describe the temperature distribution in the nozzle and that was generated by Flow Model T. The overall mesh configuration is shown in Figure 6.22, whilst a detailed view of the mesh at the entrance and throat region, clearly indicating the location of TPZ elements is shown in Figure 6.23. To demonstrate the significant difference in the mesh density applied in the TPZ band in comparison to the rest of the model, Figure 6.24 displays the mesh employed adjacent to SRN2's throat.

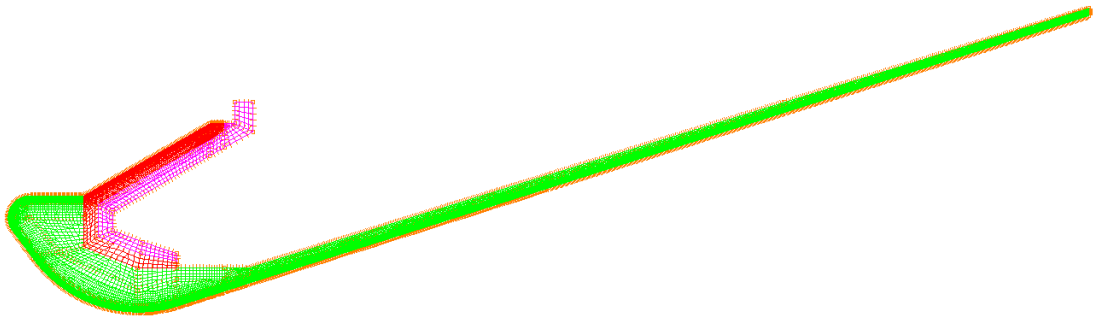

Figure 6.22 Structural Model T finite element mesh.

As it had yet to be determined whether or not the thermal loading condition simulated by Flow Model T would induce a vibratory structural response in SRN2, Structural Model T was solved dynamically. For the sake of uniformity, the time step configurations applied in all Flow Model T simulations were employed in the associated Structural Model T simulations.

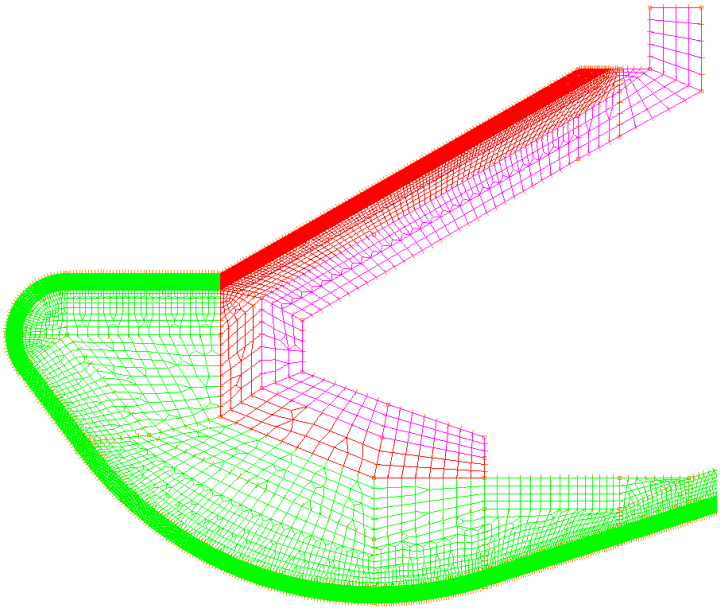

Figure 6.23 Mesh detail at the entrance and throat region.

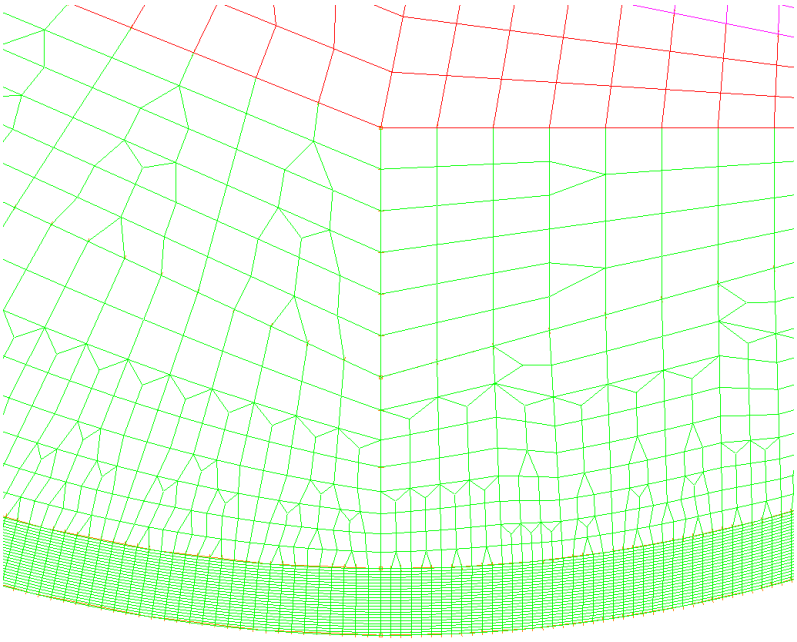

Figure 6.24 Comparative element sizing at SRN2's throat.

6.6.2 Structural Model P

As a consequence of the satisfactory performance of the first SRN2 structural model described in Chapter 5, Structural Model P was a copy of this model in every respect. However, as it had been demonstrated that no inertial effects manifested in the response of this model to pressure loading alone, the fluid-structure interaction solution incorporating Structural Model P employed a less costly static solution regime.

6.6.3 Burn Period Structural Model

The Burn Period Structural Model featured the same materials, element groups, full fixity constraint and finite element mesh as Structural Model P. However, to describe pressure loading, the constant pressure distribution derived from the 1 s Flow Model T simulation was applied, instead of using Structural Model P's FSI boundary condition.

The pressure distribution was defined in reference to the same eleven geometry points used to define the temperature distribution in the Burn Period Thermal Model, shown in Figure 6.20, and was applied in an identical manner on the basis of ten spatial functions. The pressure magnitudes prescribed at each point are quantified in Table 6.7.

Geometry Point	Prescribed Pressure (Pa)
1	5.663e6
2	5.663e6
3	5.658e6
4	5.598e6
5	2.945e6
6	1.714e6
7	1.408e6
8	1.270e6
9	3.907e5
10	1.989e5
11	1.032e5

Table 6.7 Prescribed pressures at geometry points.

In terms of solution parameters, the problem was resolved using a static solution regime over 600 time steps, each 0.1 s in length.

6.6.4 Results Sampling

The results of the thermal penetration zone element size sensitivity study provided a clear indication that thermally-induced stresses far more severe than those attributable to pressure loading could be expected in regions adjacent to the heated walls of SRN2. Furthermore, they indicated that the highest thermal stresses would be encountered at positions on the wall itself. In consideration of these indications, it was apparent that the most suitable locations at which to record response histories would be at points positioned along the wetted surface of the nozzle. Five points were therefore selected for this purpose on the basis of the insight it was believed they would be able offer into the response characteristics of the nozzle. Labelled A, B, C, D and E, their locations are illustrated in Figure 6.25. Also shown in this figure is the cross-section denoted Y-Y, along which distributions of thermal and pressure stresses were to be compared.

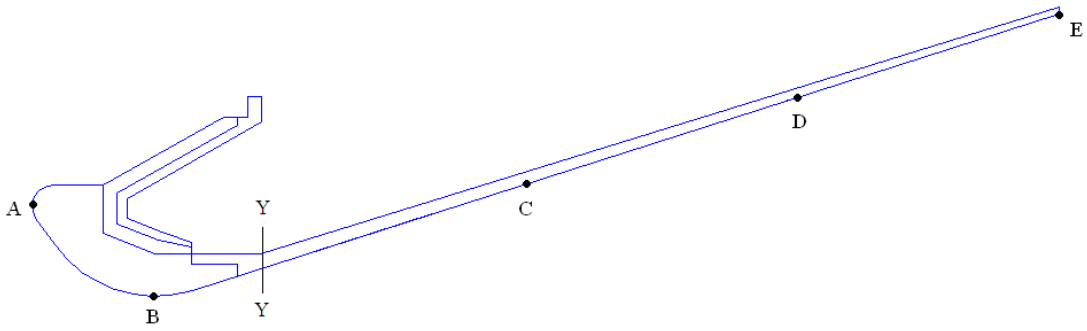

Figure 6.25 Position of sampling points A, B, C, D & E and cross-section Y-Y.

6.7 Results and Discussion

6.7.1 Flow Model T Flow Field Assessment

Band plots representing Mach number, pressure and density distributions in the flow field obtained from the 0.6 s transient simulation at times of 0.005 s, 0.02 s and 0.3 s are shown in Figures 6.26-6.28, respectively.

A comparison of these results to those reflected in the previous chapter for equivalent solution times in Figures 5.19-5.21, indicates that the refinement of the Flow Model T mesh has led to a slightly altered evolution in the predicted flow field.

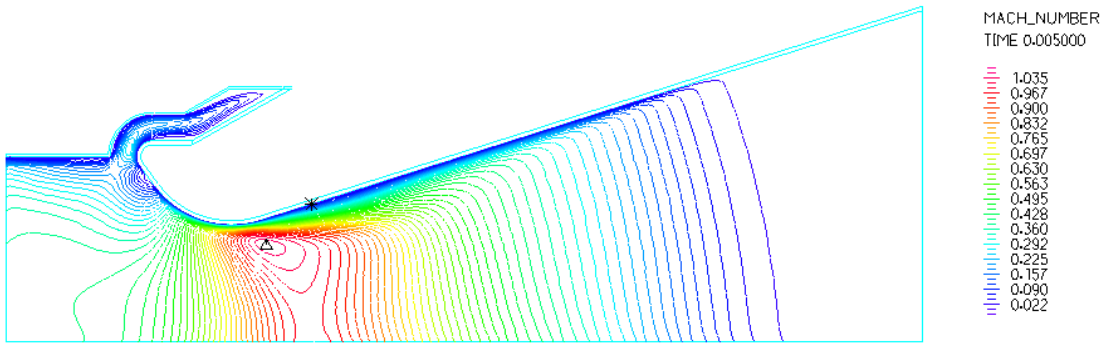

(a)

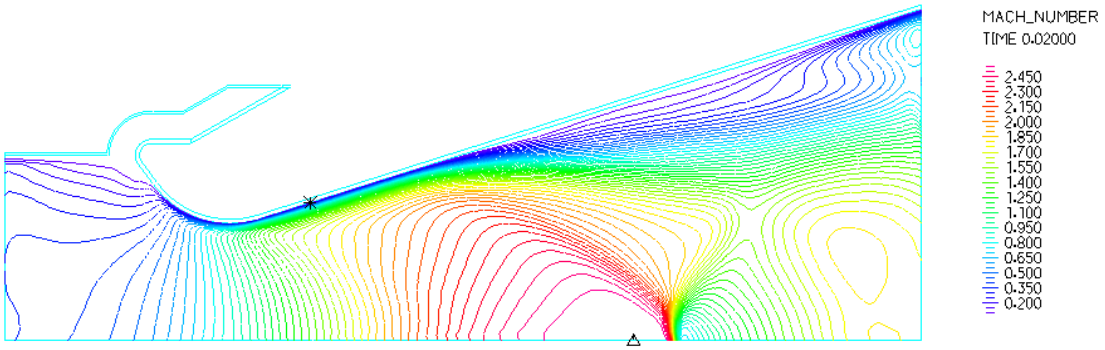

(b)

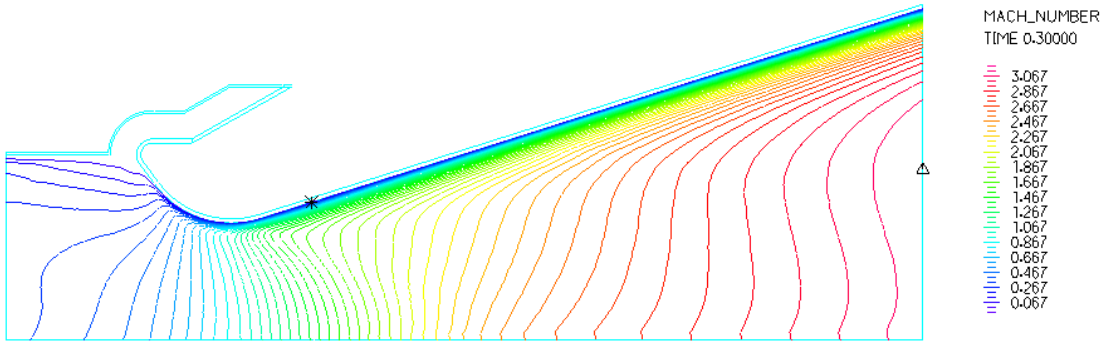

(c)

Figure 6.26 Mach number distributions at (a) t = 0.005 s,
(b) t = 0.002 s and (c) t = 0.3 s.

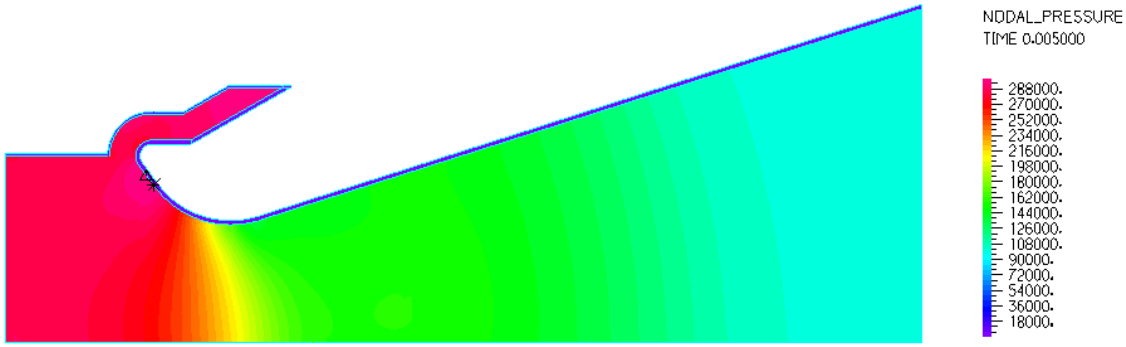

(a)

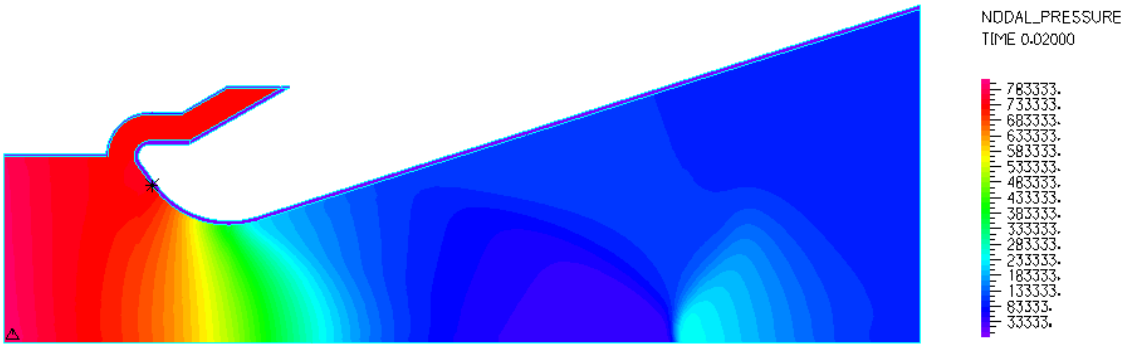

(b)

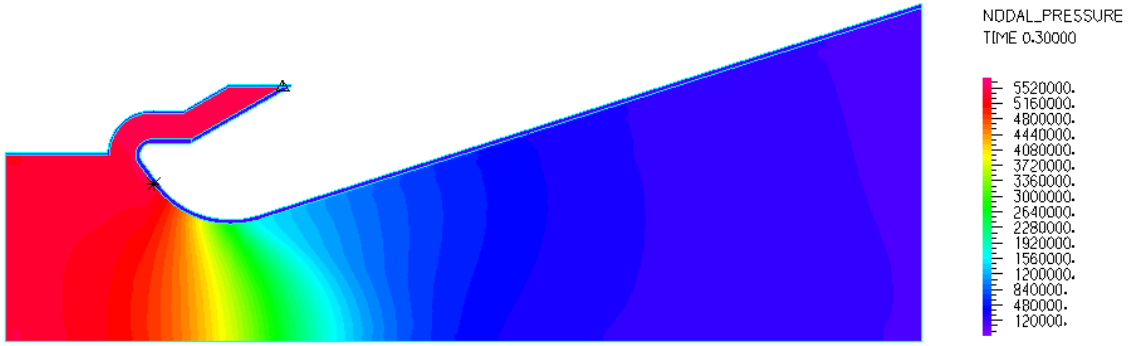

(c)

Figure 6.27 Pressure distributions at (a) t = 0.005 s,
(b) t = 0.002 s and (c) t = 0.3 s.

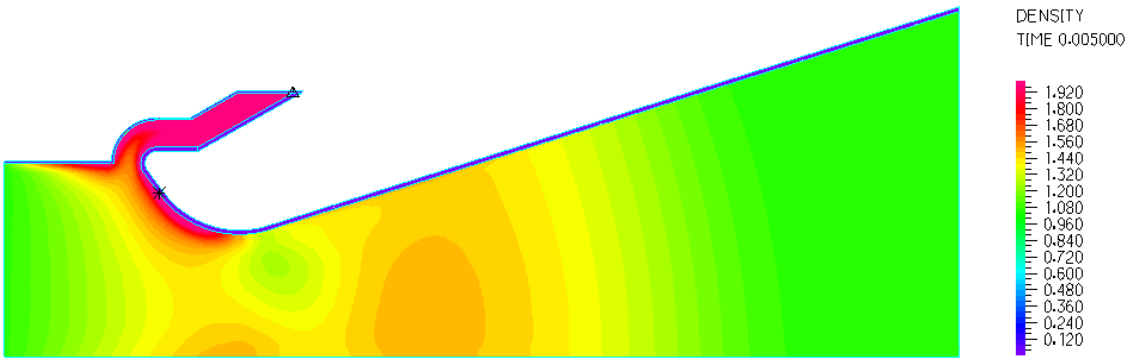

(a)

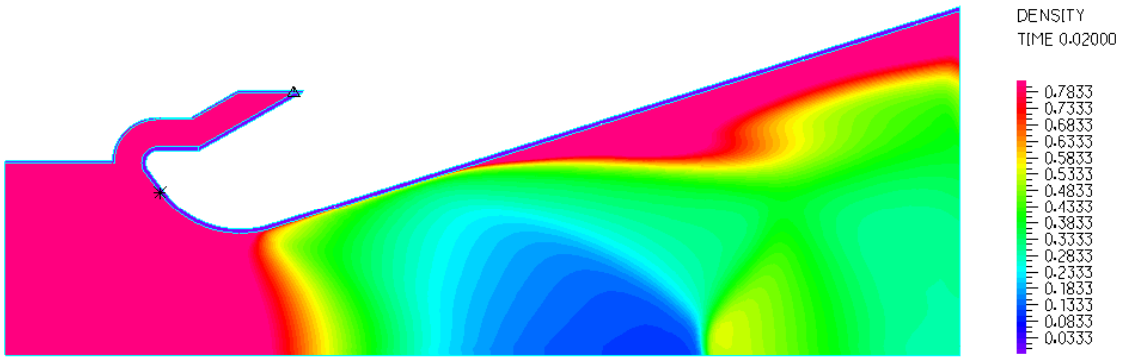

(b)

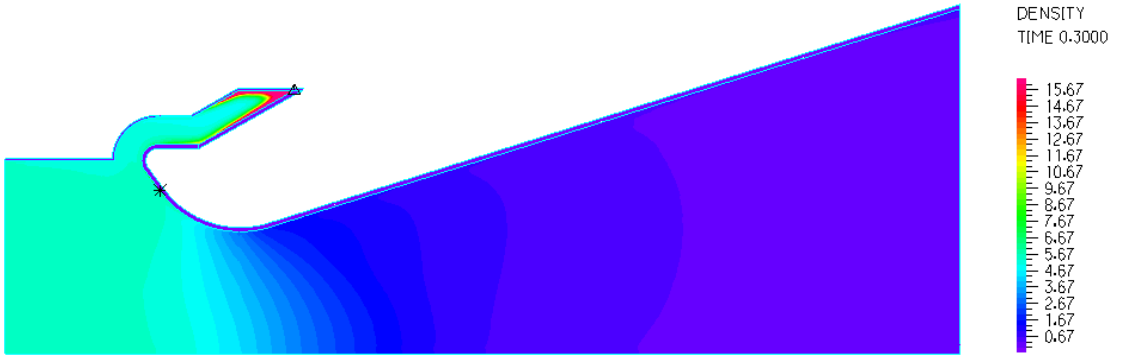

(c)

Figure 6.28 Density distributions at (a) t = 0.005 s, (b) t = 0.002 s (truncated scale range) and (c) t = 0.3 s.

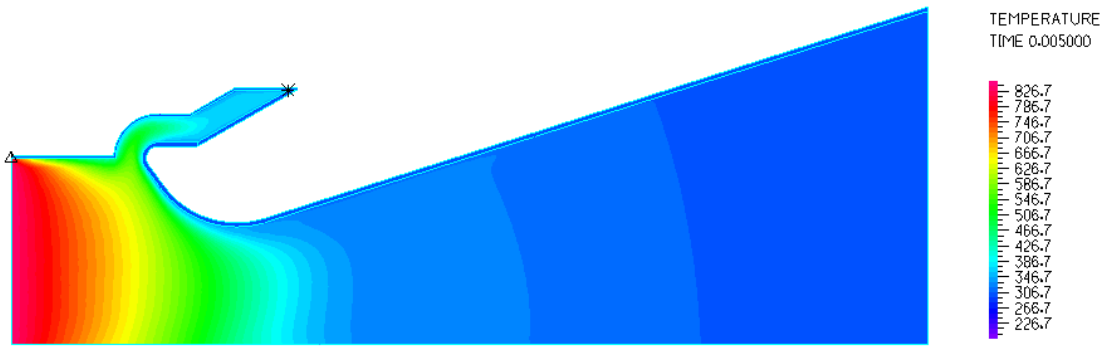

(a)

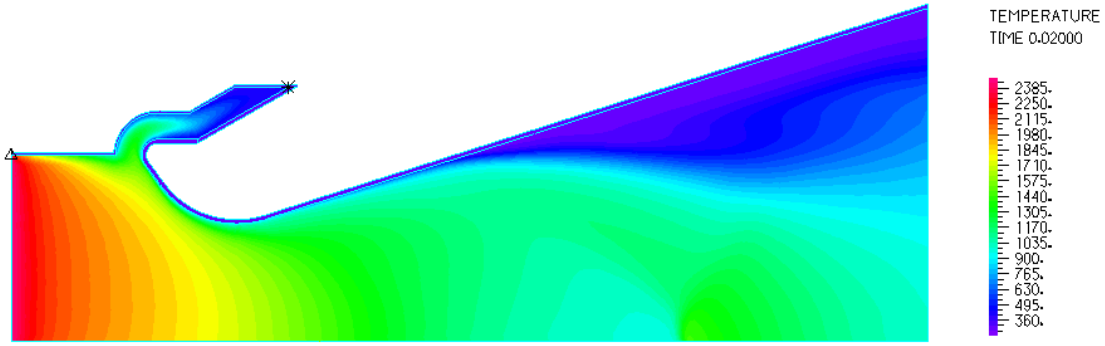

(b)

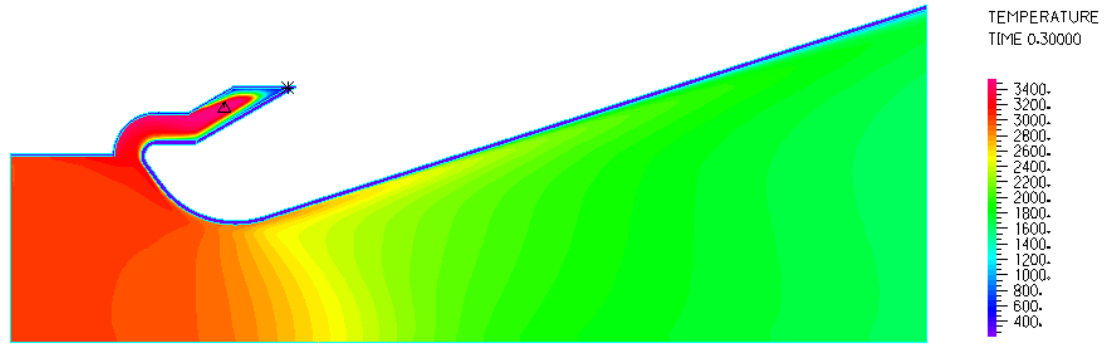

(c)

Figure 6.29 Temperature distributions at (a) t = 0.005 s,
(b) t = 0.002 s and (c) t = 0.3 s.

For instance, the compacted gas zone that is present in the pressure distribution shown in Figure 5.20 at 0.005 s has only just begun to manifest in the associated density distribution displayed in

Figure 6.28. In addition, the normal compression shock, which appears with significantly improved definition in Figures 6.26 and 6.28, is shown to have advanced to a lesser extent down the length of the exit cone by 0.02 s when viewed in comparison to the associated band plot in Figure 5.19. Despite these subtle differences, the overall characteristics of the flows predicted by either model are very similar.

The development of the flow field's temperature distribution is illustrated by Figure 6.29, which shows distributions at 0.005 s, 0.02 s and 0.3 s. The evolution of the thermal boundary layer in the subsonic, transonic and supersonic regions of the flow demonstrates the effects of heat absorption by TPZ elements in the solid domain of the model. In reference to the temperature flow fields depicted in Figure 6.29, Figures 6.30-6.32 show the axial variation of temperatures along Flow Model T's axis of symmetry (AOS) and wall at equivalent solution times. The decreasing discrepancy between the AOS and wall temperatures over the duration of the simulation, especially at the throat, indicates an increase in the rate of heat transfer with time which is expected as velocities in the nozzle rise. This evolution in heat transfer is confirmed in Figure 6.33, which shows heat flux vector plots predicting the degree of convective transfer into the solid domain at times of 0.005 s, 0.02 s and 0.3 s. The variation of heat flux shown here is in strong agreement with the classical distribution in rocket nozzles first predicted by Bartz (1957).

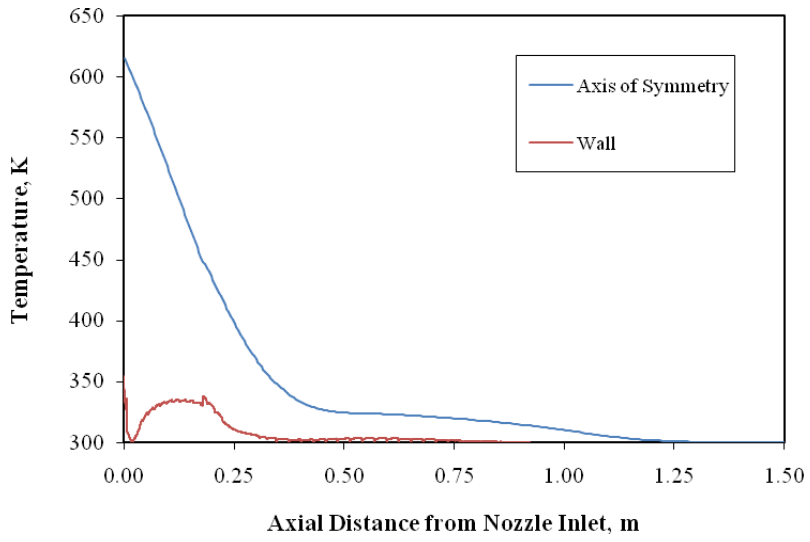

Figure 6.30 Axial temperature distributions at t = 0.005 s.

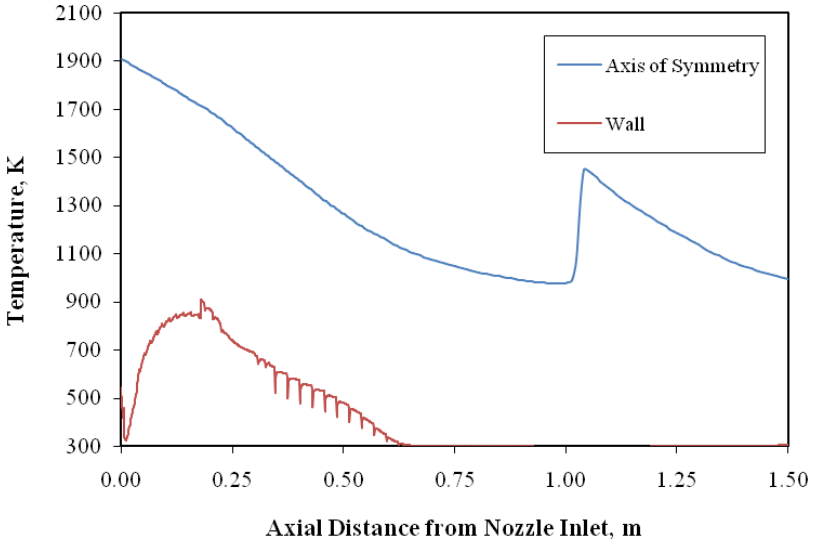

Figure 6.31 Axial temperature distributions at t = 0.02 s.

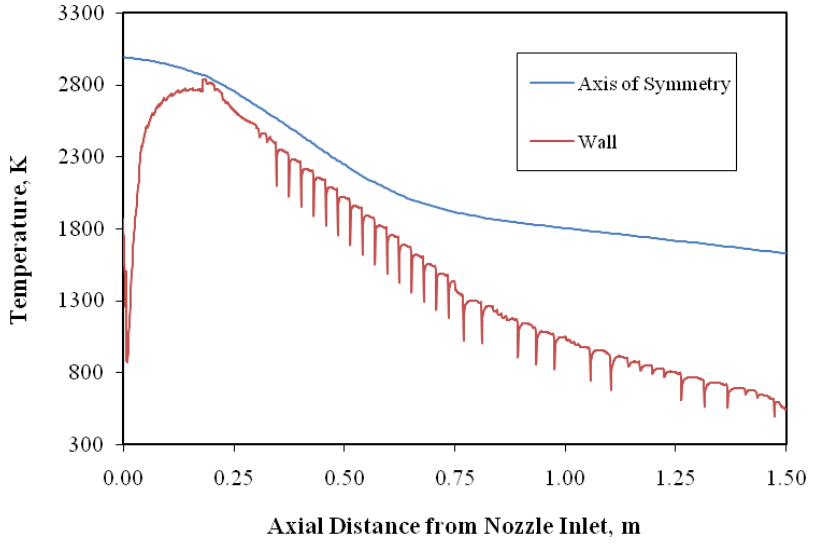

Figure 6.32 Axial temperature distributions at t = 0.3 s.

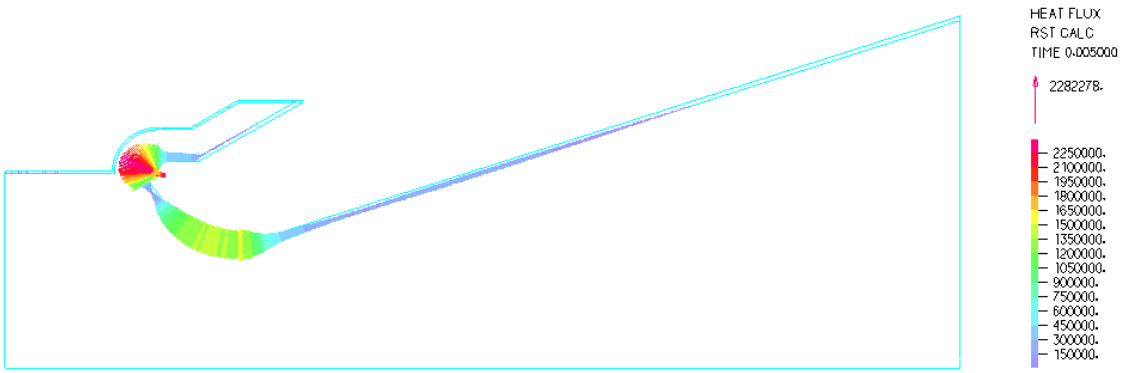

(a)

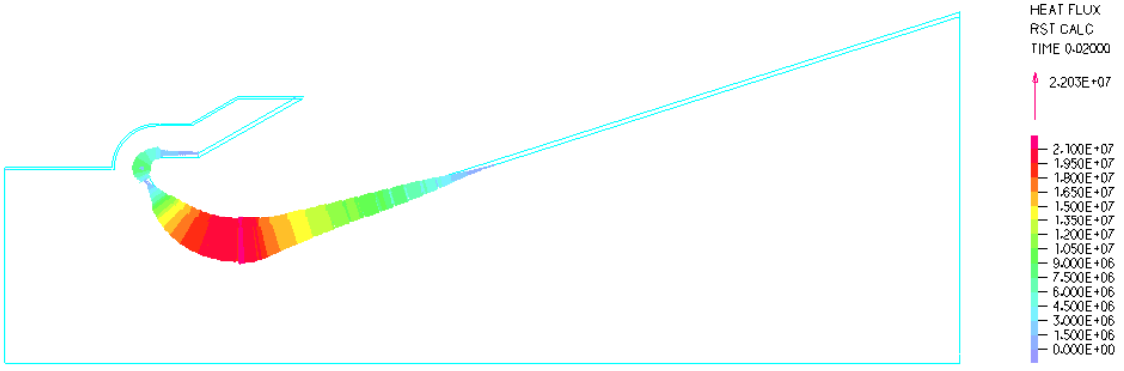

(b)

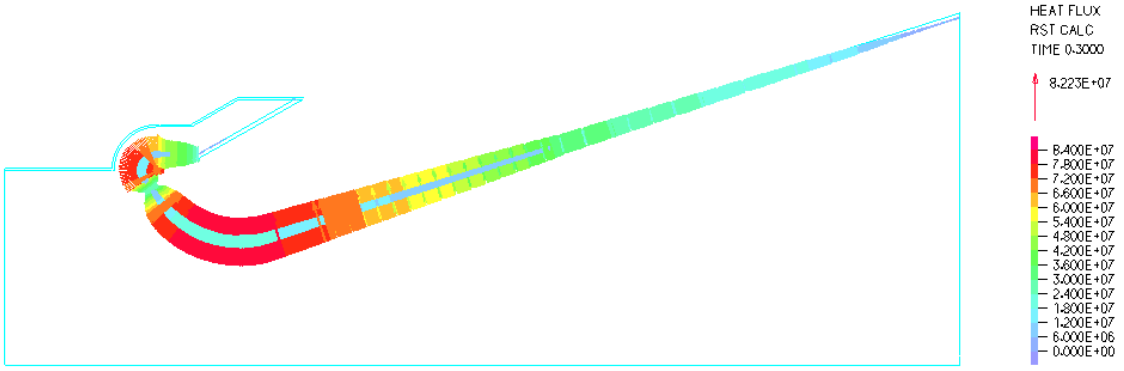

(c)

Figure 6.33 Vector plots of nozzle wall heat flux at (a) t = 0.005 s, (b) t = 0.002 s and (c) t = 0.3 s.

The dip in wall temperature shown for each solution time just after the leading edge suggests the presence of flow stagnation and a significant decrease in the local heat transfer coefficient at this location. The rapid rise in the AOS temperature distribution shown in Figure 6.31 provides an effective illustration of the position and strength of the normal compression shock at 0.02 s.

In each wall temperature distribution, particularly at 0.3 s, a sharp temperature discontinuity can be observed in the vicinity of the throat location followed by a series of temperature disturbances along the the exit cone wall. When these distributions were compared to the wall temperature distributions generated by the Chapter 5 flow simulation, which did not account for heat transfer at the wall, it was realised that these spurious effects were clearly side effects of the conjugate heat transfer solution. At the time of writing however, their exact cause had yet to be established.

Finally, to illustrate the loading conditions applied to the burn period models, wall distributions of pressure and temperature generated by the 1 s Flow Model T simulation are shown in comparison to the associated AOS distributions in Figures 6.34 and 6.35, respectively. To avoid erroneous recordings resulting from potential temperature disturbance effects at the node points defining the thermal spatial functions, data obtained at these positions were checked against temperatures at neighbouring nodes and adjusted if found to be unrepresentative.

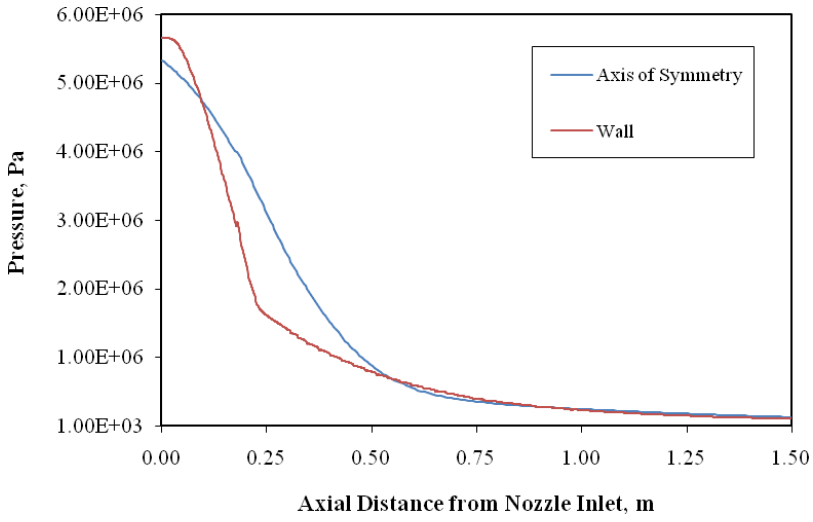

Figure 6.34 Axial pressure distributions at t = 1 s.

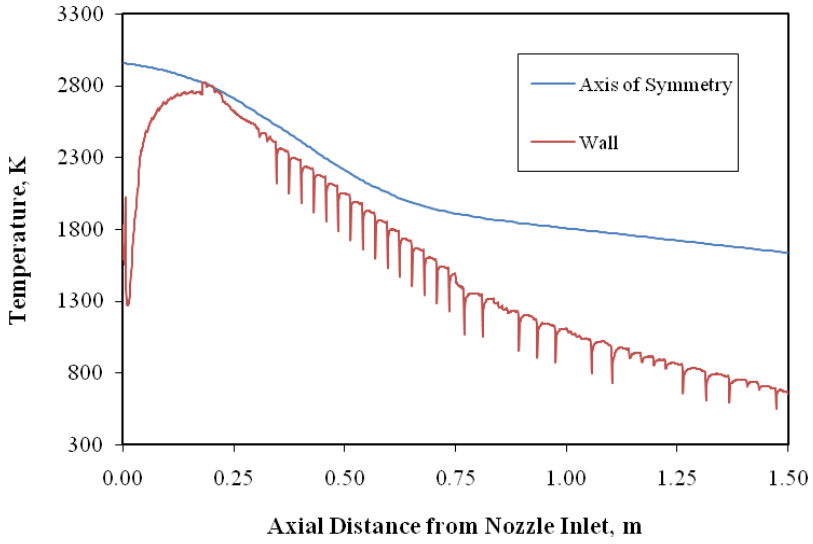

Figure 6.35 Axial temperature distributions at t = 0.1 s.

6.7.2 Stress Field Development during Burn Period

The evolution of the hoop, radial and axial stress fields in SRN2 during the simulated burn period is demonstrated by Figures 6.36-6.38, which show results recorded at 10 s, 30 s and 60 s, respectively. Associated temperature distributions in the nozzle are also shown in these figures, to allow the influence of thermoelastic effects on each stress response to be observed. Furthermore, in order for the response of the nozzle's composite substructures to be displayed clearly, the steel attach structure region was omitted from the band plots.

A review of Figures 6.36-6.38 reveals interesting response characteristics. The degree by which each response is shown to develop with time indicates the dominance of transient thermal stresses over steady pressure-induced stresses. For the most part, the general prevalence of compressive hoop, radial and axial stresses can be explained by this dominance.

At a time of 10 s, thermal penetration is still comparatively shallow, but severe stresses are already being encountered in localised areas adjacent to the wetted surfaces of the nozzle, especially in the subsonic region. The throat region of the ITE is shown to be experiencing very high compressive hoop and axial stresses, primarily as a consequence the strong thermal loading

and extreme thermal gradient at this location. The heated material zone can be seen inducing a zone of tensile hoop and axial stresses in the unheated central region of the ITE in response to significant thermal expansion. Along the entrance section and in the vicinity of the leading edge of the ITE, quite significant compressive radial stresses can be seen developing in response to the expansion resistance imposed by unheated 3D C-C material. The insulator, subjected to maximum chamber pressure loading was observed to flex inwards in response to the distortion of the attach structure, resulting in high tensile hoop stresses in this component, particularly in the area adjacent to the ITE. The negative coefficient of thermal expansion in the hoop direction of the constituent 2D C-P material contributed to this stress. The highly localised zone of intense tensile radial stress, found in the insulator towards the nozzle's motor attachment point appears to have arisen spuriously. The error, which also manifests at the subsequent solution times, is believed to be as a consequence of the application of a very low mesh density in the vicinity of the intersection between a heated and adiabatic boundary. High tensile hoop stresses were also observed at the head of the exit cone, again in response to the pressure induced distortion of the attach structure and concentrated by the geometric discontinuity created by the corner along its external surface.

By the 30 s midway point of motor operation, the increase in thermal penetration displayed by Figure 6.37, has increased the presence of compressive stresses in the nozzle, and has relieved to some extent the submerged tensile hoop stresses in the ITE. The zone of tensile axial stresses in the substructure however, has become more prolific. Significantly, the severe compressive stresses encountered in the throat region have not subsided, and the zone of compression has deepened appreciably. It is believed that this phenomenon can be attributed to the notably stiffer and insulated steel attach structure retarding the radial expansion of the ITE. An area of high tensile hoop stress can once again be seen in the insulator at its heated junction with the ITE, the magnitude of which has increased significantly. Tensile axial stresses have also been shown to increase at the corner feature at the head of the exit cone.

By the end of the burn period, at 60 s, hoop stress in the ITE and exit cone are predicted as being almost entirely compressive. The severe compressive stress zone at the nozzle's throat has deepened further and progressed in the upstream and downstream directions, although the magnitude of the highest recorded stress has decreased slightly. Tensile hoop stresses have spread across the heated surface of the insulator as a consequence of further thermally-induced

material contraction. The submerged region of tensile axial stress in the ITE has increased in size, whilst tensile axial stresses in the adjacent insulator have risen to a notable magnitude. In addition, a small zone of compressive radial stress can also be seen developing at the head of the insulator as a result of the significant differential expansion in the radial direction.

When considering the stresses arising from the unequal expansion of separate substructures such as the ITE and insulator, it is important to bear in mind that in reality, expansions gaps and slip surfaces are designed into the nozzle structure for the specific purpose of alleviating these stresses. Even in the case that substructures are bonded together with adhesives, a significant amount of expansion stress can be dissipated by the characteristically low modulli of elasticity associated with these adhesives. As these features were not included in the SRN2 design or structural models, and in consideration of the novelty of the design itself, it is clear that to a degree, simulated stress magnitudes in certain zones of the Burn Period Structural Model were unavoidably overestimated. Having said this however, it is believed that the fidelity of the ignition period structural response was substantially less affected by these technical simplifications as an elementary consequence of the highly localised nature of heat penetration.

To gain a more precise understanding of the stress magnitudes encountered during the burn period, hoop, radial and axial stress histories were recorded at the five sample points A, B, C, D and E, and are exhibited in Figures 6.38-6.43, respectively. The establishment of histories at these points was important as it would allow ignition period and burn period responses to be compared at identical locations.

The most marked observation made in relation to these results is that at each point, with the exception of the axial stress history, the highest stress magnitudes recorded were shown to be reached by the first time step of the simulation. Furthermore, the magnitude of the predominant hoop and axial stresses at the nozzle's surface declined considerably from this peak over the remaining duration of the simulation, as the depth of thermal penetration increased and relieved the constricting effect imposed by unheated regions. This decline wasn't as significant in the hoop stress history recorded at point B, however. It is suggested that the trend was not followed at this point as a result of the radial expansion constriction imposed by the attach structure. Nonetheless, this observation was notable as it indicated the significance of the ignition period in generating nozzle surface stresses and the role played by thermoelasticity in this regard.

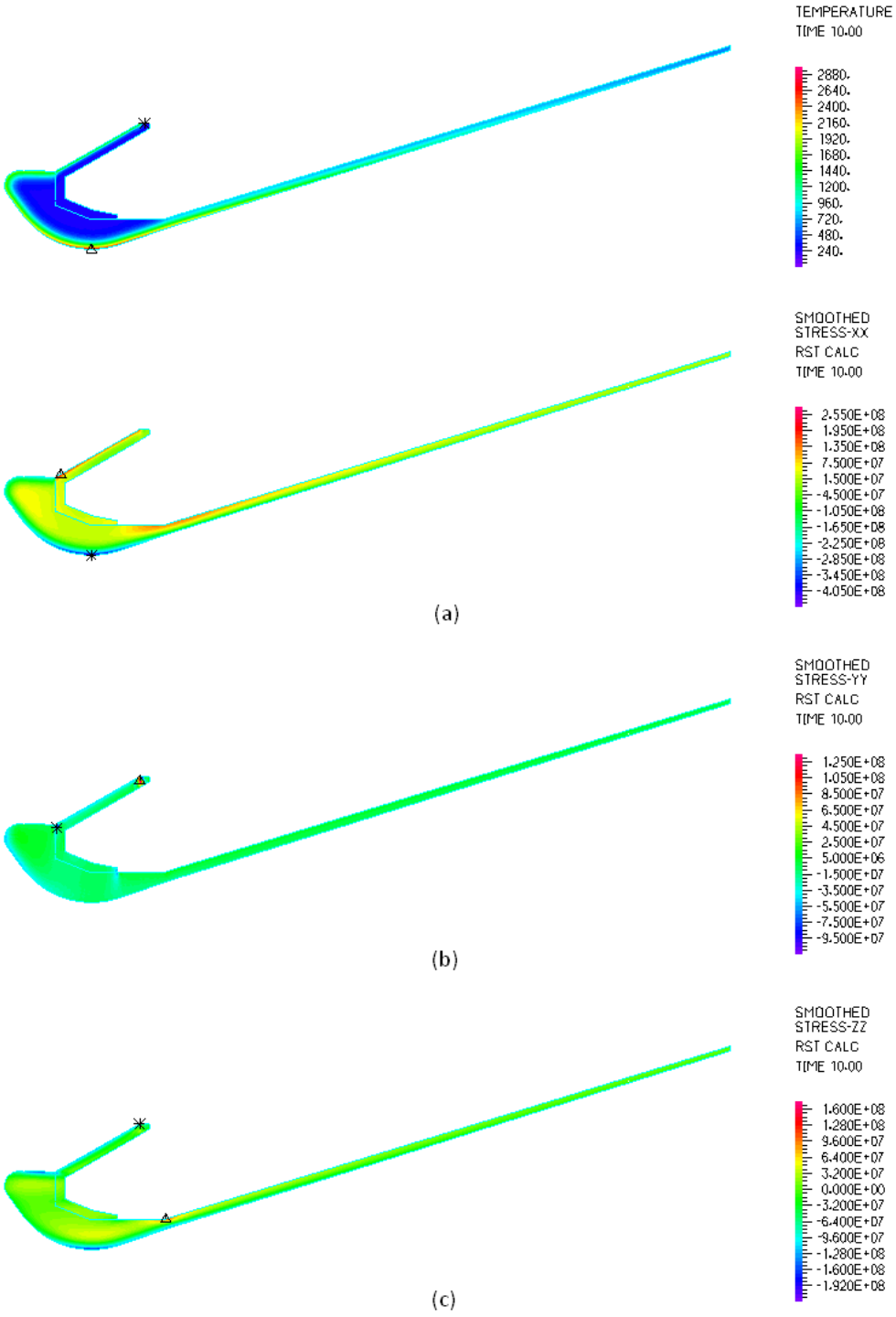

Figure 6.36 Temperature distribution and (a) hoop, (b) radial and (c) axial stress fields at t = 10 s.

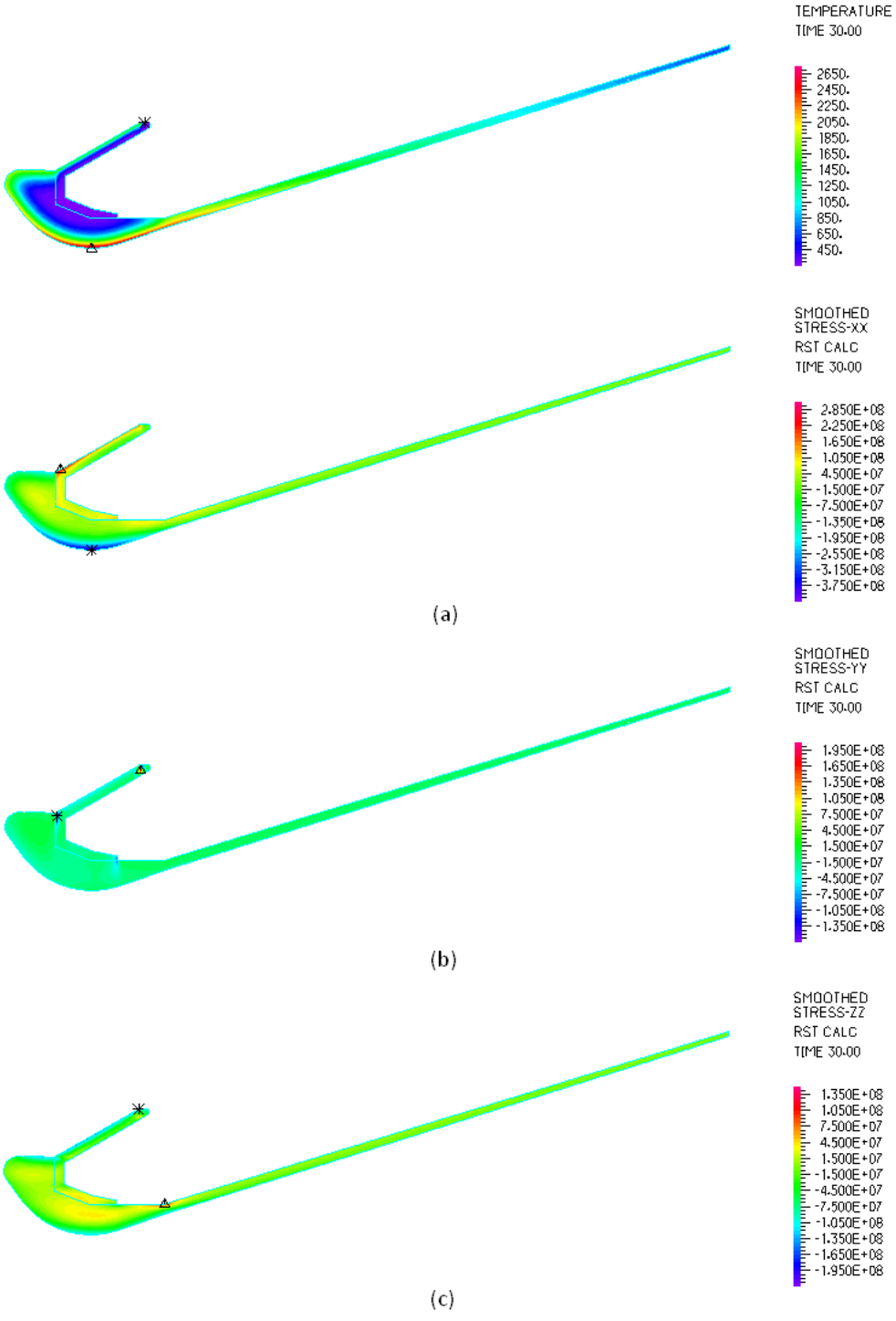

Figure 6.37 Temperature distribution and (a) hoop, (b) radial and (c) axial stress fields at t = 30 s.

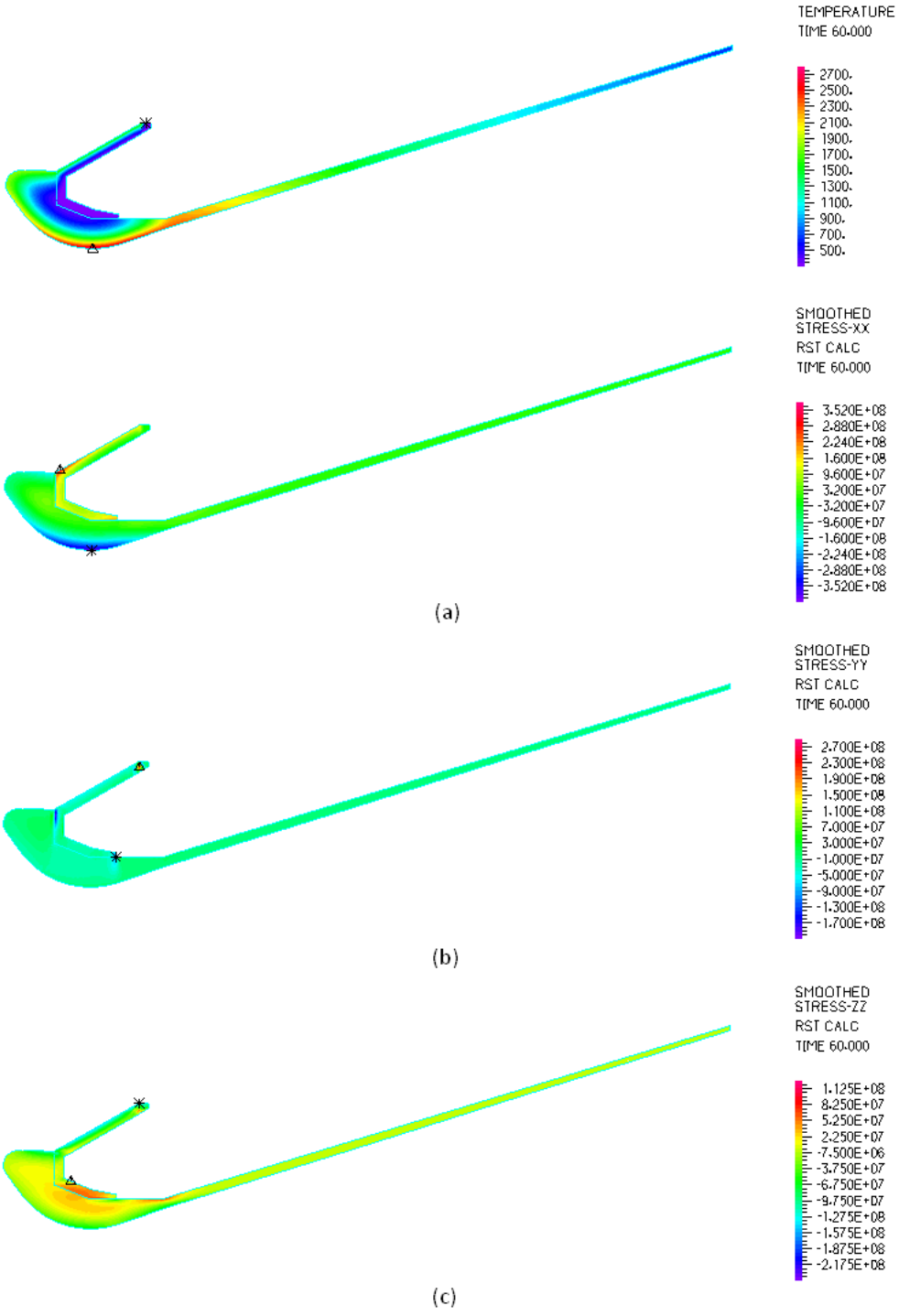

Figure 6.38 Temperature distribution and (a) hoop, (b) radial and (c) axial stress fields at t = 60 s.

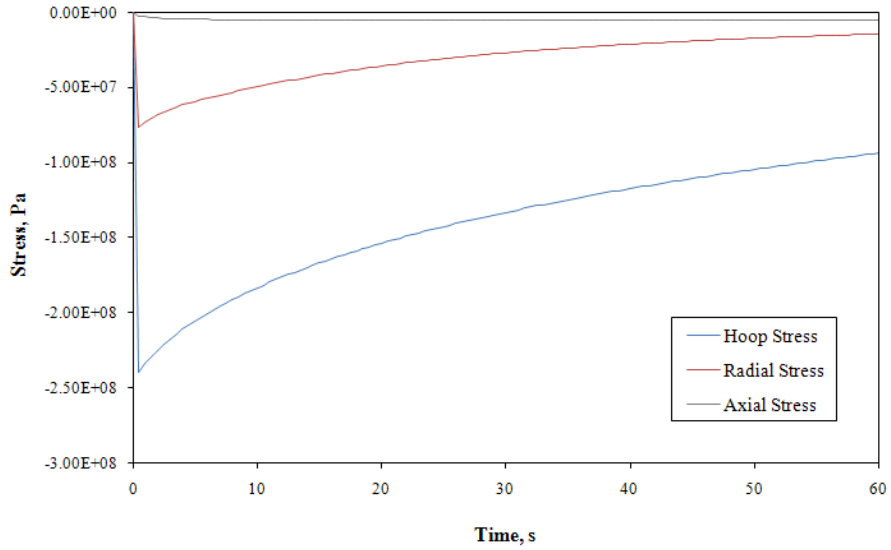

Figure 6.39 Burn duration hoop, radial and axial stress histories at point A.

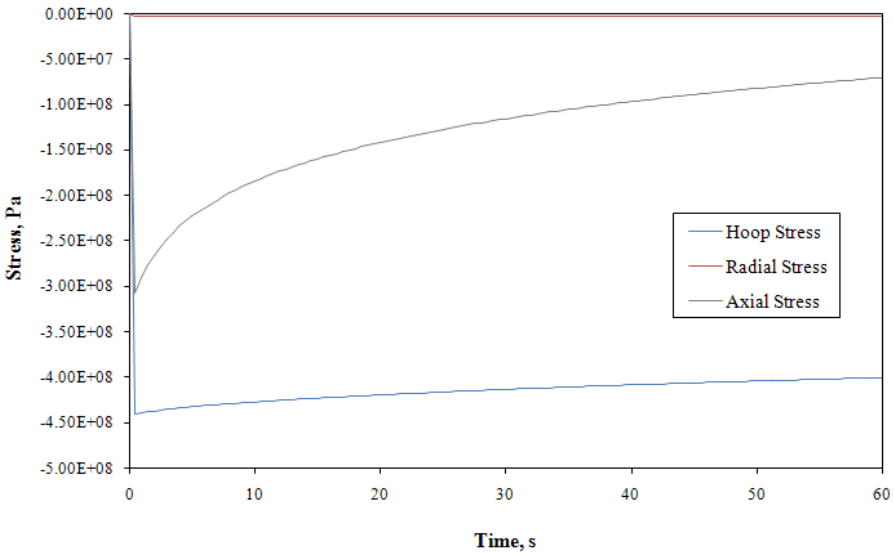

Figure 6.40 Burn duration hoop, radial and axial stress histories at point B.

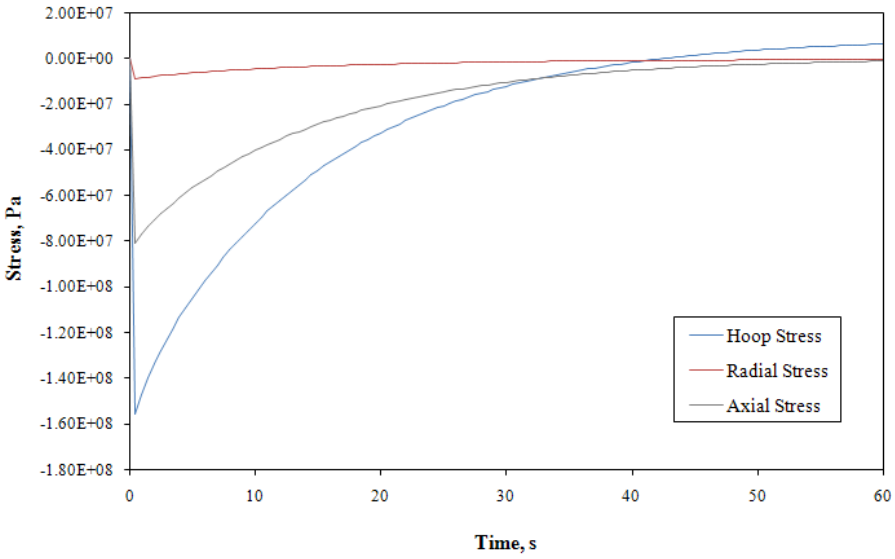

Figure 6.41 Burn duration hoop, radial and axial stress histories at point C.

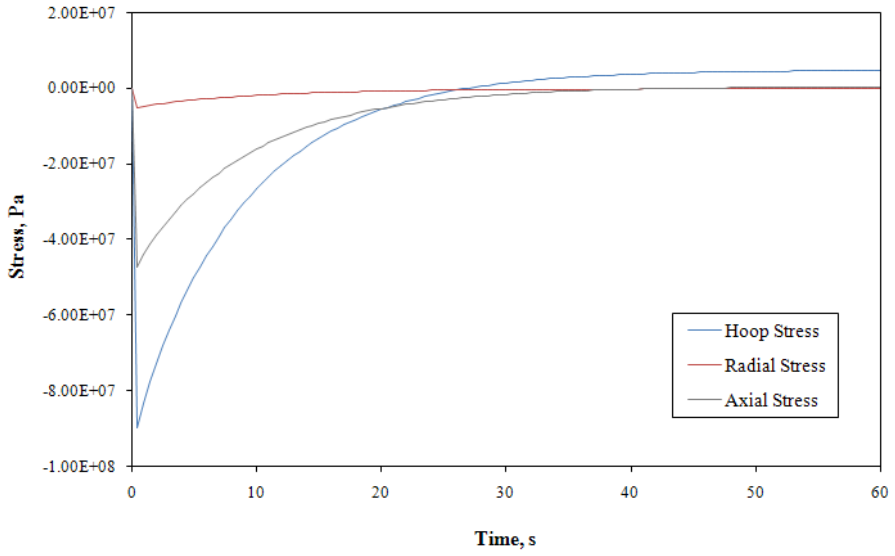

Figure 6.42 Burn duration hoop, radial and axial stress histories at point D.

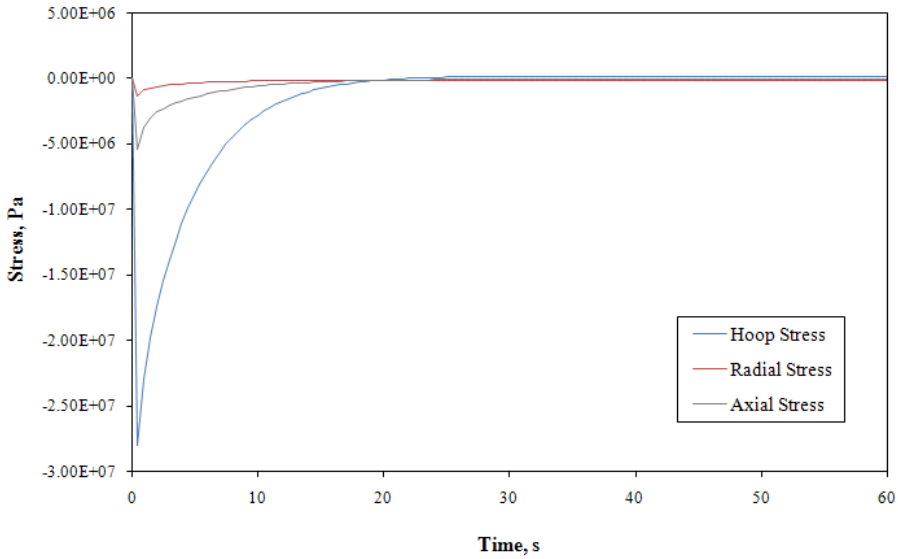

Figure 6.43 Burn duration hoop, radial and axial stress histories at point E.

Also noted was the apparent directional hierarchy amongst the hoop, radial and axial responses. In general, surface stresses in the hoop direction were shown to be most severe, followed by axial stresses, whilst radial stresses appeared to remain insignificant for the duration of the simulation. As a result of point A's perpendicular orientation relative to the other points, a slightly different hierarchy was observed in which the axial stress response as opposed to the radial stress response was shown to be comparatively negligible. As far as stress direction is concerned, almost every response remained compressive throughout the simulation, although interestingly, the hoop stress histories at points C and D were observed to become slightly tensile in the second half of the time interval.

6.7.3 Nozzle Displacements Attributable to Ignition Period Pressure and Thermal Loading

In spite of the ADINA-FSI program being unable to account for thermal loading during a coupled ignition transient simulation, the effect of incorporating SRN2's thermoelastic response in regards to the degree of aeroelastic coupling that would subsequently be induced, could still be indirectly explored.

The kinematic condition (Eqn. N) employed in the FSI solution algorithm implies that the degree of coupling that occurs between the nozzle and its flow field is effectively governed by the

distortion of the nozzle in response to the loading imposed upon it by the flow field. The distortion clearly needs to be of sufficient magnitude to alter the flow field, and for the altered flow field to in turn load the nozzle in an altered manner. As was demonstrated in Chapter 5 however, when SRN2 was subjected to pressure loading alone, an insufficient distortion of the nozzle arose to induce any notable coupling effects in the structural response. If, therefore, the distortion of the nozzle during exposure to thermal loading alone could be compared its distortion in response to pressure loading, the potential for thermoelasticity to induce aeroelastic coupling could be estimated. As such, displacement magnitude histories at points A-E were derived from the Structural Model P simulation and compared to those resolved in the Structural Model T simulation, as shown in Figures 6.44-6.48, respectively.

Two interesting characteristics in the results are observed. Firstly, at points positioned in the stiffer regions of the nozzle, namely points A and B, the thermally-induced displacements are significantly smaller in magnitude in comparison to those induced by pressure loading – as evidenced by Figures 6.44 and 6.45. At points C, D and E however, where the structure is notably more flexible, the thermally-induced displacements are of comparable magnitude towards the end of the simulation period.

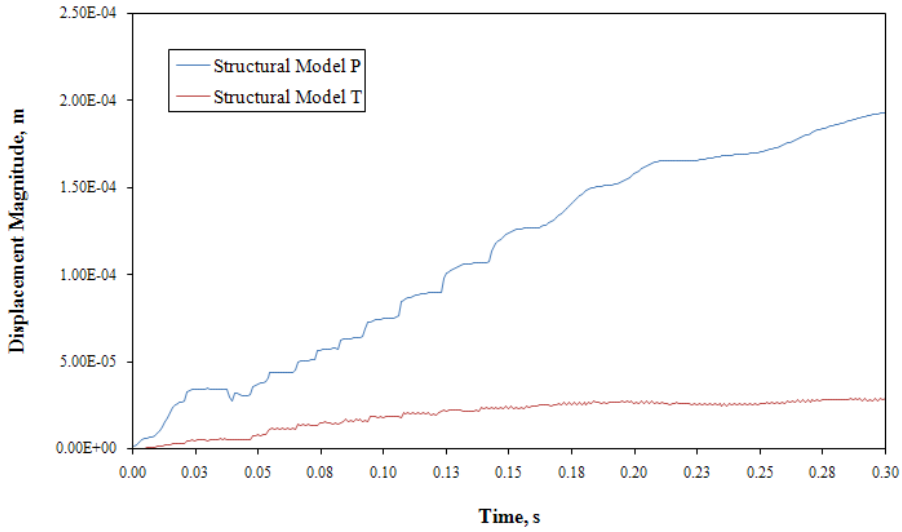

Figure 6.44 Displacement magnitude histories at point A.

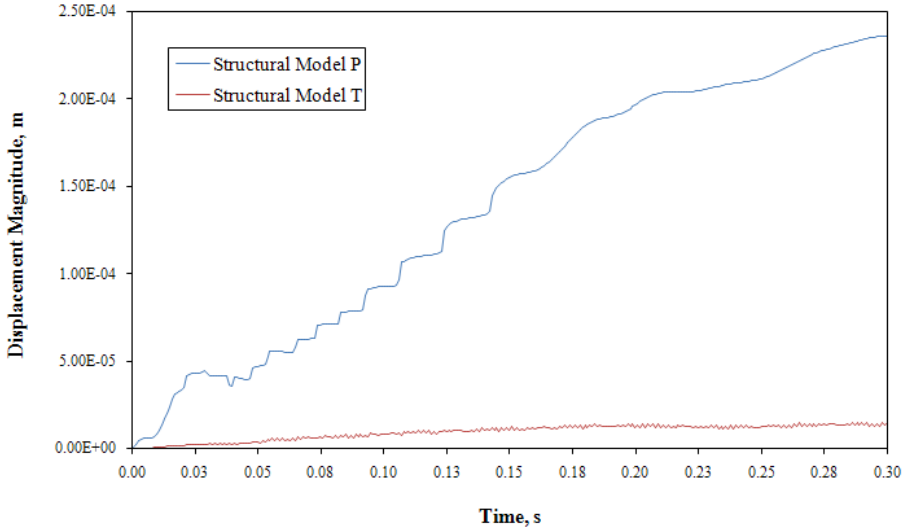

Figure 6.45 Displacement magnitude histories at point B.

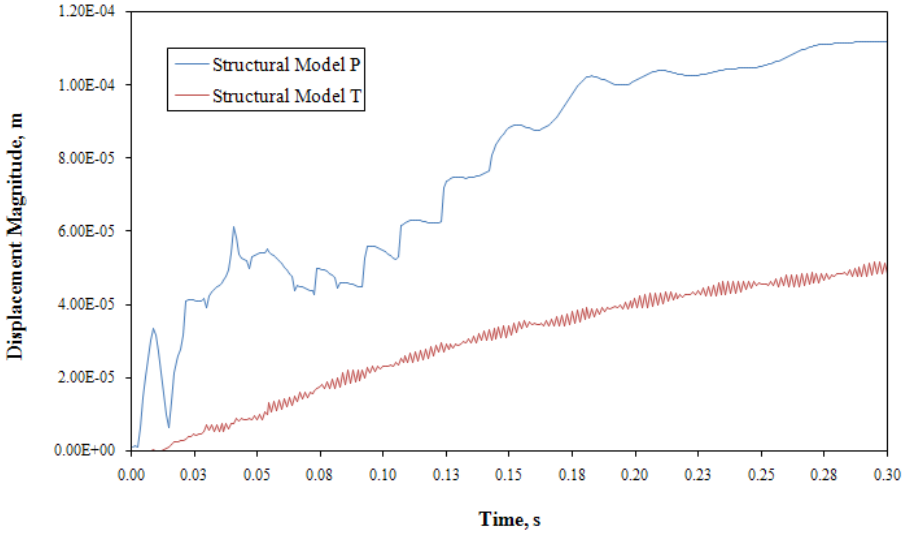

Figure 6.46 Displacement magnitude histories at point C.

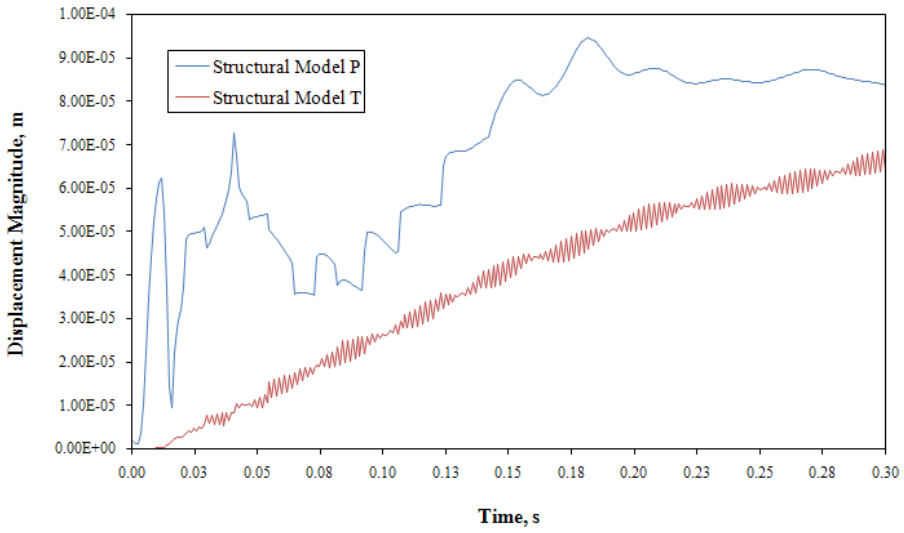

Figure 6.47 Displacement magnitude histories at point D.

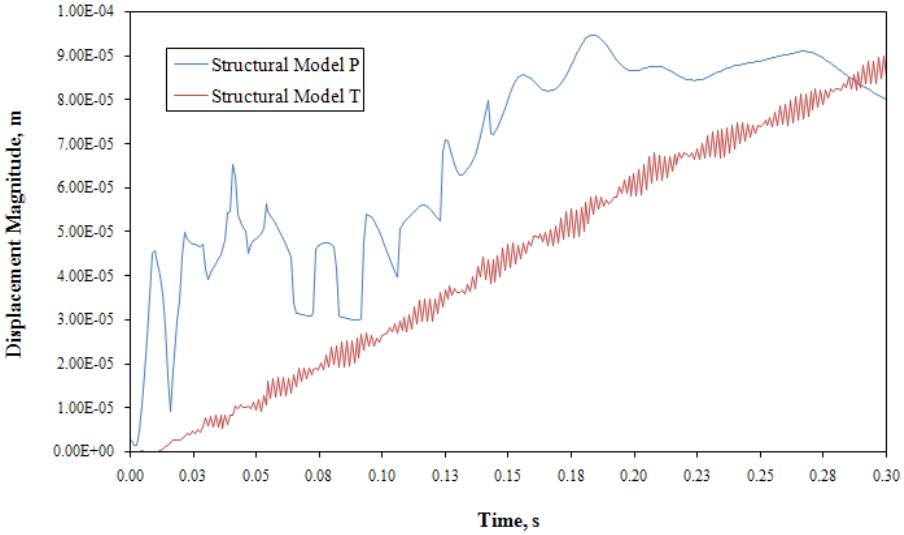

Figure 6.48 Displacement magnitude histories at point E.

The steady growth in thermally-induced displacements from a time just after the start of the simulation is believed to be attributable to the outward expansion of the entire exit cone as the depth of heat penetration increases. The second response characteristic of interest is the vibratory

nature of the thermally-induced displacement histories at all five points, although significantly stronger at points C-E. The frequency of oscillation appears to be too small to be associated with the propagation of elastodynamic waves, but suggests the presence of global structural vibration. Although the source of this vibratory response could not be confirmed, the vibration may well be attributable to differential heating of the nozzle.

Ultimately however, it was concluded that whilst thermally-induced displacements along the exit cone are appreciable, they are not sufficiently larger than pressure-induced displacements to suggest that any significant aeroelastic coupling would arise in their inclusion in an FSI simulation.

6.7.4 Transient Stress Distributions Attributable to Pressure and Thermal Loading

To establish the distinct characteristics of the stress responses induced by pressure and thermal loading during the ignition period, results derived from Structural Model P and Structural Model T for the 0.6 s transient were compared at sample times of 0.005 s, 0.02 s and 0.3 s. In this regard, band plots of hoop, radial and axial stress distributions are shown in Figures 6.49-6.57.

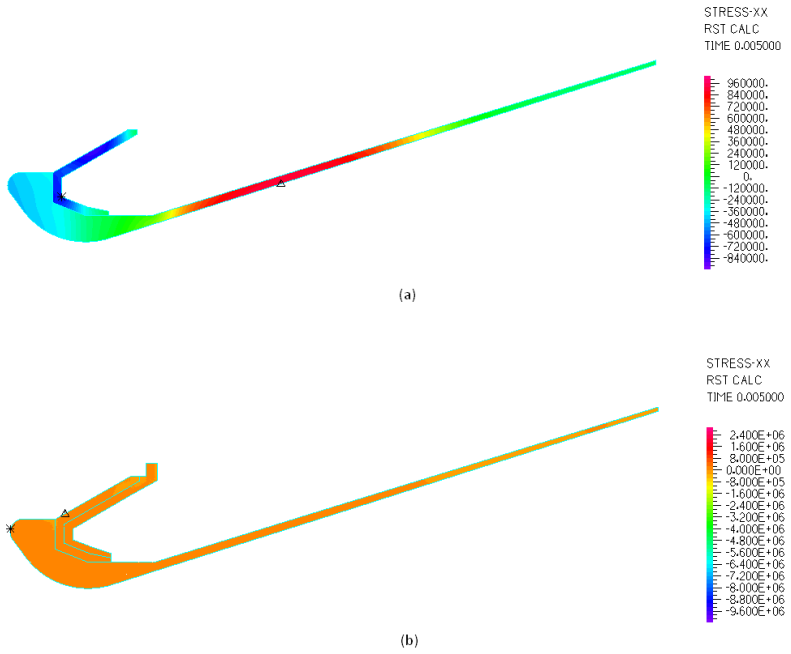

Figure 6.49 (a) Pressure and (b) thermal hoop stress distributions at 0.005 s.

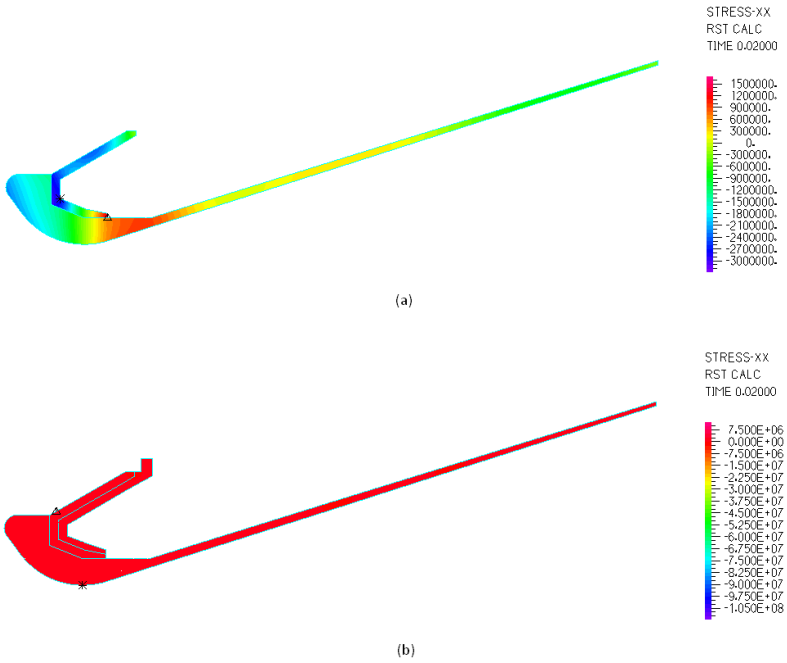

Figure 6.50 (a) Pressure and (b) thermal hoop stress distributions at 0.02 s.

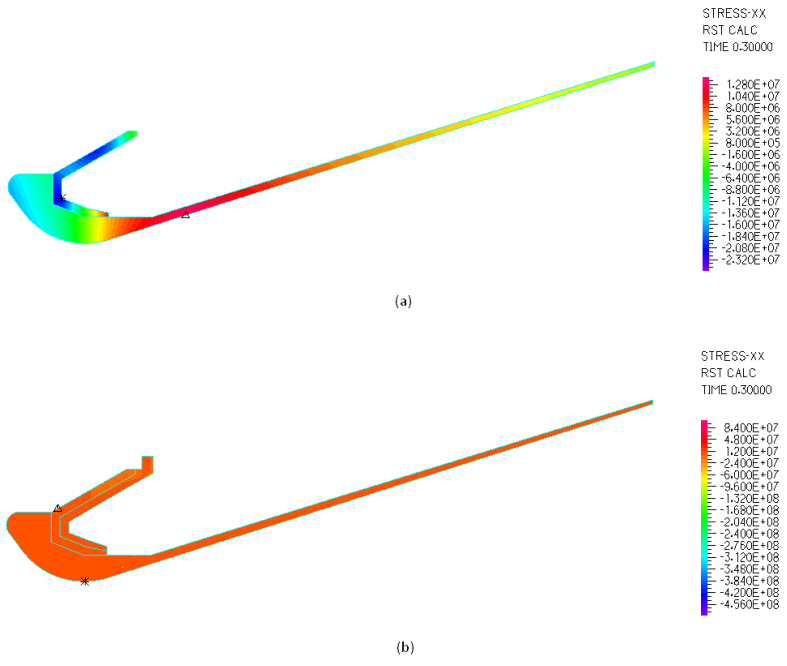

Figure 6.51 (a) Pressure and (b) thermal hoop stress distributions at 0.3 s.

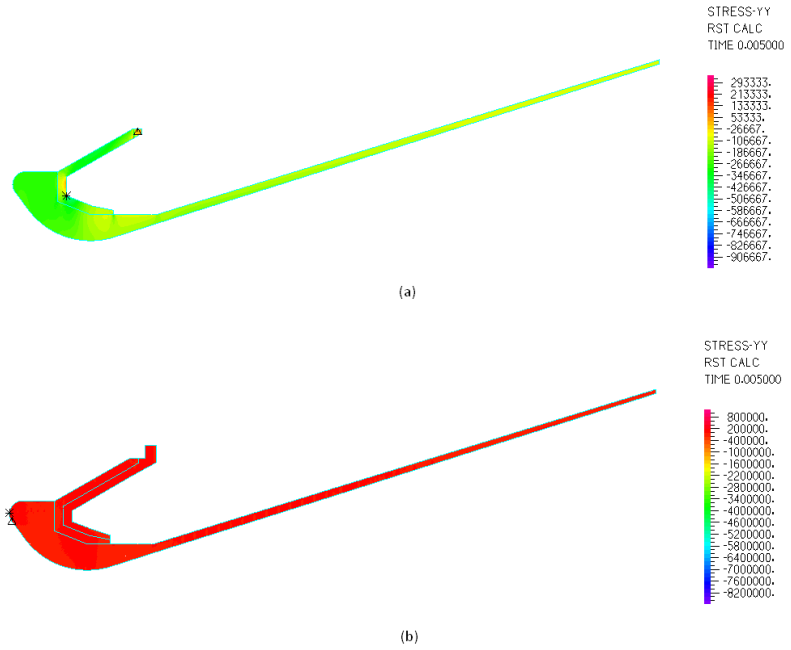

Figure 6.52 (a) Pressure and (b) thermal radial stress distributions at 0.005 s.

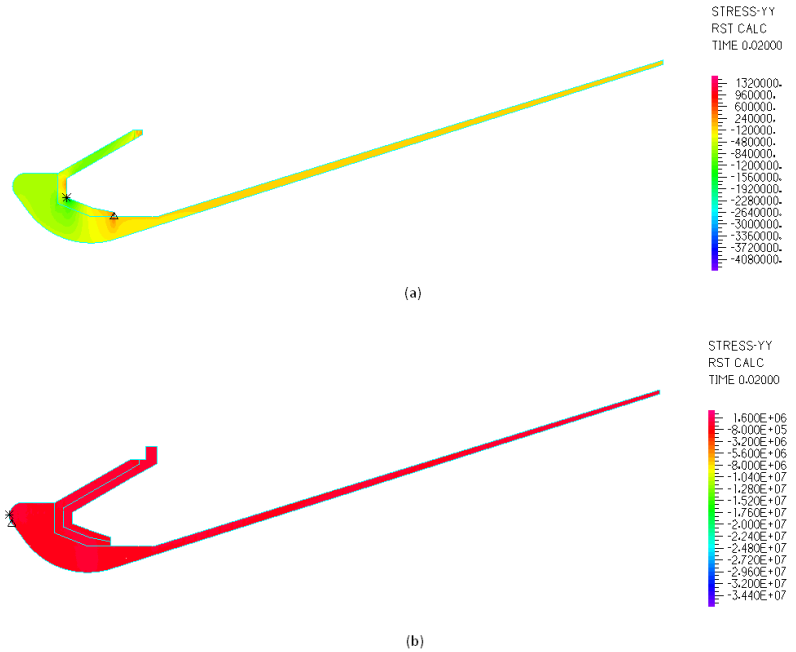

Figure 6.53 (a) Pressure and (b) thermal radial stress distributions at 0.02 s.

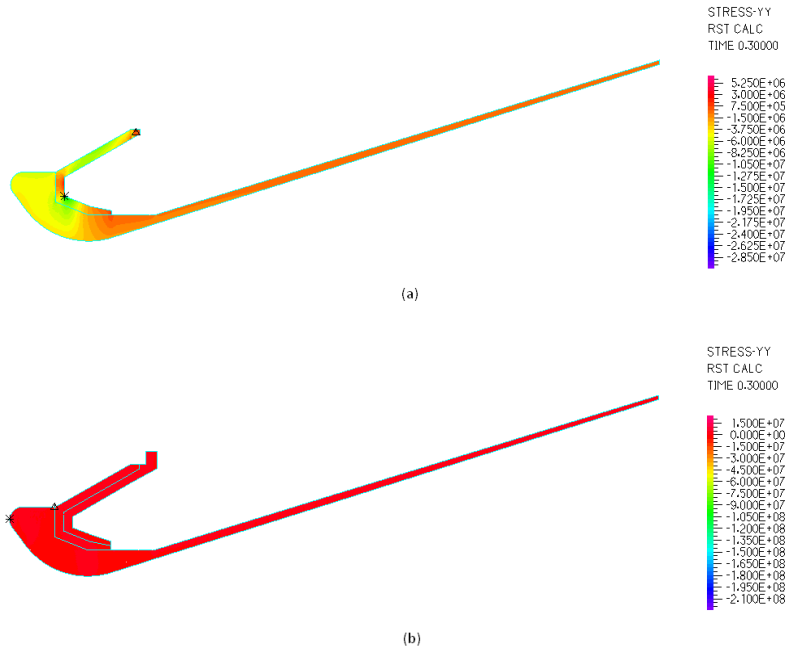

Figure 6.54 (a) Pressure and (b) thermal radial stress distributions at 0.3 s.

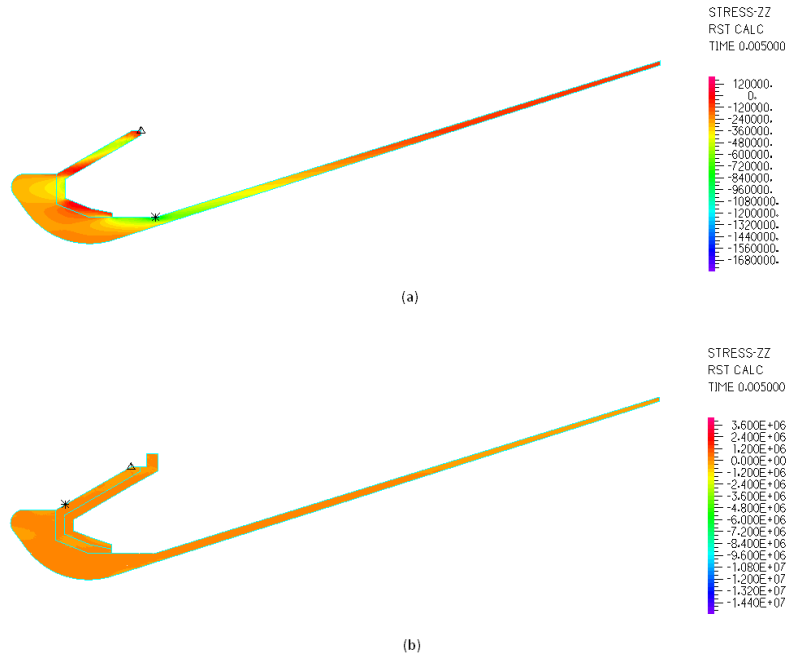

Figure 6.55 (a) Pressure and (b) thermal axial stress distributions at 0.005 s.

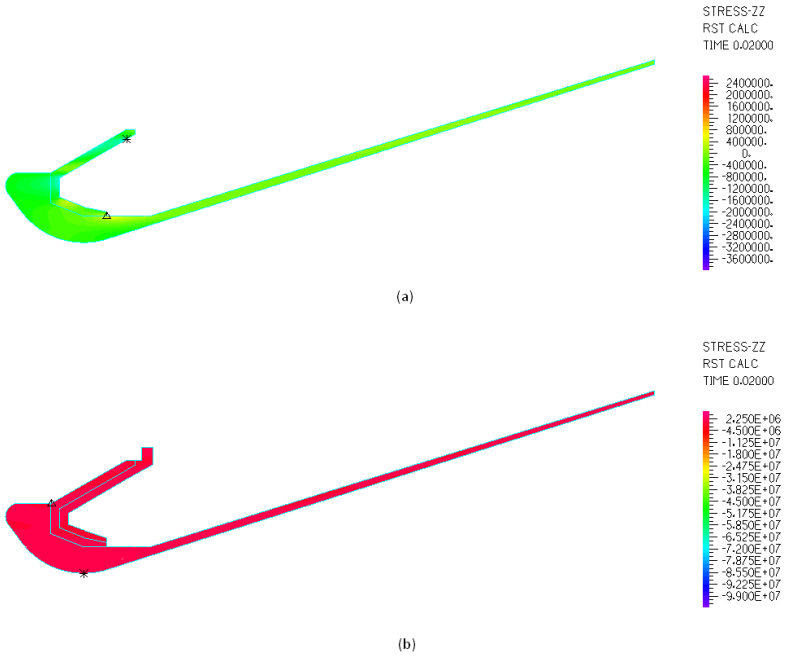

Figure 6.56 (a) Pressure and (b) thermal axial stress distributions at 0.02 s.

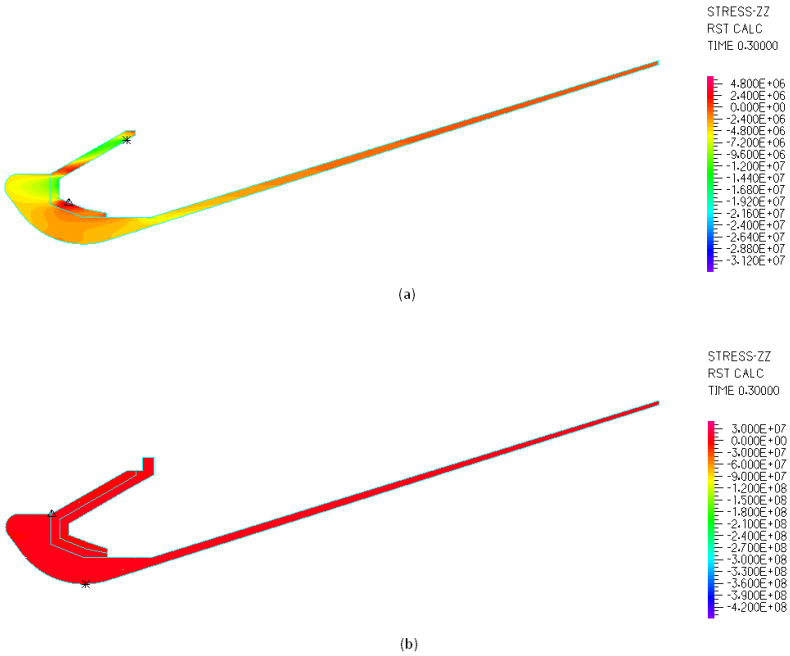

Figure 6.57 (a) Pressure and (b) thermal axial stress distributions at 0.3 s.

Upon inspection of these figures, the differences in the stress field distributions that are induced by either loading source, becomes immediately apparent. The pressure-based hoop, radial and axial stress fields show fairly wide-ranging distributions, which are predicted to evolve significantly as the flow field develops within the nozzle. Both compressive and tensile stresses are shown to manifest in the composite substructures, with stresses in all directions rising steadily to moderate levels during the course of ignition.

In comparison, thermally induced stresses are shown to leave the SRN2 structure almost entirely unaffected. A review of the stress magnitude scales shown adjacent to the Structural Model T band plots however, indicates the development of significant compressive stresses that are particularly severe in the hoop and axial directions. As demonstrated in Figure 6.58, which displays the thermal hoop stress distribution at the entrance and throat region at 0.3 s, closer inspection of the thermal stress band plots reveals the presence of highly localised compressive hoop, radial and axial stress distributions adjacent to the nozzle's wetted surface. This compressive stress zone is shown in relation to the TPZ element band in Figure 6.59, and demonstrates the conservative nature of the finite element discretization scheme. With respect to magnitude, these stresses are estimated to be highest at the surface, whilst rapid dissipation occurs with increasing submergence. This behaviour was predicted by the TPZ element size sensitivity steady and is ultimately a product of the high thermal gradients generated by rapid convective heating of the nozzle during ignition.

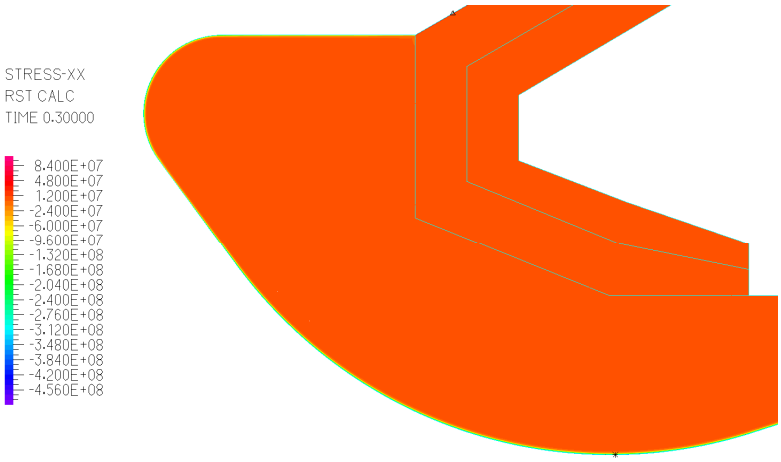

Figure 6.58 Distribution of hoop stress at the entrance and throat at 0.3 s.

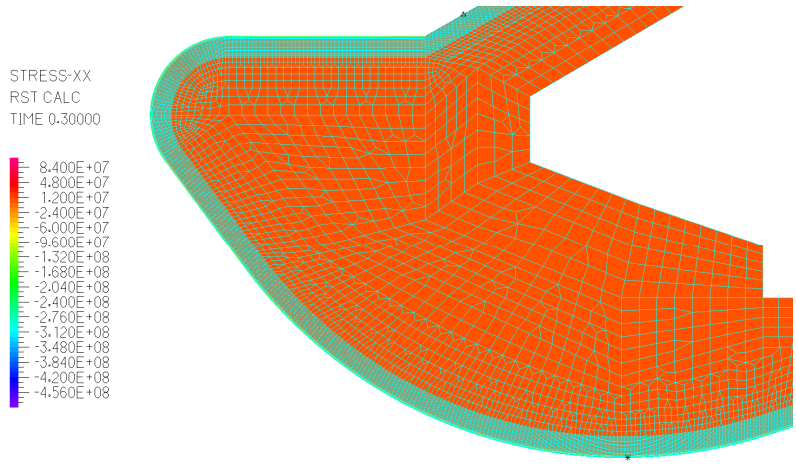

Figure 6.59 Hoop stress distribution with the Structural Model T mesh overlay.

To provide an example of the significant difference between the distribution characteristics of the pressure and thermal stress responses, Figures 6.60 and 6.61 show stress profiles over the cross-section Y-Y at the head of the exit cone induced by pressure and thermal loading, respectively. The profiles, which are shown at three solution times, clearly indicate the significant differences in stress magnitudes and gradient.

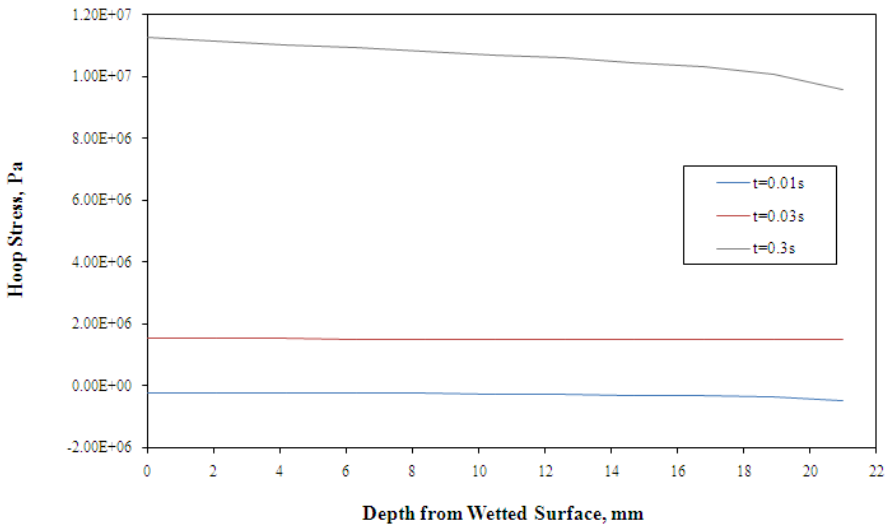

Figure 6.60 Pressure hoop stress profiles over cross-section Y-Y.

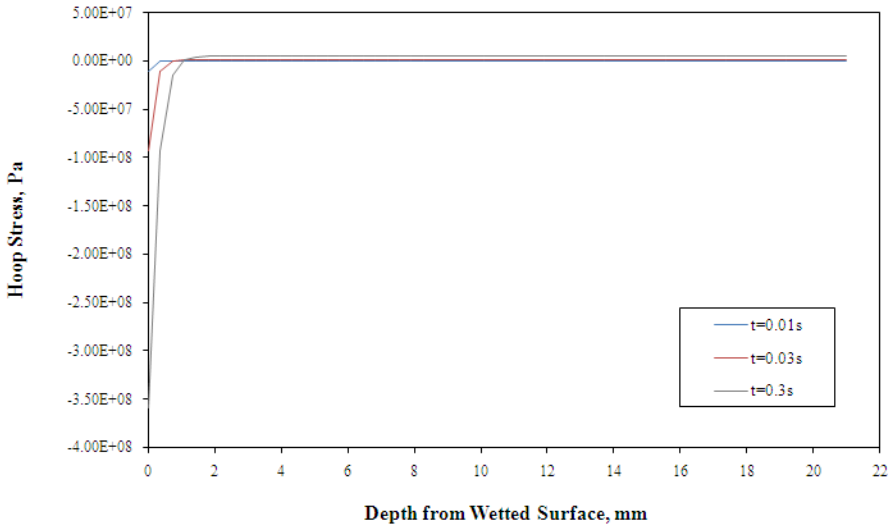

Figure 6.61 Thermal hoop stress profiles over cross-section Y-Y.

From a review of the overall distribution and intensity of pressure- and thermally-induced stresses in the nozzle, two conclusions can be drawn. Firstly, in terms of absolute magnitude, thermal stresses are predicted to be considerably more severe than pressure stresses, and secondly, on the assumption of response superposition, the highest effective stresses generated in the nozzle during ignition occur along its wetted surface. This deduction clearly indicates the appropriate location of the sample points A-E in establishing the worst-case stresses during ignition.

6.7.5 Evaluation of Effective Surface Stresses

To quantitatively gauge the evolution of the surface stress response along the length of SRN2's wall, histories for effective hoop, radial and axial stresses were evaluated at sample points A-E. The resulting data generated by superimposing the associated pressure and thermal stress components at each position and solution time, are depicted in Figures 6.62 and 6.64-6.67.

Upon inspection of the recorded responses, it becomes apparent that certain surface stress histories display a period of strong oscillation occurring roughly between 0.02 s and 0.17 s, particularly at points A-C. In consideration of the high stiffness of the structure at points A and B, one would expect any manifestation of inertial vibration to occur at the high frequencies

associated with elastodynamic vibration rather than at a low frequency indicative of structural vibration. The relatively low frequency of the recorded response is therefore inconsistent with the local stiffness of the structure. Furthermore, the asymmetry of the apparent waveform relative to the time-scale of the response also suggests that this behaviour does not have physical origins.

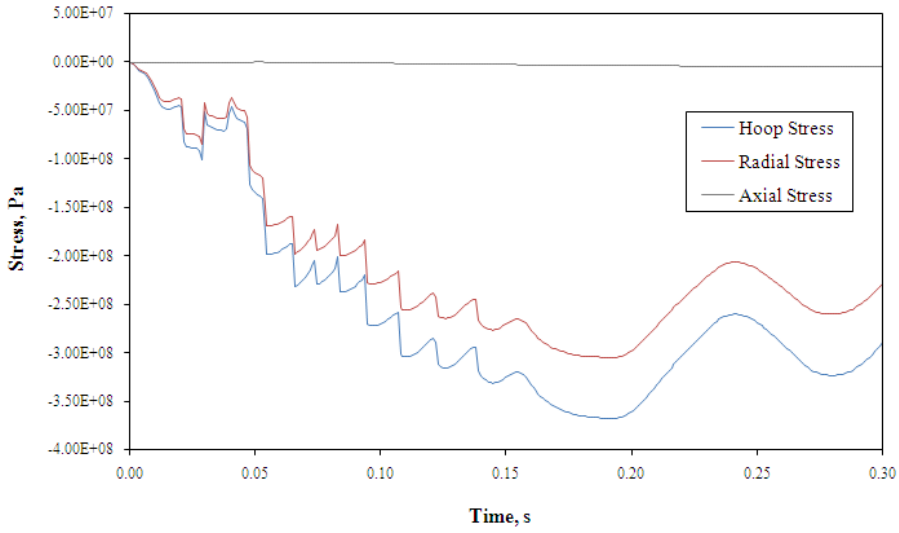

Figure 6.62 Effective hoop, radial and axial stress histories at point A.

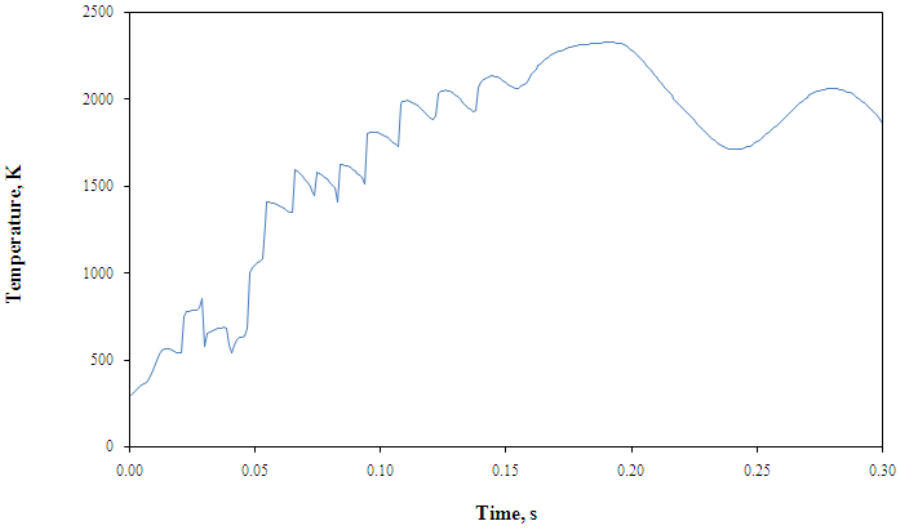

Figure 6.63 Temperature history at point A.

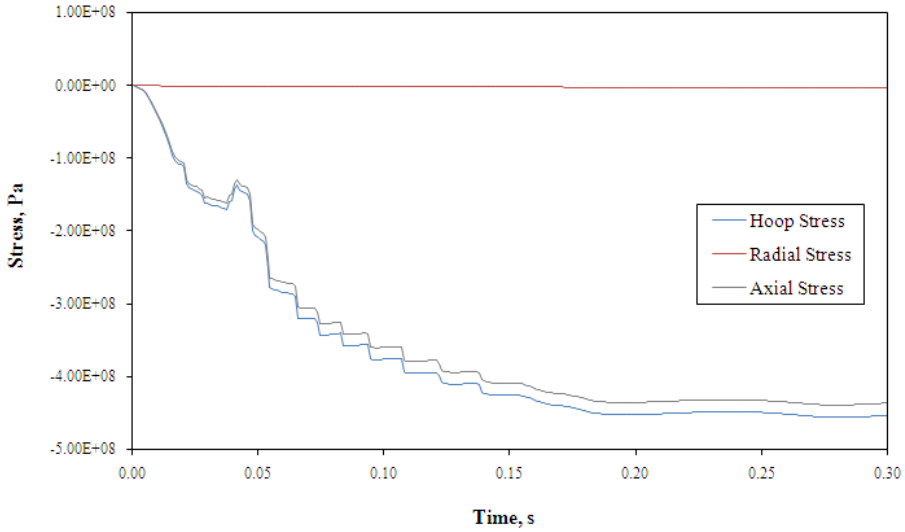

Figure 6.64 Effective hoop, radial and axial stress histories at point B.

.

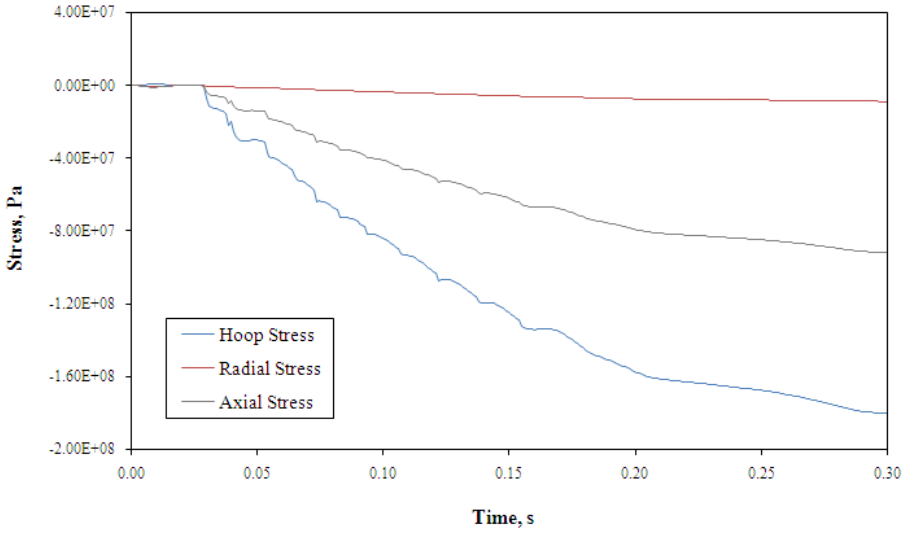

Figure 6.65 Effective hoop, radial and axial stress histories at point C.

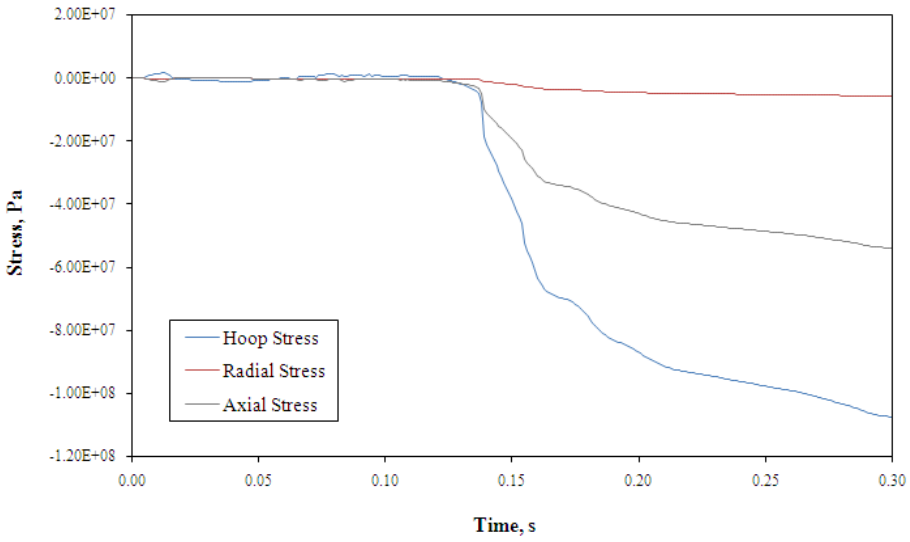

Figure 6.66 Effective hoop, radial and axial stress histories at point D.

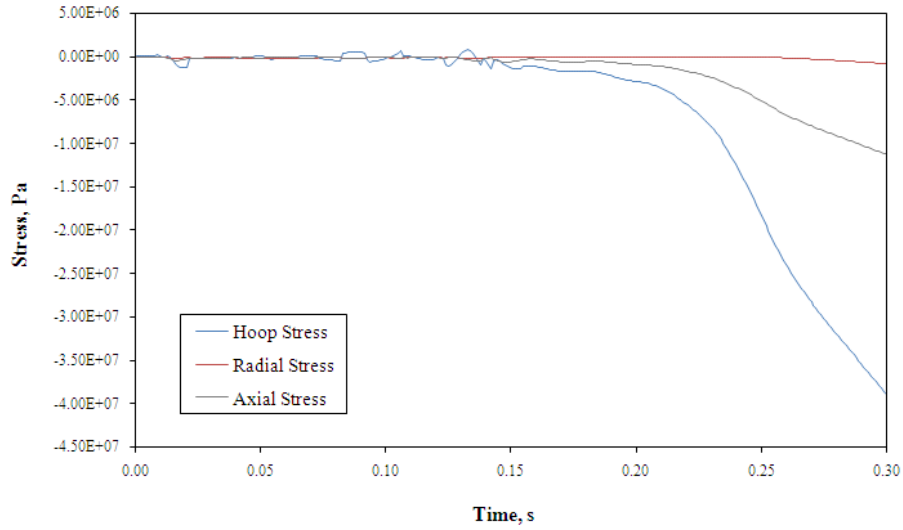

Figure 6.67 Effective hoop, radial and axial stress histories at point E.

The temperature history at point A, shown in Figure 6.63, presents with similar perturbations and provides an indication of their most probable source. When the associated stress response histories at point A are compared to the point's temperature history, it becomes clear how

strongly the combined stress response is dependent on thermal loading – based on the manner in the stress histories track the temperature history. As the thermoelastic stress contributions at any point are derived solely on the basis of the temperature at that point, one can deduce that the perturbations are caused by the numerically erroneous resolution of the conjugate heat transfer problem in Flow Model T. Based on this conclusion, it would appear that the perturbations in time observed here, are related to the perturbations in space observed in the wall temperature distribution of the 1 s solution to the same flow model. It is speculated that this error could either be attributed to an insufficient time discretization resolution and/or the inherent lack of variable conservation in time associated with the finite element method. Conveniently however, the perturbations appear to dissipate before the time maximum stress values are encountered, preserving the usefulness of the results.

Another distinct characteristic of the predicted responses is the same magnitude hierarchy among the hoop, radial and axial stress components observed during the burn duration response. In all but one scenario, that of point A, the greatest stress encountered was in the hoop direction, followed by that in the axial direction. For points B-E, the radial stress component encountered was negligible in comparison, confirming the minor influence that pressure-induced stresses appear to have had on the combined response within the exit cone. As the direction of heat flux encountered at point A was effectively in the axial direction, it is understandable that the axial stress component was calculated to be small in comparison to the hoop and radial components, as the ITE was free to expand in the axial direction.

The stress responses at points C, D and E, shown in Figures 6.65-6.67, indicate that an interesting thermal loading phenomenon is occurring at these locations. In comparison to the histories recorded at points A and B, where the effective stresses suggest that thermal loading occurs from the outset of the simulation, the histories of points C, D and E depict response delays of increasing time lengths, which suggest a delayed exposure to thermal loading at these points. These response delays can be quite adequately explained in the context of the developing flow of combustion gases, by the progression of the jet separation point down the length of the exit cone as the SRM chamber pressure increases. Before the arrival of this point, the local surface is exposed to temperatures not much greater than the ambient temperature as it is insulated from the hot core flow by a stagnant zone. As the point passes over the surface, it is rapidly exposed to heat of the boundary layer flow, which results in an equally rapid rise in

compressive surface stresses. It is this effect that is being observed in the stress responses at the exit cone points. In this regard, it is important to note that the ability of the solution scheme to provide accurate definition to the boundary layer is therefore critical if stress histories are to be reasonably predicted at these locations.

Figures 6.66 and 6.67 also indicate that the stress responses at points D and E have not yet reached their peaks by the end of the simulation period, before the thermal penetration zone deepens and subsequently relieves stresses at the surface of the nozzle. In spite of these compressive stress peaks not being registered, it is essentially impossible that the maximum stresses recorded in this region of the nozzle would greater than those further upstream. This is as a simple consequence of the fact that whilst the material in this region is the same, the magnitude of the thermal loading it is subjected to is considerably lower. In regards to maximum stresses, Table 6.8 compares maximum tensile and compressive stresses predicted to occur at each point by the ignition period and burn period structural simulations.

Stress Direction	**Simulation**	**Surface Stress (Pa)**				
		Point A	**Point B**	**Point C**	**Point D**	**Point E**
Tensile	Ignition Period	1.49E+05	1.19E+05	1.11E+06	1.61E+06	8.19E+05
	Burn Period	-	-	6.45E+06	4.70E+06	1.97E+05
Compressive	Ignition Period	-3.68E+08	-4.56E+08	-1.80E+08	-1.07E+08	-3.89E+07
	Burn Period	-2.39E+08	-4.41E+08	-1.55E+08	-8.98E+07	-2.80E+07

Table 6.8 Maximum tensile and compressive stresses predicted by ignition period and burn period simulations.

Results from these two sources are compared to demonstrate how the use of instantaneously applied burn period loading conditions and a significantly coarser mesh can approximate the maximum ignition period stresses to a fair degree of accuracy. In addition, this comparison confirms the superiority of surface stresses induced during ignition to those experienced during the steady operation of the SRM.

The ignition period simulation results shown in Table 6.8 provide a clear indication of the severity of the compressive stresses encountered on SRN2's wetted surface during the ignition

event. By contrast, the tensile stresses predicted by the ignition period simulation are shown to be of negligible magnitude. In the context of the typical compressive strength capacity of spatially reinforced carbon-carbon composite materials, the magnitude of the maximum compressive stresses indicated here is extreme and suggests that a thin zone of compressive material failure could develop across a fair portion of the nozzle's wetted surface during the ignition transient period. Importantly, it is conceivable that surface layer damage of this nature caused to the I.T.E and exit cone subcomponents during ignition, could potentially play a role in accelerating the initial rates nozzle ablation and erosion during nominal operation.

Although the failure mechanisms of spatially reinforced C-C materials have not been specifically considered in the current study, the above results indicate that a more advanced analysis of material failure in the context of the current problem needs to be undertaken, in order to establish a better understanding of the damage that is likely to be induced in such structures during SRM ignition. Furthermore, the similarity in the scale of the predicted thermal and stress penetration depths and the scale of the reinforcement rods employed in spatially reinforced C-C materials suggests that homogeneous material representation is an inaccurate simplification.

In terms of the overall performance of the SRN2 during ignition therefore, it can be concluded that although severe thermal stresses are induced during this period, the holistic distribution of effective stresses is insufficient to endanger the structural integrity of the nozzle structure as a whole.

6.7.6 Sensitivity of Thermostructural Response to Inertial Effects

The structural response results presented in the previous chapter failed to indicate the presence of inertial vibration in the nozzle when subjected to transient pressure loading. To clarify if such phenomena manifested in the apparently more oscillatory response of the structure to thermal loading, dynamic and quasi-static thermal stress responses were computed and compared at points B and E, as shown in Figures 6.67 and 6.68.

Points B and E were selected to provide insight into the response predicted at relatively stiff and flexible parts of the SRN2 structure. As can be seen, the solutions at point B are in excellent agreement with no vibrations and thus no detectable discrepancies present. The solutions at point E are also in very good agreement, although very minor vibrations are indicated to occur by the

dynamic solution between 0.05 s and 0.2 s. Given the flexibility in this region of the nozzle and in consideration of the highly transient loading, this negligible level of oscillation is reasonable.

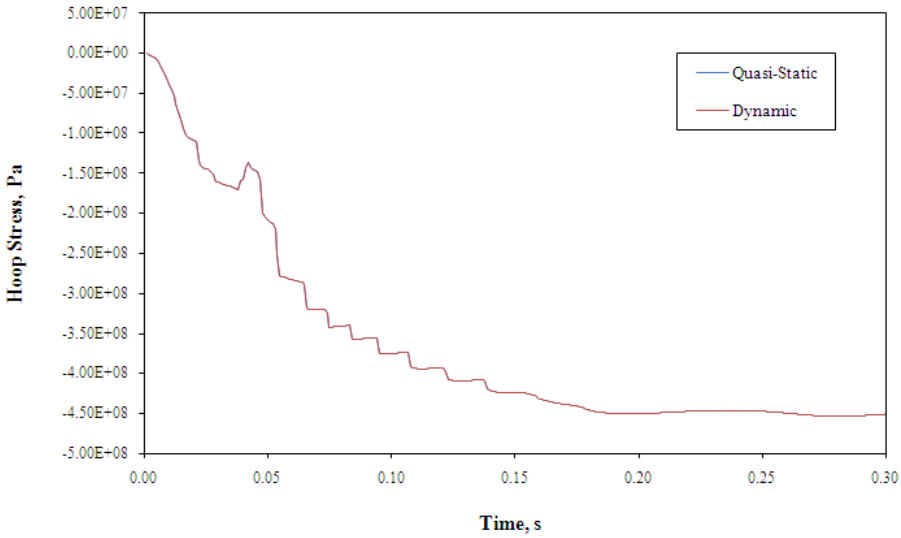

Figure 6.68 Comparison of quasi-static and dynamic hoop stress solutions at point B.

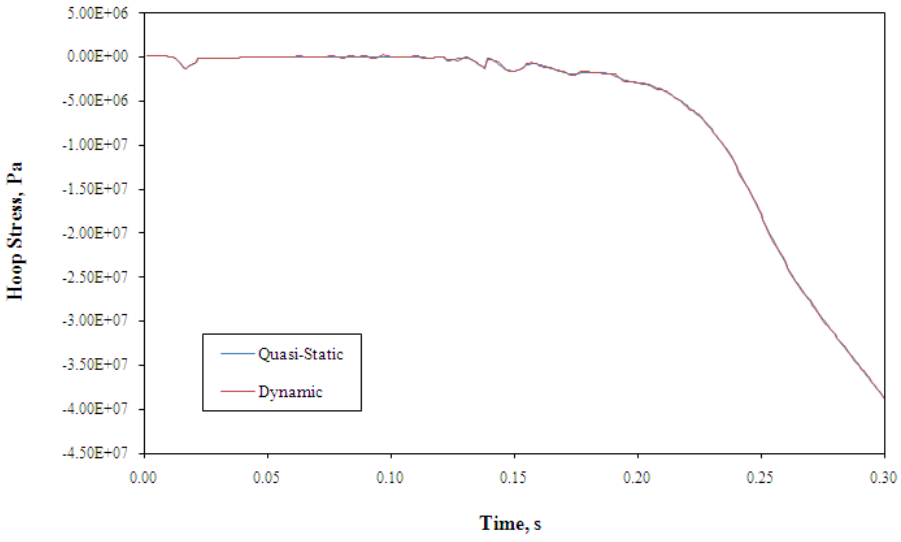

Figure 6.69 Comparison of quasi-static and dynamic hoop stress solutions at point E.

In an overall sense however, the solution agreement illustrated in Figures 6.67 and 6.68 provide a very clear indication that for the current conditions, inertial effects do not manifest appreciably in the response of SRN2 to thermal loading. It can therefore be deduced on the basis of response superposition, that the structure's inertia does not influence its response during the transient ignition period.

6.7.7 Sensitivity of Effective Structural Response to Ignition Rate

The final numerical investigation undertaken compared the simulated structural response of SRN2 in respect of the 0.6 s ignition transient, to the response of the structure simulated for the scaled 0.45 s and 0.75 s transients. Once again, data were recorded at sample points A-E to allow comparative response histories to be established. Fifteen sets of histories describing the evolution of hoop, radial and axial stresses at each point were compiled and analysed to determine the sensitivity of the structural response to the rate of SRM ignition. Selected results are now presented in Figures 6.69-6.75.

A review of these results indicates the presence of the same perturbations in the 0.45 s and 0.75 s responses that are observed in the 0.6 s response. If one considers the general nature of each perturbation, it would appear as though instead of growing smoothly with time, stresses remain roughly constant or decline, and then after a characteristic periodic time suddenly rise to updated values. An important observation is that the "update" period of the perturbations in the scaled transient responses at points A, C, D and E increases significantly at a time roughly halfway through the solution. Interestingly, the time step size in these two simulations is increased significantly over a period of 50 time steps from $1x10^{-4}$ s to $1x10^{-3}$ s at a simulation time of 0.15 s. The simultaneous change in perturbation characteristics therefore suggests a sensitivity of this phenomenon to the temporal discretization resolution, which is a useful observation.

The compromised scaled transient results make it difficult to draw absolute conclusions with regards to the impact that varying the rate of the ignition event has on stress generation in the nozzle. However, the general trend that unperturbed results would generate can be predicted to an extent. At point A, as displayed in Figures 6.69 and 6.70, it can clearly be seen that an increase in the ignition rate contributes to the generation of higher maximum hoop and radial stress magnitudes in the leading edge region. Interestingly, the retardation of the rate appears to induce a stronger response as well. This observation could be the result of a longer exposure to

heat flux elevated by the movement of combustion gases into the annular propellant grain pocket over a longer duration.

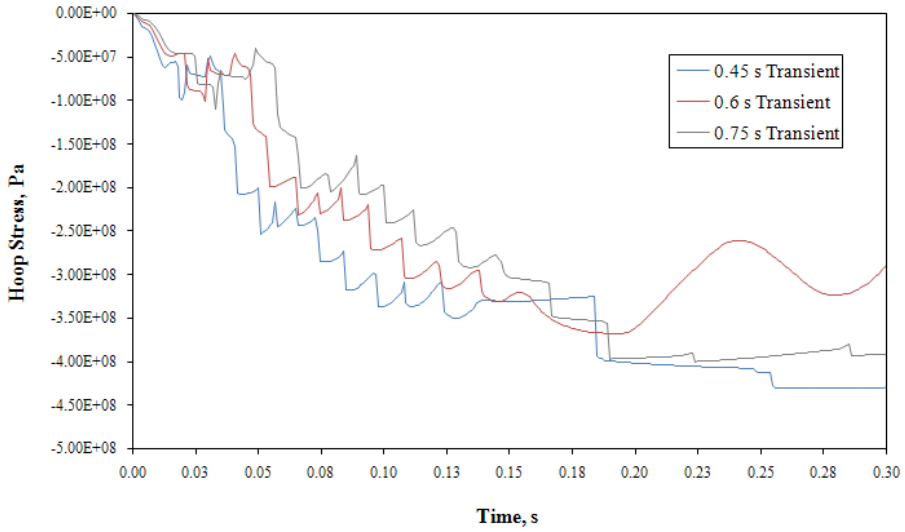

Figure 6.70 Comparative hoop stress histories at point A.

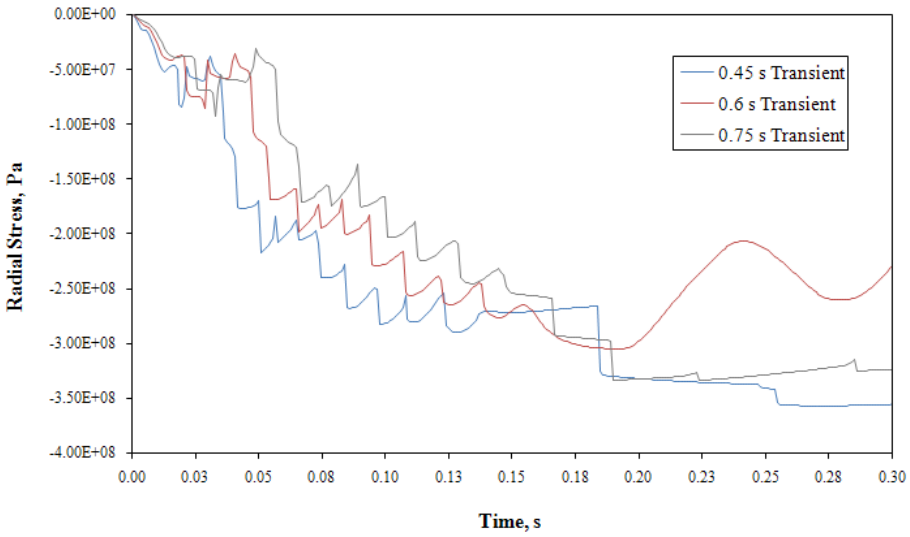

Figure 6.71 Comparative radial stress histories at point A.

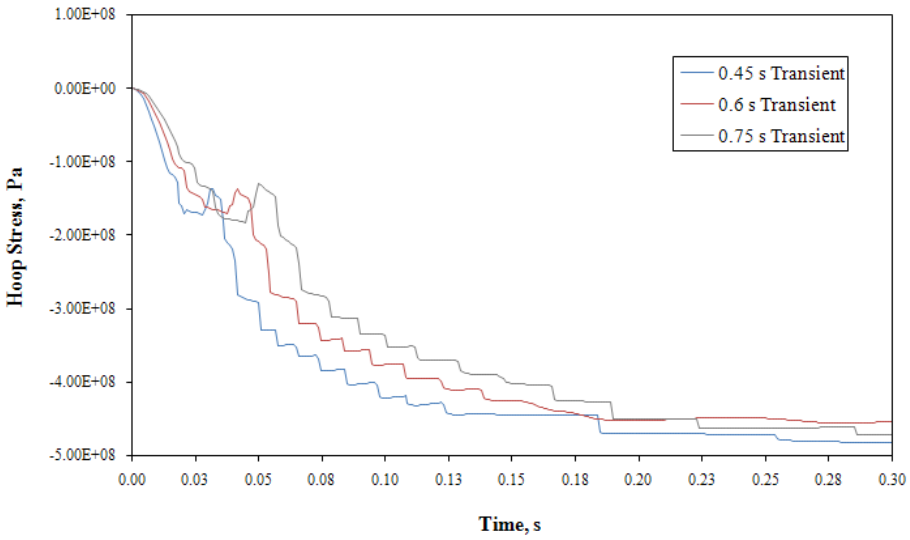

Figure 6.72 Comparative hoop stress histories at point B.

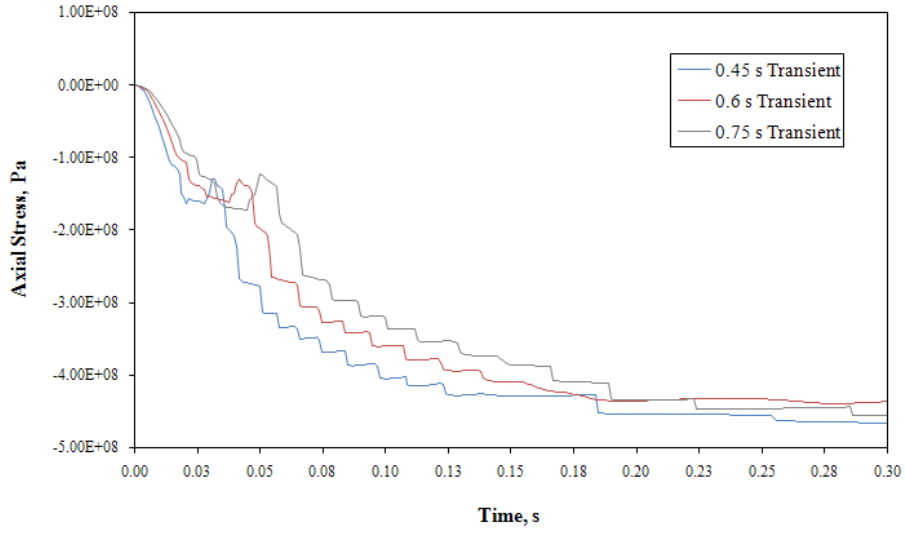

Figure 6.73 Comparative axial stress histories at point B.

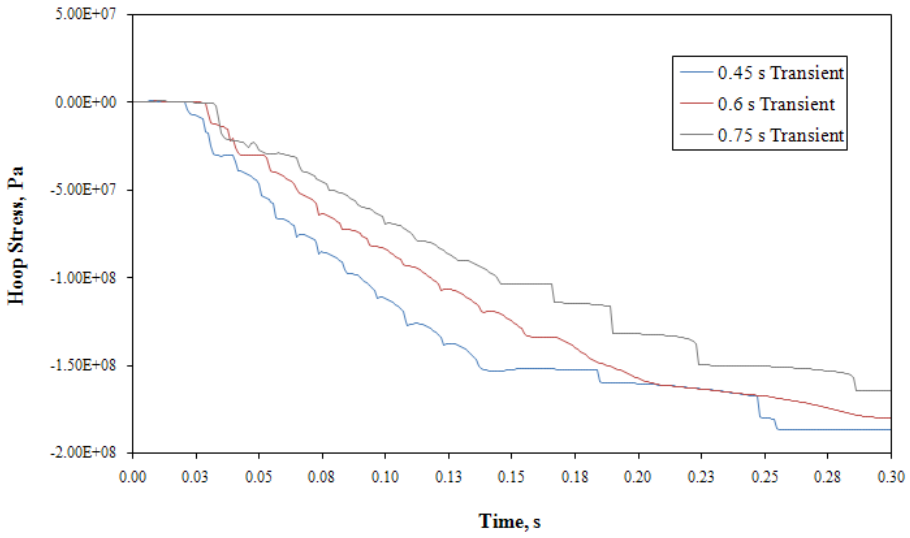

Figure 6.74 Comparative hoop stress histories at point C.

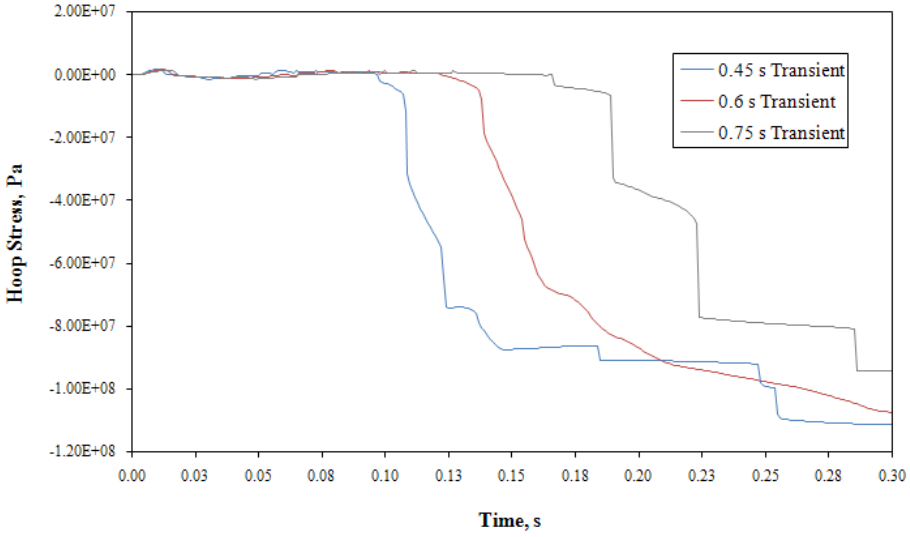

Figure 6.75 Comparative hoop stress histories at point D.

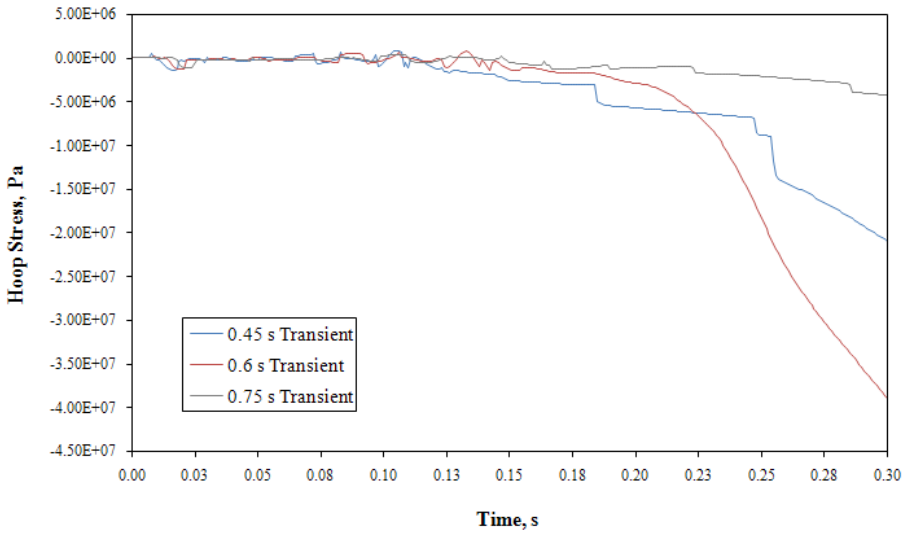

Figure 6.76 Comparative hoop stress histories at point E.

At the nozzle's throat on the other hand, only minor differences in the hoop and axial stress responses are observed, with the scaled transients again yielding slightly higher surface stresses. Along the exit cone, scaled separation point arrival times can clearly be seen, particularly in the responses at points D and E, shown in Figures 6.74 and 6.75, respectively. By the end of the simulation period at points D and E, the 0.75 s transient appears to have induced a lower hoop stress in comparison to the 0.6 s benchmark response, whilst the faster 0.45 s transient is shown to have generated a higher hoop stress. This result may well be attributable to an increase in the local heat transfer coefficient with an increase in separation point velocity.

Although the hoop stress histories at point E were still in a state of evolution at the end of the simulation, it can still clearly be seen that this phenomenon is not repeated at the tip of the exit cone. The responses in Figure 6.75 indicate that in spite of the separation point in the 0.45 s simulation arriving slightly ahead of that predicted by the benchmark simulation, hoop stress rises to a greater magnitude and more rapidly in the latter solution.

In an overall sense therefore, it can be concluded that rate at which the ignition event is prescribed to occur does notably affect the characteristics of the associated structural response of SRN2. In general, the faster 0.45 s transient induced higher hoop stresses at the nozzle surface

than the benchmark 0.6 s transient, although the magnitude by which the former response exceeded the latter varied considerably. The trend relating to the slower 0.75 s transient was less clear, however.

6.8 Conclusion

The numerical simulation of the ignition period structural response of the SRN2 nozzle to transient pressure and thermal loading conditions has been described in the current chapter. In addition, the solution approach developed to account for thermoelasticity in this response was outlined and the development of the constituent numerical models was detailed.

An element size sensitivity study was undertaken to determine the expected depth of the thermal penetration zone in the nozzle during the simulation period, and to establish the finite element discretization scheme that would most effectively and efficiently capture the associated thermoelastic response in this region. The discretization schemes subsequently employed in Flow Model T and Structural Model T were derived on the basis of the results of this study.

A burn period structural response simulation was conducted to evaluate the development of the temperature and stress fields within SRN2 during this period and, in addition, to enable a frame of reference to be provided to the ignition period structural response results. An evaluation of these results indicated that along the nozzle's wetted surface, maximum stresses were in encountered immediately after the application of loading.

Results derived from the ignition period structural response simulation highlighted a number of important response characteristics associated with this loading regime. Pressure loading was generally shown to induce a slightly larger distortion of the nozzle, which suggests that the incorporation of the ignition period thermoelastic response in the FSI solution would not greatly increase the degree of aeroelastic coupling that was demonstrated to occur between the nozzle and its flow field in Chapter 5.

In terms of the stress response, pressure loading induced a wide-ranging stress profile, low to moderate in magnitude, whereas thermal loading induced severe, highly localised stresses isolated to within a few millimetres of the wetted surface. Significantly, a comparison of thermostructural response results generated by quasi-static and dynamic solutions did not

suggest that the instigation of structural vibration or elastodynamic waves had occurred in response to the simulated ignition period thermal loading.

Finally, the stress response histories computed on the basis of the scaled ignition transients were compared to equivalent histories associated with the benchmark transient, to establish whether the surface stress response of the nozzle showed sensitivity to the rate at which motor ignition was specified to occur. The results obtained for the current conditions indicate that a degree of sensitivity does in fact exist, appearing stronger at SRN2's leading edge and towards the rear of its exit cone.

CHAPTER 7

Concluding Remarks

The objective of this study was to employ numerical modelling techniques to simulate and investigate the structural response of a composite solid rocket motor nozzle during the motor ignition period. In the distinct absence of published literature providing treatment to this problem, several important determinations relating to SRM nozzle behaviour during ignition were sought. Furthermore, to provide quantitative and qualitative context to this response, comparisons were made to the predicted response of the nozzle during the motor burn period.

Three ignition period response simulations were conducted using a number of flow, thermal and structural models and through the implementation of the ADINA multiphysics finite element code. To as great an extent as possible, the validity of ADINA's high-speed compressible flow and orthotropic elasticity models was established with reference to a review of associated literature. The validity of its orthotropic thermal conduction and thermoelasticity models was established by means of a specific validation study as described in Chapter 3.

The simulations were carried out with respect to two SRM nozzle designs, developed by the author on the basis of established nozzle design practice. The first design, Solid Rocket Nozzle 1, was analysed in the initial simulation described in Chapter 4, whilst the second design, Solid Rocket Nozzle 2, was considered in the second and third simulations, outlined in Chapters 5 and 6, respectively. Both designs comprised four fundamental substructures and employed spatially reinforced carbon-carbon composites for thermal lining components, a tape wound carbon-phenolic composite for insulation and steel for motor attach structures. Materials were modelled as being homogeneous and linearly elastic in all cases.

Each simulation was conducted to characterise the response of the constituent upon subjection to a particular loading regime. The first simulation considered the instantaneous application of steady thermal and pressure loading conditions derived from results published in literature, and utilised two numerical models. A thermal model calculated the transient temperature distribution within the SRN1 nozzle, whilst a structural model determined the response of the nozzle in

respect of this temperature distribution and the pressure loading condition. The ignition period structural response was resolved in terms of both the dynamic and quasi-static forms of the equilibrium equations to assess the significance of considering the inertial terms in developing the solution. The results obtained were presented by the author at the *6th International Conference on Composite Science and Technology* and later published in the international journal, *Composite Structures* (Morozov and Pitot de la Beaujardiere (2009)).

The second simulation computed the ignition period structural response of SRN2 to a transient pressure loading condition in isolation. The loading condition was generated by a laminar flow model developed to simulate the unsteady flow of combustion gases through the nozzle during an ignition event. The resulting transient wall pressure distribution was applied to an associated structural model in coupled and uncoupled fluid-structure interaction simulations, where the structural response was solved for dynamically. A comparison between the coupled and uncoupled structural solutions allowed the degree of ignition period aeroelastic coupling occurring between the nozzle and its flow field to be determined in reference to pressure loading alone. Conclusions relating to the inertial nature of the nozzle's response to a significantly more representative loading condition could also be drawn. The results of this work were presented by the author at the *9th International Conference on Computational Structures Technology* and published in the conference's refereed proceedings (Pitot de la Beaujardiere et al (2008)).

The final simulation predicted the ignition period structural response of SRN2 to the combined effects of transient thermal and pressure loading, by employing two sets of flow and structural models. The first flow model generated the pressure loading condition for an associated structural model in a manner identical to the previous simulation. The second flow model incorporated solid elements and used a conjugate heat transfer technique to resolve the temperature distribution in the thermal penetration zone of the nozzle during the ignition period. This thermal data was mapped to a related structural model which was used derive the thermoelastic response of SRN2. Separate thermal and structural models were developed to determine the structural response of the nozzle during the burn period, in a manner identical to that employed in the first simulation detailed in Chapter 4. The comprehensive set of results obtained in the current simulation represented the most advanced response predictions generated in this study and allowed a number of important ignition period behavioural characteristics to be observed. Most of the results reported in Chapter 6 were presented by the author at the

45th AIAA/ASME/SAE/ASEE Joint Propulsion Conference & Exhibit and published in the conference's refereed proceedings (Pitot de la Beaujardiere et al (2009)).

In assessment of the overall results presented in this dissertation, determinations have been made with respect to each of the important ignition period structural response characteristics highlighted in Chapter 1. These findings will now be outlined on an individual basis in reference to pertinent simulation results.

As far as the inertial characteristics of the response are concerned, the correct treatment of the equilibrium equations by the solution algorithm was in question. The results in Chapter 4 showed that in the case of the instantaneous application of thermal and pressure loading, an elastodynamic response was indicated and that a dynamic solution approach was needed to sufficiently capture the response. The introduction of a more realistic transient pressure loading condition in the simulation discussed in Chapter 5 however, demonstrated that at a significantly lower loading rate, inertial effects did not manifest in the response. The incorporation of thermoelastic effects in the simulation described in Chapter 6 did not lead to the generation of structural or elastodynamic vibration either. It is therefore concluded that under the current conditions, the ignition period response of a composite SRM nozzle is not influenced by inertial effects and the simulation thereof does not require the application of a dynamic solution regime.

In terms of the degree of aeroelastic coupling that occurs between an SRM nozzle and its associated exhaust stream during the ignition period, results presented for the coupled and uncoupled fluid-structure interaction simulations outlined in Chapter 5, showed that the consideration of transient pressure loading in isolation did not give rise to significant coupling between the flow and structure. The thermoelastic response of the SRN2 structure could not be explicitly incorporated in the FSI simulations, which made it impossible to derive an overall conclusion regarding aeroelasticity directly. However, comparisons were made between the pressure-induced structural displacements of SRN2 predicted in the simulations above and the thermally-induced displacements estimated in the related Chapter 6 simulation. These comparisons indicated that for the most part, nozzle distortions attributable to thermal loading were slightly lower in magnitude and therefore indicated less potential to influence the exhaust flow. On these grounds and for the nature of the simulations undertaken, it was concluded that

the aeroelastic coupling occurring between a composite SRM nozzle and the exhaust flow during ignition is of negligible consequence.

In regards to the manner and magnitude in which thermal and mechanical load sources contributed to the ignition period structural response of a nozzle, the differences were significant. The independent resolution of the pressure-induced and thermally-induced structural responses of SRN2 in the simulation outlined in Chapter 6 provided a convenient means to make this assessment. An observation of results revealed that pressure loading during the ignition period generally instigated greater displacements in the nozzle than the associated thermal loading. Furthermore, it was shown to induce a widely-distributed stress response of low to moderate magnitude, whereas thermal loading generated high to severe stresses in the very shallow thermal penetration zone adjacent to the nozzle's wetted surface. As a result of this observation it can be concluded that during motor ignition, the displacement response of a composite SRM nozzle is dominated by pressure loading, whilst in terms of the associated stress response, thermal loading should be of most concern.

Regarding the sensitivity of the response induced in composite SRM nozzles to the rate of motor ignition, results presented in Chapter 6 indicate that such sensitivity does appear to exist, despite the manifestation of spurious perturbations in the stress response histories analysed. In particular, ignition rate dependence appeared to a greater degree at SRN2's leading edge and towards the rear of its exit cone.

The significance of SRN2's ignition period structural response in the context of that simulated during the remaining burn period was well illustrated by the final simulation described in Chapter 6. Whilst it could be deduced that the structural response of the nozzle at internal locations was more significant during the burn period than at the same positions during the ignition period, stresses encountered at the wetted surface were predicted to be markedly high towards the end of ignition than at any other point in time. Furthermore, maximum ignition period surface stresses were shown to be of comparable magnitude to the maximum stresses encountered during the entire burn period. Having said this, the distribution of intense thermoelastic stresses was limited to a highly localised zone and did not appear to threaten the overall integrity of the SRN2 structure. In respect of these findings, it can be concluded that

maximum stresses encountered during the ignition period are significant and can reach potentially damaging levels in the thermal penetration zone.

Although this finding does not necessarily influence the exercise of structural optimisation of composite SRM nozzles, it does indicate that thermally-induced surface damage may occur during the SRM ignition process. The effect that such damage would subsequently have on local ablation/erosion rates is therefore brought into question, and it is felt that the matter clearly requires more advanced investigation.

In this regard, much potential exists for the fidelity of the numerically-derived ignition period structural response to be improved. With the incorporation of adequate turbulence and two-phase modelling and the accommodation of combustion product reactivity, SRM nozzle flows can be predicted with considerable accuracy. Furthermore, the asymmetric flow effects that have been reported in literature to occur during ignition could be captured with the specification of a three-dimensional solution domain. In terms of boundary conditions, more elaborate modelling of the SRM ignition process could be undertaken and the flow domain could be extended to simulate flow external to the nozzle. The inclusion of the radiation heat transfer mode would increase the accuracy with which nozzle wall heat flux could be modelled.

As far as structural modelling is concerned, the specification of material temperature dependence and an appropriate pseudo-plastic material model to describe carbon-carbon components would be highly beneficial. In addition, the incorporation of a damage modelling facility to predict the progressive deterioration of the composite substructures would enable an improved prediction of failure modes.

Regardless of such refinements, it is believed that the results predicted on the basis of the current numerical simulation methodology have been demonstrated to provide novel and useful insight into the response behaviour of composite solid rocket motor nozzles during motor ignition.

REFERENCES

ADINA R&D, Inc., “ADINA System 8.5 Release Notes”, Copyright ADINA R&D, Inc., Watertown, United States of America, 2008.

Aubard, X., “New Advances in Damage Mechanics and Computational Methods for Composites: from Research to Industry for Spatial Applications”, Composites Science and Technology, No. 61, pp. 2337-2344, 2001.

Aubard, X., Cluzel, C., Guitard, L. and Ladevèze, P., “Modelling of the Mechanical Behaviour of 4D Carbon/Carbon Composite Materials”, Composites Science and Technology, No. 58, pp. 701-708, 1998.

Bartz, D. R., “A Simple Equation for Rapid Estimation of Rocket Nozzle Convective Heat Transfer Coefficient”, Jet Propulsion, Vol. 27, No. 1, pp. 49-51, 1957.

Bathe, K. J., “Finite Element Procedures”, Prentice Hall, Pearson Education, Inc., United States of America, 2006.

Bathe, K. J., Zhang, H. and Wang, M. H., “Finite Element Analysis of Incompressible and Compressible Fluid Flows with Free Surfaces and Structural Interactions”, Computers and Structures, Vol. 56, No. 2/3, pp. 193-213, 1995.

Bathe, K. J., Zhang, H. and Ji, S., “Finite Element Analysis of Fluid Flows Fully Coupled with Structural Interactions”, Computers and Structures, Vol. 72, pp. 1-16, 1999.

Berdoyes, I. and Thebault, J., “Thermostructural Composite Materials: from Space to Advanced Fission Applications”, Euromat 2005 Conference, Prague, Czech Republic, 5-9 September, 2005.

Berdoyes, M., “SRM Nozzle Design Breakthroughs with Advanced Composite Materials”, Proceedings of the 29th AIAA, SAE, ASME, and ASEE, Joint Propulsion Conference and Exhibit, Monterey, United States of America, 28-30 June, 1993.

Bianchi, D., Nasuti, F. and Martelli, E., “Coupled Analysis of Flow and Surface Ablation in Carbon-Carbon Rocket Nozzles”, Proceedings of the 40th Thermophysics Conference, Seattle, United States of America, 23-26 June, 2008.

Bussiere, M. and Mora, B., “Ariane 5 Booster Nozzle: Components Description and Dimensioning”, Acta Astronautica, Vol. 34, pp. 83-89, 1994.

Chang, I. S., “Three-Dimensional Supersonic Internal Flows”, AIAA Paper 76-423, July, 1976.

Chang, I. S., “One- and Two-Phase Nozzle Flows”, AIAA Journal, Vol. 18, No. 12, pp. 1455-1461, 1980.

Chang, I. S., “Three-Dimensional, Two-Phase Supersonic Nozzle Flows”, AIAA Journal, Vol. 21, No. 5, pp. 671-678, 1983.

Chang, I. S., “Three-Dimensional, Two-Phase, Transonic, Canted Nozzle Flows”, AIAA Journal, Vol. 28, No. 5, pp. 790-797, 1990.

Chang, I. S., Chang, C. L. and Chang, S. C., “Unsteady Navier-Stokes Rocket Nozzle Flows”, Proceedings of the 41st AIAA/ASME/SAE/ASEE Joint Propulsion Conference and Exhibit, Tucson, United States of America, 11-13 July, 2005.

Chang, I. S., Chang, C. L. and Chang, S. C., “3D Unsteady Navier-Stokes Rocket Nozzle Flows”, Proceedings of the 42nd AIAA/ASME/SAE/ASEE Joint Propulsion Conference and Exhibit, Sacramento, United States of America, 9-12 July, 2006.

Chase, C. A., “IUS flight motor designs and full-scale development program”, Proceedings of the 14th American Institute of Aeronautics and Astronautics and Society of Automotive Engineers, Joint Propulsion Conference, Las Vegas, United States of America, 25-27 July, 1978.

Chen, C. L. AND Chakravarthy, S. R., “Numerical Investigation of Separated Nozzle Flows”, AIAA Journal, Vol. 32, No. 9, p. 1836, 1994.

Cho, H., Kardomateas, G. A. and Valle, C. S., “Elastodynamic Solution for the Thermal Shock Stresses in an Orthotropic Thick Cylindrical Shell”, Transactions of the ASME: Journal of Applied Mechanics, Vol. 65, pp. 184-193, 1998.

Courant, R. and Friedrichs, K., “Supersonic Flow and Shock Waves” 1st Edition, Interscience, New York, 1948.

Cozart, A. and Shivakumar, K., “Stress Analysis of a 3-D Braided Composite Ablative Nozzle”, Proceedings of the 40th AIAA/ASCE/AHS/ASC Structures, Structural Dynamics and Materials Conference, St Louis, United States of America, 12-15 April, 1999.

Day, L. E., “The Space Shuttle - Development challenge of the 1970's”, Proceedings of the AIAA Test Effectiveness in the 70’s Conference, Palo Alto, United States of America, 1-3 April, 1970.

Dao-Sheng, L., “Analysis of Transient Thermal Stress in Cylindrically Orthotropic Tubes”, Applied Mathematics and Mechanics, English Edition, Vol. 24, No. 12, pp. 1398-1402, 2003.

Delneste, L. and Perez, B., “An Inelastic Finite Element Model of 4D Carbon-Carbon Composites”, AIAA Journal, Vol. 21, No. 8, pp. 1143-1149, 1983.

Ellis, R. A., “Development of a Carbon-Carbon Nozzle for the Trident I C4 Third Stage Nozzle”, Proceedings of the JANNAF 1973 Propulsion Conference, Las Vegas, United States of America, 6-8 November, 1973.

Ellis, R. A., “Nozzle Efficiency Improvements with Advanced Materials”, Proceedings of the 1974 JANNAF Propulsion Meeting, San Diego, United States of America, 22-24 October, 1974.

Ellis, R. A., “Solid Rocket Motor Nozzles – NASA Space Vehicle Design Criteria (Chemical Propulsion)”, NASA SP-8115, National Aeronautics and Space Administration, United States of America, 1975.

Ellis, R. A., “Solid Rocket Motor Nozzles”, Notes from Presentation Delivered at the University of Alabama in Huntsville, United States of America, 2006.

Ellis, R. A. and Berdoyes, M., “An Example of Successful International Cooperation in Rocket Motor Technology”, Acta Astronautica, Vol. 51, No. 1-9, pp. 47-56, 2002.

Evseev, E. G. and Morozov, E. V., “Aeroelastic Interaction of the Shock Waves with the Thin-Walled Composite Shells”, Composite Structures, Vol. 54, pp. 153-159, 2001.

Hendriana, D. and Bathe, K. J., “On a Parabolic Quadrilateral Finite Element for Compressible Flows”, Computer Methods in Applied Mechanics and Engineering, No. 186, pp. 1-22, 2000.

Hildreth, J. H., “Advances in Solid Rocket Motor Nozzle Design and Analysis Technology since 1970”, Chapter Two in “Design Methods in Solid Rocket Motors”, AGARD Lecture Series LS 150, Advisory Group for Aerospace Research and Development, NATO, revised 1988.

Holden, M. S., “A Study of Flow Separation in Regions of Shock Wave-Boundary Layer Interaction in Hypersonic Flow”, Proceedings of the 11th AIAA Fluid and Plasma Dynamics Conference, Seattle, United States of America, 1978.

Hwang, C. J. and Chang, G. C., “Numerical Study of Gas-Particle Flow in a Solid Rocket Nozzle”, AIAA Journal, Vol. 26, No. 6, pp. 682-689, 1988.

Jacques, L. J. and Seguin, J. A. M., “Two-Dimensional Transonic Two-Phase Flow in Axisymmetric Nozzles”, AIAA Paper 74-1088, 1974.

Johnston, W. A., “Flow-Structural Analysis of the Ariane 5 Solid Rocket Motor During Ignition Transient” Proceedings of the 34th AIAA Aerospace Sciences Meeting and Exhibit, Reno, United States of America, 15-18 January, 1996.

Johnston, W. A. and Murdock, J. W., “Flow-Structure Interaction Inside a Solid Rocket During Ignition Transient”, Proceedings of the 30th AIAA/ASME/SAE/ASEE Joint Propulsion Conference, Indianapolis, June, 1994.

Jones, V. And Shukla, K. N., “Fluid Flow in Rocket Nozzles”, AIAA Paper 98-3840, 1998.

Jorant, P., “Ariane 5 Family”, Proceedings of the Space Programs and Technologies Conference and Exhibit, Huntsville, United States of America, 21-23 September, 1993.

Kardomateas, G.A., “The Initial Phase of Transient Thermal Stresses due to General Boundary Thermal Loads in Orthotropic Hollow Cylinders”, Transactions of the ASME: Journal of Applied Mechanics, Vol. 57, pp. 719-724, 1990.

Kliegel, J. R. and Nickerson, G. R., “Axisymmetric Two-Phase Perfect Gas Performance Program”, TRW Systems Group, Vols. I and II, Redondo Beach, United States of America, April, 1967.

Lacoste, M., Lacombe, A., Joyez, P., Ellis, R. A., Lee, J. C. and Payne, F. M., “Carbon/Carbon Extendible Nozzles”, Acta Astronautica, Vol. 50, No. 6, pp. 357-367, 2002.

Ladevèze, P., Guitard, L., Champaney, L. and Aubard, X., “Debond Modeling for Multidirectional Composites”, Computer Methods in Applied Mechanics and Engineering, No. 185, pp. 109-122, 2000.

Lapp, P. and Quesada, B., “Analysis of Solid Rocket Motor Nozzle”, Proceedings of the 28th AIAA/ASME/SAE/ASEE Joint Propulsion Conference, Nashville, United States of America, 6-8 July, 1992.

Lefrançois, E., Dhatt, G. And Vandromme, D., “Fluid-Structure Interaction with Application to Rocket Engines”, International Journal for Numerical Methods in Fluids, No. 30, pp. 865-895, 1999.

Lefrançois, E., “Numerical Validation of a Stability Model for a Flexible Over-Expanded Rocket Nozzle”, International Journal for Numerical Methods in Fluids, No. 49, pp. 349-369, 2005.

Lemoine, L., “Solid Rocket Nozzle Thermostructural Behaviour”, Proceedings of the 11th AIAA/SAE Propulsion Conference, Anaheim, United States of America, 29 September – 1 October, 1975.

Montesano, J., Greatrix, D. R., Behdinan, K. And Fawaz, Z., “Structural Oscillation Considerations for Solid Rocket Internal Ballistics Modeling”, Proceedings of the 41st AIAA/ASME/SAE/ASEE Joint Propulsion Conference and Exhibit, Tucson, United States of America, 11-13 July, 2005.

Montesano, J., Behdinan, K., Greatrix, D. And Fawaz, Z., “Internal Chamber Modeling of a Solid Rocket Motor: Effects of Coupled Structural and Acoustic Oscillations on Combustion”, Journal of Sound and Vibration, No. 311, pp. 20-38, 2008.

Moríñigo, J. A. and Salvá, J. J., “Numerical Study of the Start-up Process in an Optimized Rocket Nozzle”, Aerospace Science and Technology, Vol. 12, pp. 485-489, 2008.

Morozov, E. V. and Pitot de la Beaujardiere, J. F. P., “Numerical Simulation of the Dynamic Thermostructural Response of a Composite Rocket Nozzle Throat”, Composite Structures, No. 91, pp. 412-420, 2009.

Mouronval, A. S., Hadjadj, A., Kudryavtsev, A. N. and Vandromme, D., “Numerical Investigation of Transient Nozzle Flow”, Shock Waves, Vol. 12, pp. 403-411, 2002.

Mouronval, A. S. and Hadjadj, A., “Numerical Study of the Starting Process in a Supersonic Nozzle”, Journal of Propulsion and Power, Vol. 21, No. 2, p. 374, 2005.

Mukherjee, N. and Sinha, P. K., “Thermostructural Analysis of Rotationally Symmetric Multidirectional Fibrous Composite Structures”, Computers and Structures, Vol. 65, No. 6, pp. 809-817, 1997.

NASA Image Exchange Website, http://nix.larc.nasa.gov.

Nasuti, F. and Onofri, M., “Viscous and Inviscid Vortex Generation During Startup of Rocket Nozzles”, AIAA Journal, Vol. 36, No.5, p. 809, 1998.

Östlund, J., “Flow Processes in Rocket Engine Nozzles with Focus on Flow Separation and Side-loads”, TRITA-MEK Technical Report 2002:09, Department of Mechanics, Royal Institute of Technology, Stockholm, Sweden, 2002.

Parsons, I. D., Alavilli, P., Namazifard, A., Acharya, A., Jiao, X. and Fiedler, R., “Coupled Simulations of Solid Rocket Motors”, Proceedings of the 36th AIAA/ASME/SAE/ASEE Joint Propulsion Conference and Exhibit, Huntsville, United States of America, 16-19 July, 2000.

Pitot de la Beaujardiere, J. F. P., Morozov, E. V. and Bright, G., “Simulation of Fluid-Structure Interaction Phenomena of a Composite Rocket Nozzle”, Proceedings of the 9th International Conference on Computational Structures Technology, Athens, Greece, 2-5 September, 2008.

Pitot de la Beaujardiere, J. F. P., Morozov, E. V. and Bright, G., “Numerical Simulation of the Aerothermostructural Response of a Composite Solid Rocket Motor Nozzle During Motor Ignition”, Proceedings of the 45th AIAA/ASME/SAE/ASEE Joint Propulsion Conference & Exhibit, Denver, United States of America, 2009.

Ramesh Kumar, R., Vinod, G., Renjith, S., Rajeev, G., Jana, M. K., Harikrishnan, R., “Thermo-Structural Analysis of Composite Structures”, Materials Science and Engineering A, No. 412, pp. 66-70, 2005.

Regan, J. F., Thompson, H. D. and Hoglund, R. F., “Two-Dimensional Analysis of Transonic Gas-Particle Flows in Axisymmetric Nozzles”, Journal of Spacecraft and Rockets, Vol. 8, p. 346, 1971.

Reismann, H. and Padlog, J., "Forced Axisymmetric Motions of Cylindrical Shells", Journal of the Franklin Institute, Vol. 284, No. 5, 1967.

Schlichting, H., “Boundary-Layer Theory”, 7th edition, McGraw-Hill Company, New York, pp. 333, 1979.

Schwane, R. And Xia, Y., “Investigation of Nozzle Stability by Numerical Fluid Structure Interaction Calculation [for rocket engine nozzles]”, Proceedings of the 43rd AIAA Aerospace Sciences Meeting and Exhibit, Reno, United States of America, 10-13 January, 2005.

Schwane, R. And Xia, Y., “Time-Accurate CFD Predictions and Data Validation for Side Load Generation by Flow-Structure Coupling in Over-Expanded Rocket Nozzles”, Journal of Mathematical Modelling and Algorithms, Vol. 4, No. 1, pp. 53-65, 2005.

Serra, R. A., “Determination of Internal Gas Flows by a Transient Numerical Technique”, AIAA Journal, Vol. 10, No. 5, p. 603, 1972.

Shibato, Y. and Kuroda, S., “History of Liquid Propellant Rockets in Japan”, Proceedings of the 56th International Astronautical Congress of the International Astronautical Federation, the International Academy of Astronautics, and the International Institute of Space Law, Fukuoka, Japan, 17-21 October, 2005.

Shimada, T., Sekiguchi, M. and Sekino, N., “Flow Inside a Solid Rocket Motor with Relation to Nozzle Inlet Ablation”, AIAA Journal, Vol. 45, No. 6, 2007.

Sirko, R., “Boeing Launch Vehicles and Systems”, Proceedings of the 21st International Communications Satellite Systems Conference and Exhibit”, Yokohama, Japan, 15-19 April, 2003.

Stanton, E. L. and Kipp, T. E., “Nonlinear Mechanics of Two-Dimensional Carbon-Carbon Composite Structures and Materials”, AIAA Journal, Vol. 23, No. 8, pp. 1278-1284, 1984.

Sutton, G. P., “Rocket Propulsion Elements: An Introduction to the Engineering of Rockets”, 3rd Edition, John Wiley & Sons, New York, 1963.

Sutton, G. P. and Biblarz, O., “Rocket Propulsion Elements: An Introduction to the Engineering of Rockets”, 7th Edition, John Wiley & Sons, New York, 2001.

Tarnopol’skii, Y. M., Zhigun, I. G. and Polyakov, V. A., “Spatially Reinforced Composites”, Technomic, Lancaster, Pennsylvania, United States of America, 1992.

Thakre, P. and Yang, V., “Chemical Erosion of Carbon-Carbon/Graphite Nozzles in Solid-Propellant Rocket Motors”, Journal of Propulsion and Power, Vol. 24, No. 4, pp. 822-833, 2008.

Timoshenko, S. P. and Woinowsky-Krieger, S., “Theory of Plates and Shells”, Second Edition, McGraw-Hill, 1959.

Truchot, A., “Design and Analysis of Solid Rocket Motor Nozzle”, Chapter 3 in “Design Methods in Solid Rocket Motors”, AGARD Lecture Series LS 150, Advisory Group for Aerospace Research and Development, NATO, revised 1988.

Vandenboom, M. and Heister, S. D., “Application of Advanced Materials in a Composite Rocket Nozzle”, Proceedings of the 34th AIAA/ASME/SAE/ASEE Joint Propulsion Conference and Exhibit, Cleveland, United States of America, 13-15 July, 1998

Verma, S. B., Stark, R. and Haidn, O., “Relation between Shock Unsteadiness and the Origin of Side-loads inside a Thrust Optimized Parabolic Rocket Nozzle”, Aerospace Science and Technology, Vol. 10, pp. 474-483, 2006.

Windhorst, T. and Blount, G., “Carbon-Carbon Composites: A Summary of Recent Developments and Applications”, Materials & Design, Vol. 18, No. 1, pp. 11-15, 1997.

Xi, W., Kui, Z., Wei, Z. and Ju Bing, C., “Theoretical Solution and Finite Element Solution for an Orthotropic Thick Cylindrical Shell under Impact Load”, Journal of Sound and Vibration, No. 236, pp. 129-140, 2000.

Yoo, J. S., Cho, I. H., Kim, C. G., “Thermoelastic Analysis of a Kick Motor Nozzle Incorporating Spatially Reinforced Composites”, Journal of Spacecraft and Structures, Vol. 40, No.1, pp. 83-91, 2003.

Yoo, J. S., Lee, S. E. and Kim, C. G., “Prediction of Mechanical Behavior of Spatially Reinforced Composites for Kick Motor Nozzle”, Composite Structures, Vol. 54, pp. 57-65, 2001.

Zhang, H., Zhang, X., Ji, S., Guo, Y., Ledezma, G., Elabbasi, N. and deCougny, H., “Recent Development of Fluid-Structure Interaction Capabilities in the ADINA System”, Computers and Structures, Vol. 81, pp. 1071-1085.

APPENDICIES

APPENDIX A – SRN Nozzle Geometries

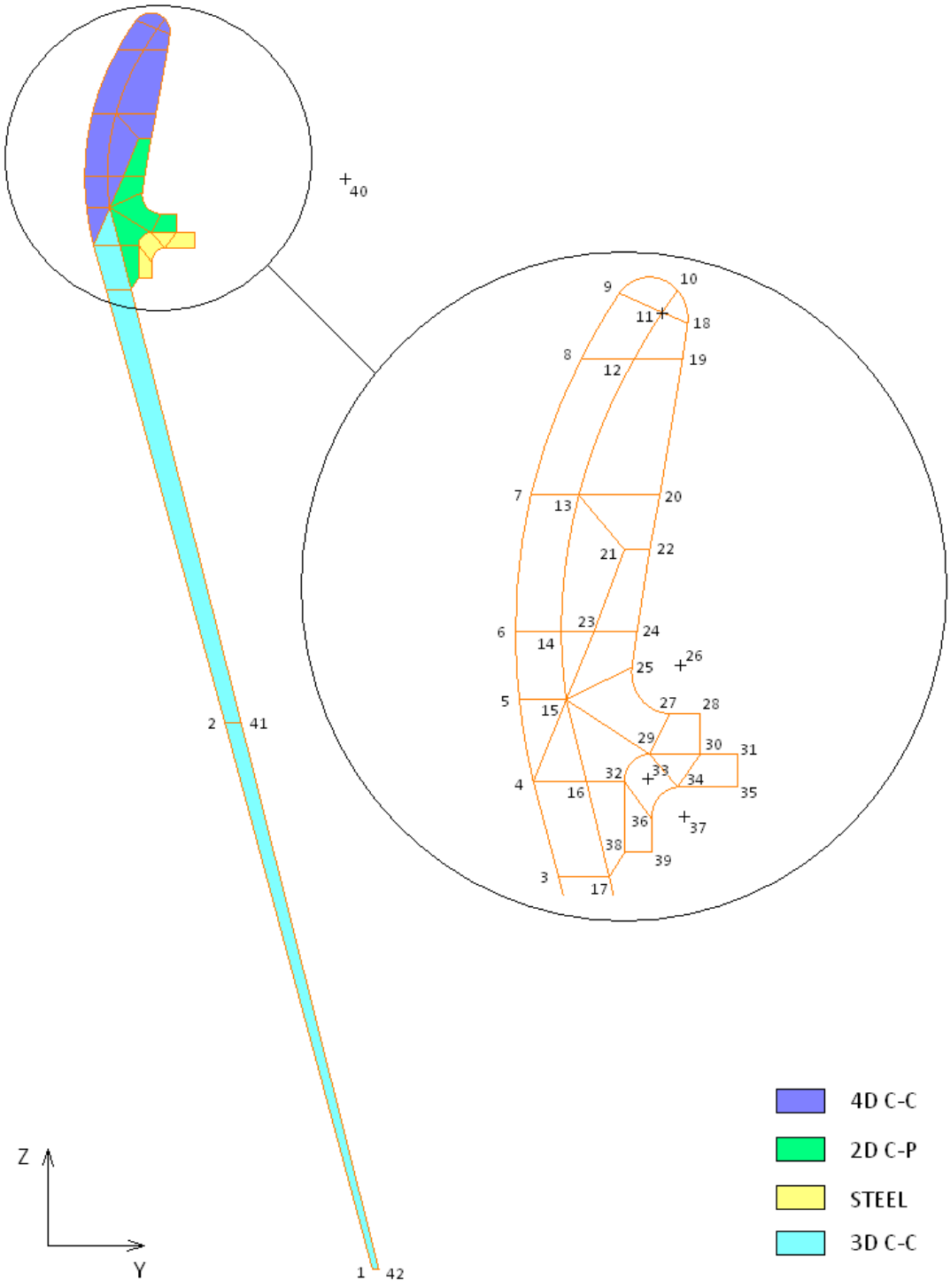

Figure A-1 SRN1 design geometry and constituent points.

POINT NUMBER	Y-COORDINATE (m)	Z-COORDINATE (m)
1	0.302	0
2	0.184	0.435
3	0.089	0.78
4	0.079	0.815
5	0.0735	0.845
6	0.072	0.87
7	0.078	0.92
8	0.098	0.97
9	0.113	0.994
10	0.136	0.995
11	0.13	0.987
12	0.119	0.97
13	0.097	0.92
14	0.09	0.87
15	0.092	0.845
16	0.1	0.815
17	0.109	0.78
18	0.14	0.983
19	0.138	0.97
20	0.129	0.92
21	0.115	0.9
22	0.125	0.9
23	0.103	0.87
24	0.12	0.87
25	0.118	0.857
26	0.133	0.855
27	0.133	0.84
28	0.145	0.84
29	0.125	0.825
30	0.145	0.825
31	0.16	0.825
32	0.115	0.815
33	0.125	0.815
34	0.136	0.813
35	0.16	0.813
36	0.126	0.801
37	0.136	0.801
38	0.115	0.789
39	0.126	0.789
40	0.281	0.87
41	0.197	0.435
42	0.307	0

Table A-1 Constituent point coordinates for the SRN1 design.

ARC	CONSTITUENT POINTS	CENTRE POINT
1	4, 5, 6, 7, 8 & 9	40
2	9, 10 & 18	11
3	10, 11, 12, 13, 14 & 15	11
4	25 & 27	26
5	29 & 32	37
6	34 & 36	37

Table A-2 Arc definitions.

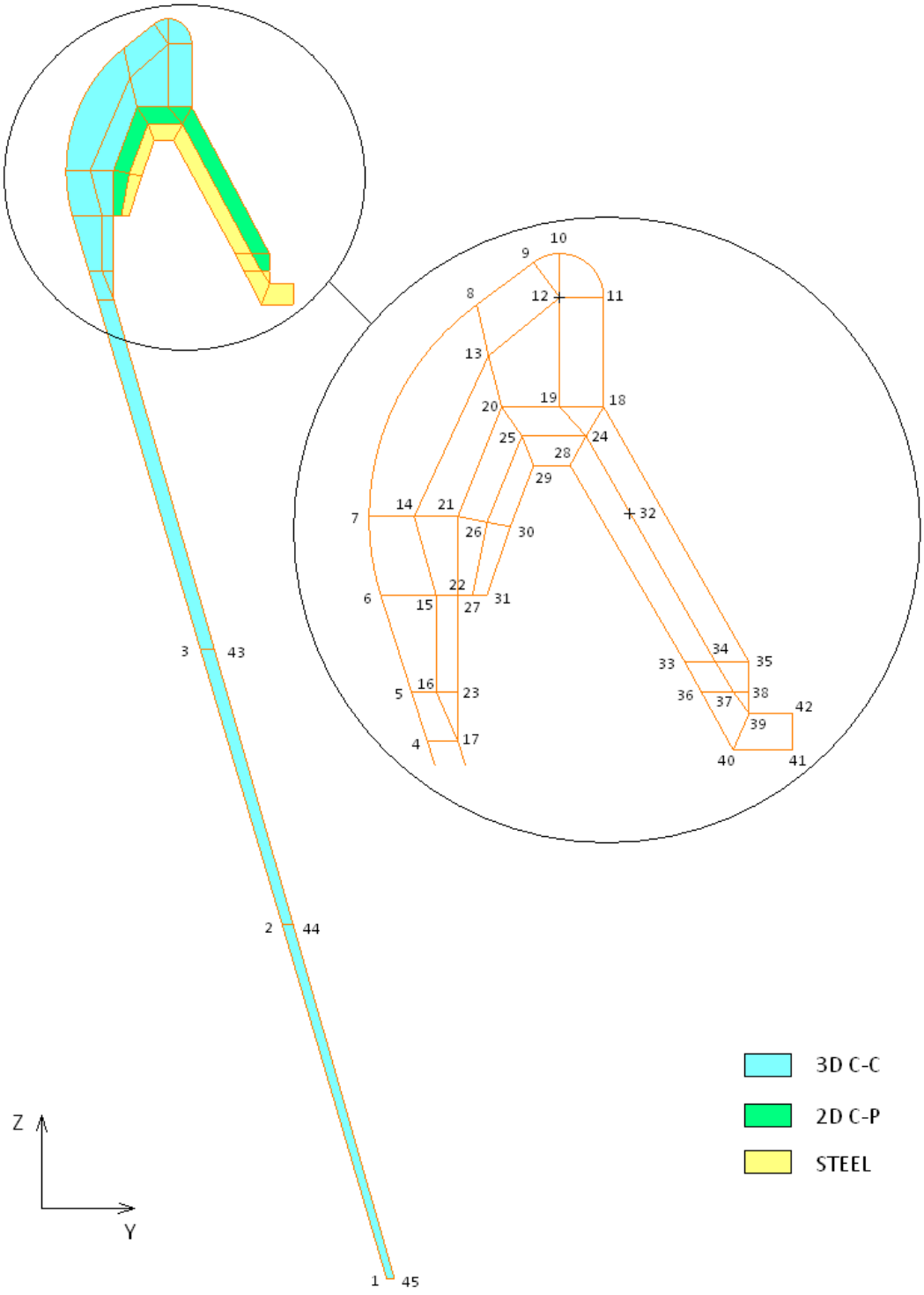

Figure A-2 SRN2 design geometry and constituent points.

POINT NUMBER	Y-COORDINATE (m)	Z-COORDINATE (m)
1	0.636	0
2	0.502	0.422
3	0.397	0.75
4	0.265	1.166
5	0.254	1.2
6	0.233	1.266
7	0.225	1.32
8	0.299	1.465
9	0.338	1.494
10	0.356	1.5
11	0.386	1.47
12	0.356	1.47
13	0.307	1.43
14	0.256	1.32
15	0.271	1.266
16	0.271	1.2
17	0.286	1.166
18	0.386	1.395
19	0.356	1.395
20	0.316	1.395
21	0.286	1.32
22	0.286	1.266
23	0.286	1.2
24	0.374	1.375
25	0.33	1.375
26	0.306	1.316
27	0.296	1.266
28	0.363	1.355
29	0.338	1.355
30	0.322	1.313
31	0.306	1.266
32	0.405	1.32
33	0.442	1.22
34	0.463	1.22
35	0.486	1.22
36	0.453	1.2
37	0.475	1.2
38	0.486	1.2
39	0.486	1.185
40	0.475	1.16
41	0.516	1.16
42	0.516	1.185
43	0.415	0.75
44	0.516	0.422
45	0.646	0

Table A-3 Constituent point coordinates for the SRN2 design.

ARC	CONSTITUENT POINTS	CENTRE POINT
1	6, 7 & 8	32
2	9, 10 & 11	12

Table A-4 Arc definitions.

APPENDIX B – Publications

Appendix B

Publications

[Not included in this format of the thesis]

Pitot de la Beaujardiere, J. F. P., Morozov, E. V. and Bright, G., "Simulation of Fluid-Structure Interaction Phenomena of a Composite Rocket Nozzle", Proceedings of the 9th International Conference on Computational Structures Technology, Athens, Greece, 2-5 September, 2008.

Pitot de la Beaujardiere, J. F. P., Morozov, E. V. and Bright, G., "Numerical Simulation of the Aerothermostructural Response of a Composite Solid Rocket Motor Nozzle During Motor Ignition", Proceedings of the 45th AIAA/ASME/SAE/ASEE Joint Propulsion Conference & Exhibit, Denver, United States of America, 2009.